

Search for particles with anomalous charge in the IceCube detector

Ward Van Driessche



Search for particles with anomalous charge in the IceCube detector

Ward Van Driessche

Auteur

DATUM

Goedgekeurd door

prof. dr. Dirk Ryckbosch
Thesis Promotor

Aanvaard door

prof. dr. Philippe Smet
Hoofd Examenjury

Promotor: prof. dr. Dirk Ryckbosch
Co-promotor: prof. dr. Didar Dobur

Proefschrift ingediend tot het verkrijgen van de academische graad van
Doctor in de Wetenschappen: Fysica

Leden van de examenjury:

Prof. dr. Philippe Smet, voorzitter (Universiteit Gent)
Prof. dr. Herwig Dejonghe (Universiteit Gent)
Prof. dr. Nathalie Jachowicz (Universiteit Gent)
Prof. dr. Klaus Helbing (Bergische Universität Wuppertal)
Prof. dr. Ioana Maris (Université libre de Bruxelles)

Vakgroep Fysica en Sterrenkunde
Faculteit Wetenschappen
Universiteit Gent
Academiejaar 2018-2019



Dankwoord - Acknowledgements

All I can be is me - whoever that is ~ Bob Dylan

- Blub

*If you can keep your head when all about you
Are losing theirs and blaming it on you,
If you can trust yourself when all men doubt you,
But make allowance for their doubting too;
If you can wait and not be tired by waiting,
Or being lied about, don't deal in lies,
Or being hated, don't give way to hating,
And yet don't look too good, nor talk too wise:*

*If you can dream—and not make dreams your master;
If you can think—and not make thoughts your aim;
If you can meet with Triumph and Disaster
And treat those two impostors just the same;
If you can bear to hear the truth you've spoken
Twisted by knaves to make a trap for fools,
Or watch the things you gave your life to, broken,
And stoop and build 'em up with worn-out tools:*

*If you can make one heap of all your winnings
And risk it on one turn of pitch-and-toss,
And lose, and start again at your beginnings
And never breathe a word about your loss;
If you can force your heart and nerve and sinew
To serve your turn long after they are gone,
And so hold on when there is nothing in you
Except the Will which says to them: 'Hold on!'*

*If you can talk with crowds and keep your virtue,
Or walk with Kings - nor lose the common touch,
If neither foes nor loving friends can hurt you,
If all men count with you, but none too much;
If you can fill the unforgiving minute
With sixty seconds' worth of distance run,
Yours is the Earth and everything that's in it,
And - which is more - you'll be a Man, my son!*

~ Rudyard Kipling

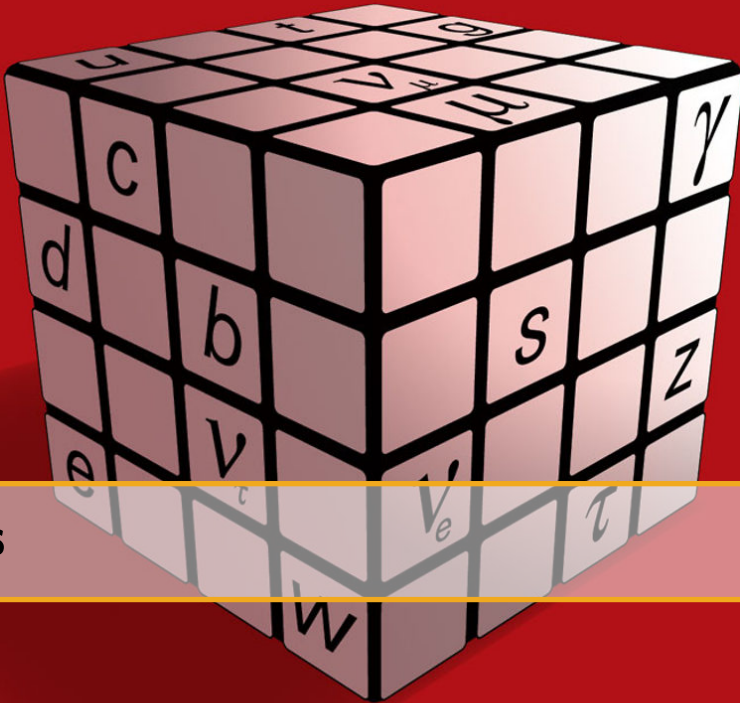


Table of Contents

Nederlandstalige samenvatting 7

Introduction 9

I

Theory and Experiment

1	The Standard Model of Particle Physics	13
1.1	What we call matter: fermions	13
1.1.1	Leptons	14
1.1.2	Quarks	15
1.2	How particles communicate: interactions	15
1.2.1	Gravity	15
1.2.2	Electromagnetism	16
1.2.3	Weak force	17
1.2.4	Strong force	17
1.2.5	A note about bosons	17
1.3	The Standard Model in theory	18
1.3.1	SU(3): quantum chromodynamics	19
1.3.2	SU(2) \times U(1): electroweak	19
1.3.3	Brout-Englert-Higgs mechanism	20
1.3.4	Particle mixing	23
1.4	A success story	26
1.4.1	Predictions	26
1.4.2	Precision tests	26
1.5	The need for physics beyond the Standard Model	27
1.5.1	Unifying theories	30
1.5.2	How to look for new physics	31
2	Motivation of the Analysis	33
2.1	Introduction	33

2.2	Theory	33
2.3	Previous searches	34
2.3.1	Searches with accelerators and fixed targets	34
2.3.2	Colliders	35
2.3.3	Searches for particles with telescopes	35
2.4	Properties of the signal	36
3	Cosmic Rays and Neutrinos	39
3.1	Cosmic rays	39
3.1.1	Discovery of cosmic rays	39
3.1.2	What are cosmic rays?	40
3.1.3	Acceleration mechanism	45
3.1.4	Propagation	50
3.2	Air showers	50
3.2.1	Hadronic component	51
3.2.2	Muonic component	52
3.2.3	Electromagnetic component	52
3.3	Neutrinos	53
3.3.1	Conventional	53
3.3.2	Prompt	54
3.3.3	Astrophysical	55
3.3.4	Other neutrino sources	55
4	Relativistic Particles in Matter	57
4.1	Cherenkov effect	57
4.2	Neutrino interactions	59
4.3	Propagation	60
4.3.1	Cascades	61
4.3.2	Muon tracks	61
4.4	Energy loss formulae	63
4.4.1	Ionization	63
4.4.2	Bremsstrahlung	64
4.4.3	Photonuclear	65
4.4.4	Pair production	65
4.4.5	Conclusion	66
5	The IceCube Experiment	67
5.1	Geometry	67
5.1.1	In-ice array	69
5.1.2	DeepCore	69
5.1.3	IceTop	69
5.1.4	IceCube coordinate system	70
5.2	Hardware components	71
5.2.1	Digital optical modules	71
5.2.2	Calibration	73
5.2.3	Cable systems	73
5.2.4	IceCube laboratory	73

5.3	Deployment	75
5.4	Data taking	75
5.4.1	Triggers	75
5.4.2	Filters	77
5.4.3	Data handling	78
5.5	IceCube event topology	78
5.6	Antarctic ice	79
5.6.1	Ice simulation	79
5.6.2	Systematic uncertainties	81
5.7	Future upgrades	81
5.7.1	IceCube Upgrade	81
5.7.2	IceCube Gen2	82
5.8	Beyond the Standard Model searches	84
5.8.1	Lorentz invariance violation	84
5.8.2	Dark matter	85
5.8.3	Magnetic monopoles	85

II

Simulation, Processing and Analysis

6	Simulation: Event Generation and Propagation	89
6.1	The software framework	89
6.2	Generation	91
6.2.1	Background simulation	91
6.2.2	Signal simulation	94
6.3	Propagation	96
6.3.1	PROPOSAL	96
6.3.2	Photoelectron generators	97
6.4	Detector simulation	98
6.5	Processing	99
6.6	Simulation validation: burn sample	99
6.7	Event viewer	100
7	Reconstruction, Cleaning and Analysis Techniques	101
7.1	Reconstruction	101
7.1.1	Likelihood	101
7.1.2	Line-Fit	102
7.1.3	SPE and MPE	103
7.1.4	Paraboloid	106
7.1.5	Millipede	107
7.1.6	FiniteReco	109
7.2	Pulse cleaning	109
7.3	IceHive	109
7.3.1	HiveSplitter	111
7.3.2	HiveCleaning	112
7.3.3	Remark	112

7.4	CoincSuite	112
7.5	Event cleaning and reconstructions: summary	113
7.6	Minimal-Redundancy-Maximum-Relevance	113
7.7	Boosted Decision Tree classifiers	114
7.7.1	Structure	114
7.7.2	Training	115
7.7.3	Boosting	115
7.7.4	Overtraining	116
8	The SPACE Analysis	119
8.1	Filter selection	120
8.1.1	VEF	121
8.1.2	LowUp	121
8.1.3	Online Muon L2	121
8.1.4	DeepCore	121
8.1.5	Burn sample checks	123
8.2	Level 3	123
8.2.1	The zenith angle cut	124
8.2.2	The rlogL cut	124
8.2.3	The NPE cut	125
8.2.4	The starting rlogL cut	125
8.2.5	The stopping rlogL cut	126
8.3	Level 4	126
8.3.1	Cleaning and quality cuts	127
8.3.2	Variable construction	129
8.3.3	Variable selection	141
8.4	Level 5	141
8.4.1	BDT result	144
8.4.2	Pull-validation	144
8.4.3	Model Rejection Factor	146
8.4.4	Systematic uncertainties	149
8.5	Results	153
8.5.1	Unblinding	153
8.5.2	Limits	153
9	Summary and Conclusion	157

III

Additions

	Appendices	161
A	Distributions	163
A.1	Spherical random numbers	163
A.2	Power law distributions	164
A.3	Angular distributions	165
A.4	Weighting	165
B	Boosted Decision Trees: examples	169
B.1	Decision Tree: simple example	169
B.2	AdaBoost: simple example	169

C	Resampling Methods	173
C.1	Bootstrapping	173
C.2	Cross-validation	173
D	Additional BDT Checks	175
E	Data Events at Final Level	177
	Bibliography	181

Nederlandstalige Samenvatting

Denkt aleer gij doende zijt en doende, denk dan nog ~ Guido Gezelle

De aanpak om nieuwe dingen te ontdekken binnen de fysica is de laatste eeuwen sterk geëvolueerd. De overgang van eenvoudige verklaringen naar theorieën die fenomenen niet alleen konden uitleggen, maar ook experimenteel konden reproduceren, bleek een cruciale stap naar een nieuwe methode in fysisch onderzoek. Als gevolg bracht deze methode nieuwe voorspellingen met zich mee; een theorie kon iets verklaren maar ook fenomenen beschrijven die tot dan toe nog niet werden geobserveerd. Deze fenomenen werden nadien ofwel waargenomen ofwel werd de theorie weerlegd. Hieruit volgde een natuurlijke evolutie in wetenschappelijke aanpak waarbij theorie en experiment elkaar horen te bevestigen.

In de loop van de 20ste eeuw viel er door de technologische ontwikkelingen veel te ontdekken. Men begon langzamerhand beter te begrijpen hoe de wereld in elkaar zit en hoe de wetten van de fysica neergeschreven konden worden. Wiskunde was daarin de taal van fysici om een theorie te ontwikkelen en experimenten te beschrijven. Experimentele deeltjesfysica kende zijn (eerste) hoogdagen in de jaren '60 waarbij deeltjesversnellers het ene na het andere nieuwe deeltje ontdekten: de "particle zoo". Fysici drongen aan op een theorie die een beter beeld kon geven; een handvol basisstenen (fundamentele deeltjes) en regels hoe deze deeltjes zich gedragen en hoe ze tot uiting komen. Die theorie werd de daaropvolgende jaren ontwikkeld en is gekend als het *standaardmodel van de deeltjesfysica*. Het blijkt tot op heden een van de meest succesvolle ooit binnen het vakdomein van de fysica.

Met de ontdekking van het Brout-Englert-Higgs deeltje in 2012 werd de laatste bouwsteen, die door het standaardmodel voorspeld was, gevonden. Het model verklaart echter niet alles. We hebben bijvoorbeeld nog geen idee wat donkere materie precies is, waarom er zoveel minder antimaterie is in vergelijking met materie, enzovoort. Ook de schijnbaar wiskundige willekeur in het standaardmodel roept tot op heden nog steeds vragen op. Er lijken drie types leptonen te zijn. Waarom drie? En waarom zijn er welbepaalde symmetrieën die het standaardmodel beschrijven terwijl er ontelbaar veel andere symmetrieën mogelijk zijn? Waarom deze niet? Om deze redenen proberen fysici in experimenten op zoek te gaan naar processen die met de huidige, aanvaarde modellen nog niet beschreven kunnen worden. Dit zou ons een betere controle kunnen geven welk soort nieuwe theorie - waar er honderden van zijn - de juiste is. Deze experimenten worden steeds complexer: ze worden groter of minutieuzer en veelal een combinatie van beide. Deze complexiteit brengt een groter kostenplaatje met zich mee waardoor deze projecten goed argumenteerbaar moeten zijn: ze zijn een gerichte tast in het duister.

Er zijn ook andere experimenten die met de waarnemingen van gekende deeltjes proberen om beter te achterhalen hoe bepaalde processen in ons universum tot stand komen. Een voorbeeld hiervan is het IceCube neutrino observatorium dat gesitueerd is in het ijs centraal op de Zuidpool. Het voornaamste doel van dit experiment is om neutrino's te detecteren, deeltjes die zelden met materie interageren en net daarom een grote bron aan informatie bevatten omdat ze veel vertellen over hun oorsprong. We weten tot op heden nog maar weinig over de precieze werking van de bronnen van deze neutrino's.

Om zoveel mogelijk gebruik te maken van bestaande infrastructuur worden bestaande detectoren zoals IceCube ook gebruikt in zoektochten naar nieuwe fysica. Het doel van dit werk is om met behulp van het IceCube experiment na te gaan of er deeltjes bestaan met een elektromagnetische lading die het standaardmodel niet voorspelt.

Het IceCube experiment werkt met behulp van lichtgevoelige modules die per 60 aan een kabel bevestigd zijn. 86 van zo'n kabels zijn verspreid in een hexagonaal vlak in het ijs dat in totaal ongeveer een kubieke kilometer van volume inneemt. Geladen deeltjes zoals elektronen en muonen die uit een neutrino-interactie kunnen komen, produceren licht in het ijs dat door deze modules waargenomen kan worden. Dit fenomeen is gekend als het Cherenkov-effect en zegt dat de hoeveelheid licht dat geproduceerd wordt afhangt van de lading van het deeltje. Aangezien de enige vrije deeltjes die we kennen een lading hebben die een veelvoud is van de elementaire lading van een elektron e , is het in theorie mogelijk om een onderscheid te maken tussen de gekende deeltjes en deeltjes met een lading die lager is dan e . Deze laatste maken geen deel uit van het standaardmodel en hun observatie zou een nieuwe start kunnen geven voor een meer omvattende theorie die mogelijks andere onopgeloste vragen helpt te verklaren.

De voornaamste uitdaging om op zoek te gaan naar dergelijke deeltjes blijkt de beperking van de detector zelf te zijn. Gekende deeltjes met een hele lage energie blijken niet eenvoudig te onderscheiden van deeltjes met een lage lading. Dit komt voornamelijk omdat de modules van de detector minimaal 17 meter van elkaar liggen. Hierdoor gaat veel van het licht verloren omdat het de optische instrumenten niet kan bereiken. In dit werk wordt er beschreven hoe deze nieuwe deeltjes onderscheiden kunnen worden van muonen en elektronen. Deze laatste ontstaan uit botsingen van kosmische straling met onze atmosfeer waar ze veelvuldig worden geproduceerd in zogenoemde "air showers". Ze kunnen ook de detector betreden als secundaire deeltjes nadat neutrino's interageren met het ijs. Deze neutrino's kunnen geproduceerd worden in kosmische processen zoals gamma ray bursts of supernova's, maar zijn er vooral in grote getale aanwezig door de voorgenoemde air showers.

De analyse beschrijft hoe er vanuit de IceCube data een selectie gemaakt kan worden om deze nieuwe fysica - als ze er is - zo goed mogelijk zichtbaar te maken. Na een reeks selecties om de kwaliteit van de data te verhogen, werden meerdere variabelen gebruikt en ontwikkeld om nadien geïmplementeerd te worden in een "Boosted Decision Tree", i.e. een machine learning techniek die wordt gebruikt in datamining. Er werd tevens ook gebruik gemaakt van een resampling techniek genaamd "pull-validation" om de beperkte statistische mogelijkheden beter te handhaven. De enige mogelijke conclusie die getrokken kon worden was dat er geen indicatie was voor de aanwezigheid van deeltjes met een lage lading. Er werd een bovenlimiet opgesteld waarbij ook rekening gehouden werd met meerdere onzekerheden die deze limiet zouden kunnen beïnvloeden zoals de eigenschappen van het ijs waardoor het licht schijnt. Deze limieten zijn een verbetering van voorgaande experimenten en werden berekend volgens de techniek van Feldman en Cousins binnen een 90% betrouwbaarheidsinterval.

Dit werk was een eerste poging om gebruik te maken van het IceCube experiment om op zoek te gaan naar nieuwe fysica in de vorm van deeltjes met een lading die tot op heden nog nooit zijn geobserveerd. Dergelijke deeltjes werden niet waargenomen waardoor een bovenlimiet werd opgesteld in de mate van hun aanwezigheid mochten ze weldegelijk bestaan.



Scientists have become the bearers of the torch of discovery in our quest for knowledge ~ Stephen Hawking

Having a quest for knowledge seems to be a trait that belongs to human kind. The last couple of centuries, there was a transition from providing simple explanations of physical phenomena to *really understanding* the problem and properly describing it. More and more, a critical mindset became important in having new insights; being convinced of having the final answer is no longer enough. Theories are tested and are only accepted if they can be reproduced in experiments. This approach is not the most easy one and more than often, scientists encounter many obstacles along their way. However, I believe that the feeling scientists get when they have solved a puzzle and see their theory confirmed in an experiment is the driving force behind new discoveries and pushing the limits of current theories. Wanting to know what is beyond our current understanding has made us discover our planet (and others) and never stops us to come up with new questions.

Experimental particle physics is a field that tries to find the smallest detectable particles that make up matter and radiation. These particles carry certain properties such as mass, charge, spin, etc. and allow them to interact with each other. There are only a handful of fundamental interactions known to date: gravity, the strong force, the weak force and the electromagnetic force. It appears that nature follows certain physical rules that can be expressed in a mathematical form. Mathematics made it possible to write down our findings and to expand our knowledge. The theory that describes the last three of the four forces and classifies all known fundamental particles is called the Standard Model (SM) of particle physics. In Chapter 1, an overview is given of the properties of particles and interactions and ends with why physicists think the SM in its current form cannot be the final answer.

There are many theories that try to expand the SM and are called “Beyond-the-Standard-Model theories” (BSM). They introduce new symmetries, new particles, new interactions, etc. Some of these theories also predict the existence of free particles with an electromagnetic charge that is lower than the electron charge, e . Quarks are known to have charges lower than e , but cannot exist freely. In Chapter 2 we motivate the possible existence of these particles and describe their assumed properties.

With the discovery of cosmic rays, a new field of physics was born: astroparticle physics. Experiments could be done on particles that could not originate from our solar system. The energy of these particles also has a wide range and offers to examine particles with a very high energy that do not have to be accelerated by man-made objects. For example, positrons, muons, pions, and kaons were first discovered in cosmic ray interactions. Cosmic rays play a crucial role in modern multimessenger astronomy along with gamma rays, gravitational waves and neutrinos. Each one of these fields has its strengths and weaknesses and many different experiments try to look for these respective signatures. Luckily, some of these experiments can also be used to look for BSM physics but have to account for the processes these experiments are designed to be sensitive too. Therefore, in Chapter 3, we give an overview of the physical processes that are visible in neutrino detectors. We will describe the origin of cosmic rays and neutrinos and how showers of particles are produced from cosmic ray interactions.

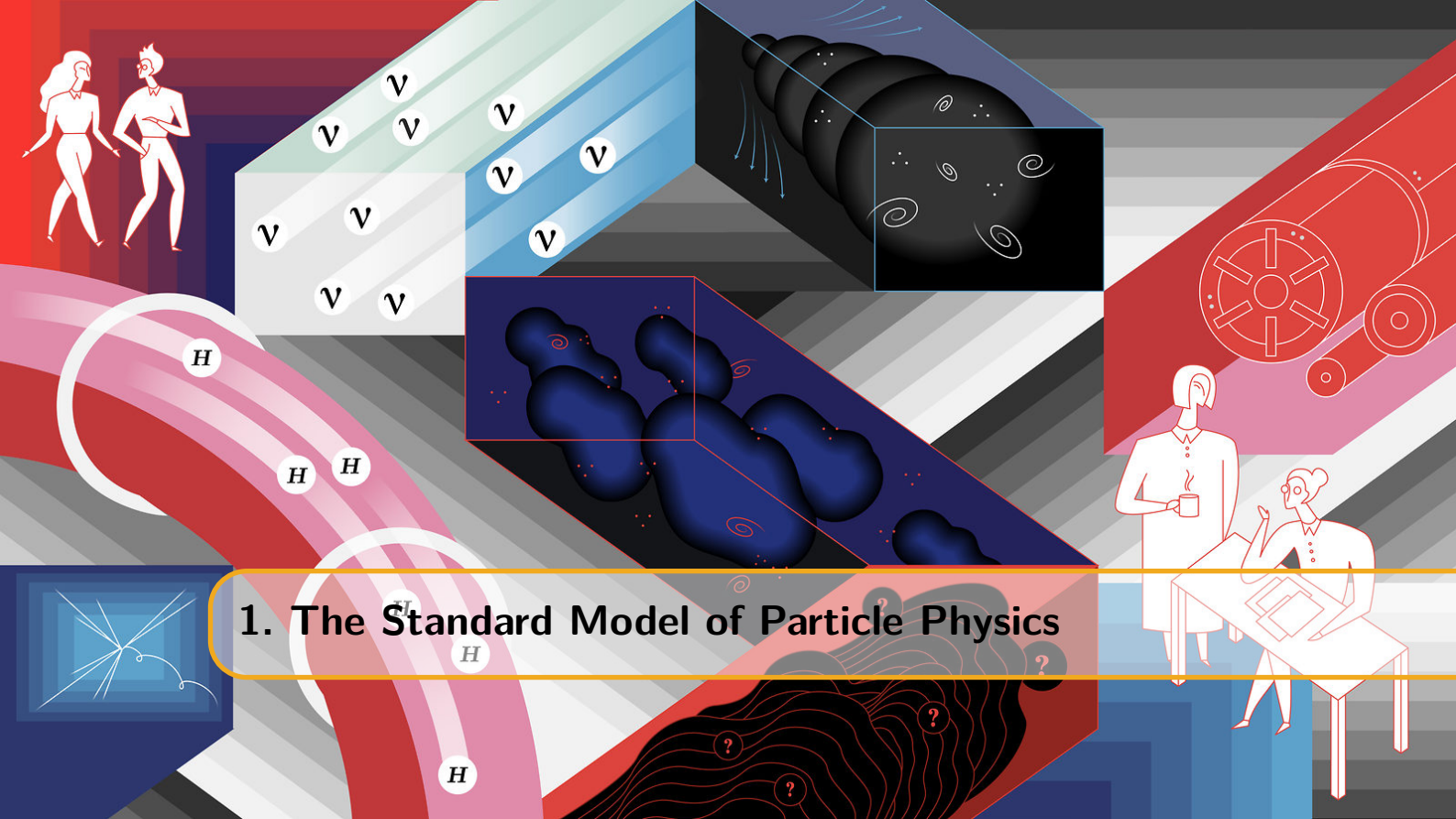
Charged particles can be detected by the production of Cherenkov radiation. These particles can be exotic particles, particles produced in cosmic air showers or secondaries that are created from neutrino interactions. The Cherenkov effect is explained in Chapter 4, together with how charged particles lose their energy when traveling through matter. To be able to detect high-energetic neutrinos, it is crucial to make the instrumented volume of a detector as large as possible. In Chapter 5, we describe how the IceCube Neutrino Observatory is constructed in the ice at South Pole. We describe the hardware components and how the ice is used and modeled for neutrino and charged particle detection.

The next part of this work has a larger focus on the technical details of this analysis that is dedicated to search for particles with an anomalous charge. The simulation steps are discussed in Chapter 6 and several reconstruction and analysis techniques that were used in this work are explained in Chapter 7. In Chapter 8, an overview of the analysis is given and how it was possible to discriminate background events from events that originate from these particles that are not expected from the Standard Model. We conclude if there are hints that these particles exist or, when no new physics is found, we present the maximal abundance that is measurable in the IceCube detector of these particles.

Chapter 9 provides a summary and discussion of this work.

Theory and Experiment

1	The Standard Model of Particle Physics	13
1.1	What we call matter: fermions	
1.2	How particles communicate: interactions	
1.3	The Standard Model in theory	
1.4	A success story	
1.5	The need for physics beyond the Standard Model	
2	Motivation of the Analysis	33
2.1	Introduction	
2.2	Theory	
2.3	Previous searches	
2.4	Properties of the signal	
3	Cosmic Rays and Neutrinos	39
3.1	Cosmic rays	
3.2	Air showers	
3.3	Neutrinos	
4	Relativistic Particles in Matter	57
4.1	Cherenkov effect	
4.2	Neutrino interactions	
4.3	Propagation	
4.4	Energy loss formulae	
5	The IceCube Experiment	67
5.1	Geometry	
5.2	Hardware components	
5.3	Deployment	
5.4	Data taking	
5.5	IceCube event topology	
5.6	Antarctic ice	
5.7	Future upgrades	
5.8	Beyond the Standard Model searches	



1. The Standard Model of Particle Physics

A physicist is an atom's way of knowing about atoms ~ George Wald

The aim of this chapter is to give a summary of the framework that is used in particle physics. This framework was developed in stages throughout the latter half of the 20th century and is known as the Standard Model of particle physics. This model is a quantum field theory that is able to describe most of what is seen in particle physics experiments, and proved to be successful in predicting later experimental discoveries. In this chapter, a brief historical overview of the development of this theory will be given together with a limited description in order to familiarize the reader with concepts that will be used throughout this work. For a more in-depth and exhaustive discussion I refer to Refs. [1, 2, 3, 4]. We start with an overview of the constituent particles of the Standard Model, linking them to our everyday life. Secondly, a general description is given of the nature of forces. Thirdly, we go to a more mathematical and in-depth description of the Standard Model. Lastly, we present the many successes of this model and finish with an argumentation of why there is a need for physics beyond this model.

1.1 What we call matter: fermions

Physics (from Ancient Greek: φυσική - *physikē*, “knowledge of nature”) is the natural science that studies matter. Matter is made up of *atoms* (from Greek: ἄτομος - *atomos**), “indivisible” that can bind together into molecules and account for what is around us in our everyday life. Atoms are made up of a positively charged *nucleus* that is surrounded by one or more *electrons*. The nucleus and electrons are bound to each other via the electromagnetic force. The nucleus is made up of one or more *protons* and, typically, an approximately equal amount of *neutrons*. Because of their similar characteristics, protons and neutrons are often referred to as *nucleons* and together they make up more than 99.9% of an atom’s mass. Nucleons are made up of smaller particles called *quarks*[†], which are, as far as we know, *fundamental particles*. This means that

*Coined by ancient Greek philosophers Leucippus and his pupil Democritus who believed matter was made up of discrete units.

[†]The word “quark” originally appeared in the novel *Finnegans Wake* written by the Irish author James Joyce (1882–1941). The protagonist of the book dreams that he is serving beer to a drunken seagull. Instead of asking for “three quarts for Mister Mark” the inebriated bird says “three quarks for Muster Mark”. Murray Gell-Man had the habit of using names like “squeak” and “squark” for peculiar objects and after encountering the sentence in the book the name struck him as appropriate since the (then hypothetical) particle came in threes.

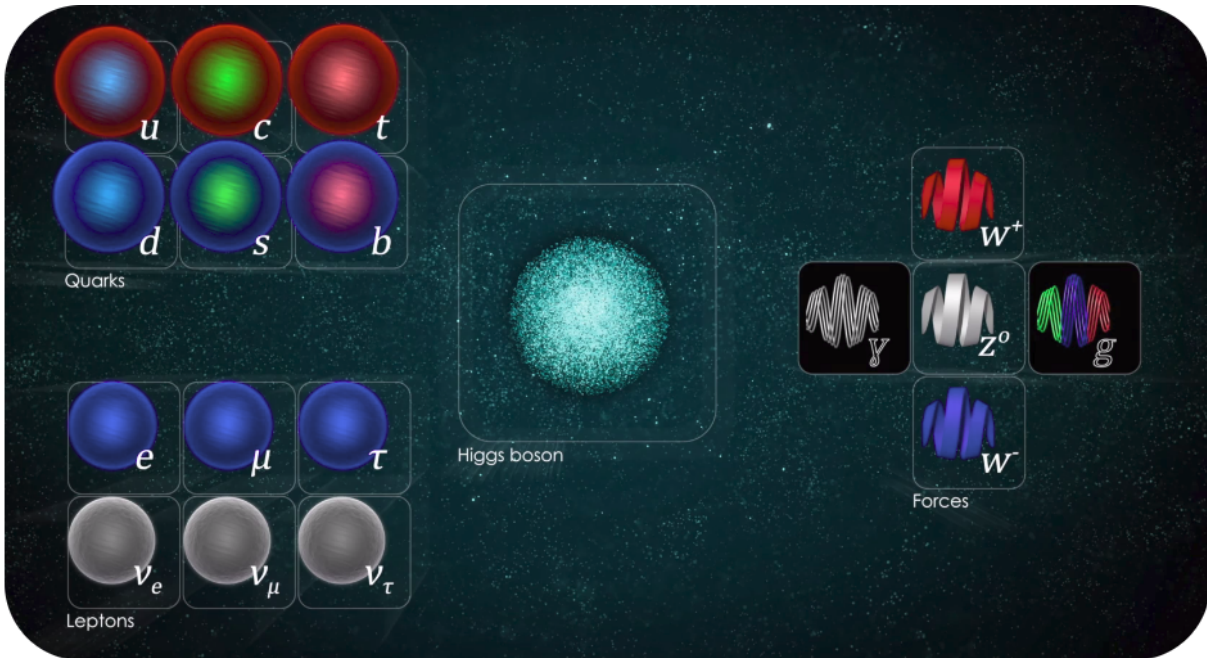


Figure 1.1: The Standard Model of particle physics distinguishes fermions (left) from bosons (right). The Brout-Englert-Higgs boson (middle) is more peculiar as it has no intrinsic spin and plays a special role in the theory. Charges for fermions are not explicitly written to account for antiparticles. Illustration from Ref. [5].

we believe that there are no smaller substructures making up these objects and they are in essence mathematically best described as infinitely small. Because of this, they are often referred to as pointlike. In the Standard Model (SM), these particles are found to be *fermions*, which have odd half-integer spins, obeying the laws of quantum mechanics. The spin of a particle is often illustrated with its classical counterpart in which an object is spinning and thus carries an intrinsic angular momentum. This analogy cannot be extrapolated to pointlike particles, but the property happens to hold the same units as the classical orbital momentum. The spin of a particle seems to be just another property particles have, like charge or mass. Fermions follow Fermi-Dirac statistics and therefore obey the Pauli exclusion principle. As a consequence, fermions cannot occupy the same place at the same time (more formally: no two fermions may be described by the same quantum numbers). This agrees with our macroscopic observations of matter in everyday life: matter interacts with matter; people cannot walk through walls!

In total, the SM distinguishes 24 different fermions that can be subdivided into two distinct classes: *quarks* and *leptons*. There are six quarks (up, down, charm, strange, top and bottom), and six leptons (electron, electron neutrino, muon, muon neutrino, tau and tau neutrino), along with the corresponding antiparticle for each of these fermions. A summary of all the particles in the Standard Model is given in Figure 1.1.

1.1.1 Leptons

Leptons* can be subdivided in two classes: electromagnetically charged particles (e^- , μ^- and τ^-) and the neutral neutrinos† (ν_e , ν_μ and ν_τ). Because of their charge, electrons are the well-known particles that combine together with nucleons into atoms. Being the lightest of the three charged leptons, the electron is said to be part of the first *generation*, together with the electron neutrino.

*λεπτός (leptos) meaning thin, delicate, lightweight, or small. Originally, leptons were considered the “light” particles and hadrons the “heavy” particles, but the discovery of the tau lepton in 1975 broke that rule.

†The Italian word for neutron (neutrono) sounds like the word neutral (neutro) with an augmentative suffix (-one) tacked on the end, making the word a little wordplay. In Italian, it sounds something like “big neutral”. Replace the augmentative suffix -one with the diminutive suffix -ino and you have a “little neutral”, which is a good description of what a neutrino is — a diminutive neutral particle.

Muons differ only from electrons in mass* and make up the second generation together with muon neutrinos. Similarly, tau particles and tau neutrinos define the third generation. All leptons have a corresponding antiparticle indicated by a positive charge (e.g. e^+) or a bar (e.g. $\bar{\nu}_e$). Neutrinos are proven to have a very small mass [6] and interact only via the weak force (Section 1.2.3), making them inherently very hard to detect.

1.1.2 Quarks

The six quarks are called up, down, charm, strange, top and bottom quarks ((u, d), (c, s), (t, b)). Each generation is made up of a particle with charge $+2/3$ and one with $-1/3$ (also visualized in Figure 1.1). These charges are multiples of the absolute electron charge. The difference between generations is again essentially the bare mass of the particles. Because quarks also interact through the strong force (see Section 1.2.4), they combine into *hadrons*[†] (of which nucleons are the best known examples). Due to their color charge and the intrinsic behavior of the strong force, quarks cannot be observed freely: they always combine into color neutral particles, a property called *confinement*. When a hadron, with its constituent quarks, is pulled apart, the attractive force between the quarks does not fall down rapidly since gluons carry color charge themselves. When these particles are pulled apart far enough, it becomes energetically more favorable to produce new quark-antiquark pairs, which again combine into color neutral particles[‡]. The energy requirement for the production of new particles is far below the one to separate the quarks far enough from each other to observe them separately. Antiquarks are again denoted with a bar (i.e. \bar{u}).

Because of their ability to interact via the strong force, particle accelerators in the 1960s led to the discovery of a plethora of possible quark combinations, something that is often referred to as the “particle zoo”.

1.2 How particles communicate: interactions

There are four fundamental interactions known to exist: gravity and electromagnetism, which produce significant long-range forces, and the strong and weak forces that only express themselves at (sub)atomic distances and govern nuclear interactions. These are explained in more detail below and an overview is given in Table 1.1.

Particles interact with each other through the exchange of *gauge bosons* or *force carriers*[§]. Gauge bosons are bundles of energy, *quanta*, and can be seen as excitations of one of the force fields.

Fields are a mathematical approach used by physicists to describe what we observe in experiments. Although the use of fields is very natural, the concept might feel a bit unfamiliar. In the following, the known forces are described in more detail. Gravity plays less of a role in subatomic physics, but is added for completeness and is mainly used to make the reader more familiar with the concept of a field.

1.2.1 Gravity

Gravity (from Latin/old French: *gravitas*/grave, “weighty, heavy”) is the phenomenon wherein massive objects are attracted to each other. Gravitation is famously described by the theory of general relativity proposed by Einstein in 1915. Compared to the other forces, gravity is intrinsically very weak[¶] and is not described in the SM (see Section 1.3). This is why gravity

*This characteristic is often referred to as *lepton universality*.

[†]ἀδρός (adros) meaning thick, robust, massive, or large. This name alludes to the ability of the point-like quarks to bind together and form particles that are massive in a certain sense.

[‡]This process is called *hadronization* and results into the production of “jets” in particle accelerators [7].

[§]A classic and very simplistic way of looking at force carriers is to imagine two people standing on a boat. The force carrier is a heavy ball that can be thrown from one person to the other. Doing so, both persons will move in opposite direction.

[¶]Two magnets that fit in the palm of your hand can deliver a force which is of similar strength as the force that our entire planet exerts on a human body.

Table 1.1: Summary of the known forces and their properties. The relative strengths are quoted in terms of a dimensionless coupling constant (α_g , α_w , α and α_s). These “constants” actually depend on the energy. These numbers were obtained from Ref. [8].

Interaction	Gravitational	Weak	Electromagnetic Electroweak	Strong
Acts on	mass/energy	weak flavor	electric charge	color charge
Couples to	all particles	all fermions	electrically charged particles	quarks, gluons
Mediation	not yet observed	W^+, W^-, Z	γ	gluons
Rel. strength	10^{-39}	10^{-6}	$1/137$	1

is often left out in discussions of particle physics experiments, but is crucial for understanding astronomical objects and how they influence each other. It can, however, be used to explain the concept of a field in a very natural way.

A very good description of gravitation was already provided centuries ago. First published on July 5th, 1686 was Newton’s work *Philosophiae Naturalis Principia Mathematica* (“the Principia”) that first introduced several formulas that are still widely used today. The equation of the force exerted by two massive bodies takes the following form,

$$F = G \frac{m_1 m_2}{r^2}, \quad (1.1)$$

where F is the gravitational force acting between two objects, m_1 and m_2 are the masses of the objects, r is the distance between their center of mass, and G is the gravitational constant.

Newton’s law states that two massive bodies will exert a force on one another that is proportional to their masses, but inversely proportional to the square of the distance between them. Newton realized this would mean that at any given instant in time all massive objects in the universe would know from every other object in the universe where it is located and how massive it is*. Because of this, Newton himself believed his explanation could not be the final answer. The answer is fully described in Einstein’s work of general relativity, but the first idea in the right direction was introduced by Laplace in 1783. Laplace explained that massive objects do not “feel” each other but distort space and time in such a way that objects that are attracted, “fall” towards each other. Field theory makes it possible to treat the laws of physics as a local property instead of an action from a distance.

To date, it has not been possible to describe gravity in the framework of quantum field theory like the other fundamental forces, although, there is still much ongoing work. The gauge bosons from such a quantum field theory for gravity are mostly referred to as *gravitons*.

1.2.2 Electromagnetism

The electromagnetic field (from Ancient Greek: ἥλεκτρον *ēlektron*, “amber”, and μαγνῆτις λίθος, *magnetis lithos*, which means “Magnesian stone”†) presents itself in the electrical and magnetical forces. In the late 1870s, the publication of Maxwell’s *A Treatise on Electricity and Magnetism* showed that the electric and magnetic interactions of negative and positive charges are mediated by one force: electromagnetism. Particles carrying a charge of one of these forces can attract or repel each other.

Similar to the gravitational field, the electromagnetic field pervades all around us, providing the necessary description of how charged particles interact with each other. The interaction of nuclei, which have a positive electric charge, and electrons makes up most of what is described in chemistry.

The force carrier of electromagnetism is called a *photon*, or in other words: light.

*Imagine the attraction of the Moon to the Earth: how are both “communicating”?

†In 1641, Kircher described the magnetic properties of the Magnesian stone in his book *Magne sive de arte magnetica opus tripartitum* [9].

1.2.3 Weak force

The weak force is one aspect of the overarching electroweak theory that combines electromagnetism and the weak force. As opposed to gravity and electromagnetism, it only takes place at very small subatomic distances*. One well known phenomenon that is governed by the weak force is *beta decay* in which free neutrons decay into protons and produce an extra electron and antielectron neutrino. Another beautiful example of the weak force is the driving mechanism in the Sun's thermonuclear process that makes it shine. This process cannot be explained by chemical processes but with the fusion of hydrogen cores into helium where two out of four protons are converted to neutrons. This conversion of the proton into a neutron is explained by the weak force.

The force carriers of the weak force are the W^+ , W^- and Z bosons. Quantum field theory tells us that the interaction strength of particles depends on the coupling constants and the properties of the mediator particles. The coupling constants of the weak force are of similar magnitude as those in electromagnetism. However, because of the mass of the weak force carriers, the interaction strength at low energies, such as radioactive decay, becomes much smaller†. This makes the force seem weak, hence the name‡.

The weak force also has some peculiar properties that are unique in a number of respects:

- it is the only interaction that violates parity symmetry and even does so maximally (V-A interaction),
- its force carriers are massive as opposed to all other force carriers,
- it is the only force capable of changing quarks from one family into a quark of another family.

1.2.4 Strong force

As indicated in Section 1.1, nuclei are made up of protons and neutrons. However, up to now the forces described in this section cannot explain how they can make up a stable combination. The positive/neutral electromagnetic charge of the protons/neutrons would even suggest the opposite. Protons and neutrons are made up by quarks that carry a quantity called *color charge*. Particles carrying a color charge participate in interactions of the strong force. Due to the principle of *self interaction*, the strong force only manifests itself on very small scales§.

The force carriers of the strong force are called *gluons*. These gluons carry a color charge themselves and are massless.

Aside from holding nucleons together, the strong force is also responsible for around 99% of the mass of the nucleon's mass. The massless gluons have a *quantum chromodynamics binding energy* so large that it makes up the bulk of the mass via Einstein's $E = mc^2$ relation. Only a small percentage of the total nucleon mass comes from the bare quark masses.

1.2.5 A note about bosons

As opposed to fermions, which obey Fermi-Dirac statistics and cannot occupy the same quantum state, bosons follow Bose-Einstein statistics¶. Bosons carry integer spins ($s = 0, 1, 2$, etc.) while fermions carry half-integer spins ($s = 1/2, 3/2$, etc.). As a result, bosons have no problem

*The reason being is that the force carriers are massive; more info in Section 1.3.

†The mediator term for photons scales with $\frac{1}{q^2}$ with q the momentum of the mediator. W and Z boson mediator terms scale with $\frac{1}{q^2 - M^2}$ with M the mass of the mediator. When q is low, for example in radioactive decays, this term becomes very small due to the mass of the bosons. On the other hand, if q and M are of similar magnitude, the weak force is strong. For example, the top quark decay will most likely happen via the weak force.

‡It was Fermi who first came up with a proper description of the beta decay in 1933. However, he described the interaction as a 4-point interaction, making it only valid up to energies below 100 GeV.

§As opposed to the weak force where the short distance behaviour is explained due to the mass of the force carriers.

¶The name “boson” originates from Dirac who wanted to commemorate the contributions of Indian physicist S.N. Bose who, together with Einstein, theorized the characteristics of elementary particles that follow Bose-Einstein statistics [10].

occupying the same place at the same time (more formally: two or more bosons may be described by the same quantum numbers). As an example, lasers are very powerful tools that make large numbers of photons to have almost exactly the same energy (which is expressed in having the same color) and direction. Fermions, on the other hand, cannot share the same quantum number, e.g. electrons cannot have the same orbit in an atom. If electrons were bosons, chemistry and matter all around us would be nothing like we see today.

1.3 The Standard Model in theory

Most of the text below is based on the very elaborate book from Franz Mandl and Graham Shaw, *Quantum Field Theory* [11].

The Standard Model is a *quantum field theory*, meaning its fundamental objects are fields of a quantum nature that are defined at all points in spacetime. These fields are

- fermion fields, ψ , which describe “matter particles”;
- electroweak boson fields, W^1, W^2, W^3 and B ;
- gluon fields, G^a ; and
- the Higgs field, ϕ .

Quantum field theory treats particles as excited states of one of these underlying fields, so called *field quanta*. The difference between classical and quantum fields is that they are operator-valued. Classical fields can in principle take on distinct values at each point in space whereas a quantum field accommodates observations of quantum mechanics such as

- objects have characteristics of both particles and waves (called “wave-particle duality”);
- the quantization of energy, meaning that only discrete energy values are possible;
- the lowest achievable energy is not equal to absolute zero, but has a zero-point energy*.

The dynamics of the quantum state and the fundamental fields are determined by the Lagrangian density \mathcal{L} . Writing the time and space coordinates in the form $(t, \mathbf{x}) = (x^0, x^1, x^2, x^3) = x^\mu$, the equations of motion of these fields can be written as:

$$\frac{\partial}{\partial x_\mu} \left[\frac{\partial \mathcal{L}}{\partial (\partial \phi / \partial x^\mu)} \right] - \frac{\partial \mathcal{L}}{\partial \phi} = 0, \quad (1.2)$$

which follow from the principle of least action. The Lagrangian function depends on the fields and how these fields change in spacetime: $\mathcal{L}(\phi, \nabla \phi)$. Quantization of these fields can be obtained by interpreting the coordinates and momenta as Heisenberg operators, and subjecting these to canonical commutation relations.

Furthermore, the Standard Model is a gauge theory in which the Lagrangian is invariant under certain Lie groups (referred to as the symmetry group or the gauge group of the theory) of local transformations. For quantized gauge groups, the quanta of the gauge fields are referred to as *gauge bosons*. A gauge theory is a mathematical model that has a gauge freedom; there are mathematical degrees of freedom that are redundant. In other words: different mathematical expressions describe the exact same physical system and are in that sense not physical. An experiment could never uniquely determine their values, even in principle†. If the phase of the wavefunction is changed by a different amount at each point in spacetime and the physics remains unchanged, the Lagrangian is said to follow a *local gauge symmetry* [11].

The Standard Model is defined by the local $SU(3) \times SU(2) \times U(1)$ gauge symmetry. Each element gives rise to one of the three fundamental forces.

*The zero-point energy follows from the Heisenberg uncertainty principle that states that the position and momentum of a particle are not fixed but have a small range of variance: $\sigma_x \sigma_p \geq \frac{\hbar}{2}$. A system having zero energy would imply a motionless system at a fixed location, violating the uncertainty principle and is therefore forbidden.

†Imagine a perfect cylinder that can be twisted without deforming. It is not possible to distinguish a cylinder that has been twisted or not. To be able to determine it, an initial gauge has to be present. A horizontal line drawn on the cylinder can determine if the cylinder has been deformed or not.

1.3.1 SU(3): quantum chromodynamics

The quantum chromodynamics (QCD) sector defines the interactions between quarks and gluons. Since leptons do not carry color charge, they do not participate in this interaction. The Dirac Lagrangian of the quarks coupled to the gluon fields is given by

$$\mathcal{L}_{QCD} = \sum_{\psi} \bar{\psi}_i \left(i\gamma^\mu \left(\partial_\mu \delta_{ij} - ig_s G_\mu^a T_{ij}^a \right) - m_\psi \delta_{ij} \right) \psi_j - \frac{1}{4} G_{\mu\nu}^a G_a^{\mu\nu}, \quad (1.3)$$

where we sum over the fields of the strong charge and

ψ_i is the Dirac spinor of the quark field (the subscript $i = r, g, b$ represents the color charges);

γ^μ are the Dirac matrices;

G_μ^a is the 8-component ($a = 1, 2, \dots, 8$) SU(3) gauge field;

T_{ij}^a are the 3×3 Gell-Mann matrices (generators of the SU(3) color group);

$G_{\mu\nu}^a$ are the field strength tensors for the gluons;

g_s is the strong coupling constant;

m_ψ corresponds to the quark masses.

1.3.2 SU(2) \times U(1): electroweak

The electroweak (EW) sector is a Yang-Mills gauge theory with the symmetry group $SU(2)_L \times U(1)$. The Lagrangian is given by

$$\begin{aligned} \mathcal{L}_{EW} &= \sum_{\psi} \bar{\psi} \gamma^\mu \left(i\partial_\mu - \frac{g'}{2} Y_W B_\mu - \frac{g}{2} \vec{\tau}_L \vec{W}_\mu \right) \psi - \frac{1}{4} W_a^{\mu\nu} W_{\mu\nu}^a - \frac{1}{4} B^{\mu\nu} B_{\mu\nu} \\ &= \bar{Q}_i i D_\mu \gamma^\mu Q_i + \bar{u}_i i D_\mu \gamma^\mu u_i + \bar{d}_i i D_\mu \gamma^\mu d_i + \bar{L}_i (i D_\mu \gamma^\mu) L_i + \bar{l}_{R,i} (i D_\mu \gamma^\mu) l_{R,i} \\ &\quad - \frac{1}{4} W_a^{\mu\nu} W_{\mu\nu}^a - \frac{1}{4} B^{\mu\nu} B_{\mu\nu}, \end{aligned} \quad (1.4)$$

where

B_μ is the U(1) gauge field;

Y_W is the weak hypercharge* (the generator of the U(1) group);

\vec{W}_μ is the 3-component SU(2) gauge field;

$\vec{\tau}_L$ are the Pauli matrices (infinitesimal generators of the SU(2) group with subscript L to indicate that they only act on left-chiral fermions);

g' (weak hypercharge) and g (weak isospin) are the U(1) and SU(2) coupling constants respectively;

$W^{a\mu\nu}$ ($a = 1, 2, 3$) and $B^{\mu\nu}$ are the field strength tensors for the weak isospin and weak hypercharge fields;

Q, u and d are the left-handed doublet, right-handed singlet up and right-handed singlet down quark fields;

L and l are the left-handed doublet and right-handed singlet lepton fields.

The field strengths are given by

$$\begin{aligned} W_{\mu\nu}^a &= \partial_\mu W_\nu^a - \partial_\nu W_\mu^a + g \epsilon^{abc} W_\mu^b W_\nu^c, \\ B_{\mu\nu} &= \partial_\mu B_\nu - \partial_\nu B_\mu, \end{aligned}$$

and the covariant derivative for the left- and right-handed fermions by,

$$\begin{aligned} D_\mu \psi_L &= \left(\partial_\mu - i \frac{g}{2} \tau_a W_\mu^a - i \frac{g'}{2} Y_W B_\mu \right) \psi_L, \\ D_\mu \psi_R &= \left(\partial_\mu - i \frac{g'}{2} Y_W B_\mu \right) \psi_R, \end{aligned}$$

*The weak hypercharge follows the relation $Y_W = 2(Q - T_3)$ where Q is the electric charge and T_W the third component of the weak isospin.

where one simply has to fill in the appropriate weak hypercharge for the corresponding quark and lepton fields.

It is worth noting that no terms are included for fermion masses. These would have the form of $m\bar{\psi}\psi$ but are forbidden as they would break the $SU(2)_L \times U(1)$ gauge invariance. Neither is it possible to add explicit mass terms for the $U(1)$ and $SU(2)$ gauge fields.

1.3.3 Brout-Englert-Higgs mechanism

To come to a viable description of the elementary particles, one is required to introduce masses into a chiral theory. The masses of the W and Z bosons are explained by use of the Brout-Englert-Higgs (BEH) mechanism formulation. Introducing one or more scalar fields, the Higgs fields, which can acquire a vacuum expectation value (vev), make it possible to spontaneously break a symmetry in the Lagrangian. We say that electroweak symmetry is broken down to a weak symmetry and electromagnetism.

Since the electroweak theory after symmetry breaking should contain three massive gauge bosons (W^+ , W^- and Z), the scalar fields of the Higgs fields should contain at least three degrees of freedom. The simplest approach to do this is by introducing a complex, scalar $SU(2)$ doublet Φ with positive hypercharge ($Y_W = 1$),

$$\Phi = \begin{pmatrix} \phi^+ \\ \phi^0 \end{pmatrix} = \frac{1}{\sqrt{2}} \begin{pmatrix} \phi_1 + i\phi_2 \\ \phi_3 + i\phi_4 \end{pmatrix}, \quad (1.5)$$

Similar to the $SU(2)$ symmetry of the EW theory, four new gauge particles are introduced: H^+ , H^- , H^0 and H .

Massive bosons

Having introduced this scalar doublet, one needs to add the corresponding Lagrangian term to the electroweak Lagrangian from Eq. 1.4,

$$\mathcal{L}_S = (D^\mu \Phi)^\dagger (D_\mu \Phi) - V(\Phi), \quad \text{with } V(\Phi) = \mu^2 \Phi^\dagger \Phi + \lambda (\Phi^\dagger \Phi)^2. \quad (1.6)$$

The first term is the kinetic term while the second corresponds to the potential of the scalar field*. The linear term in the potential needs to be positive to ensure an absolute minimum in the Lagrangian. The quadratic term can either be positive or negative, depending on whether $\mu^2 > 0$ or $\mu^2 < 0$. This is illustrated in Figure 1.2. In the former case, the scalar potential has an absolute minimum at the origin:

$$\langle 0 | \Phi | 0 \rangle \equiv \Phi_0 = \begin{pmatrix} 0 \\ 0 \end{pmatrix}. \quad (1.7)$$

From Eq. 1.6 and 1.7, one can see that the kinetic term does not give rise to massive particles in this scenario†. In the case of $\mu^2 < 0$, the minimum is no longer located at the origin of the fields: $\partial_{|\Phi|} V(|\Phi|) = 0$ for $|\Phi| = \sqrt{-\frac{\mu^2}{2\lambda}}$, hence one possible solution is‡

$$\langle 0 | \Phi | 0 \rangle \equiv \Phi_0 = \begin{pmatrix} 0 \\ \frac{v}{\sqrt{2}} \end{pmatrix}, \quad \text{with } v = \sqrt{-\frac{\mu^2}{\lambda}}. \quad (1.8)$$

v is referred to as the *vacuum expectation value* to reflect that the Higgs field is always “on”. To investigate the terms, we can expand the field around the minimum:

$$\Phi(x) = \begin{pmatrix} \theta_2(x) + i\theta_1(x) \\ \frac{v+H(x)}{\sqrt{2}} - i\theta_3(x) \end{pmatrix} = e^{i\theta_a \tau_a} \begin{pmatrix} 0 \\ \frac{v+H(x)}{\sqrt{2}} \end{pmatrix}. \quad (1.9)$$

*The form of the potential is not known from first principles, but is the simplest form that can explain the spontaneous symmetry breaking mechanism.

†Easy to see when substituting $v = 0$ in Eq. 1.13.

‡It is not possible for the charged part of the fields to have a vacuum expectation value as this would not be in agreement with electromagnetism. The upper part in Eq. 1.8 is therefore set to zero.

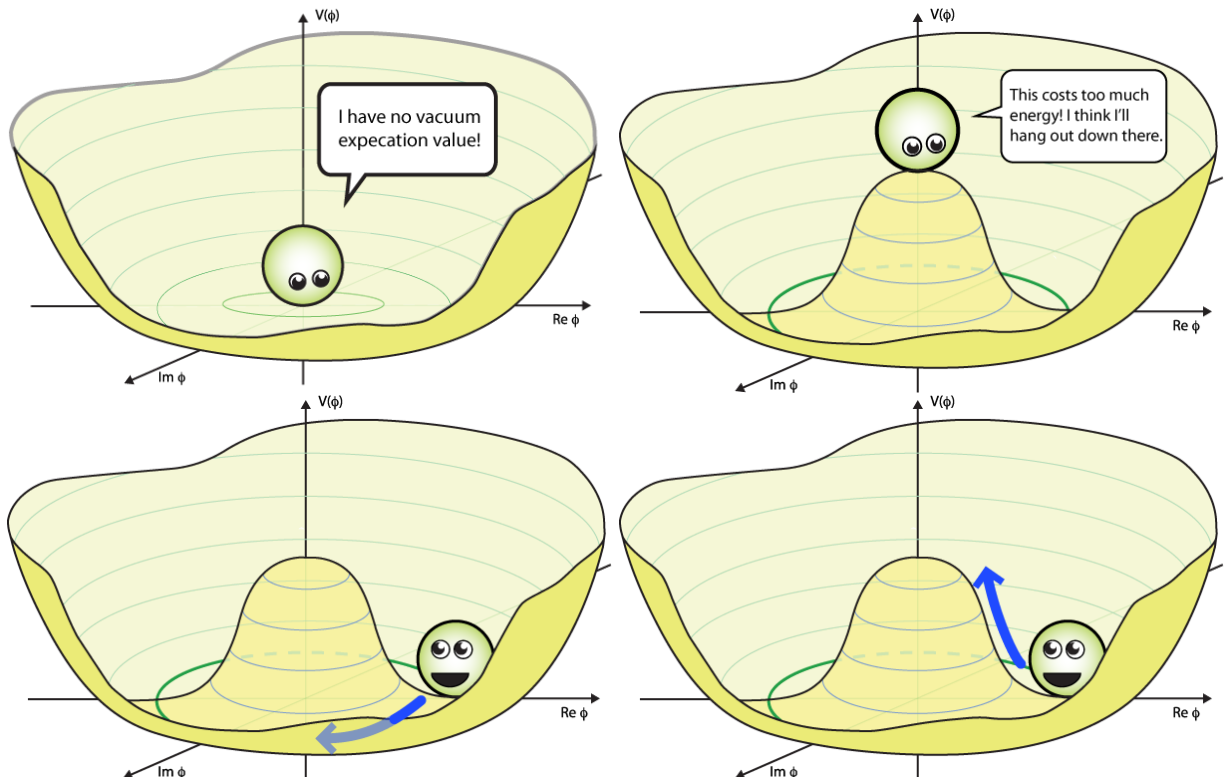


Figure 1.2: In this example the Higgs potential is illustrated in function of a complex scalar field (2D). The principle is the same for a complex scalar doublet but a lot harder to visualize. *Top left:* the Higgs potential with $\mu^2 > 0$, there is no vacuum expectation value. *Top right:* $\mu^2 < 0$, the origin is now a maximum and not stable; the scalar field will move to the lowest possible energy state. *Bottom left:* a flat direction in the potential corresponds to a massless Goldstone mode (remember there are two extra scalar fields in the full theory, meaning there are a total of three). *Bottom right:* the concave shape of the potential near the minimum defines the Higgs boson mass. Illustrations from Ref. [12].

Implementing this into Eq. 1.6 would yield the existence of unphysical fields $\phi_{1,2,3}$ that give rise to three extra degrees of freedom that were not present in the original Lagrangian*. Since a change of variables cannot alter the number of d.o.f. of a system, one can conclude that three fields do not represent physical fields. They can be removed by fixing a gauge, the unitary gauge, that breaks the original symmetry of the system.

$$\Phi(x) \rightarrow e^{-i\theta_a \tau_a} \Phi(x) = \begin{pmatrix} 0 \\ \frac{v+H(x)}{\sqrt{2}} \end{pmatrix}, \quad (1.10)$$

where we have introduced a new scalar field $H(x)$. After inserting this in the kinetic part of the scalar Lagrangian (Eq. 1.6) and redefining the gauge fields as

$$\begin{aligned} W_\mu^\pm &= \frac{1}{\sqrt{2}} (W_\mu^1 \mp iW_\mu^2), \\ Z_\mu &= \frac{1}{\sqrt{g^2 + g'^2}} (gW_\mu^3 - g'B_\mu), \\ A_\mu &= \frac{1}{\sqrt{g^2 + g'^2}} (gW_\mu^3 + g'B_\mu), \end{aligned} \quad (1.11)$$

we find for the kinetic part of the scalar Lagrangian:

$$|D_\mu \Phi|^2 = \frac{1}{2} (\partial_\mu H)^2 + \frac{1}{2} g^2 (v + H)^2 W_\mu^+ W^{-\mu} + \frac{1}{8} (v + H)^2 (g^2 + g'^2) Z_\mu Z^\mu. \quad (1.12)$$

Since mass terms enter this equation in the general form of $M_W^2 W_\mu W^\mu$ for the W bosons and $\frac{1}{2} M_Z^2 Z_\mu Z^\mu$ for the Z boson, the mass terms of the gauge bosons after spontaneous symmetry breaking can be written down as:

$$\begin{aligned} M_W &= \frac{1}{2} vg, \\ M_Z &= \frac{1}{2} v \sqrt{g^2 + g'^2}, \\ M_A &= 0, \end{aligned} \quad (1.13)$$

where it is clear that the photon remains massless†.

Using the potential term in Eq. 1.6 together with the vev in Eq. 1.10, we find for the Lagrangian of the Higgs boson

$$\mathcal{L}_H = \frac{1}{2} (\partial_\mu H) (\partial^\mu H) - \lambda v^2 H^2 - \lambda v H^3 - \frac{\lambda}{4} H^4. \quad (1.14)$$

The first term again corresponds to the kinetic term, whereas the third and fourth refer to the three- and four-point self-interactions of the Higgs, respectively. Scalar masses have the general form $\frac{1}{2} m\phi^2$; the Higgs boson mass is thus equal to

$$m_H = 2\lambda v^2 = -2\mu^2, \quad (1.15)$$

and needs to be determined experimentally.

Working through the interaction terms of the Lagrangian, one can show that the electric charge e is related to the couplings of the weak isospin g and hypercharge g' .

*In Eq. 1.6, the vector fields are massless and each give rise to 2 d.o.f. The vev makes the three vector fields massive, thus adding 3 d.o.f. and introduce three unphysical fields.

†Because the W and Z bosons are massive, it costs energy to produce them and so the weak force is only really effective over a short distance. This is in contrast to the massless photons that result into a long range electromagnetic force. Thus, the Higgs field is responsible for the “weakness” of the weak force.

$$e = g \sin \theta_W = g' \cos \theta_W, \quad (1.16)$$

where the Weinberg angle is denoted as θ_W and indicates the magnitude of rotation of the boson fields after spontaneous symmetry breaking:

$$\begin{pmatrix} \gamma \\ Z \end{pmatrix} = \begin{pmatrix} \cos \theta_W & \sin \theta_W \\ -\sin \theta_W & \cos \theta_W \end{pmatrix} \begin{pmatrix} B^0 \\ W^0 \end{pmatrix}, \quad (1.17)$$

and is related to the weak isospin and hypercharge:

$$\cos \theta_W = \frac{g}{\sqrt{g^2 + g'^2}} \quad \text{and} \quad \sin \theta_W = \frac{g'}{\sqrt{g^2 + g'^2}}. \quad (1.18)$$

Massive fermions

A term like $-m\bar{\psi}\psi = -m[\bar{\psi}_L\psi_R + \bar{\psi}_R\psi_L]$, where we have decomposed the equation into the left- and right-handed chiral states* is not gauge invariant in the Lagrangian. The left-handed fermions form an isospin *doublet* and the right-handed fermions form isospin *singlets*. They transform differently under $SU(2)_L \times U(1)_Y$:

$$\begin{aligned} \chi_L &\rightarrow \chi'_L = \chi_L e^{i\vec{\tau}_L \vec{W} + i\alpha Y_W}, \\ \psi_R &\rightarrow \psi'_R = \psi_R e^{i\alpha Y_W}. \end{aligned} \quad (1.19)$$

It is possible for the fields to couple to the complex Higgs doublet, defined in Eq. 1.5, by adding Yukawa couplings. This results into terms that are singlets under $SU(2)_L$ and $U(1)_Y$:

$$\mathcal{L}_{Yuk} = \lambda_e \overline{L} \Phi e_R - \lambda_d \overline{Q} \Phi d_R - \lambda_u \overline{Q} \tilde{\Phi} u_R + h.c., \quad (1.20)$$

where we have introduced the conjugate of Φ , $\tilde{\Phi} = i\tau_2 \Phi^*$, which has a negative hypercharge. After spontaneous symmetry breaking (Eq. 1.10), we find:

$$\begin{aligned} L_{Yuk} &= -\frac{1}{\sqrt{2}} \lambda_e (\bar{\nu}_e, \bar{e}_L) \begin{pmatrix} 0 \\ v + H(x) \end{pmatrix} e_R + \dots \\ &= -\frac{1}{\sqrt{2}} \lambda_e (v + H(x)) \bar{e}_L e_R + \dots, \end{aligned} \quad (1.21)$$

where we highlighted only the electron part. Fermion mass terms have the general form $m_f \bar{f}_L f_R + h.c.$. Therefore, one finds:

$$m_e = \frac{\lambda_e v}{\sqrt{2}}, \quad m_u = \frac{\lambda_u v}{\sqrt{2}}, \quad m_d = \frac{\lambda_d v}{\sqrt{2}}. \quad (1.22)$$

The mass of the fermions is again not predicted since the Yukawa coupling parameters are free parameters.

1.3.4 Particle mixing

In Eq. 1.20, we introduced Yukawa coupling constants to explain the mass of fermions. In its most general realizations, these couplings are not constants but matrices. This will introduce possible mixing of *flavor eigenstates* into different *mass eigenstates*. Let us write out the second term in Eq. 1.20:

* $\psi_L = P_L \psi = \frac{1-\gamma^5}{2} \psi$ and $\psi_R = P_R \psi = \frac{1+\gamma^5}{2} \psi$.

$$\begin{aligned} \lambda_d \overline{Q_L} \Phi d_R &= \Lambda_{ij}^d \overline{Q_{Li}^I} \Phi d_{Rj}^I = \Lambda_{ij}^d (\text{up-type down-type})_{Li}^I \begin{pmatrix} \phi^+ \\ \phi^0 \end{pmatrix} (\text{down-type})_{Rj}^I \\ &= \begin{pmatrix} \Lambda_{11} \overline{(u\ d)_L^I} \begin{pmatrix} \phi^+ \\ \phi^0 \end{pmatrix} & \Lambda_{12} \overline{(u\ d)_L^I} \begin{pmatrix} \phi^+ \\ \phi^0 \end{pmatrix} & \Lambda_{13} \overline{(u\ d)_L^I} \begin{pmatrix} \phi^+ \\ \phi^0 \end{pmatrix} \\ \Lambda_{21} \overline{(c\ s)_L^I} \begin{pmatrix} \phi^+ \\ \phi^0 \end{pmatrix} & \Lambda_{22} \overline{(c\ s)_L^I} \begin{pmatrix} \phi^+ \\ \phi^0 \end{pmatrix} & \Lambda_{23} \overline{(c\ s)_L^I} \begin{pmatrix} \phi^+ \\ \phi^0 \end{pmatrix} \\ \Lambda_{31} \overline{(t\ b)_L^I} \begin{pmatrix} \phi^+ \\ \phi^0 \end{pmatrix} & \Lambda_{32} \overline{(t\ b)_L^I} \begin{pmatrix} \phi^+ \\ \phi^0 \end{pmatrix} & \Lambda_{33} \overline{(t\ b)_L^I} \begin{pmatrix} \phi^+ \\ \phi^0 \end{pmatrix} \end{pmatrix} \cdot \begin{pmatrix} d_R^I \\ s_R^I \\ b_R^I \end{pmatrix}, \end{aligned} \quad (1.23)$$

where the superscript I implies that the fermion fields are expressed in the *interaction (flavor)* basis. The subscript i stands for the three generations. This means that after symmetry breaking the quark mass terms break down into

$$\begin{aligned} -\mathcal{L}_{Yuk}^{\text{quarks}} &= \Lambda_{ij}^d \overline{d_{Li}^I} \frac{v}{\sqrt{2}} d_{Rj}^I + \Lambda_{ij}^u \overline{u_{Li}^I} \frac{v}{\sqrt{2}} u_{Rj}^I + \dots \\ &= M_{ij}^d \overline{d_{Li}^I} d_{Rj}^I + M_{ij}^u \overline{u_{Li}^I} u_{Rj}^I + \dots \end{aligned} \quad (1.24)$$

where we have omitted the hermitian conjugate terms and the Higgs field interaction terms. Note that the u - and d -terms in the equation still each represent the three up- and down-type quarks respectively. There is mixing between the flavor fields as there is no reason why the matrix M should be diagonal*.

To obtain proper mass terms, one has to diagonalize the mass matrices M^u and M^d and find proper eigenstates. We introduce unitary matrices V as follows

$$\begin{aligned} M_{diag}^d &= V_L^d M^d V_R^{d\dagger}, \\ M_{diag}^u &= V_L^u M^u V_R^{u\dagger}, \end{aligned} \quad (1.25)$$

which can be done when the matrices V are unitary ($V_L^{d,u\dagger} V_L^{d,u} = \mathbb{1}$). Eq. 1.24 can now be expressed as follows:

$$\begin{aligned} -\mathcal{L}_{Yuk}^{\text{quarks}} &= \overline{d_{Li}^I} M_{ij}^d d_{Rj}^I + \overline{u_{Li}^I} M_{ij}^u u_{Rj}^I + \dots \\ &= \overline{d_{Li}^I} V_L^{d\dagger} V_L^d M_{ij}^d V_R^d V_R^d d_{Rj}^I + \overline{u_{Li}^I} V_L^{u\dagger} V_L^u M_{ij}^u V_R^u V_R^u u_{Rj}^I + \dots \\ &= \overline{d_{Li}^I} (M_{ij}^d)_{diag} d_{Rj}^I + \overline{u_{Li}^I} (M_{ij}^u)_{diag} u_{Rj}^I + \dots \\ &\quad , \end{aligned} \quad (1.26)$$

where the V matrices have been absorbed in the quark flavor eigenstates and have formed mass eigenstates. These mass eigenstates couple differently to the gauge fields of the weak interaction. Working out one term from Eq. 1.4, the mixing of the flavor eigenstates is clearly visible

$$\begin{aligned} \mathcal{L}_{kinetic}(Q_L) &= i \overline{Q_{Li}^I} \gamma_\mu D^\mu Q_{Li}^I \\ &= \frac{g}{\sqrt{2}} \overline{u_{Li}^I} \gamma_\mu W^{-\mu} d_{Li}^I + \frac{g}{\sqrt{2}} \overline{d_{Li}^I} \gamma_\mu W^{+\mu} u_{Li}^I + \dots \\ &= \frac{g}{\sqrt{2}} \overline{u_{Li}^I} (V_L^u V_L^{d\dagger})_{ij} \gamma_\mu W^{-\mu} d_{Lj}^I + \frac{g}{\sqrt{2}} \overline{d_{Li}^I} (V^d V^{u\dagger})_{ij} \gamma_\mu W^{+\mu} u_{Lj}^I + \dots \end{aligned} \quad (1.27)$$

*The question and answer of flavor/mass mixing can be put as: Q: “Why is there mixing?”; A: “Because it’s possible.”

The combination of matrices $\left(V_L^d V_L^{u\dagger}\right)_{ij}$, a unitary 3×3 matrix is known as the *Cabibbo-Kobayashi-Maskawa (CKM)* mixing matrix. By convention, the interaction and flavor eigenstates of the up-type quarks are chosen to be equal. The down-type quarks are therefore chosen to be rotated:

$$\begin{aligned} u_i^I &= u_i, \\ d_i^I &= V_{CKM} d_i, \end{aligned} \quad (1.28)$$

or explicitly:

$$\begin{pmatrix} d^I \\ s^I \\ b^I \end{pmatrix} = \begin{pmatrix} V_{ud} & V_{us} & V_{ub} \\ V_{cd} & V_{cs} & V_{cb} \\ V_{td} & V_{ts} & V_{tb} \end{pmatrix} \begin{pmatrix} d \\ s \\ b \end{pmatrix}. \quad (1.29)$$

Because the choice of the global phases of the quark fields is arbitrary and the matrix is unitary, the nine unknown complex elements can be reduced to three real numbers and one phase*. The matrix is most often written as:

$$V_{CKM} = \begin{pmatrix} c_{12}c_{13} & s_{12}c_{13} & s_{13}e^{-i\delta} \\ -s_{12}c_{23} - c_{12}s_{23}s_{13}e^{i\delta} & c_{12}c_{23} - s_{12}s_{23}s_{13}e^{i\delta} & s_{23}c_{13} \\ s_{12}s_{23} - c_{12}c_{23}s_{13}e^{i\delta} & -c_{12}s_{23} - s_{12}c_{23}s_{13}e^{i\delta} & c_{23}c_{13} \end{pmatrix}, \quad (1.30)$$

where $c_{ij} = \cos(\theta_{ij})$ and $s_{ij} = \sin(\theta_{ij})$ for $i < j = 1, 2, 3$ and δ is the *CP*-violating phase.

The mixing of the flavor quantum states is necessary to explain charged current interactions changing the strangeness with 1 [13] and *CP*-violating processes [14].

Without going into detail, it is worth noting that a similar matrix exists that connects the lepton flavor and mass eigenstates. In contrast to the quarks, the down-type interaction doublet states are chosen to be the same as the mass eigenstates. Therefore, the mixing of the mass and interaction eigenstates is in the neutrino sector. The three eigenstates of the weak interaction form an orthonormal basis. Left-handed neutrinos and leptons form doublets L as can be seen in Eq. 1.20: $\begin{pmatrix} \nu_e \\ e \end{pmatrix}$, $\begin{pmatrix} \nu_\mu \\ \mu \end{pmatrix}$ and $\begin{pmatrix} \nu_\tau \\ \tau \end{pmatrix}$. One can also construct an eigenbasis out of three neutrino states with a definite mass, ν_1 , ν_2 and ν_3 that diagonalize the neutrino's free-particle Hamiltonian. Similar to quarks, this mass-eigenbasis is rotated relative to the flavor-eigenbasis:

$$\begin{pmatrix} \nu_e \\ \nu_\mu \\ \nu_\tau \end{pmatrix} = \begin{pmatrix} U_{e1} & U_{e2} & U_{e3} \\ U_{\mu 1} & U_{\mu 2} & U_{\mu 3} \\ U_{\tau 1} & U_{\tau 2} & U_{\tau 3} \end{pmatrix} \begin{pmatrix} \nu_1 \\ \nu_2 \\ \nu_3 \end{pmatrix} \quad (1.31)$$

This matrix is known as the *Pontecorvo-Maki-Nakagawa-Sakata (PMNS)* matrix [15],

$$\mathcal{U} = \begin{pmatrix} 1 & 0 & 0 \\ 0 & c_{23} & s_{23} \\ 0 & -s_{23} & c_{23} \end{pmatrix} \begin{pmatrix} c_{13} & 0 & s_{13}e^{-i\delta} \\ 0 & 1 & 0 \\ s_{13}e^{-i\delta} & 0 & c_{13} \end{pmatrix} \begin{pmatrix} c_{12} & s_{12} & 0 \\ -s_{12} & c_{12} & 0 \\ 0 & 0 & 1 \end{pmatrix} \quad (1.32)$$

The matrix is again parameterized by three mixing angles θ_{12} , θ_{13} and θ_{23} where s_{ij} and c_{ij} are used to denote $\sin(\theta_{ij})$ and $\cos(\theta_{ij})$. The phase δ relates to charge-parity violations. It is possible to add additional "Majorana" phases, but this will not be discussed in this work [16].

*This phase is responsible for *CP-violation*.

1.4**A success story**

Over the course of multiple decades, the Standard Model was built up into an extremely comprehensive theory. The first building blocks necessary for its construction came from experiments in the early 20th century when its quantum characteristics became more apparent. The theory was formulated as a gauge theory in the 1960s and 1970s and for decades it has been rigorously tested and checked, leading to extremely accurate experimental precision measurements that agree with the theory. Apart from precision measurements, it has led to predictions of particles and their interactions, which could only be tested years or decades after they were first proposed. In the following, we give a brief overview of some experimental results.

1.4.1**Predictions**

By 1932, scientists knew that atoms were made up by protons, neutrons and electrons. Together with the photon, a total number of four particles were known. Four grew to five when Anderson discovered the existence of positrons [17] (predicted by Dirac [18]). Then came the muon [19] and pion [20]. By the 1960s, there were “fundamental particles” with no good guiding principles to link them together. They were often referred to as the “particle zoo”.

By a series of insights by several individuals, the Standard Model as a quantum field theory became more widely accepted. Since then, the model has predicted the results of experiment after experiment. Some of them are:

- Neutral weak currents. Postulated by Salam, Weinberg and Glashow, the theory of electroweak interactions predicted the existence of a new type of weak interaction, in which the reacting particles do not change their charges. The first observation was made in 1973 in the Gargamelle experiment at the European nuclear research laboratory, CERN [21].
- Weak gauge bosons. Again postulated by the abovementioned people. These particles were discovered in the UA1 and UA2 experiments in CERN, 1983 [22, 23].
- Heavy quarks. To explain the *CP*-violations in kaon decays, M. Kobayashi and T. Maskawa predicted the existence of a third generation of quarks: the *top* and *bottom* quarks. The bottom quark was discovered in 1977 at Fermilab [24]. It took another 18 years for the top quark to be found in the same institute [25].
- Gluons. The gauge bosons of quantum chromodynamics were discovered in 1978 and 1979 [26].
- Higgs boson. On July 4, 2012, physicists at CERN announced the discovery of the only fundamental particle predicted by the Standard Model that was not yet discovered.

1.4.2**Precision tests**

Inconsistencies between experiment and theory can be signs of wrong or incomplete theories. For this reason, experimentalists are continuously testing parameters of the SM. These precision tests are most often done by testing the theory of quantum electrodynamics (QED). With the use of *renormalization theory*, many parameters of the theory can be calculated with high precision. High-precision measurements of various observables have been performed at LEP 1 and SLC [27, 28, 29, 30, 31, 32] for physics at the Z -boson mass ($\sqrt{s} \approx M_Z$) and other observables at Tevatron [33, 34], LEP 2 [34], ATLAS [35, 36] and CMS [37, 38]. Some of them are listed in Table 1.2. The parameters in the table show that the SM best-fit predictions are very consistent with what we see in experiments.

- The SM predicts kaons to decay into charged pions and a neutrino-antineutrino pair to happen once every ten billion kaon decays. The SM fit to this decay has a small uncertainty, making the search interesting for possible anomalies. A candidate event of this very rare decay has been reported by the NA62 collaboration in 2018 but is in accordance with the SM predictions [39].
- Another example is the measurement of the *Lamb shift*, a difference in energy between two energy levels of the hydrogen atom that was not predicted by the Dirac equation and currently provides a measurement of the fine-structure constant α to better than one part

Table 1.2: Observables compared with the SM best fit. Errors are the total (experimental plus theoretical) uncertainties. Results are taken from Tables 10.4 and 10.5 in [43].

Parameter	Experimental value	Theoretical value	Standard deviation
m_t [GeV]	172.74 ± 0.46	172.96 ± 0.45	-0.5
m_W [GeV]	80.387 ± 0.016	80.358 ± 0.004	1.8
	80.376 ± 0.033		0.6
	80.370 ± 0.019		0.6
	2.046 ± 0.049		-0.9
Γ_W [GeV]	2.195 ± 0.083	2.089 ± 0.001	1.3
	125.14 ± 0.15		0.0
g_V^{ee}	-0.040 ± 0.015	-0.0398 ± 0.0001	0.0
g_A^{ee}	-0.507 ± 0.014	-0.5063	0.0
τ_τ [fs]	290.75 ± 0.36	290.39 ± 2.17	0.1
$\frac{1}{2}(g_\mu - 2 - \frac{\alpha}{\pi})$	$(4511.18 \pm 0.77) \times 10^{-9}$	$(4508.63 \pm 0.03) \times 10^{-9}$	3.3
M_Z [GeV]	91.1876 ± 0.0021	91.1884 ± 0.0020	-0.4
Γ_Z [GeV]	2.4952 ± 0.0023	2.4942 ± 0.0008	0.4
$\Gamma_Z(\text{had})$ [GeV]	1.7444 ± 0.0020	1.7411 ± 0.0008	-
$\Gamma_Z(\text{inv})$ [MeV]	499.0 ± 1.5	501.44 ± 0.04	-
$\Gamma_Z(l^+l^-)$ [MeV]	83.984 ± 0.086	83.959 ± 0.008	-

in a million, allowing a precision test of QED.

- Electrons have a magnetic dipole moment as a result from their intrinsic spin. A charge distribution in these particles, which we do not expect to happen for fundamental particles, would make the electron charge not seem perfectly spherical. This electron electric dipole moment (EDM) is expected from the SM only with an extremely small value from radiative corrections with CP -violating interactions, at most $10^{-38} e \cdot \text{cm}$. Recent measurements from the ACME experiment set the current upper limit at a value of $1.110^{-29} e \cdot \text{cm}$ [40].

There have been other, more challenging precision test, such as neutrino cross-section measurements [41] and measurements of the top quark mass in the CMS experiment [42]. Both are again in agreement with the SM.

1.5 The need for physics beyond the Standard Model

Despite its incredible success, many physicists believe the Standard Model is certainly not the full story. There are a number of features that seem arbitrary, but also some that cannot be explained by the theory alone. Below, I give a list of open questions:

- Why are there **three families** for both leptons and quarks? Why not two? Or four? Or even a thousand?
- What is the **cause of the symmetries** we see in the Standard Model? Why is, for example, QCD not an SU(4) gauge theory?
- There are a number of **parameters** in the SM that cannot be explained by first principles. We have no good explanation for why the top quark is 75 000 times heavier than the up quark. Why is the vev of the Higgs potential 246 GeV? Why is the Higgs mass 125 GeV? There are in total 26 parameters in the SM that are determined by experiments and can be found in Table 1.3.
- Why does the Higgs potential have this **Mexican hat shape**? In other words, why is μ^2 in $\lambda(\Phi^\dagger\Phi)^2 + \mu^2(\Phi^\dagger\Phi)$ negative? Also, the vev, the mass of the Higgs boson and the mass of the fermions due to the Yukawa couplings all appear in Table 1.3. This makes us believe there is something we do not fully understand about the BEH mechanism.
- Right-handed neutrinos can be introduced into the SM. They are singlets with respect to the strong and weak interaction and would therefore not carry an electric charge, weak

hypercharge or weak isospin. Due to this lack of charge, right-handed neutrinos would be extremely difficult to detect. They have Yukawa interactions with other leptons and the Higgs boson, but its coupling would be extremely small. Neutrinos can become massive with Dirac mass terms in the same way charged leptons become massive in the BEH mechanism. Their **extremely small masses** suggest another mechanism in which the very light left-handed neutrinos are accompanied with extremely heavy right-handed neutrinos. This mechanism is called the *Seesaw mechanism* and requires the addition of Majorana mass terms.

Aside from these, there are a number of unexplained phenomena that probably cannot be explained in a simple extension of the Standard Model but need a non-trivial approach. For example:

- It is a natural assumption that the universe is neutral with all conserved charges. Both the SM and general relativity give no explanation for the **matter-antimatter imbalance** we see in the universe. The Big Bang was expected to produce equal amounts of matter and anti-matter, yet we see that the observable universe consists almost exclusively out of baryonic matter*. The most likely explanation is that in the early universe physical laws we know today were absent or have acted differently. The observed *CP*-violation is insufficient to account for the observed baryon asymmetry of the universe given the limits on baryon number violation.
- The stars, planets, interstellar clouds, etc. we see in space consist of baryonic matter. Assuming general relativity is the correct theory to describe gravity on cosmological scales, the Lambda-CDM model predicts that the matter we see is only around 15% of the total matter present in our visible universe [44]. To explain the galaxy rotation curves [45], galaxy velocity dispersions [46], galaxy cluster masses [47], gravitational lensing [48], and many more, it is predicted that around 85% of the mass is not yet observed. This matter is referred to as **dark matter** as it cannot interact electromagnetically because it would have already been observed otherwise. No known particles in the SM can explain this phenomenon.
- Similar to dark matter, the Lambda-CDM model predicts that the total energy in the visible universe should consist mostly out of a constant energy density for the vacuum called **dark energy**. 5% of the total energy consists of baryonic matter, 26% should be dark matter and the remaining 69% of dark energy is necessary to explain the expansion of the universe†.
- General relativity is generally accepted to describe gravity on cosmological scales. Thusfar, it has not been possible to describe **gravity** on a quantum scale, as is the case for the Standard Model, and still be valid on very large scales. The inclusion of the graviton would for example not recreate what is observed experimentally without other modifications to the SM, which have not been observed. There is a need for a more complete theory beyond the range of their combined applicability [49].
- Why is the *CP*-violation in the strong interaction extremely small or even zero?
- Often referred to as the muon g-2 anomaly, there are possible hints of new physics as the theoretical prediction of magnetic moment of the muon and experimental values have a small but significant offset (see Table 1.2).
- Why is there much more mixing in the lepton sector (PMNS) compared to the quark sector (CKM)?
- To explain the apparent quantum fluctuations on cosmological scales together with the horizon, flatness and magnetic monopole [50] problems, we have a theory of exponential expansion of space in the early universe: **cosmic inflation**. The theory states that between

*Why are there protons, neutrons and electrons everywhere while it is perfectly possible for antiprotons and antineutrons to form atomic nuclei with positrons?

†If there is only matter and the Big Bang acceleration only happened in the beginning of the creation of the universe, then one would expect the expansion to diminish due to the gravitational pull of matter. Measurements say the opposite is true: the universe is expanding and in an accelerating rate.

Table 1.3: The 26 free parameters in the Standard Model that have to be measured experimentally.

Parameter	Description	Value	Uncertainty	Reference
m_e	Electron mass	511 keV	$\pm 3.1 \cdot 10^{-6}$ keV	[43]
m_μ	Muon mass	105.7 MeV	$\pm 2.4 \cdot 10^{-6}$ MeV	[43]
m_τ	Tau mass	1.78 GeV	$\pm 1.2 \cdot 10^{-4}$ GeV	[43]
m_u	Up quark mass	2.2 MeV	$[-0.4, +0.5]$ MeV	[43]
m_d	Down quark mass	4.7 MeV	$[-0.3, +0.5]$ MeV	[43]
m_c	Charm quark mass	1.275 GeV	$[-0.035, +0.025]$ GeV	[43]
m_s	Strange quark mass	95 MeV	$[-3, +9]$ MeV	[43]
m_t	Top quark mass	173.0 GeV	± 0.4 GeV	[43]
m_b	Bottom quark mass	4.18 GeV	$[-0.03, +0.04]$ GeV	[43]
$\theta_{12,\text{CKM}}$	CKM 12-mixing angle	13.04°	$\pm 0.05^\circ$	[43]
$\theta_{23,\text{CKM}}$	CKM 23-mixing angle	2.38°	$\pm 0.06^\circ$	[43]
$\theta_{13,\text{CKM}}$	CKM 13-mixing angle	0.201°	$\pm 0.011^\circ$	[43]
$\delta_{CP,\text{CKM}}$	CKM CP violation phase	1.20 rad	± 0.08 rad	[43]
$\alpha^{-1}(M_Z)$	Electromagnetic coupling constant *	127.955	± 0.010	[43]
$\sin^2 \theta_W(M_Z)$	Weinberg angle *	0.23122	$\pm 3 \cdot 10^{-5}$	[43]
$\alpha_s(M_Z)$	Strong coupling constant *	0.1187	0.0016	[43]
θ_{QCD}	QCD vacuum angle	$< 10^{-9}$	/	[51]
v	Higgs vacuum expectation value	246 GeV	/	[52]
m_H	Higgs mass	125.09 GeV	$\pm 0.21(\text{stat}), \pm 0.11(\text{syst})$ GeV	[53]
$m_{\nu 1}$	Neutrino mass parameter	$\sum_i m_{\nu i} < 120$ meV	95% C.L.	[54]
$m_{\nu 2}$	Neutrino mass parameter	$\frac{\Delta m_{21}^2}{10^{-5}\text{eV}^2} = 7.39$	$[-0.20, +0.21]$	[55, 56]
$m_{\nu 3}$	Neutrino mass parameter	$\frac{\Delta m_{31}^2}{10^{-3}\text{eV}^2} = 2.525$	$[-0.032, +0.033]$	[55, 56]
$\theta_{12,\text{PMNS}}$	PMNS 12-mixing angle†	33.82°	$[-0.76^\circ, +0.78^\circ]$	[55, 56]
$\theta_{23,\text{PMNS}}$	PMNS 23-mixing angle†	49.6°	$[-1.2^\circ, +1.0^\circ]$	[55, 56]
$\theta_{13,\text{PMNS}}$	PMNS 13-mixing angle†	8.61°	$[-0.13, +0.13^\circ]$	[55, 56]
$\theta_{CP,\text{PMNS}}$	PMNS CP violation phase†	215°	$[-29^\circ, +40^\circ]$	[55, 56]

* The coupling constants depend on the energy scale: “running of the coupling constants”.

† Assuming normal mass ordering, for inverted ordering see reference.

10^{-36} and 10^{-32} seconds after the Big Bang, a rapid exponential expansion happened. This could explain the apparent thermal equilibrium between parts of the visible universe that are not in causal contact with each other and the even distribution of the cosmic microwave background. The hypothetical field that is thought to be responsible for inflation, the inflaton field, is not observed and would be an extension of the Standard Model.

- With the use of renormalization theory, it is possible to show that bare parameters should not be the same as parameters measured in experiments. These parameters, such as the mass of particles, depend on the energy scale at which they are probed and physics far beyond the scope of the probed energy scale can influence these parameters. An example are the screening and anti-screening effects. If one believes that all forces can be described by one theory at higher energies, these constants can converge at higher energy scales which is not the case when extrapolating these parameters as can be seen in Figure 1.3. Similarly, one-loop corrections to the Higgs boson mass* will have radiative corrections with a quadratic dependence on the cutoff scale. Virtual particles in one-loop corrections can have infinite momenta that should contribute to the total mass of the Higgs boson. Since we expect new physics to be present at energies close to the Planck mass ($\approx 10^{18}$ GeV), these loop corrections should push the Higgs mass to similar energy ranges. But, we see that the Higgs mass is around 125 GeV. This would mean that there are other parameters which should almost *exactly* cancel these absurdly large numbers. This is called *fine-tuning*, and it’s the intuition of most physicists that this incredible fine-tuning has a deeper, yet unknown, meaning. This problem is often referred to as the **hierarchy problem**.

Many of these problems can be seen as unwarranted. Why there are three families and why

*Fermions and bosons are not affected by higher energy physics in the same way as a scalar particle is.

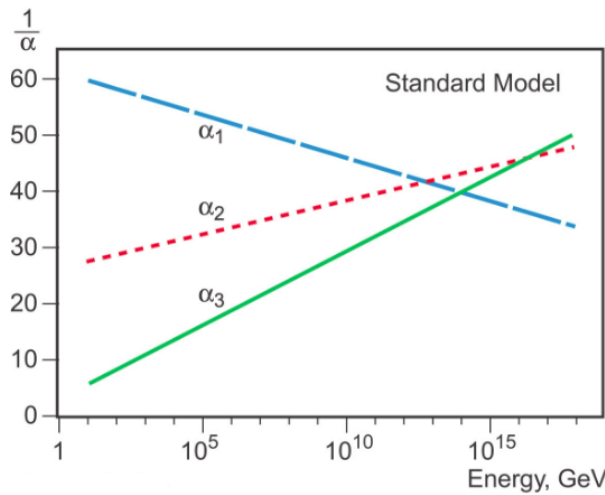


Figure 1.3: Running of the coupling constants in the Standard Model. Figure from [57].

so many parameters in the Standard Model have no fundamental explanation could just be because it's just the way it is. Maybe there is a multiverse, a plethora of universes with similar Standard Models, which have slightly or vastly different parameters. Some questions might even be impossible to answer because of a lack of statistics: we only have one universe and mankind has not been around very long in the timescale of the universe. This consideration might be valid but again doesn't answer all our questions, it does not solve the question of dark matter for example.

This argumentation should not prevent us to try and find a more general theory for the Standard Model and general relativity. A better explanation could be fairly simple, but infinitely hard as well. There is only one way in trying to find a better understanding: experiments.

Unification is the most popular approach in describing physics beyond the Standard Model. Unification would mean that well-established theories are low-energy approximations of a more grand unified theory. Historically, this has worked very well: the unification of celestial gravitation of Kepler with terrestrial gravitation of Galileo into universal gravitation and the unification of electricity, magnetism, and later optics into electromagnetism. Gravity was overhauled by the much broader theory of general relativity. Lastly, the birth of gauge theories have combined QED and the weak interaction into the combined electroweak theory. The similarities in QCD and the electroweak theory, both being gauge theories, has led people to believe a unification is possible. This would unify the forces and particles known from the Standard Model into a *Grand Unified Theory* or GUT. A theory that would add gravity is called a *Theory Of Everything* or TOE.

1.5.1 Unifying theories

Linking the seemingly arbitrary parameters in the Standard Model has been ongoing for the last couple of decades. Combining these theories is not straightforward since they exhibit very different behaviors. Electromagnetism is long-ranged, the weak force is short-ranged and the strong force is weak in high-energy environments such as the early universe and strong where the probing energy is low. Many GUTs predict that quarks and leptons are part of a single representation of a gauge group with one single hypercharge and would explain why the electric charge of electrons and protons seem to be exactly the same [58].

The simplest GUT is SU(5), which would break down into the Standard Model at lower energies due to spontaneous symmetry breaking. Other possible extensions are, for example, SO(10) [59], SU(8) [60] and O(16) Lie groups. Another example is string theory, a theoretical framework that starts with the idea that point-like particles of particle physics can be replaced by one-dimensional objects called strings. These strings can propagate through space and interact with each other. Properties that we are more familiar with, such as charge, mass, etc. are determined by the vibrational state of the strings.

Unfortunately, the full theory does not have a definition in all circumstances and describes

an enormous landscape of possible universes and is mainly used to describe quantum gravity. However, charge quantization is often not assumed in string theory, making particles with an anomalous charge plausible [61, 62].

Without experimental results there is still much ongoing debate into which theory is the correct one. There are many more theories aside from the possible extentions that are listed here such as Supersymmetry, Little Higgs, Technicolor... but go beyond the scope of this work.

1.5.2 How to look for new physics

In general, one could say there are two possible ways to look for new physics. Essentially all of the physics in our solar system can be explained with what we know from the Standard Model. Interactions in controlled laboratory environments are currently on the order of ~ 10 TeV center of mass energy in the experiments at the LHC. This could still be well below the energy levels to produce new, exotic, particles. In the energy frontier it is the goal to reach the highest energies possible in order to get as close to the energy requirements where new physics becomes more prominent. As a consequence, more and more cosmic ray experiments have found an interest in searches for physics beyond the Standard Model. This is sometimes called the *cosmic frontier*. This analysis tries to explore this possibility in more detail for the IceCube experiment. Cosmic ray experiments have the disadvantage that they are not fully contained experiments and information is lost as the primary interaction is unknown and important parameters such as energy, direction, type,... of the particle have to be reconstructed, often with large uncertainties.

The other approach tries to extract information from precision experiments and is therefore reliant on lowering the statistical and systematical uncertainties. In these experiments, the intensity of the beam of particle accelerators is pushed to its highest value and this is therefore referred to as the intensity frontier. This strategy tries to generate huge numbers of particles needed to study rare or exotic subatomic processes. Rare processes could give us a lot of information on unknown physics. Some parameters which can be calculated in the SM have a small offset with respect to what is measured in experiments.

The difference between the two methods can be summarized by saying that new physics at higher energies can produce new particles at high-energy collisions that are sought for in the energy frontier. The higher the scale where new physics enters, the more energy is needed in particle collisions. However, parameters from our current theories that not include new physics could also have a small but measurable offset at lower energies (the ones we are able to probe currently), which is what is measured in the intensity frontier.

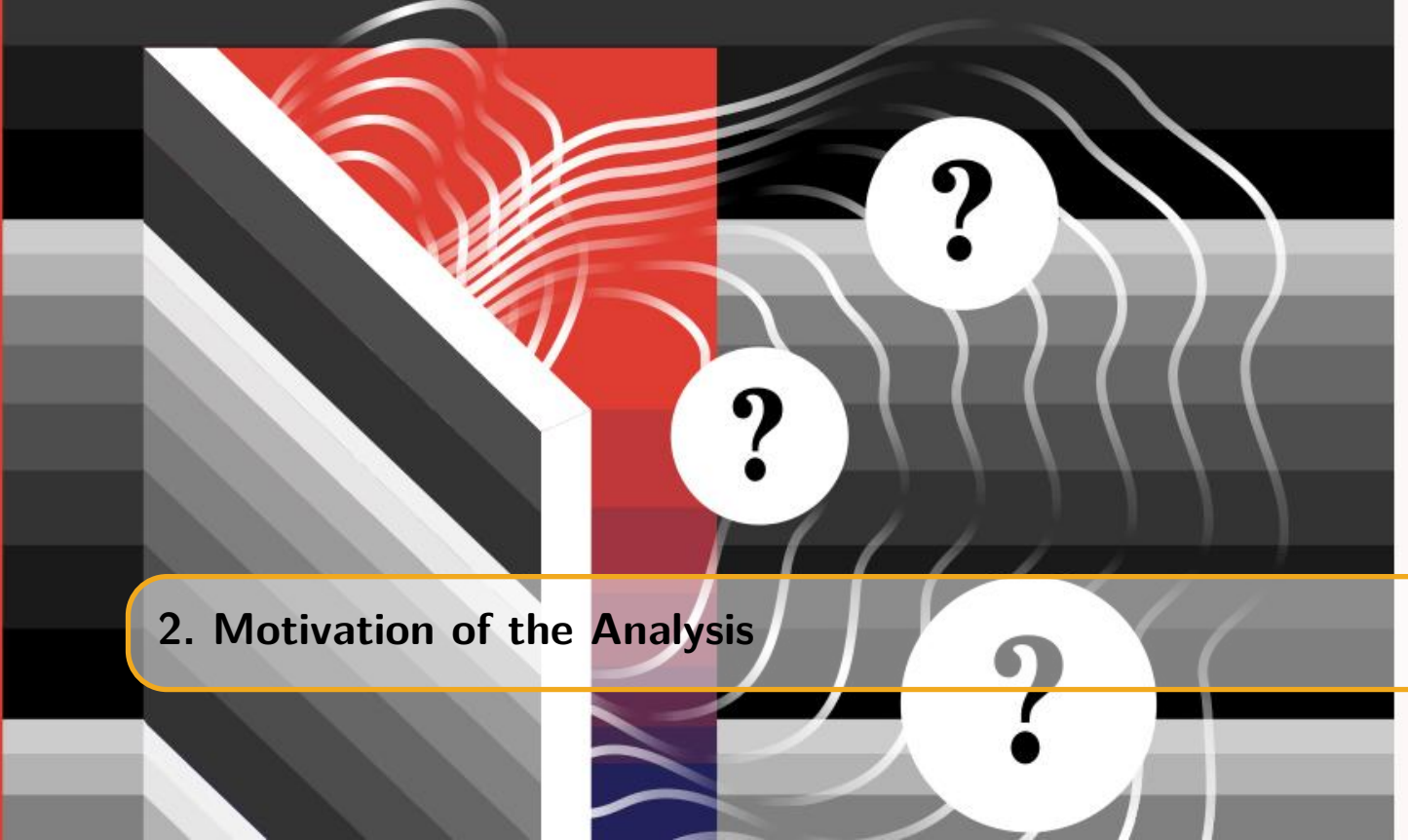
I'd like to finish this chapter with quotes from Steven Weinberg in an interview with Nova about his vision on string theory. It shows the apparent stalemate physicists seem to find themselves in: there are no theoretical breakthroughs regarding long standing problems.

"I believe that there is a simple theory that governs everything—the four forces we know about, perhaps other forces as well. I'm not sure that's true. It may be that nature is irreducibly messy. I'm sure that we should assume it's not, because otherwise we're never going to find a fundamental theory. But even so, we're not guaranteed that we'll find it. We may not be smart enough. Dogs are not smart enough to understand quantum mechanics. I'm not sure that people are smart enough to understand the whatever-it-is that unifies everything. I think we probably are, because of our ability to link our minds through language, but I'm not certain."

"There was a marvelous period from, I'd say, the mid-'60s until the late '70s when theoretical physicists actually had something to say that experimentalists were interested in. Experimentalists made discoveries that theoretical physicists were interested in. Everything was converging toward a simple picture of the known particles and forces, a picture that eventually became known as the Standard Model. I think I gave it that name. And it was a time when graduate students would run through the halls of a physics building saying they had discovered another particle and it fit the theories, and it was all so exciting."

"Since the late '70s, I'd say, particle physics has been in somewhat of a doldrums. Partly it's just the price we're paying for the great success we had in that wonderful time then. I think cosmology now, for example, is much more exciting than particle physics. The string theorists are trying to push ahead without much support from relevant experiments, because there aren't any relevant experiments that can be done at the kind of scales that the string theorists are interested in."

Even though it might take us a long time to find the answers we are looking for, this current stalemate should not prevent us doing more fundamental research. We still do not know everything and it's probably even foolish to think we almost do. Finding some answers might be difficult but probably all the more fulfilling once we have them.



2. Motivation of the Analysis

The world is divided into people who think they are right ~ Anonymous

As seen in Chapter 1, there is an ongoing debate which beyond-the-Standard-Model physics models could help explain questions we do not have answers for. Over the last decades, this quest has proven to be non-trivial since many accelerator experiments have not given any clear hints towards physics that cannot be explained by the Standard Model. A big part of the physics community is trying its best to help answer these riddles and dedicated experiments have been constructed in the search for new physics. Other collaborations try to make use of their detector in the most efficient way possible. These experiments most often try to look for BSM physics by searching for signals in their detector that could not be explained by the particles we know today. One example, and also the subject of this work, is to try to look for particles that have a lower electromagnetic, but non-zero, charge compared to the charged particles of the Standard Model.

2.1 Introduction

In the previous chapter, we have seen that all free particles have an electromagnetic charge that is a multiple of the absolute electron charge, e , equal to 1.602×10^{-19} C. Elementary particles such as (anti)quarks have fractional charges equal to $\pm \frac{1}{3}e$ and $\pm \frac{2}{3}e$, but have never been seen as isolated particles due to *confinement* as explained in Section 1.1.2. No other particles are expected to have a charge lower than e and therefore, such particles with lower charges are perfect candidates for searches beyond the Standard Model. Different experiments have sought these anomalously charged particles, which are referred to as *Lightly Ionizing Particles (LIPs)* or *Stable Massive Particles (SMPs)*. Throughout this work the latter denomination is used, indicating they do not rapidly decay and have masses significantly higher than the lightest leptons.

2.2 Theory

In Section 1.5.1, possible extensions of the Standard Model were already introduced. One of the simplest possible extensions of the $SU(3) \times SU(2) \times U(1)$ groups is the $SU(5)$ gauge group. It is the smallest Lie group that can contain the group of the Standard Model without introducing any new fermions. It could explain charge quantization [58], has complex representations and can accommodate fractional charges. In this scheme, new vector bosons, usually called X and

Y bosons, occur with charges $\frac{4}{3}$ and $\frac{1}{3}$. Extensions of the SU(5) models allow for color singlet particles with charges $\frac{1}{3}$ and $\frac{2}{3}$ [63]. Other possible extensions are based on the SU(7) [64], SU(8) [60], SO(14) [65], and SO(18) [66], SO(10) \times SO(8) groups [67].

It should be noted that the simplest form of an SU(5) gauge group is already highly constrained as proton decay is allowed in this model and the proton lifetime is estimated to be around $10^{30} - 10^{31}$ years. However, experimental results have shown the lifetime to be $> 1.6 \times 10^{34}$ years ($\tau(p \rightarrow \pi^0 e^+)$) and $> 7.7 \times 10^{33}$ years ($\tau(p \rightarrow \pi^0 \mu^+)$) [68].

There are also some string theories where massive particles with a fractional charge are predicted [61, 69]. This was later confirmed to occur very often in certain compactifications [62].

More recently, there has been an increasing interest in searches for millicharged particles. New particles could couple to the Standard Model via a “kinetic mixing” or “hypercharge portal” [70, 71]. And in recent years, they were studied as possible candidates for dark matter [72, 73, 74, 75]. However, the charges of these particles are often $< 10^{-3}e$ and therefore no ideal candidates in neutrino Cherenkov experiments. It is possible to look for them in neutrino experiments [76], but more targeted toward future experiments such as DUNE [77] and SHiP [78]. A more detailed explanation of these particles can be found in Ref. [79]. The most stringent upper limit in millicharged particles known to the author is given in Ref. [80].

There are many other possible extensions, but these go beyond the scope of this work. One should just keep in mind that no free particles with an anomalous charge less than e are expected in the SM and that, if seen, they give clear hints of beyond-the-Standard-Model physics and would help in finding a clearer picture of what is possibly hidden beyond the realms of our understanding.

2.3 Previous searches

There are several ways one can assume to produce fractional charge particles. Different assumptions lead to different possible searches with previous and current detectors. In the following, the results of several experiments are shown. Accelerator and fixed-target experiments look for particles that might be created in particle collisions, resulting in upper limits for production cross sections if no candidate events are found. Telescope experiments, on the other hand, often assume a flux of incoming particles that is bound to an upper limit if no candidate events are found.

2.3.1 Searches with accelerators and fixed targets

The total energy of the interaction should be large enough to produce particles of a certain mass. The square of the center of mass energy is given by:

$$\begin{aligned} s &= (p_1 + p_2)^2 \\ &= m_1^2 + m_2^2 + 2E_1 E_2 - 2\vec{p}_1 \cdot \vec{p}_2, \end{aligned} \tag{2.1}$$

where $p_{1,2}$ are the four-momenta of the two particles and c , the speed of light, is set to 1 in natural units. Assuming E is the energy of the incoming particle with mass m_i and m_t the mass of a target particle in rest and $E \gg m_t, m_i$, the maximal mass reach of a search is given by:

$$m_{max} \approx \sqrt{2m_t E}. \tag{2.2}$$

If I is the incoming particle from the input beam and N a nucleus, the production of exotic particles can then be denoted as

$$I + N \rightarrow F + X, \tag{2.3}$$

Table 2.1: Highest-energy fractional charge particle searches in electron-positron colliders. No evidence for fractionally charged particles was found.

\sqrt{s} (GeV)	Charges sought	Collider	Reference
1-1.4	$\frac{2}{3}$	VEPP-2M	[83]
29	$\frac{1}{3}, \frac{2}{3}$	PEP	[84]
130-209	$\frac{2}{3}, \frac{4}{3}, \frac{5}{3}$	LEP	[85]
130-136, 161 and 172	$\frac{2}{3}$	LEP	[86]
91.2 (m_Z)	$\frac{2}{3}, \frac{4}{3}$	LEP	[87]
91.2 (m_Z)	$\frac{4}{3}$	LEP	[88]

Table 2.2: Highest-energy fractional charge particle searches in proton-(anti)proton colliders. No evidence for fractionally charged particles was found.

\sqrt{s} (GeV)	Type	Charges sought	Collider	Reference
540	$p\bar{p}$	$\frac{1}{3}, \frac{2}{3}$	SPS	[89]
1800	$p\bar{p}$	$\frac{2}{3}, \frac{4}{3}$	Tevatron	[90]
1800	$p\bar{p}$	$\frac{1}{3}, \frac{2}{3}$	Tevatron	[91]
7000	pp	$\frac{1}{3}, \frac{2}{3}$	LHC	[92]

where F stands for the fractional charged particle and X for the other particles that are produced in the interaction. No experiments that used accelerators and fixed targets found evidence for the existence of fractional charge particles [81]. The highest-energy search used muons with a beam energy of 200 GeV, resulting in an m_{max} of 19 GeV [82].

2.3.2 Colliders

Particle colliders can reach much higher energies than most fixed-target experiments. We see from Eq. 2.1 that the maximal mass of new particles in a storage ring that is colliding particles of energy E with $E \gg m_1, m_2$ scales with the energy:

$$s = 4E^2, \\ \rightarrow m_{max} = 2E \quad (2.4)$$

There is a big difference in lepton and hadron accelerator experiments since much less particles are being produced in the former due to the absence of strong interactions. The production is “cleaner” and the sought particles are easier to distinguish from other productions. But, it is more difficult to reach higher energies for lepton accelerators*. An overview of electron-positron colliders is given in Table 2.1. No evidence for fractionally charged particles was found.

Experiments that use proton-antiproton colliders have reached larger masses but have also found no evidence of fractionally charged particles. An overview is given in Table 2.2.

A more recent search was performed at the LHC, a proton-proton collider, when operating at a center of mass energy of 7 TeV. No evidence of particles with a fractional charge was found. An upper limit of 95% confidence level was set for particles with electric charge $\frac{2}{3}$ up to a mass of 310 GeV and 140 GeV for those with charge $\frac{1}{3}$ [92].

2.3.3 Searches for particles with telescopes

There are several ways that particles with a fractional charge could be produced in cosmological events;

- the particles were produced early on in the Universe and are a stable component of the present matter;

*The radiative power of synchrotron radiation scales with a factor of m^{-4} : particles with low mass lose much more energy in circular accelerators with a fixed radius.

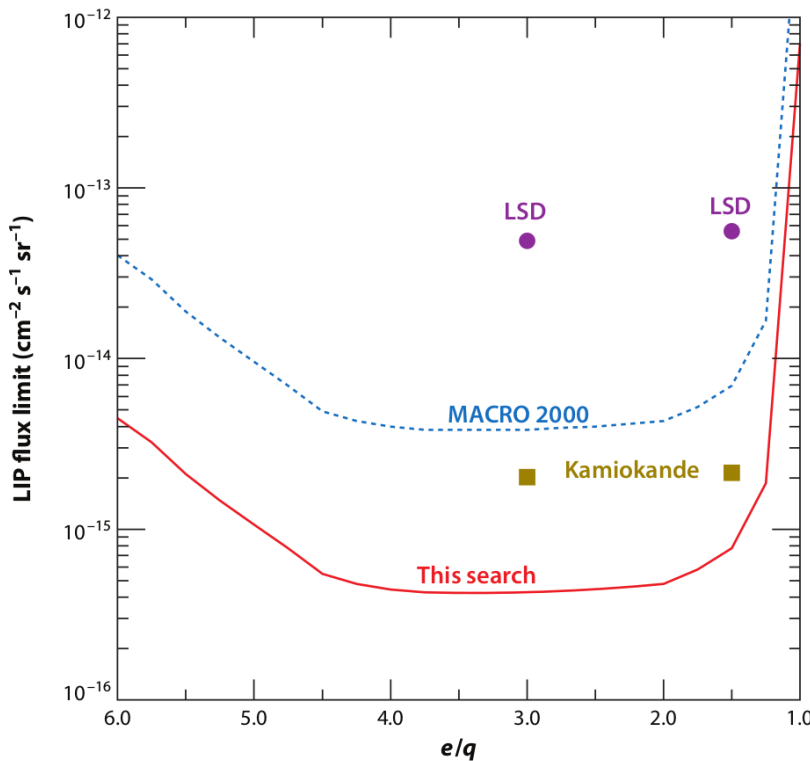


Figure 2.1: Upper limits on fluxes of particles close to the respective detectors. LIP stands for *Lightly Ionizing Particles*. “This search” refers to an unpublished result from the MACRO experiment that compares the published results from other experiments. Figure taken from Ref. [93], where I have changed the Kamiokande results which are wrong in the original figure.

- the particles are rare but can be continuously produced in high-energy astrophysical events; or
- the particles are produced in cosmic ray processes near Earth.

Because there is no clear preference for one of these possibilities, most telescope experiments express their search sensitivity as an incoming flux close to the detector in units of [$\text{cm}^{-2} \text{s}^{-1} \text{sr}^{-1}$]. This analysis has adopted the same search strategy and aims to improve on previous results. The most stringent upper limit was realized by the MACRO experiment found on the arXiv (not published, Ref. [93]) that compares results from older searches and can be seen in Figure 2.1. The best published result is set by Kamiokande II with upper limits of $2.1 \times 10^{-15} \text{ cm}^{-2} \text{s}^{-1} \text{sr}^{-1}$ and $2.3 \times 10^{-15} \text{ cm}^{-2} \text{s}^{-1} \text{sr}^{-1}$ for particles with charges $\frac{1}{3}$ and $\frac{2}{3}$ respectively [94].

2.4 Properties of the signal

Because there are many possible scenarios what these particles are, where they originate from, or how they are produced, one has to make certain assumptions about the properties of the signal. A particle traveling at the speed of light with a lifetime < 0.1 seconds traversing a detector will not give the same signal properties as one that has a very long lifetime. Therefore, I have assumed that the particles I am looking for

- behave leptonically, similar to muons. The particles will therefore produce long tracks instead of cascades in the IceCube detector (more info in Chapter 4);
- have a long lifetime and will not rapidly decay within the IceCube detector, or at least have a very low probability to do so;
- follow an energy spectrum with a spectral index of -2*;
- are assumed to produce an isotropic flux close to the detector.

*More information about spectra can be found in Section 3.1.2.

These assumptions are consistent with previous searches that are mentioned in Section 2.3. The behavior of such particles in the detector will depend on the charge (see Section 4.3.2.1) and, to a lesser extent, the mass. In this work the particles are assumed to have a

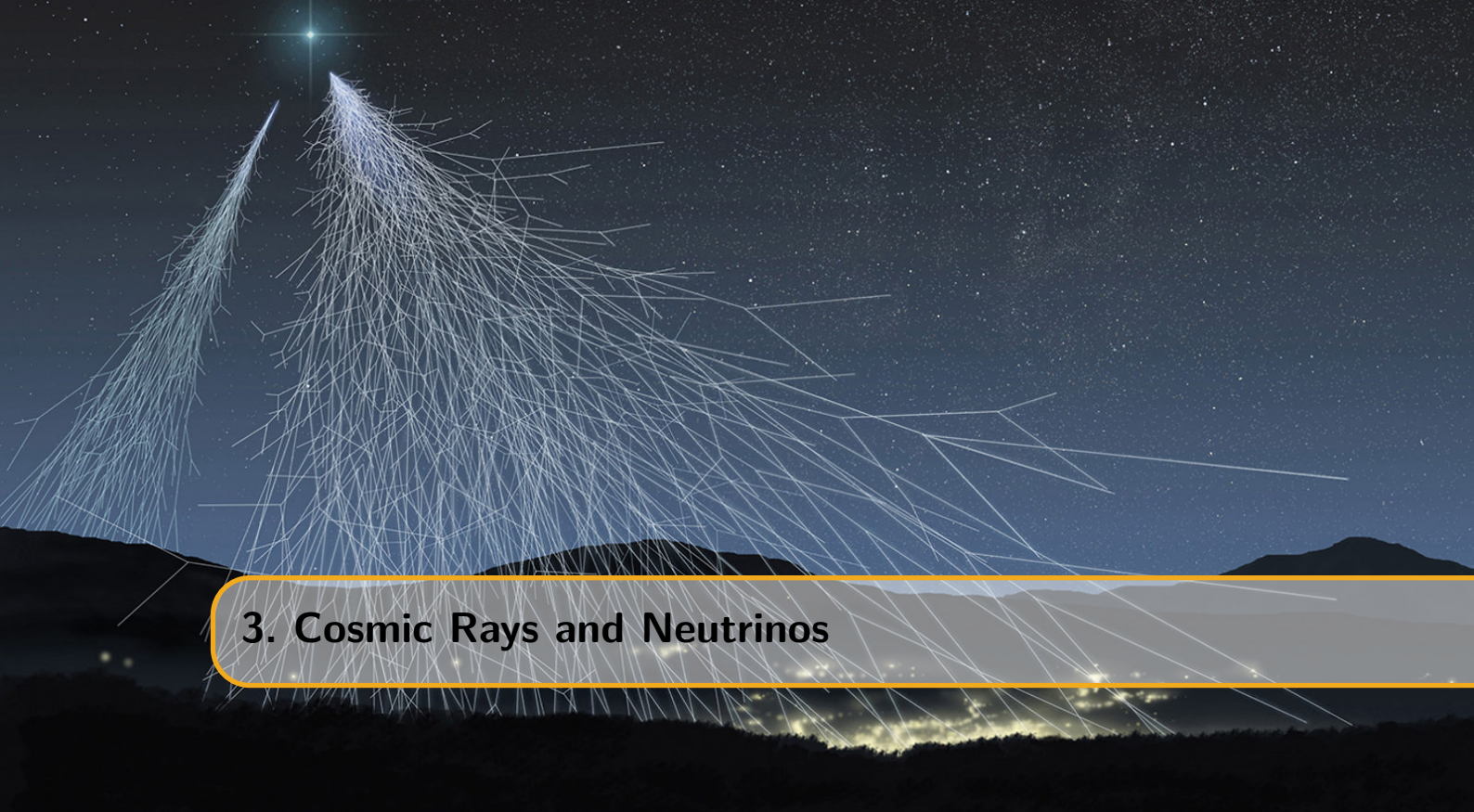
- charge of 1/3, 1/2 or 2/3;
- mass of 10 GeV, 100 GeV, 1 TeV, 10 TeV or 100 TeV,

where I have referred to the charge of the particles as relative to the absolute electron charge, e^* . The possible combinations result into a total of 15 unique signal samples that will be searched for.

The detector used in this analysis, the IceCube detector, is a neutrino telescope. The properties of the signal were defined to be able to compare this work to the results seen in Figure 2.1. The best limits were set by the MACRO and Kamiokande experiments. The former was a multipurpose underground detector located at Gran Sasso, Italy and designed to search for magnetic monopoles with the use of liquid scintillators and streamer tubes [95]. This design also made it possible to operate as a neutrino detector and cosmic ray observatory and allowed for BSM searches such as particles with a fractional charge.

The Kamiokande observatory, a water Cherenkov detector (see Chapter 4) was designed to search for proton decay and located deep underground to shield the detector from cosmic ray muons (see Chapter 3). Because of its design and very efficient shielding from cosmic rays, the detector also operates as a neutrino observatory and can also be used to search for particles with a fractional charge. The experiment was later extended to Kamiokande II, III and Super-Kamiokande.

*This will be done throughout this work from this point on.



3. Cosmic Rays and Neutrinos

We sit in the mud, my friend, and reach for the stars ~ Ivan Turgenev

Cosmic rays, contrary to their name, almost exclusively exist of particles with a finite rest mass. The term *rays* was historically attributed to these particles as they were thought to be mostly electromagnetic radiation. They are particles coming from outer space, impinging on our atmosphere and producing other particles and large showers of electromagnetic radiation. The interest in cosmic rays within the field of modern particle physics is clear: many new particles were discovered from the interactions at energies that were higher than most experiments could reach. Positrons, muons, pions, and kaons were first discovered in cosmic ray experiments in the 1930s and 1940s. Today, high-energy cosmic ray interactions are still of interest as the highest energies of these particles go beyond what is feasible even at the most powerful accelerators such as the LHC.

Complementary to cosmic ray experiments is the field of neutrino astronomy as neutrinos are expected to be produced together with cosmic rays, near the source or close to Earth. This makes neutrino astronomy an interesting and possibly powerful part of modern day astronomy.

This chapter serves as an overview of the origin of cosmic rays and neutrinos and describes their properties. Both produce particles that are visible in neutrino telescopes such as the IceCube experiment and are important backgrounds in this analysis. For a more exhaustive description of cosmic rays I refer the reader to Ref. [96].

3.1 Cosmic rays

3.1.1 Discovery of cosmic rays

With the use of electrometers, the Austrian physicist Victor Hess performed several groundbreaking balloon flight experiments in 1912 to prove that the amount of ionizing radiation increases with altitude [97]. This was in strong contradiction with the widespread belief that ionizing radiation on Earth's surface mostly originates from radioactive substances in its crust. Hess concluded that extremely penetrating radiation existed. He described this radiation to be coming from space that enters Earth's atmosphere. Hess later ruled out the possibility that cosmic rays originate from the Sun as his observations showed no particular difference in night and day and during solar eclipses. In the late 1920s, first evidence was found that cosmic rays

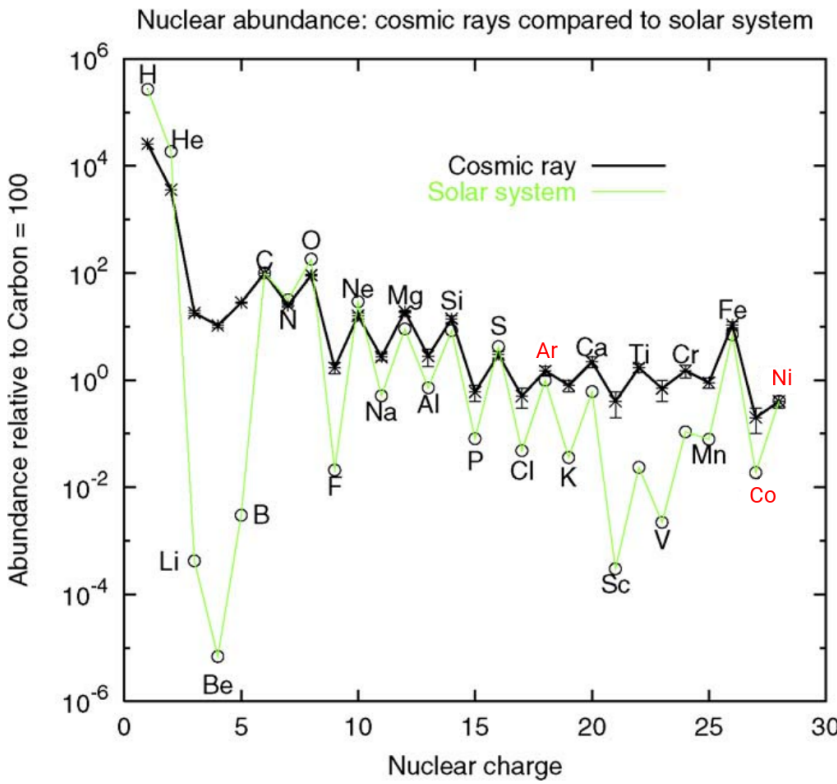


Figure 3.1: The cosmic ray elemental abundances with energy < 100 TeV measured on Earth compared to the solar system abundances, all relative to ${}^6\text{C} = 10^2$. Figure from Ref. [100], with minor corrections in red.

were charged due to a variation of their intensity with latitude, which indicated that they were deflected by the geomagnetic field [98].

Hess's ideas proved to be correct, but it was wrongfully attributed to electromagnetic radiation by Robert Millikan in the 1920s [99].

3.1.2 What are cosmic rays?

Cosmic rays are, almost exclusively, nuclei that are stripped of their electrons, making them electrically charged, heavy particles. Around 90% of the particles are ionized hydrogen atoms or protons; 9% are alpha particles and 1% are nuclei of heavier elements. A much smaller fraction of incoming particles are electrons, positrons and antiprotons.

There is a striking resemblance between the relative abundance of cosmic rays and elements in the solar system as seen in Figure 3.1. There are, however, two important differences between cosmic rays and elements from our solar system. Firstly, the two groups of elements Li, Be, B and Sc, Ti, V, Cr, Mn are many orders of magnitude more abundant in cosmic rays than in the solar system. More massive cosmic rays (mainly C, O and Fe) can produce these nuclei in the process of *spallation*; they are produced by collisions of cosmic rays with the interstellar medium. Therefore, these nuclei are sometimes referred to as *secondary nuclei*. Spallation effects in our solar system are orders of magnitude lower compared to cosmic rays, explaining the difference we see in the relative abundance of these two groups. The second difference is that nuclei with an atomic number $Z > 1$ are much more abundant with respect to hydrogen in cosmic rays. This phenomenon is not yet well understood but might be attributed to the difficulty to ionize hydrogen, necessary for acceleration processes.

The flux of cosmic rays seen on Earth is expressed in units of $[\text{m}^{-2}\text{s}^{-1}\text{sr}^{-1}]$. We can see in Figure 3.2 that the cosmic ray flux follows a power law energy spectrum

$$dN \propto E^\gamma dE, \quad (3.1)$$

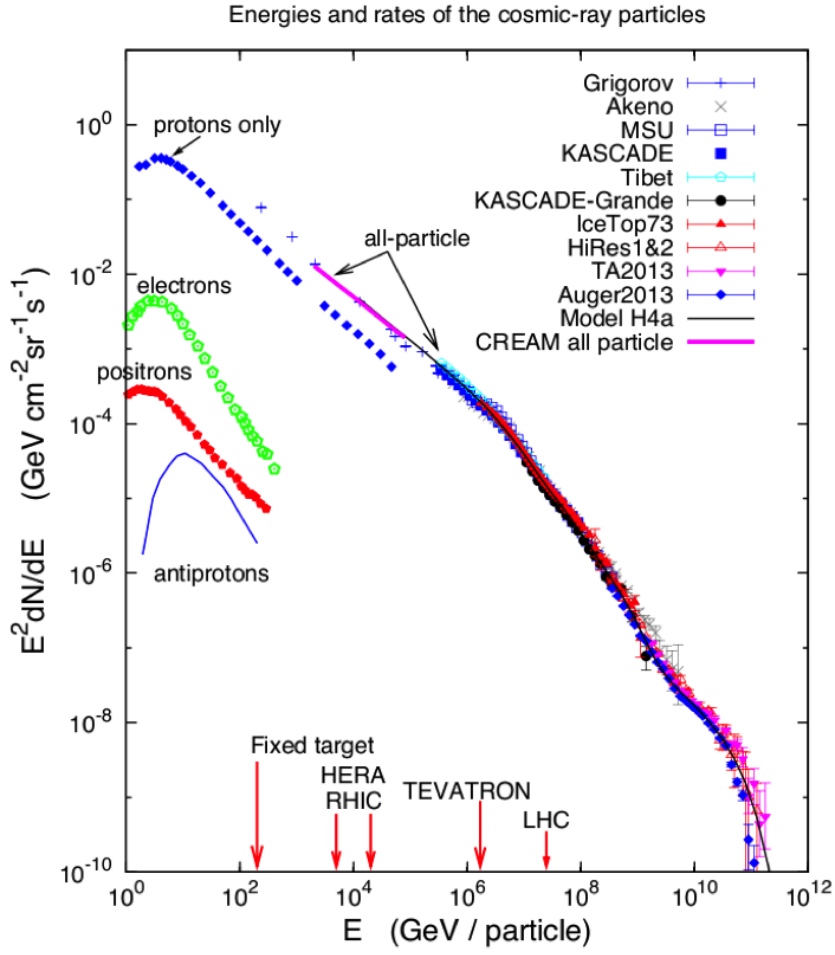


Figure 3.2: Spectrum of cosmic rays at Earth. The all-particle spectrum measured by different experiments is plotted together with the proton-only spectrum. Subdominant contributions to the total flux from electrons, positrons and antiprotons as measured by the PAMELA experiment are also shown. The primary particle energies are compared to accelerator experiments by showing what energy the primary particle should have to reach a similar center-of-mass energy compared to these accelerators, see Eq. 2.2. Figure from Ref. [101].

where γ is called the *spectral index*. Because of the steepness of the spectrum, it is often multiplied by a higher power of energy as can be seen in Figure 3.2*.

We can divide the global spectrum in four regions. Between 10 GeV and 1 PeV, the differential spectral index is around -2.7. From 10 PeV to 1 EeV, it's around -3.1. Below 10 GeV, there is a strong suppression of cosmic rays due to an effect called *solar modulation*[†]. Above 10 EeV, the spectrum again flattens to an index around -2.6 and an apparent cutoff region is present at around 10^{20} eV. The transition of this first to second region at around 3 PeV is referred to as the *knee*. The second to third region transition is called the *ankle*. It might be possible to describe the full cosmic-ray spectrum with sources within our galaxy. However, a more generally accepted theory is that the knee in the spectrum originates from the end of a population of particles that are accelerated within our Milky Way [102]. Around 100 PeV is the *second knee*, believed to be a feature of the iron drop-off (see Section 3.1.2.1).

*The broad range in both energy and flux, visible in Figure 3.2, should convince the reader that many types of detectors are necessary to study the behavior of cosmic rays. Low-energy particles are abundant and high-energy particles are much more rare. Both the energy and the incoming flux will determine the type and size of the detector.

[†]In the solar system, a stream of charged particles (electrons, protons and alpha particles) is released from the Sun, creating a magnetic field. Cosmic rays coming into the solar system interact with these particles and magnetic field where the influence is greatest on particles with the lowest energies.

The origin of cosmic rays has been a topic of discussion for many years. We now know that most particles originate from sources in the local galaxy, having spent on average 10^7 years in diffusive motion in the interstellar medium [102]. This is consistent with the similar features of the relative abundances of cosmic rays and elements from our solar system. However, there is no general consensus about the origin of the cosmic rays with energies above 3 EeV. In the following, the above-mentioned energy regions are discussed in more detail.

3.1.2.1 Galactic component

It is believed that low-energy cosmic rays have a galactic origin. The most probable acceleration mechanism is by shocks driven by expanding supernova remnants (SNRs) [103]. This is supported by observations of a lower gamma-ray emissivity from π^0 decay from Magellanic Clouds compared to the Milky-Way [104] and the detection of a typical π^0 -decay in the γ -spectrum from SNRs [105].

With their approximate energy density of around 0.5 eV/cm^3 in our local galaxy, the cosmic ray energy density results into a total power of around

$$L_{CR} = 7 \times 10^{40} \text{ erg/s}, \quad (3.2)$$

where erg is a unit often used in astronomy*. If one assumes a supernova explosion rate of around one per every 30 years, then the total power output of type II supernovae with a mass output of around ten times the mass of the Sun at a velocity close to $5 \times 10^8 \text{ cm/s}$ would result in a power of

$$L_{SN} \sim 3 \times 10^{42} \text{ erg/s}. \quad (3.3)$$

These numbers are not set in stone and hold large uncertainties, but it shows that with an acceleration efficiency on the order of a couple of percent, supernova explosions could be a prominent source of energetic cosmic rays, if not the dominant one.

It is still unclear if the galactic component is solely due to SNRs or if other possible sources, such as pulsars, have a measurable contribution.

From the ratio of primary to secondary nuclei, it can be inferred that cosmic rays travel distances thousands of times greater than the thickness of the disk of the galaxy. There is also an apparent decrease in the amount of matter that is traversed by cosmic rays with higher energies than with lower. Higher-energy cosmic rays seem to spend less time in the galaxy than lower-energy ones which suggests that cosmic rays are accelerated before most propagation occurs [96].

The way the cosmic ray spectrum is fit is not set in stone. Here I will use the convention used by Gaisser, Stanev and Tilav described in Ref. [102]: the spectrum is subdivided in three populations. The first population corresponds to the particles that are primarily accelerated by supernova remnants, with the knee signaling the cutoff of this population. The second population is a higher-energy galactic component of unknown origin. The third generation will be described in more detail in Section 3.1.2.2. Analogously to Ref. [102], we assume that the *magnetic rigidity*, R , is an appropriate variable for interpreting changes in the spectrum due to propagation and acceleration in magnetic fields. The rigidity is defined as

$$R = \frac{pc}{Ze}, \quad (3.4)$$

where Ze is the charge of a nucleus of total energy $E_{tot} = pc$. This assumption follows from the consideration that cosmic rays are accelerated via moving magnetic fields.

The magnetic rigidity relates to the gyroradius of a particle, r_g , in a given magnetic field B as

$$r_g = \frac{R}{B}. \quad (3.5)$$

* $1 \text{ erg} = 10^{-7} \text{ J}$.

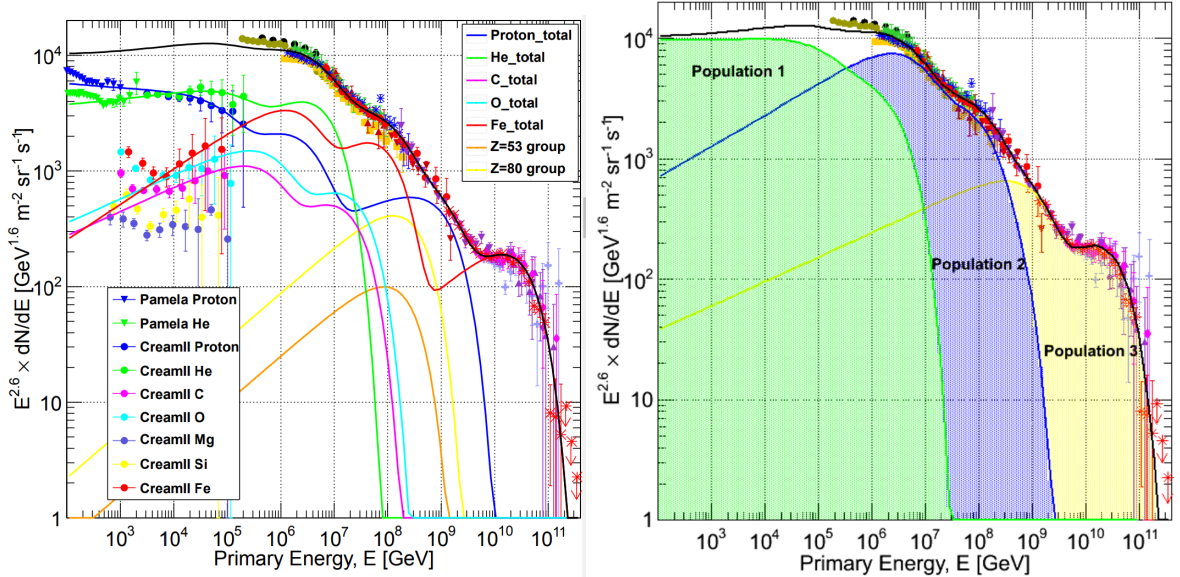


Figure 3.3: Overview of the categorization of the cosmic-ray spectrum as done in Ref. [102]. The individual components are shown on the left, and the total contribution of the three proposed populations are shown on the right.

If there is a characteristic rigidity, R_e , above which a particular acceleration process reaches a limit, then the feature will show up in total energy first for protons, then for helium and so forth for heavier nuclei according to

$$E_{tot} = Ze \times R_e. \quad (3.6)$$

This effect is visualized in Figure 3.3 and indicates that as one population reaches its maximum, the composition becomes heavier. The second knee, reported by KASCADE-Grande [106] and GAMMA [107] could be explained with an “iron knee” bump.

3.1.2.2 Extragalactic component

Very-high-energy cosmic rays are almost certainly from extragalactic origin and result in a flux at the highest energies that is exceedingly small. The number of events at energies above 5 EeV is around one per square kilometer per century. There are only two experiments in the world capable of detecting the highest-energy cosmic rays in a statistically meaningful way: Telescope Array, located in the Northern Hemisphere (instrumented area of $\approx 700 \text{ km}^2$) and the Pierre Auger Observatory in the Southern Hemisphere (instrumented area of $\approx 3000 \text{ km}^2$).

Both experiments see a suppression of the flux above $6 \times 10^{19} \text{ eV}$ as seen in Figure 3.4. The cutoff is consistent with the expected Greisen-Zatsepin-Kuzmin (GZK) effect [108, 109] where cosmic rays interact with the cosmic microwave background radiation (CMB)

$$\gamma_{\text{CMB}} + p \rightarrow \Delta^+ \rightarrow p + \pi^0 \quad (3.7)$$

or

$$\gamma_{\text{CMB}} + p \rightarrow \Delta^+ \rightarrow n + \pi^+. \quad (3.8)$$

The Pierre Auger experiment reported to see higher compositions at the highest energies [110]. If the particle is a nucleus with A nucleons, then the GZK limit applies to its nucleons, which carry only a fraction $1/A$ of the total energy. For iron nuclei, this would for example result in a limit of $2.8 \times 10^{21} \text{ eV}$. In contrast, the TA experiment interpreted their data as implying a light primary composition (mainly p and He) at the highest energies. Both experiments use a different interpretations for crucial quantities of these measurements and a thorough joint analysis conducted by both experiments states that, at the current level of statistics and understanding of

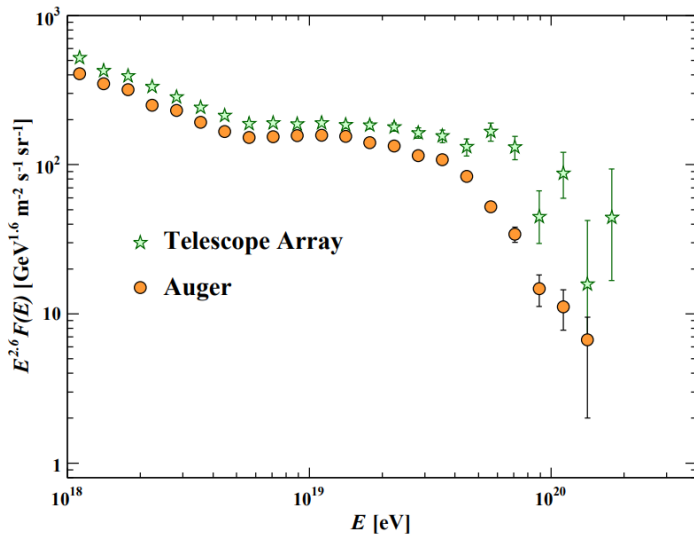


Figure 3.4: Expanded view of the highest energy portion of the cosmic-ray spectrum from data of the Telescope Array and the Pierre Auger Observatory [43].

systematics, both data sets are compatible with being drawn from the same parent distribution [43].

It is also possible that the cutoff corresponds to the “end-of-steam” for cosmic accelerators [111] and that the differences in PA and TA lies at a fundamental difference between northern and southern skies.

The exact origin of Ultra High Energy Cosmic Rays (UHECR) is uncertain. We will see in Section 3.1.3.1 that the maximum energy from shock acceleration by a supernova remnant is insufficient to explain UHECRs. Particles can be accelerated if the trajectory of the particles can be changed and energy can be transferred multiple times. The magnetic fields responsible for the course change of these particles have to be sufficient in magnitude in order for these particles not to escape and go beyond the reach of the source responsible for the acceleration. This limitation is expressed by the gyroradius of the accelerator, $r_L = E/ZeB$ similar to Eq. 3.5, requiring it to be smaller than the physical radius of the accelerator: $r_L < R$ or $E < ZeBR$.

Even if only qualitative, this relation provides an interesting criterion to identify possible sources of UHECRs by looking at the accelerator related term BR . This was done in a classic paper by Hillas [112], illustrated in the more recent Figure 3.5. Accelerators necessary to explain the amount of UHECRs are not populated (enough) in our galaxy, making them more likely to be of extra-galactic origin. Active galactic nuclei, gamma ray bursts, starburst galaxies, and galaxy clusters, which are currently thought to be the sources of UHECRs, are therefore also briefly explained.

To this date, it has not been proven that these sources all contribute and if they are the sole contributors. There are also more exotic theories on the origin of UHECRs, such as the decay of super-heavy particles [114].

The Pierre Auger Observatory also reported evidence for an anisotropic distribution of the arrival directions of the highest-energy cosmic rays from a direction where the distribution of galaxies is relatively high and does not coincide with the galactic plane [115]. These observations, together with our lack of known possible sources within our galaxy for these ultra-high energies, are compelling evidence that these particles have an origin from outside our galaxy. From pion decay, there is also an expected flux from extragalactic neutrinos (more information in Section 3.3.3). The flux, spectrum and angular distribution of the excess neutrino signal detected by IceCube between ≈ 50 TeV and ≈ 2 PeV are also inconsistent with those expected for Galactic sources [116].

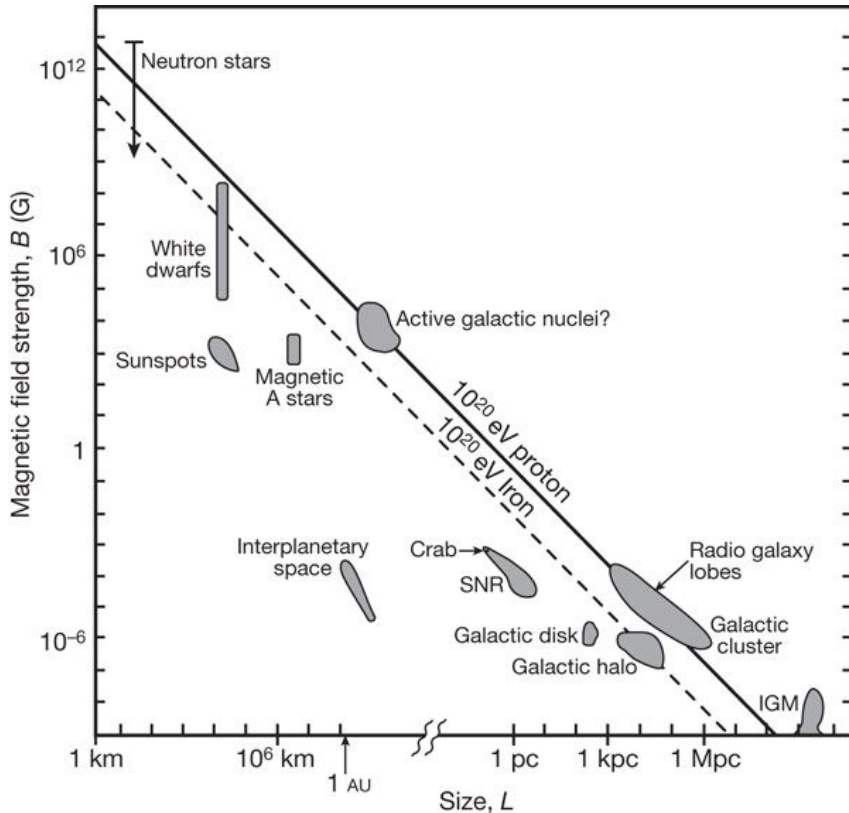


Figure 3.5: The Hillas plot of potential cosmic ray accelerators determines objects according to size and magnetic field. Objects to the left of the diagonal lines cannot accelerate particles to 10^{20} eV (proton: solid, iron: broken). Image obtained from Ref. [113].

3.1.3 Acceleration mechanism

How cosmic rays get their signature slope and the intricate details in the energy spectrum have been under discussion for multiple decades. To this date, there is no clear detailed picture how these particles are accelerated. It is beyond the scope of this work to give a comprehensive overview of all possible acceleration mechanisms or possible sources. Most calculations are left out and for a more detailed discussion, the reader is referred to specialized books or the references in the text.

The acceleration of the particles can be subdivided into two questions. First, where are the particles accelerated? Does it happen on large scales, cosmological distances in galaxies or near specific sources? Secondly, how are these particles exactly accelerated? What is the driving mechanism? Since primary cosmic rays are all electromagnetically charged particles, these mechanisms should clearly be sought for in places where electric and/or magnetic fields play a dominant role. Below, a summary of the possible sources is given.

3.1.3.1 Supernova (remnants)

Supernovae can be broadly subdivided in two categories: type I and type II. Type I supernova explosions happen in binary star systems. In those systems, one of the two stars is a carbon-oxygen white dwarf that accretes matter from the second star. When the total mass of the white dwarf reaches the Chandrasekhar limit of around 1.44 solar masses, it cannot longer hold itself under the gravitational pressure and collapses in on itself. Within seconds, the carbon component in the white dwarf starts nuclear fusion and enough energy is released to produce an explosion brighter than the Sun with a factor of around 5 billion. A resulting shock wave can reach up to around 3% of the speed of light.

Type II supernova explosions differ by being single star systems. When a star reaches the end of its life cycle, the subsequent fusion reactions reach a halt. If the star has enough mass (at least

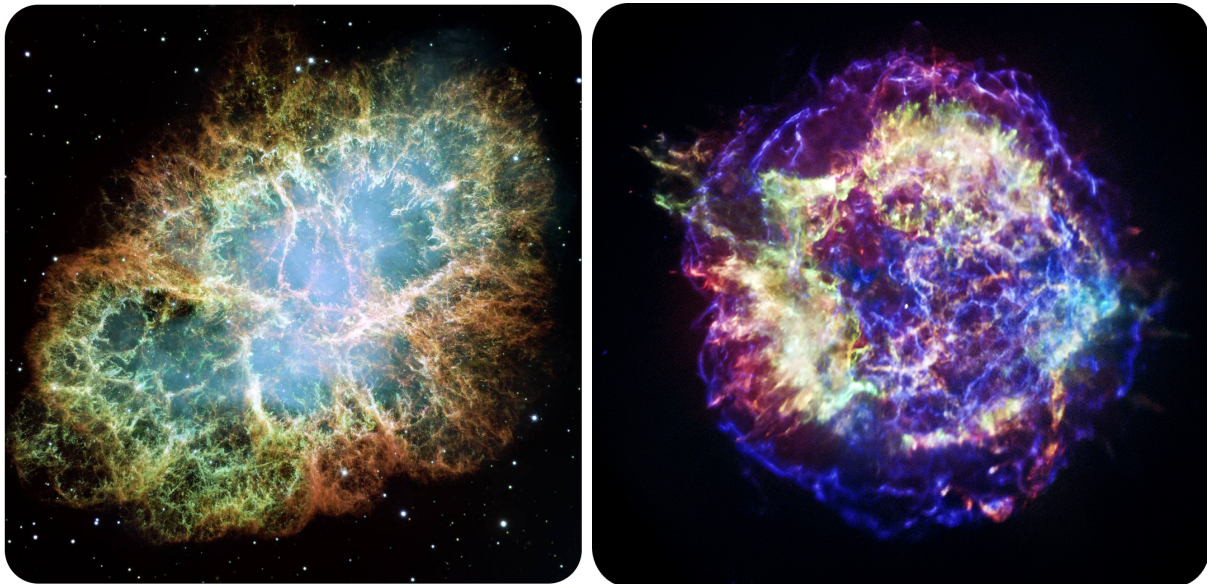


Figure 3.6: *Left:* the Crab Nebula is a supernova remnant approximately one thousand years old. The supernova was noted by Chinese astronomers in the year 1054 AD. *Right:* Chandra X-ray observatory picture of the Cassiopeia A supernova remnant (pictures from NASA).

8 times the mass of the Sun), it is possible for the inner core to again reach the Chandrasekhar limit and collapse in on itself due to the lack of *electron degeneracy*. Without the outward pressure of nuclear fusion reactions and the support of the core, the outer layers of the star collapse under the gravitational pressure. The compression of the electrons and protons into neutrons results in a very hot, dense, neutron core. The velocity of the inward falling layers can reach a staggering 23% of the speed of light and recoil when hitting the remaining core. The outward going shock wave hits the remaining outer layers forming the supernova explosion*. This violent core collapse is an additional neutrino production mechanism.

Because of their brightness, supernovae within our galaxy can be seen with the naked eye (provided they are not obscured). The last recorded supernova from our galaxy was by Kepler in 1604 but the earliest recordings go back to 185 AD by Chinese astronomers†.

The question remains how supernovae can serve as cosmic ray accelerators. In 1949, Fermi proposed a mechanism where particles can gain energy by collisions with moving interstellar ionized gas clouds. Only later, it was realized that a large, plane shock front moving with a certain velocity is able to accelerate charged particles much more efficiently. This first mechanism results in an energy transfer proportional to the squared velocity of the cloud and is thus called *second order Fermi acceleration*. Shock front acceleration energy transfer is proportional to the velocity and is called *first order Fermi acceleration*. Supernova remnants provide an explanation for the origin of these shock fronts.

First- and second-order Fermi acceleration

Suppose we have a magnetic cloud in the interstellar medium traveling with a certain velocity \vec{V} and a particle with velocity \vec{v} enters the cloud under an angle θ_1 (see Figure 3.7, left). If we assume collisionless scattering (no energy is dissipated from the particle to the cloud) due to

*To get a better feeling of how extraordinary these events really are, I'd like to illustrate what it would be like if one could be close to a supernova event. From Figure 3.11, one can calculate that the number of solar neutrinos going through our hand per second is around *one trillion*. Yet, they are so weakly interacting that, on average, only one will interact with an atom in our body every few years. Supernova explosions are vast, releasing around 10^{57} neutrinos. This number is large enough that even if an observer is a distance of 2.3 AU away from the event, he would still receive a fatal radiation dose of *neutrinos alone*. Another example: looking at a supernova at a distance of 1 AU is 10^9 times brighter than detonating a hydrogen bomb pressed against your eyeball.

†From observations of other galaxies, supernovae are expected to occur, on average, once every thirty years. Not all of these will be visible to the naked eye, but would almost certainly be observable with modern astronomical telescopes.

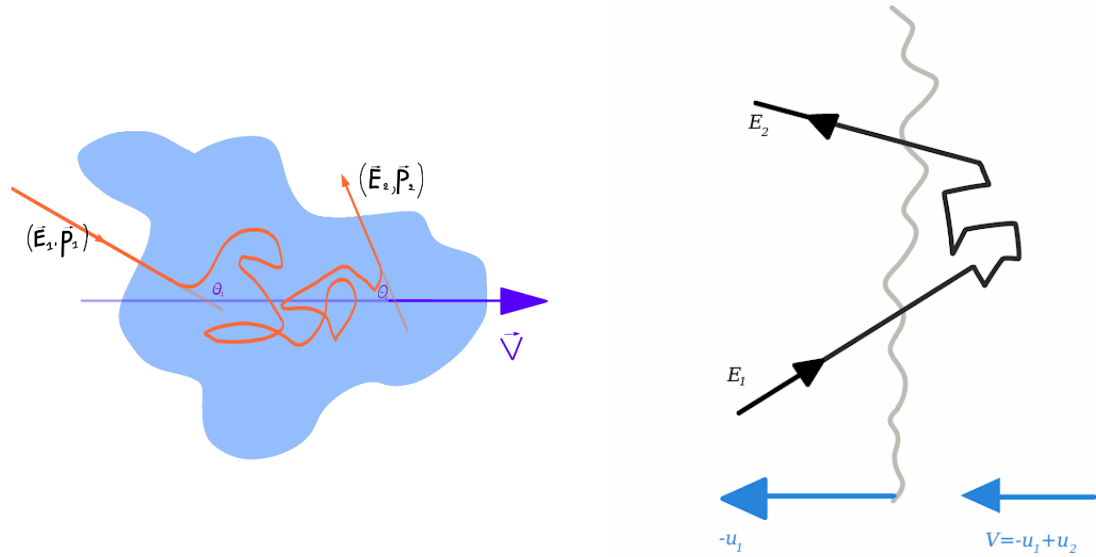


Figure 3.7: *Left:* magnetic cloud showing second-order Fermi acceleration. *Right:* shock waves typically have magnetic inhomogeneities both preceding (downstream) and following them (upstream). If a charged particle travels through the shock wave, it can gain velocity through first-order Fermi acceleration. In the illustration, a particle travels from upstream to downstream and back upstream. At every back and forth movement, the particle effectively gains energy. For a particle with a velocity u_1 relative to the shock front, the front seems to come at him with velocity $-u_1$. The downstream medium has a velocity relative to the shock front of $u_2 < u_1$ making it seem coming towards the particle with velocity $u_1 - u_2$.

the magnetic fields in the cloud, the magnitude of the momentum in the rest frame of the cloud will not change ($E'_1 = E'_2$, where the apostrophe denotes the cloud rest frame). From special relativity we know that:

$$\begin{aligned} E'_1 &= \gamma (E_1 - p_{1,\parallel} V) \\ &= \gamma E_1 (1 - \beta \cos \theta_1), \end{aligned} \quad (3.9)$$

with $\beta = V/c$ and γ the Lorentz factor. Similarly, and using $E'_1 = E'_2$

$$\begin{aligned} E_2 &= \gamma E'_2 (1 + \beta \cos \theta'_2) \\ &= \gamma^2 E_1 (1 - \beta \cos \theta_1) (1 + \beta \cos \theta'_2) \end{aligned} \quad (3.10)$$

and

$$\frac{\Delta E}{E} = \frac{E_2 - E_1}{E_1} = \frac{1 - \beta \cos \theta_1 + \beta \cos \theta'_2 - \beta^2 \cos \theta_1 \cos \theta'_2}{1 - \beta^2} - 1. \quad (3.11)$$

By hypothesis, the escaping particles are isotropic in the cloud frame: $\langle \cos \theta'_2 \rangle = 0$. One can show that $\langle \cos \theta_1 \rangle = -\frac{\beta}{3}$ [96], leading to

$$\frac{\Delta E}{E} = \frac{4}{3} \frac{\beta^2}{1 - \beta^2} \approx \frac{4}{3} \beta^2, \quad (3.12)$$

showing that for molecular clouds, the energy gain is indeed proportional to the square of β , thus second-order Fermi acceleration.

If a particle is incoming to an expanding shock (see Figure 3.7, right), one can prove that $\langle \cos \theta_1 \rangle$ is equal to $-2/3$ and $\langle \cos \theta'_2 \rangle$ is equal to $2/3$, leading to

$$\frac{\Delta E}{E} = \frac{\frac{4}{3}\beta + \frac{13}{9}\beta^2}{1 - \beta^2} \approx \frac{4}{3}\beta, \quad (3.13)$$

where β is now equal to $u_1 - u_2$, as explained in the caption of Figure 3.7. We have shown that for shock fronts the energy gain is indeed proportional to β for first-order Fermi acceleration.

Power

The energy gain of a “single collision” results in a powerlaw spectrum when considering a process in which a test particle increases its energy by an amount proportional to its energy with each encounter. Let us assume $\Delta E = \xi E$, then, after n encounters:

$$E_n = E_0 (1 + \xi)^n, \quad (3.14)$$

where E_0 is the energy when the particle first enters the accelerator medium. To reach a certain energy E' , the particles must undergo a number of collisions

$$n(E') = \frac{\ln\left(\frac{E'}{E_0}\right)}{\ln(1 + \xi)}. \quad (3.15)$$

To reach energies of E' or higher, the number of collisions will be proportional to

$$\begin{aligned} N(\geq E') &\propto \sum_{m=n}^{\infty} P_{present}(m) = \sum_{m=n}^{\infty} (1 - P_{esc})^m \\ &= (1 - P_{esc})^n \left((1 - P_{esc}) + (1 - P_{esc})^2 + \dots \right) \\ &= \frac{(1 - P_{esc})^n}{P_{esc}}, \end{aligned} \quad (3.16)$$

where $P_{present}$ is the probability of a particle still being present in the accelerator and P_{esc} the probability of the particle to escape per collision. Making use of $a^{\ln b} = e^{\ln a \ln b} = b^{\ln a}$ and inserting Eq. 3.15 yields

$$N(\geq E') \propto \frac{1}{P_{esc}} \left(\frac{E'}{E_0} \right)^{-\gamma}, \quad (3.17)$$

with

$$\gamma = \frac{\ln\left(\frac{1}{1-P_{esc}}\right)}{\ln(1 + \xi)} \approx \frac{P_{esc}}{\xi}. \quad (3.18)$$

The power law spectrum becomes visible in the derivative of the number of particles in energy

$$\frac{dN}{dE} \sim E^{-(\gamma+1)}, \quad (3.19)$$

in agreement with Eq. 3.1 (although γ is not the same variable here). Shock wave fronts have an expected $\gamma \approx 1$, giving rise to a different spectrum to what is seen on Earth but which can be explained by propagation from the source to Earth (see 3.1.4). The spectrum from Fermi shock acceleration is thus expected to follow an E^{-2} powerlaw behavior.

Maximum energy

The highest energies that particles can be accelerated to can be defined by

- the differential energy gain per collision dE/dt , and
- the total time the particle can be accelerated.

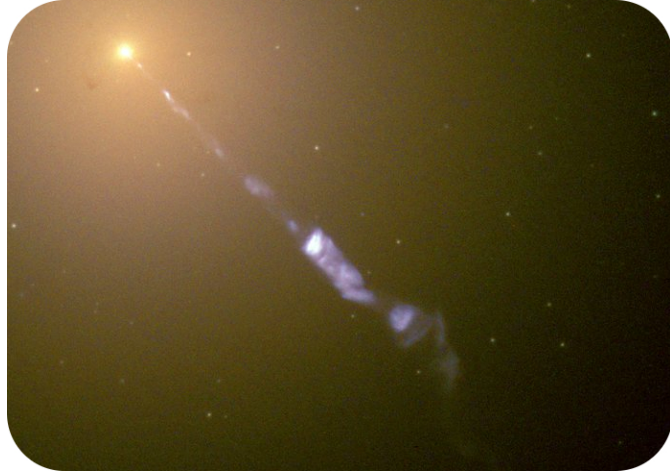


Figure 3.9: Image from the Hubble telescope where we see a jet streaming out from the center of galaxy M87.

The energy gain is given by

$$\frac{dE}{dt} = \frac{\xi E}{T_{cycle}}, \quad (3.20)$$

where T_{cycle} is the characteristic time for one acceleration cycle. T_{cycle} depends on the diffusion coefficients and velocities of the upstream and downstream regions and is set to $T_{cycle} \geq 20E/(3u_1ZeB)$ by Lagage and Cesarsky [117] for a strong shock and arguing that the diffusion length, λ_D , cannot be smaller than the Larmor radius of the particle. Particles with a Larmor radius greater than the irregularities holding a magnetic field are not prone to be heavily influenced by them. Lagage and Cesarsky therefore concluded that

$$E_{max} \leq \frac{3}{20} \frac{u_1}{c} ZeB(u_1 T_{ST}), \quad (3.21)$$

where T_{ST} is the Sedov-Taylor time where particles are less prone to escape and is ~ 1000 years. For $u_1 \sim 10^9$ cm/s [118] and $B \sim 3\mu G$ the Lagage and Cesarsky limit reads

$$E_{max} \leq Z \times 2.4 \times 10^{14} \text{ eV}. \quad (3.22)$$

Therefore, SNR are most probably not the origin if UHECRs.

3.1.3.2 Active Galactic Nuclei

Active Galactic Nuclei (AGNs) are no stars at the end of their life cycle but active black holes located in the center of galaxies. It is believed that most massive galaxies have supermassive black holes in their centers by the accretion of matter from surrounding large gas clouds [119, 120]. However, this is still under debate. AGN masses in current models range from 10^6 to 10^{10} solar masses [121].

The efficient conversion of gravitational potential energy to kinetic energy and radiation make AGNs the most luminous persistent sources of electromagnetic radiation in the universe. As such, they serve as very good tools to discover distant objects. The accretion discs heat up due to friction from the inward falling matter and produce light peaking in the ultraviolet waveband. Certain emission lines are also expected due to the radiation from excited cold atomic material. Some accretion discs produce jets, which point opposite to each other. Their direction is defined by either the spin of the black hole, the accretion disc, or a combination of both. The most powerful AGNs are classified as *quasars* and AGNs with a jet pointing toward the Earth are called *blazars*.

Charged particles can have a large magnetic rigidity in AGNs and the relativistic jets could provide the necessary mechanisms to accelerate particles to ultra-high energies. The Pierre Auger collaboration hinted to a correlation of the highest-energy cosmic rays with the positions of nearby active galactic nuclei [122].

3.1.3.3 Gamma Ray Bursts

The most catastrophic deaths of massive stars or mergers of two neutron stars or of a neutron star and a black hole result into Gamma Ray Bursts (GRBs). GRBs are named after the burst of gamma rays that is followed by a longer-lived afterglow of electromagnetic radiation at longer wavelengths. These bursts are the most energetic explosions in the electromagnetic spectrum and occur when a high-mass star collapses to form a neutron star or black hole. A typical burst releases as much energy in a few seconds as the Sun does in its entire 10 billion-year lifetime and temporarily outshines the rest of the galaxy*. GRBs are isotropically distributed, making them extragalactic in origin [124].

An often used model to explain how charged particles could reach extremely high energies is called the *fireball model*. This internal-external shock model assumes that kinetic energy of an ultra-relativistic flow is dissipated in internal collisions.

Although there is still much ongoing discussion, GRBs are usually subdivided into two groups: *long gamma ray bursts* ($t_{burst} > 2$ s) and *short gamma ray bursts* ($t_{burst} < 2$ s). Long bursts originate from collapsars: a massive star core-collapse forms a black hole and surrounding matter is pulled into an accretion disk. Short bursts hint to progenitors that are extremely compact, where neutron star-neutron star or neutron star-black hole mergers are the most probable explanation. The recent detection of gravitational waves can provide a significant contribution to the understanding of these sources [125, 126, 127, 128, 129].

3.1.3.4 Starburst galaxies

Galaxies that undergo an episode of large-scale star formation, are called *starburst galaxies*. Most of these are in the midst of a merger or close encounter with another galaxy. Several experiments have shown their gamma ray emission at several hundred GeV to be two to three orders of magnitude higher than in our own galaxy [130, 131]. Galactic scale winds from the central regions are possible sources for cosmic ray acceleration.

3.1.3.5 Galaxy clusters

When galaxies are bound together by gravity, they are referred to as *galaxy clusters*. They can contain around 100 to 1000 galaxies and have typical mass ranges around $10^{14} - 10^{15}$ solar masses. Through merging and accretion of dark matter and baryonic gas, galaxy clusters are expected to generate powerful shock waves on large scales. Shocks with significant velocities could provide the necessary conditions for cosmic ray acceleration [132].

3.1.4 Propagation

After creation, particles also encounter propagation effects on their way to Earth. For example, charged particles can be deviated in magnetic fields close to or far from their source and by the Earth's magnetic field. The particles can also interact with expelled matter from the source soon after their creation. Other possibilities are interactions with gas clouds **hoe nauwkeurig is dit?**, which lead to spallation effects or a loss of energy. The models describing these effects will not be given in this work. However, it is noteworthy to mention that in these models the measured cosmic ray flux becomes much softer than the source flux. The discrepancy between spectral indices around -2.7/-3 and a theoretical source flux around -2 is usually attributed to these propagation effects. For more information, I refer the reader to Ref. [96].

3.2 Air showers

When primary cosmic ray particles hit the Earth's atmosphere, they give rise to a large shower of secondary particles. At low- to mid-energy ranges, the abundance of cosmic rays is large enough for these showers to be analyzed with balloon or satellite experiments. As indicated in Section

*GRBs were first discovered in the late 1960s by accident. The Vela satellites had additional gamma ray detectors designed to detect very fast bursts of gamma rays that were expected to be produced by nuclear tests in space [123].

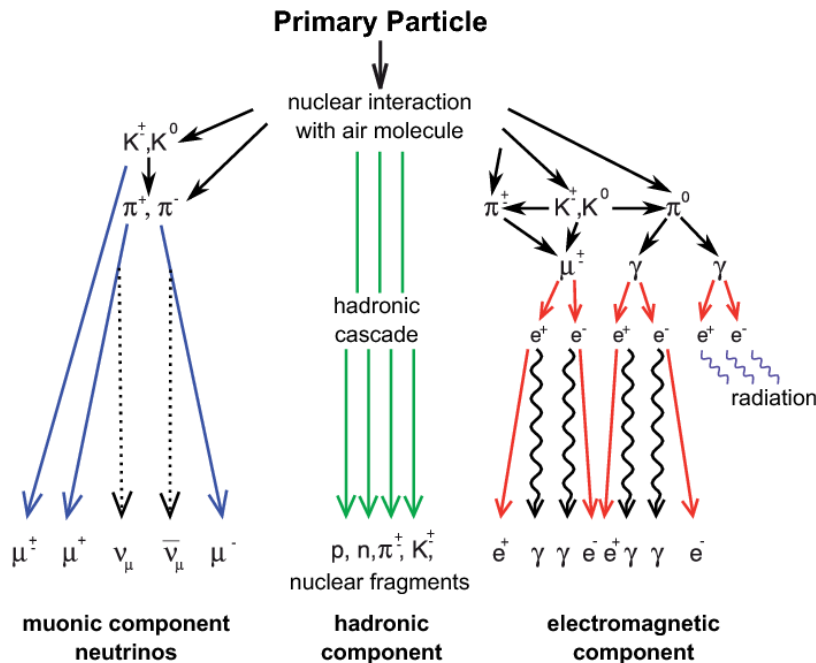


Figure 3.10: Schematic view of an extensive air shower with a clear distinction between the three components. Image from the KASKADE collaboration.

3.1.2, the flux of high-energy cosmic rays is so small that there is a need for very large-scale detectors, measuring square kilometers in instrumented area.

The interaction length of nuclei with high energies is too small for them to be able to travel as close as a couple of tens of kilometers in height as measured from the ground. They will interact with an atmospheric nucleus and produce secondary particles. These particles in their turn decay or interact further with the atmosphere and give rise to an *extensive air shower* (EAS) if the production of new particles is large enough. Some of these particles will be stopped, but others are capable of reaching the Earth or even penetrate deep inside it. Although air showers are of significant importance in cosmic ray studies, we will only give a brief summary of the most noteworthy features and its main importance for this analysis. An air shower has three components: the hadronic, muonic, and electromagnetic, but also produces neutrinos. These components are discussed in more detail in Section 3.3. The hadronic component can be seen as the core of the shower, consisting of high-energy hadrons. The interactions and subsequent decays of these hadrons fuel the electromagnetic and muonic parts. A schematic overview is given in Figure 3.10. If the primary particle is a photon, the shower is made up almost exclusively of an electromagnetic component. Because the lateral size of an electromagnetic cascade is caused by multiple scatterings of electrons and positrons, the lateral size of these showers is relatively small (radius around 1 km at sea level for a vertically downgoing 100 TeV photon). In hadronic cascades, on the other hand, the lateral size is caused by the transverse momenta of the secondary particles making these showers much larger (radius around 4 km at sea level for a vertically downgoing 100 TeV proton) [133].

3.2.1 Hadronic component

When a proton interacts with a nucleus, it interacts with another proton or a neutron and will most often produce charged or neutral pions

$$\begin{aligned} p + N &\rightarrow p + N + k\pi^+ + k\pi^- + r\pi^0, \\ p + N &\rightarrow n + N + (k+1)\pi^+ + k\pi^- + r\pi^0, \end{aligned} \quad (3.23)$$

where N stands for a nucleon of an atmospheric nucleus and k and r are the multiplicities of the produced pions. The extension to heavier nuclei from this is straightforward. On average, one-third of the hadron production will be neutral pions ($k/r \approx 3$), which decay immediately into electromagnetic particles

$$\pi^0 \rightarrow \gamma + \gamma \quad (98.8\%) \text{ or} \quad (3.24)$$

$$\pi^0 \rightarrow e^+ + e^- + \gamma \quad (1.17\%). \quad (3.25)$$

The other two-thirds will be charged particles that have a lot longer lifetime, making them much more probable to interact with air nuclei. After having traveled a distance corresponding to their mean interaction length, charged particles interact again with air nuclei if their energy is large enough. 90% of these charged particles are new pions and 10% of the daughter particles are kaons. Pions almost exclusively decay to muons ($\pi^+ \rightarrow \mu^+ + \nu_\mu$) and the most dominant kaon decay modes are (similar for K^-) [43]

$$\begin{aligned} K^+ &\rightarrow \pi^+ + \pi^0 & (20.7\%), \\ K^+ &\rightarrow \mu^+ + \nu_\mu & (63.6\%), \\ K^+ &\rightarrow \pi^0 + e^+ + \nu_e & (5\%), \\ K^+ &\rightarrow \pi^0 + \mu^+ + \nu_\mu & (3.4\%), \end{aligned} \quad (3.26)$$

where the first decay mode fuels the hadronic component further. The remaining decay modes enter in the EM and muonic components. The total number of hadrons reaching sea level is very small and when they do, they are immediately stopped.

3.2.2 Muonic component

Muons are the dominant component of charged particles reaching sea level (around 80%) [133]. Most muons that are produced in an EAS are able to reach so far due to their relativistic velocities and lifetime of $2.2 \mu\text{s}^*$. They have relatively low ionization losses compared to electrons, making them very penetrating and therefore referred to as the *hard component*. Muons can also decay and contribute to the electromagnetic component via

$$\begin{aligned} \mu^+ &\rightarrow e^+ + \nu_e + \bar{\nu}_\mu, \text{ and} \\ \mu^- &\rightarrow e^- + \bar{\nu}_e + \nu_\mu. \end{aligned} \quad (3.27)$$

3.2.3 Electromagnetic component

At each hadronic interaction, slightly more than a third of the energy goes into the electromagnetic component. Since most hadrons re-interact, eventually most of the primary energy finds its way into the electromagnetic component. Muons also produce delta electrons or electron-positron pairs from pair production (see Section 4.4.4).

At energies above a few MeV, photons interact with the electric field of atmospheric nuclei in a process called pair production and convert into electron-positron pairs. High-energy electrons and positrons primarily emit photons via bremsstrahlung. These two processes are repeated until the photons fall below the pair production threshold and bremsstrahlung energy loss starts to dominate. Because electrons lose their energy fast, they are almost immediately stopped when they reach dense matter (Earth's surface) and hence referred to as the *soft component*.

*The half-survival length of 5 GeV muons is $L = \ln(2) \times \gamma \times 2.2 \mu\text{s} \times 0.9998 \times c = \gamma \times 456 \text{ m} \approx 23 \text{ km}$. The relativistic time dilation is of crucial importance here!

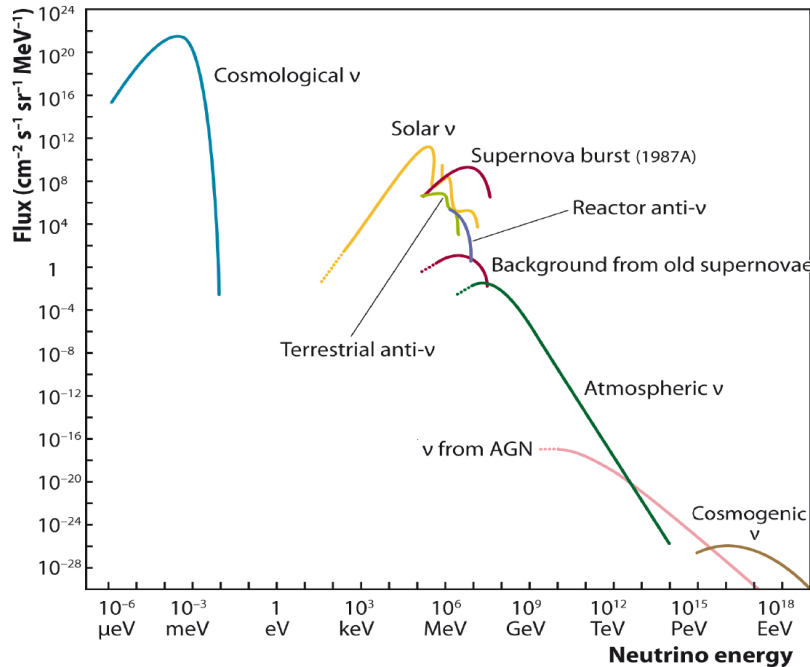


Figure 3.11: Plot illustrating several neutrino sources that cover a huge range of energy. Illustration from Ref. [134].

3.3 Neutrinos

As by-products of cosmic ray collisions with matter, neutrinos provide incontrovertible evidence for hadronic acceleration. Since these particles are weakly-interacting, they can escape much denser environments and hold crucial information about the origins of their production environments. Because these particles barely interact, their detection is difficult. Similarly to cosmic rays, neutrinos cover a broad range in energy (see Figure 3.11), calling for different types of detectors to cover this large spectrum.

Cosmic rays are deflected in magnetic fields and therefore, their arrival direction at Earth does not hold much pointing information (Figure 3.12). Light ranging from radio to gamma rays in the electromagnetic spectrum is of crucial importance in astrophysics but has its limitations: photons can be absorbed by interstellar medium, or are trapped in opaque sources. At higher energies ($\approx 10^{14}$ eV), photons interact with the CMB and produce electron-positron pairs ($\gamma + \gamma \rightarrow e^+ + e^-$). Unless the sources are close by, no photons are capable of reaching Earth (see Figure 3.13). Neutrinos escape from the sources more easily and are not deflected by magnetic fields, making them key messengers in identifying cosmic ray accelerators. As mentioned in Section 3.2, neutrinos are also produced in air showers. In the following, we will go over the different types of neutrinos that are detectable on Earth.

3.3.1 Conventional

Neutrinos are produced in large abundances in air showers (see Section 3.2; Eq. 3.26 and 3.27). The neutrinos that are produced with low to high energies (\approx MeV to PeV range) are called *atmospheric* or *conventional* neutrinos. They are primarily produced in pion or kaon decay. Due to helicity effects, pion and kaon decay to electrons/electron neutrinos is strongly suppressed compared to decays into muons/muon neutrinos. As a result, the ratio of electron neutrinos to muon neutrinos is about 2

$$\frac{N(\nu_\mu + \bar{\nu}_\mu)}{N(\nu_e + \bar{\nu}_e)} \approx 2, \quad (3.28)$$

which should be clear when we look at the example of pion decay where the muon decays as well

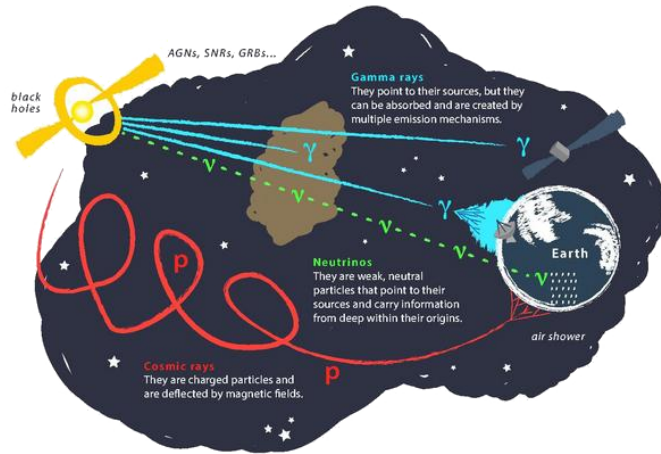


Figure 3.12: Artist impression of the path that several types of particles travel before reaching Earth.

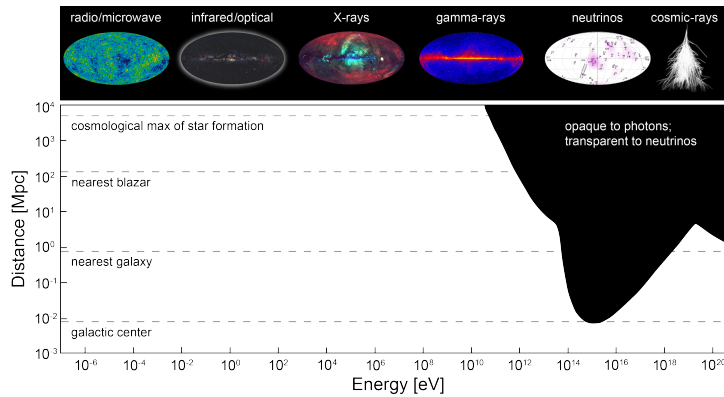


Figure 3.13: Illustration of the visibility of sources in function of their distance and the photon energy. The dip in the photon visibility comes from the pair production peak when photons interact with the CMB. Both illustrations from the IceCube collaboration.

$$\begin{aligned} \pi^+ &\rightarrow \mu^+ + \nu_\mu \\ &\rightarrow e^+ + \nu_e + \bar{\nu}_\mu + \nu_\mu. \end{aligned} \quad (3.29)$$

The most referred to calculations for the atmospheric neutrino flux were done by Honda et al. [135].

3.3.2 Prompt

Charmed mesons, also called D mesons, are the lightest particles that contain charm quarks*. Hints of charm particles were first seen in cosmic rays in 1971 by Niu et al. [137]. The production of these particles is strongly suppressed, but is expected to exhibit a harder spectrum than conventional neutrinos do. These mesons have short lifetimes (hence the name: prompt) and decay into neutrinos independent of their energy and arrival direction. Therefore, their energy spectrum is expected to follow that of primary cosmic rays. Their contribution at higher energies can be non-negligible or even become dominant. To this date, it has not been possible to observe this prompt component, but it remains an interesting signal in diffuse neutrino searches and could contribute significantly to background expectations, usually in analyses looking for high-energy

* $D^0 : c\bar{u}, \bar{D}^0 : u\bar{c}, D^+ : c\bar{d}, D^- : d\bar{c}$

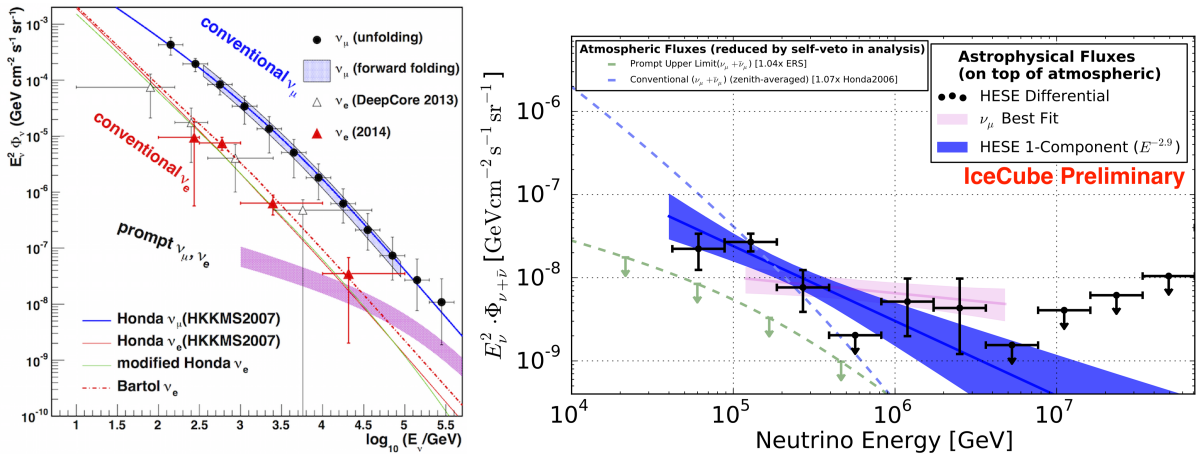


Figure 3.14: *Left:* Measurement from the IceCube collaboration showing the difference in ν_e and ν_μ flux. *Right:* Measured differential astrophysical flux using contained events (points) and a fit to that data (blue line and band), compared with the best fit obtained from throughgoing ν_μ (pink line and band). From Ref. [136].

neutrinos. The most referred to calculations for the prompt neutrino flux were done by Endberg et al. [138].

3.3.3 Astrophysical

Astrophysical neutrinos are expected to be created when cosmic rays interact close to their interaction sites. Because they are neutral and are unlikely to be absorbed, astrophysical neutrinos are expected to reveal more information about these sources. To first order, these neutrinos would follow the spectrum of cosmic rays at their production. As indicated in Section 3.1.3.1, this is equal to an E^{-2} powerlaw spectrum from Fermi shock acceleration. The majority of these neutrinos are expected to arise from decays from pions that were created in these cosmic-ray interactions ($\pi \rightarrow \mu + \nu_\mu$) followed by the muon decay ($\mu \rightarrow e + \nu_e + \nu_\mu$). The resulting flavor ratio fraction is $\nu_e : \nu_\mu : \nu_\tau = 1 : 2 : 0$ at the source. Neutrino oscillations* across cosmological distances give an expected $\nu_e : \nu_\mu : \nu_\tau = 1 : 1 : 1$ expectation at Earth. Given the tension between different analyses, as can be seen in Figure 3.14, it is still unclear if the spectrum at high energies can be described with a single power law or something more complex.

The spectrum is expected to follow a harder spectrum compared to the conventional and prompt neutrino fluxes and dominate at the highest energies.

Recently, a collaborative effort of IceCube, Fermi-LAT, MAGIC and others observed a coincidence of high-energy neutrinos and a blazar, making them very good candidates of sources of astrophysical neutrinos [139].

3.3.4 Other neutrino sources

The abovementioned neutrino sources are most important for high-energy neutrino research. Other, more abundant sources such as cosmological, solar, terrestrial and reactor neutrinos, play less of a role in kilometer scaled detectors such as the IceCube detector (see Chapter 5). Supernova and GZK neutrinos have not yet been observed but are a part of the experiment's search strategies and therefore briefly explained below.

3.3.4.1 Supernova neutrinos

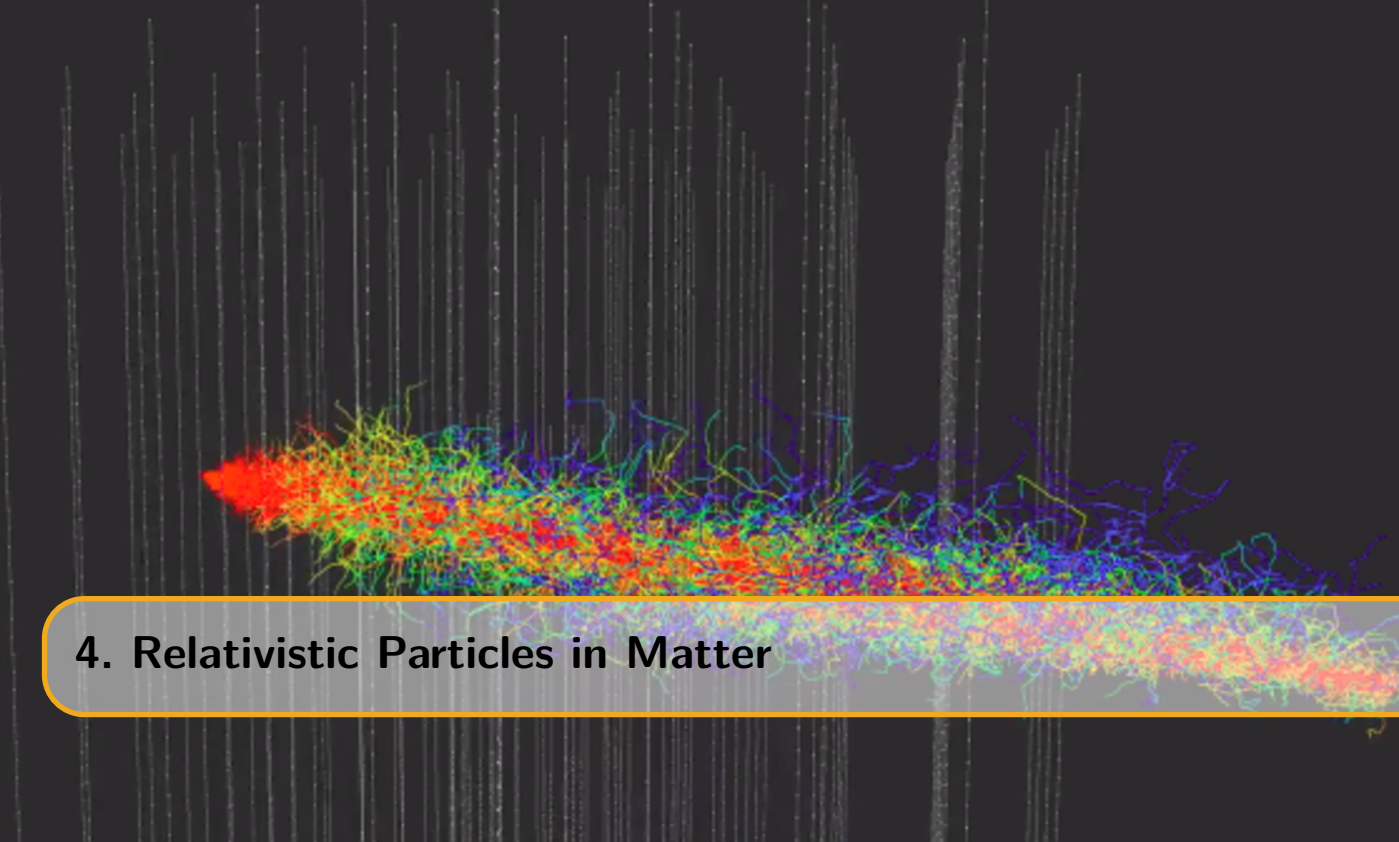
The core collapse of stars where electrons and protons are compressed into neutrons as described in Section 3.1.3.1 dissipates most of its energy in the production of neutrinos ($e^- + p^+ \rightarrow n + \nu_e$) [140]. Since the IceCube detector is designed to detect neutrinos with an energy greater than 100

*Explained in Section 1.3.4.

GeV, supernova neutrinos with an energy of a couple of MeV are only visible to the detector due to a collective raise of individual hits of the equipment. The sensitivity ranges from 20 standard deviations at the galactic edge (30 kpc) and 6 standard deviations at the Large Magellanic Cloud (50 kpc) [141].

3.3.4.2 GZK neutrinos

The GZK-effect was introduced in Section 3.1.2.2 where it was explained how high-energy cosmic rays interact with the CMB. The pions that are produced in this process can decay to neutrinos. These neutrinos are expected to have an energy above ~ 10 PeV. To this date, no neutrino events with an unquestionable GZK origin have been observed [142]. There are, however, ongoing experiments trying to measure the flux of these extremely energetic neutrinos (see Section 5.7.2.3).



4. Relativistic Particles in Matter

*Hofstadter's Law: It always takes longer than you expect, even when you take into account
Hofstadter's Law*

Charged particles that travel faster than the speed of light in that material produce light in a process that is called the *Cherenkov effect*. The production of photons makes it possible to detect particles with a non-zero charge (electrons, muons, SMPs, etc.) in a neutrino detector such as the IceCube experiment. This cubic-sized detector is able to register the light that is produced from charged particles in air showers and charged particles that are created when neutrinos interact with the ice around or inside the detector. In this chapter, an overview is given of the Cherenkov effect and the different other physical processes that are visible in the IceCube detector. These signatures have to be accounted for in the background prediction when looking for particles with an anomalous charge. Finally, the energy loss formulae of charged particles in matter are given.

4.1 Cherenkov effect

From Einstein's works on special and general relativity, it follows that the speed of light in vacuum, c , is a universal constant. The speed of light in matter can be significantly lower than that. If a particle travels through a dielectric medium at a speed that is greater than the phase velocity of light in that medium, electromagnetic radiation is emitted. This radiation is called *Cherenkov radiation* and is named after the first person who was able to detect it experimentally, Pavel Cherenkov. He was awarded the Nobel Prize in 1958 for his findings together with Frank and Tamm for their theoretical work on the subject [143].

The velocity of a propagating wave is given by the three-dimensional wave equation

$$\nabla^2\psi = \frac{1}{v^2} \frac{\partial^2\psi}{\partial^2t}, \quad (4.1)$$

where ψ is the wave function and v its group velocity. From Maxwell's equations and some vector calculus, it is straightforward to find that the wave equation for electromagnetic radiation becomes

$$\nabla^2E = \mu\epsilon \frac{\partial^2E}{\partial^2t}, \quad (4.2)$$

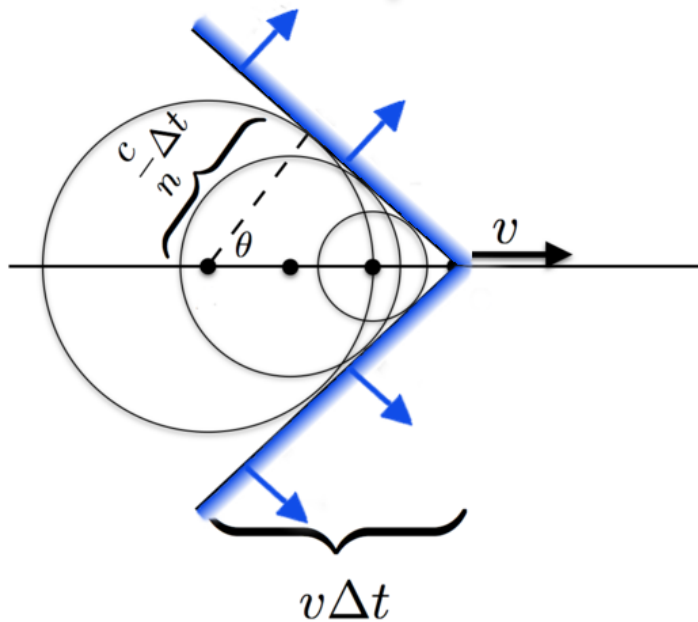


Figure 4.1: Schematic view of Cherenkov radiation from a particle traveling at a velocity v .

where E is the electric field and μ and ϵ the permeability and permittivity of the medium, respectively. From these equations it is clear that for light in a dielectric medium

$$v = \frac{1}{\sqrt{\mu\epsilon}} = \frac{1}{\sqrt{\mu_r\epsilon_r}} \frac{1}{\sqrt{\mu_0\epsilon_0}} = \frac{1}{\sqrt{\mu_r\epsilon_r}} \times c \leq c, \quad (4.3)$$

where $1/\sqrt{\mu_0\epsilon_0} = c$ and μ_r and ϵ_r are the relative (to vacuum) permeability and permittivity, respectively and are ≥ 1 . These terms are also written as the refractive index of the medium, $n = \sqrt{\mu_r\epsilon_r}$ and result in

$$v = c/n. \quad (4.4)$$

When a charged particle moves inside a dielectric medium, it excites the molecules of the medium to the higher levels and excited states. The molecules emit photons in the form of electromagnetic radiation upon returning back to their ground state. According to the *Huygens principle*, the emitted waves move out spherically at the phase velocity of the medium (which can be less than the speed of light in vacuum). If the motion of the particle is slow, the radiated waves bunch up slightly in the direction of motion, but they do not cross. However, if the particle moves faster than the speed of light, the emitted waves add up constructively, leading to a coherent radiation at an angle θ_c with respect to the particle direction; Cherenkov radiation. The coherent interference is enough to be visible to the naked eye*. The signature of the effect is a cone of emission in the direction of particle motion. Figure 4.1 shows a schematic view of the Cherenkov radiation, illustrating the typical spherical wavefront and the resulting radiation†.

From the figure we can derive that

$$\cos \theta_c = \frac{\frac{c}{n}\Delta t}{v\Delta t} = \frac{c}{vn} = \frac{1}{\beta n}. \quad (4.5)$$

Because $-1 \leq \cos \theta_c \leq 1$, the velocity of the charged particle must be $v \geq c/n$. Typical values of n are on the order of 1-2, requiring the particles to be relativistic in order to emit Cherenkov radiation. The number of photons produced per unit path length of a particle with charge ze

*The typical blue light in the cooling water at nuclear reactors is also due to this Cherenkov radiation.

†The typical cone shape of this effect can be easily seen when observing ducks. If a duck is traveling in a straight line in the water, individual concentric waves can be distinguished and a cone shaped wave is produced behind them.

and per unit energy interval of the photon was calculated by Frank and Tamm, and is often referred to as the Frank-Tamm equation [43]

$$\begin{aligned} \frac{d^2N}{dEdx} &= \frac{\alpha z^2}{\hbar c} \sin^2 \theta_c = \frac{\alpha^2 z^2}{r_e m_e c^2} \left(1 - \frac{1}{\beta^2 n^2(E)} \right) \\ &\approx 370 \sin^2 \theta_c (E) \text{ eV}^{-1} \text{cm}^{-1} \quad (z = 1), \end{aligned} \quad (4.6)$$

where r_e is the classical electron radius, m_e the electron mass and α the fine-structure constant. Equivalently, this equation can be written in function of the wavelength of the photon

$$\frac{d^2N}{dxd\lambda} = \frac{2\pi\alpha z^2}{\lambda^2} \left(1 - \frac{1}{\beta^2 n^2(\lambda)} \right), \quad (4.7)$$

where it is clear that the charge of the particle will influence the total Cherenkov light yield. A charge of $1/3e$ will reduce the light output with a factor of 9 compared to a particle with a charge equal to the electron charge, e , such as a muon.

Examples of experiments that make use of this Cherenkov effect are air Cherenkov telescopes such as MAGIC, H.E.S.S and VERITAS that look for the direct and indirect Cherenkov light from gamma rays and cosmic rays. Because the refractive index of air is close to 1 (1.000293 at sea level and smaller with increasing height) the opening angle of the Cherenkov cone is small ($\approx 1^\circ$). The particles need to be very relativistic in order for Cherenkov radiation to occur*.

In water and ice, the refractive index is ≈ 1.33 , making $\beta_{min} = 0.75$ and $E_{min} = 1.51 \cdot m_0$. Experiments using water or ice as the interaction medium are Super-Kamiokande, ANTARES and the IceCube experiment.

Most of the light that is emitted from charged particles traveling through matter originates from this Cherenkov effect, provided that their energy is not too high. At higher energies, the amount of secondary particles with an energy high enough to produce Cherenkov effects themselves, becomes so large that this becomes the primary source of light (see Section 4.4). This analysis focusses on SMPs that lie below this threshold and we see from Eq. 4.7 that the charge of the SMP enters in the photon production quadratically. SMPs with a lower charge are therefore expected to produce less photons than minimum ionizing muons.

4.2 Neutrino interactions

The IceCube experiment is a neutrino detector, but neutrinos have no electromagnetic charge. Neutrinos are only visible through their production of secondary particles with an electromagnetic charge and they emit Cherenkov radiation in the ice. Here, we briefly describe how these interactions take place.

Neutrinos interact with matter through both charged current (CC) and neutral current (NC) processes. In the former, the mediator particle is a charged W boson resulting in a charged lepton in the final state. In the latter, the mediator particle is the neutral Z boson. Both interaction types have a resulting hadronic component as daughter particles. The interactions can be written as

$$\nu_l (\bar{\nu}_l) + N \xrightarrow{W} l^- (l^+) + X^{+(-)} \quad (CC) \quad (4.8)$$

$$\nu_l (\bar{\nu}_l) + N \xrightarrow{Z} \nu'_l (\bar{\nu}'_l) + X \quad (NC), \quad (4.9)$$

*Let us assume the refractive index of air at sea level, then, from $E^2/m^2 = \gamma^2 = 1/(1 - \beta^2)$, it follows that the minimal energy is ≈ 41 times its rest mass. Since the refractive index decreases in function of height, the energies of particles interacting with the atmosphere must be even higher.

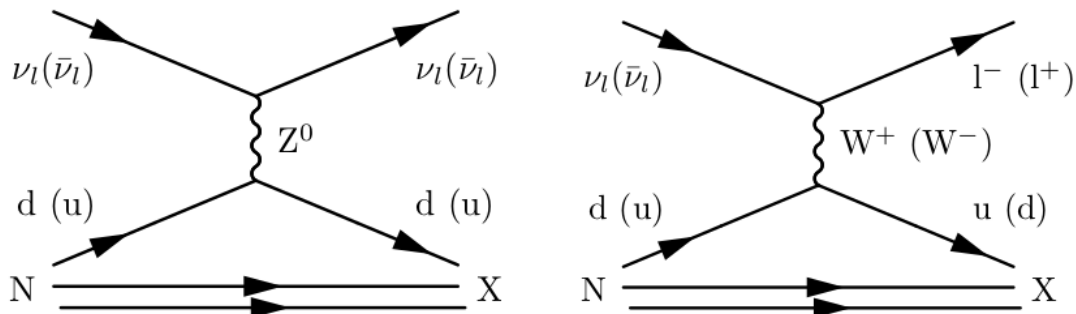


Figure 4.2: Feynman diagrams of NC (left) and CC (right) neutrino interactions. l is the lepton flavor (e, μ, τ), N denotes the initial hadronic state of the nucleus and X the final hadronic state. The antineutrino interactions are given in brackets.

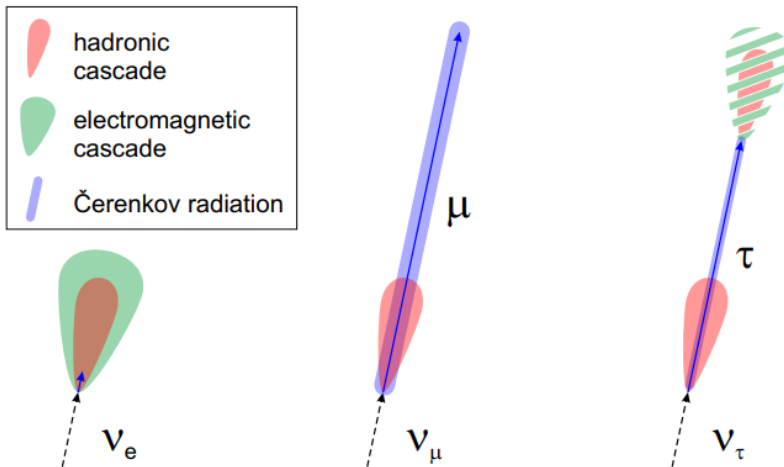


Figure 4.3: Schematic view of the charged current neutrino signatures in matter. At each interaction point there is a hadronic cascade (red). Every hadronic cascade has electromagnetic sub-showers which are not illustrated here. Muons and energetic taus can give rise to tracks. The electromagnetic and hadronic cascades have a more spherical shape but are exaggerated for illustrative purposes in the figure. Illustrations from Ref. [145].

where l is the lepton flavor (e, μ, τ), N denotes the initial hadronic state of the nucleus and X the final hadronic state. These interactions are illustrated in Figure 4.2.

The charged leptons and hadrons lead to light production via gamma ray production and Cherenkov radiation. With the right material, it is possible to detect this light production and reconstruct some of the neutrino's characteristics. Because the light production depends on the square of the charge of a particle, the IceCube detector is not powerful in detecting if the primary particle was a neutrino or antineutrino*.

4.3 Propagation

As described in Section 4.2, neutrinos give rise to several types of interactions in the surrounding medium. There are three characteristic signatures, which are the main interest in the IceCube detector (illustrated in Figure 4.3).

*Although it is not possible to distinguish neutrino from antineutrino events on an event-by-event basis, there are ways to look at differences. One example is to look at inelasticity effects as done in Ref. [144].

4.3.1 Cascades

4.3.1.1 Electrons and photons

In a charged current electron-neutrino interaction, the energetic electron gives rise to a shower of gamma rays (bremsstrahlung) and positrons and electrons (pair production). Positrons and electrons in their turn emit new gamma rays and this process continues until the photon energies fall below the pair production threshold. Because electrons/positrons lose their energy fast, they are almost immediately stopped, giving an *electromagnetic cascade* an almost spherical shape.

Let us assume E_0 is the energy of the incoming electron. In a very simplistic toy model one can say that an electron emits one photon after one radiation length, X_0 . A photon will decay into an electron-positron pair after approximately one radiation length too*. At every decay or radiation process, it is assumed that the daughter particles carry 1/2 of the energy. After t steps, the energy is equal to

$$E(t) = \frac{E_0}{2^t}. \quad (4.10)$$

The number of particles will be equal to

$$N(t) = 2^t. \quad (4.11)$$

At a critical energy E_c , the multiplication process stops (as pair production dominates over bremsstrahlung) and we find

$$t_{max} = \frac{\ln\left(\frac{E_0}{E_c}\right)}{\ln 2}, \quad (4.12)$$

the total longitudinal length of an electromagnetic shower is thus approximately equal to

$$X = X_0 \frac{\ln\left(\frac{E_0}{E_c}\right)}{\ln 2}. \quad (4.13)$$

This logarithmic dependence on the energy of the initial particle will therefore result into elongations of a couple of meters at most. Typical values in ice are $X_0 \approx 40$ cm and $E_c \approx 80$ MeV.

4.3.1.2 Hadrons

In the case of neutral current events, the breakup of the struck nucleus leads to charged byproducts. These byproducts can re-interact in the medium and produce neutral pions that decay into gamma rays. These particles again die out quickly, resulting in a spherical emission of light for *hadronic cascades*. The basic development of hadronic cascades in space is very similar to that of electromagnetic ones, but with important differences in energy loss, particle content, lateral spread and fluctuations. Hadronic cascades contain particles heavier than electrons, that have a higher Cherenkov threshold. A fraction of them are slow neutrons, which do not produce any light. Neutral pions produce gamma rays. Charged pions, on the other hand, can decay into muons and muon neutrinos; long-ranged particles that do not contribute to the cascading process. Finally, a non-negligible fraction of the energy is lost in the hadronic binding processes.

The light yield will be smaller than the one obtained from an electromagnetic cascade of equal initial energy and with much larger event-by-event variations.

4.3.2 Muon tracks

Muons are produced in charged current muon-neutrino interactions and travel much further than electrons and positrons. The relativistic muon will produce light according to the Frank-Tamm equation, Eq. 4.7, resulting in *direct Cherenkov radiation*. Ionization, bremsstrahlung,

*In fact, one radiation length actually implies $1/e$ times the initial energy. Assuming the electron loses half its energy to the photon, and with $0.63/0.5 \approx 1$, the radiation length is indeed almost equal to the average length an electron travels before emitting a photon. The total probability for pair production per unit radiation length from a photon is $\approx 7/9$, where we again assume that this is ≈ 1 .

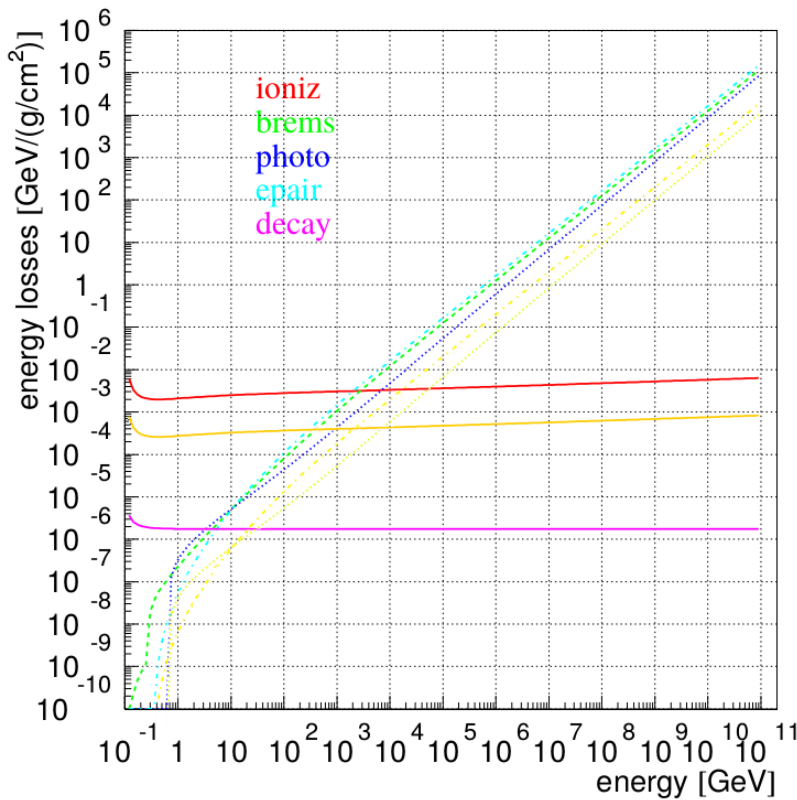


Figure 4.4: Muon energy loss from ionization (upper solid curve, red), bremsstrahlung (dashed, green), photonuclear (dotted, blue), pair production (dashed-dotted, cyan) and decay (lower solid curve, purple). Additionally, the expected energy losses of a muon with charge 1/3 are shown in orange/yellow. Ionization, photonuclear and pair production scale with z^2 , giving a factor 9 difference. Bremsstrahlung, which has a z^4 dependence is left out.

pair production, and photonuclear interactions (see Section 4.4) are also capable of producing relativistic secondary particles that produce *indirect Cherenkov radiation*. Both effects result in a Cherenkov cone with a diffuse light emission from the track in all directions behind it.

4.3.2.1 Energy loss

Below 1 TeV, muons will lose most of their energy to ionization losses. A charged particle traversing matter ionizes the material around it. When the energy transfer is high enough, electrons can be stripped away from their atoms, resulting in *delta electrons*. As can be seen in Figure 4.4, ionization losses have only a very weak energy dependence. It is therefore very difficult to distinguish for example a 50 GeV from a 500 GeV muon as the direct Cherenkov light production will be similar (Eq. 4.7) and the energy loss is from the almost-energy-independent ionization.

Above 1 TeV, however, the muon, on average, loses more energy to stochastic* effects. Here, effects such as bremsstrahlung, pair production and the photonuclear effect dominate over ionization (see Section 4.4). Therefore, indirect Cherenkov production starts to dominate and makes the energy estimation much easier.

The average energy loss from ionization and stochastic effects along the muon trajectory can be parameterized by [146]

$$-\frac{dE}{dx} = a + b \cdot E_\mu, \quad (4.14)$$

*In this context we mean that the energy losses are not deterministic: it is impossible to know when an interaction of this kind will occur. One can only make estimations of their *expected* effects.

Table 4.1: Best fits for muon energy loss parameters a and b from Eq. 4.14. Fits from Ref. [147].

Medium	$a \left(\frac{\text{GeV}}{\text{mwe}^\dagger} \right)$	$b \left(\frac{10^{-3}}{\text{mwe}} \right)$
Air	0.281	0.347
Ice	0.259	0.363
Fr. Rock	0.231	0.436
St. Rock	0.223	0.463

[†]Mwe stands for “meter water equivalent”, a unit often used in cosmic ray physics. A detector shielded by matter equal to 100 mwe would be equally shielded from cosmic rays if it were 100 meters below water.

where a and b are obtained by fitting and can be found in Table 4.1. Here a corresponds to the ionization energy loss (given by Eq. 4.17), and b corresponds to the sum of e^+e^- pair production, bremsstrahlung, and photonuclear contributions. The muon range can be found by integrating Eq. 4.14

$$R_\mu \approx \frac{1}{b} \ln \left(\frac{E_\mu}{E_{th}} + 1 \right), \quad (4.15)$$

with $E_{th} = a/b = 720$ GeV, the energy threshold above which stochastic effects are dominant.

SMPs will have very similar signatures in the IceCube detector as we have assumed that they behave leptonically (Section 2.4). The tracks will be dim compared to muon tracks due to the charge dependence in the Cherenkov effect (Section 4.1).

4.4 Energy loss formulae

As mentioned in Section 4.3.2.1, secondary interactions such as bremsstrahlung, pair production and photonuclear effect, become non-negligible at certain energies. At high energies (> 1 TeV for muons) the Cherenkov light of the secondary particles will have a significant contribution additional to the Cherenkov light coming from the primary particle. These effects are taken into account in IceCube simulations and are of great importance for high-energy muons. Since these interactions are electromagnetic in nature, they will also play a role for SMP particles, yet these effects are small for the SMPs with a primary focus on lower energies.

In this section we go over the four main components of secondary interactions. This section is largely based on the findings in Ref. [147]. The energy of the secondary particles will be expressed by $\nu = vE$, with E the energy of the incident particle and v the fraction of the energy transfer. Secondary interactions occur at all energy levels and become approximately continuous in nature below a certain energy threshold. Therefore, in many codes v_{cut} is implemented as a lower bound equal to 0.05 and a ν_{cut} equal to 500 MeV [148].

4.4.1 Ionization

Fast charged particles that move through matter interact with the electrons of atoms in the material. The interaction excites or ionizes the atoms. The Feynman diagram of this interaction is given in Figure 4.5 (left).

The cross section is expressed as

$$\frac{d^2N}{d\nu dx} = \frac{1}{2} K z^2 \frac{Z}{A} \frac{1}{\beta^2} \frac{1}{\nu^2} \left[1 - \beta^2 \frac{\nu}{\nu_{max}} + \frac{1}{2} \left(\frac{\nu}{E(1 + 1/\gamma)} \right)^2 \right],$$

with $\nu_{max} = \frac{2m_e(\gamma^2 - 1)}{1 + 2\gamma \frac{m_e}{m_t} + \left(\frac{m_e}{m_t} \right)^2}$

(4.16)

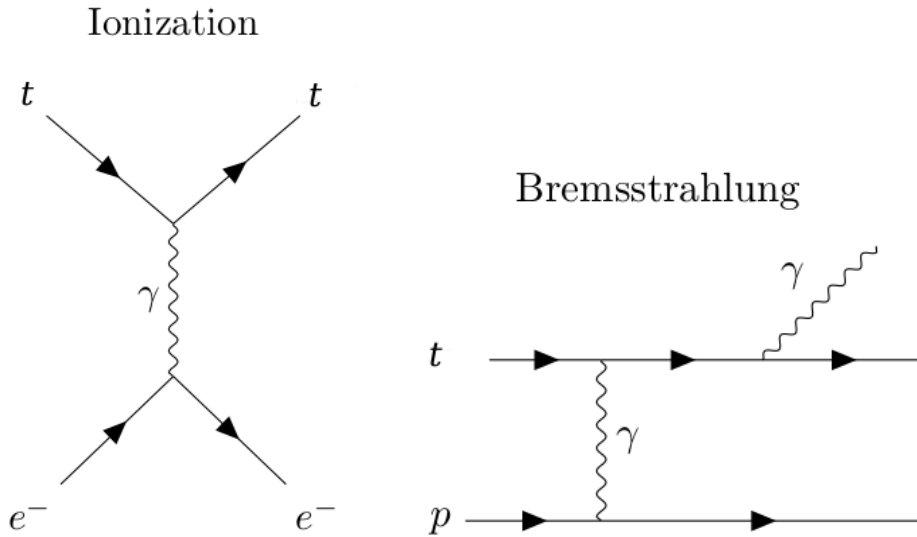


Figure 4.5: Feynman diagrams of an ionization interaction (*left*) and bremsstrahlung (*right*). t denotes the primary particle.

where negligible terms are left out and K is equal to $4\pi N_A r_e^2 m_e c^2$, N_A is Avogadro's number, r_e the classical electron radius, m_e the electron mass, z the charge of the particle (in units of the electron charge), Z the atomic number of the absorber, A the atomic mass of the absorber and m_t the mass of the throughgoing particle.

This interaction leads to an energy loss of the traveling particle and is expressed by the Bethe-Bloch formula [43]

$$-\left\langle \frac{dE}{dx} \right\rangle = K z^2 \frac{Z}{A \beta^2} \left[\frac{1}{2} \ln \left(\frac{2m_e \beta^2 \gamma^2 \nu_{upper}}{I(Z)^2} \right) - \frac{\beta^2}{2} \left(1 + \frac{\nu_{upper}}{\nu_{max}} \right) + \frac{1}{2} \left(\frac{\nu_{upper}}{2E(1+1/\gamma)} \right)^2 - \frac{\delta}{2} \right],$$

where $\nu_{upper} = \min(\nu_{cut}, \nu_{max})$

(4.17)

where I is the mean excitation energy of the absorber. The density correction δ can be found in the corresponding literature [147].

For particles in the region of $0.1 \leq \beta\gamma \leq 1000$ this is the dominant factor in the mean energy loss.

4.4.2 Bremsstrahlung

Charged particles that decelerate by another charged particle lose kinetic energy that is converted into radiation. This phenomena is known as *bremsstrahlung* and is illustrated in Figure 4.5 (right). The cross section may be represented by the sum of an elastic component and two inelastic components,

$$\sigma = \sigma_{el} + \Delta\sigma_a^{in} + \Delta\sigma_n^{in},$$
(4.18)

where σ_{el} denotes the cross section for the Coulomb scattering of the particle off the atomic nucleus and the two other terms are corrections that account for additional processes, in which the bremsstrahlung is accompanied by a change of electronic or nuclear structure of the atom in the final state.

4.4.2.1 Elastic component

$$\sigma_{el}(E, v) = \frac{\alpha}{v} \left(2z^2 Z \frac{m_e}{m_t} r_e \right)^2 \left(\frac{4}{3} - \frac{4}{3}v + v^2 \right) \left[\ln \left[\frac{m_t}{\delta} \right] - \frac{1}{2} - \Delta\sigma_a^{el} - \Delta\sigma_n^{el} \right],$$

where $\delta \approx \frac{\mu^2 \omega}{2E(E - \omega)}$,

(4.19)

where α is the fine structure constant and ω the photon's frequency with $\hbar = 1$. The atomic and nuclear form factors are equal to

$$\begin{aligned}\Delta\sigma_a^{el}(\delta) &= \left[1 + \frac{1}{\delta\sqrt{e}BZ^{-1/3}/m_e} \right] \\ \Delta\sigma_n^{el}(\delta) &= \left[\frac{D_n}{1 + \delta(D_n\sqrt{e} - 1)/m_t} \right].\end{aligned}\quad (4.20)$$

Values for B and D_n can be found in Ref. [149], here, e is the base of the natural logarithm (≈ 2.718) and other constants are as defined in Eq. 4.17. Other parameterizations can be found in the corresponding literature [147].

4.4.2.2 Inelastic component

The effect of nuclear excitation can be evaluated as

$$\Delta\sigma_n^{in} = \frac{1}{Z} \Delta\sigma_n^{el}; (Z \neq 1), \quad (4.21)$$

where $\Delta\sigma_n^{el}$ is defined in Eq. 4.20.

In the case of atomic excitation, one accounts for bremsstrahlung whereby photons radiate from the primary particle and where photons radiate from the electrons of the atom. This factor is equal to

$$\Delta\sigma_a^{in} \approx \frac{1}{Z} \ln \left[\frac{m_t/\delta}{\delta m_t/m_e^2 + \sqrt{e}} \right] - \ln \left[1 + \frac{m_e}{\delta\sqrt{e}B'Z^{-2/3}} \right], \quad (4.22)$$

where $B' = 1429$ for $Z > 2$, $B' = 446$ for $Z = 1$ and e is again the base of the natural logarithm.

4.4.3 Photonuclear

The photonuclear interaction of leptons is the process by which a lepton scatters inelastically with a nucleon or nucleus. Through a virtual photon exchange, hadrons are produced, as is illustrated in Figure 4.6 (left). The cross section formula is given by

$$\begin{aligned}\frac{d\sigma}{dv} &= \frac{z^2\alpha}{2\pi} A\sigma_{\gamma N}v \left\{ 0.75G(x) \left[\kappa \ln \left(1 + \frac{m_1^2}{t} \right) \right. \right. \\ &\quad \left. - \frac{\kappa m_1^2}{m_1^2 + t} - \frac{2m_t^2}{t} + \frac{4m_t^2}{m_1^2} \ln \left(1 + \frac{m_1^2}{t} \right) \right] \\ &\quad + 0.25 \left[\left(\kappa + \frac{2m_t^2}{m_2^2} \right) \ln \left(1 + \frac{m_2^2}{t} \right) - \frac{2m_t^2}{t} \right] \\ &\quad \left. + \frac{m_t^2}{2t} \left[0.75G(x) \frac{m_1^2 - 4t}{m_1^2 + t} + 0.25 \frac{m_2^2}{t} \ln \left(1 + \frac{t}{m_2^2} \right) \right] \right\},\end{aligned}\quad (4.23)$$

$$\text{where } t = Q_{max}^2 = \frac{m_t^2 v^2}{1-v}, \quad \kappa = 1 - \frac{2}{v} + \frac{2}{v^2}, \\ m_1^2 = 0.54 \text{ GeV}^2, \quad \text{and} \quad m_2^2 = 1.8 \text{ GeV}^2.$$

Parameters that aren't defined here can be found in the corresponding literature [147].

4.4.4 Pair production

Pair production occurs when the virtual photon radiated from the primary particle or proton splits into an electron-positron pair or muon-antimuon pair, as is illustrated in Figure 4.6 (right). The differential cross section is equal to

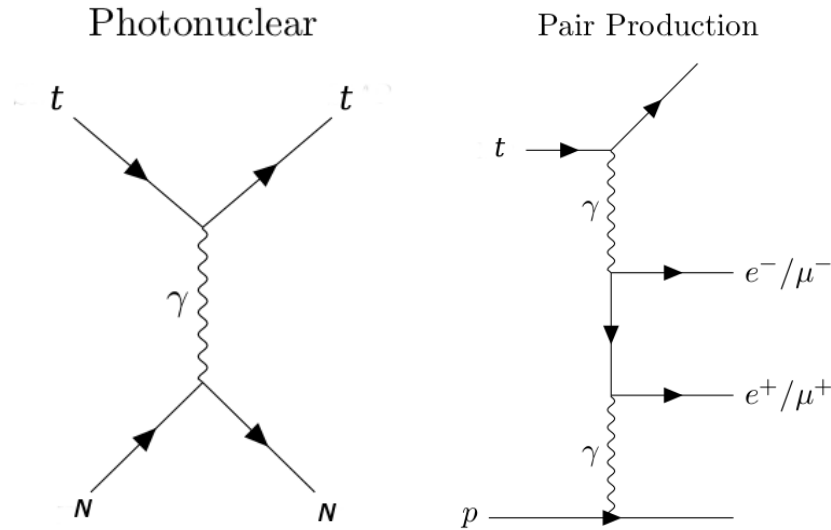


Figure 4.6: Feynman diagrams of a photonuclear interaction (*left*) and pair production (*right*). t denotes the primary particle.

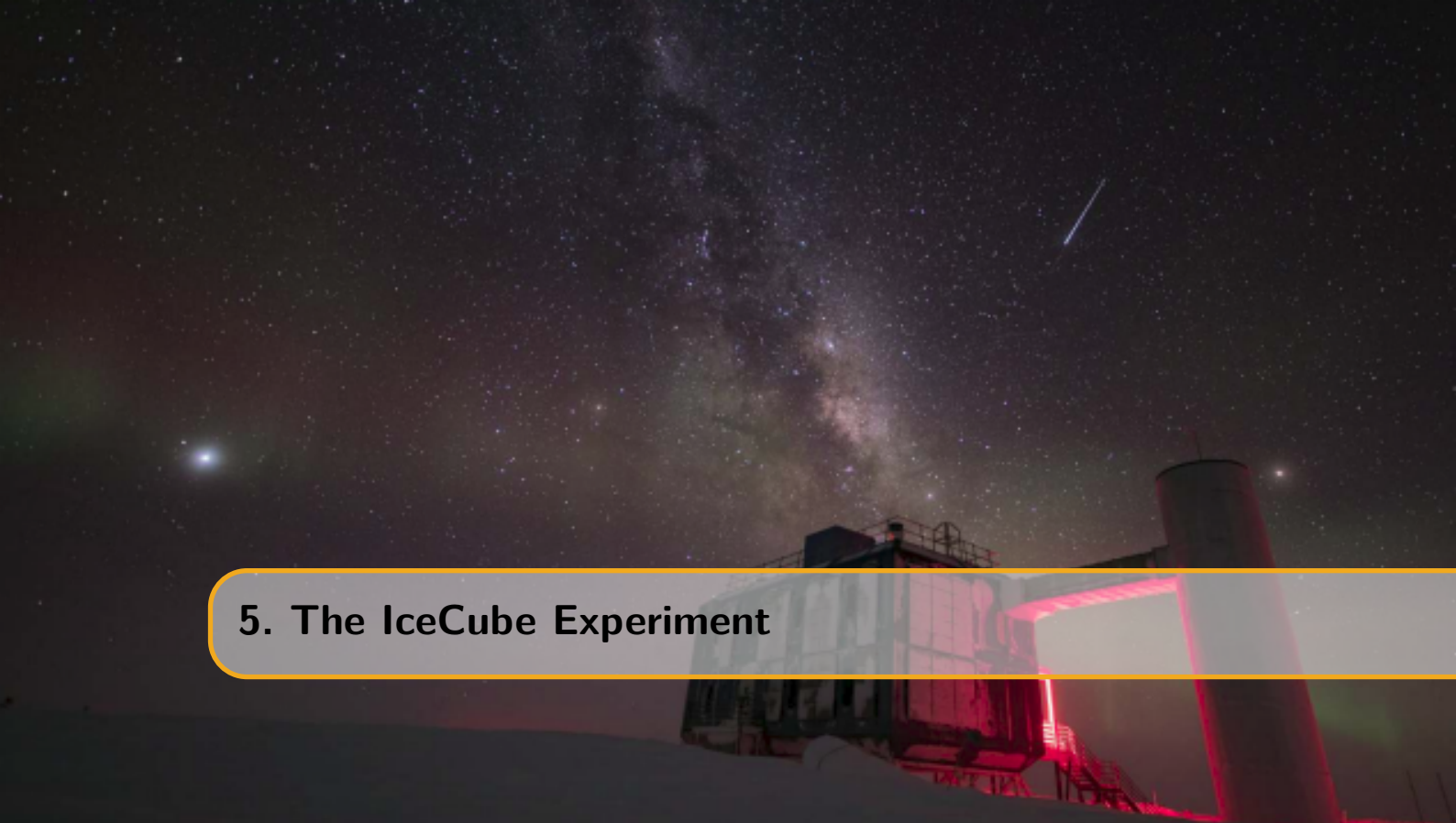
$$\frac{d\sigma(E, v, \rho)}{dv d\rho} = \frac{2}{3\pi} Z(Z + \zeta)(z\alpha r_e)^2 \frac{1-v}{v} \left(\Phi_e + \frac{m_e^2}{m_\mu^2} \Phi_\mu \right), \quad (4.24)$$

where $v = (\epsilon_+ + \epsilon_-)/E$, $\rho = (\epsilon_+ - \epsilon_-)/(\epsilon_+ + \epsilon_-)$,

and ϵ_+ and ϵ_- denote the energies of the positively and negatively charged electrons/muons. The parameters not described in detail can be found in the corresponding literature [147].

4.4.5 Conclusion

From the previous discussion we can conclude that the charge enters in the energy loss formulae quadratically for ionization, pair production and the photonuclear effect. Bremsstrahlung scales with a factor of z^4 , making it negligible compared to the other energy losses. The influence of the mass of the particle enters these equations in a non-trivial manner but has a minimal effect, again with bremsstrahlung as the exception. There, the mass enters with $1/m_t^2$, making it completely negligible for heavy particles. The effects from secondary particle production in the light yield are only substantial at very relativistic SMPs ($\approx 10^4$ times the rest mass). Due to the assumed E^{-2} signal flux (see Chapter 2), their relative contribution to the sample is very small but accounted for.



5. The IceCube Experiment

Computers are useless; they can only give you answers ~ Pablo Picasso

IceCube is a neutrino observatory located near the Amundsen-Scott South Pole Station close to the geographic South Pole. Experiments that search for astrophysical neutrinos need to be constructed with enormous instrumented volumes. IceCube is the first gigaton neutrino detector ever built and was designed specifically for this case. It is buried beneath the surface of the Antarctic ice, starting from around 1450 meters of depth and extending to around 2500 meters deep (~300 meters above bedrock). The ice acts as a medium for both the interaction of a neutrino and light propagation. This chapter serves as a general overview of the several components of the IceCube detector together with an introduction to the data processing.

The main goal of the IceCube experiment is to learn more about the distant sources that we believe to be responsible for the production of the highest-energy cosmic rays. As indicated in Section 3.3, neutrinos are crucial in gaining information about these far away sources. Large-scale detectors are necessary to observe the faint flux of neutrinos with very high energies. Detecting the Cherenkov radiation (Chapter 4) from neutrino interactions is the best way to observe these weakly interacting particles. Because hadronic, electromagnetic and muonic components from these interactions require a medium that extends to a couple of kilometers and has good light propagation characteristics, the South Pole ice sheet acts as a near ideal component of the detector. As a proof of concept, the AMANDA (Antarctic Muon And Neutrino Detector Array) experiment was built between 1996 and 2000 to show that neutrinos with energies above 50 GeV could be detected in the Antarctic ice [150, 151]. After construction was finalized, this detector consisted of 677 optical modules mounted on 19 separate strings that are spread out in a rough circle with a diameter of around 200 meters. The strings were deployed by first “drilling” holes in the ice with a hot-water hose, showing that this specific drilling technique works and can be used on larger scales. After some years of data taking, it was clear that high-energy neutrinos could be observed, paving the way for the much larger IceCube project [152].

5.1 Geometry

The IceCube detector consists of three main parts that act as different purpose physics detectors. The *in-ice* IceCube detector is the main component and consists of 4680 digital optical modules.

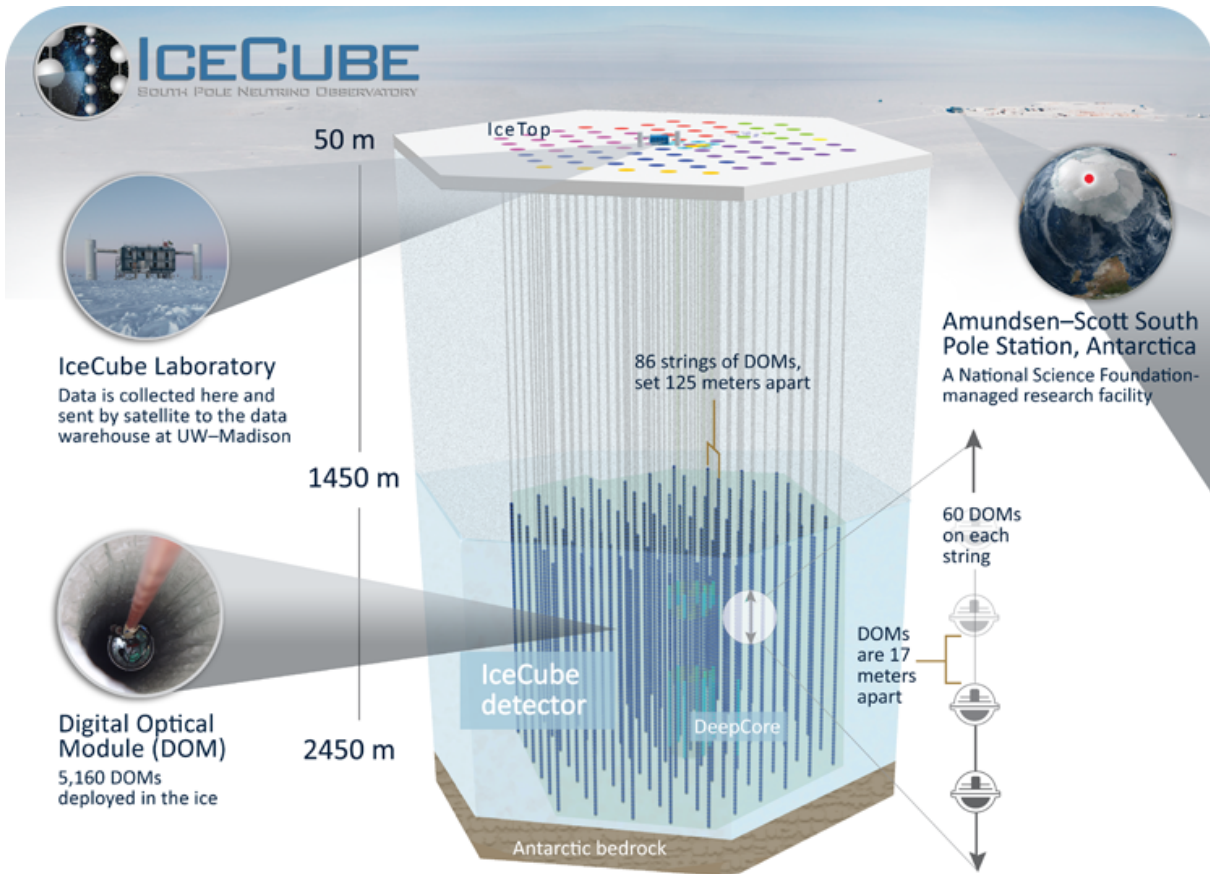


Figure 5.1: Illustration of the IceCube South Pole neutrino observatory.

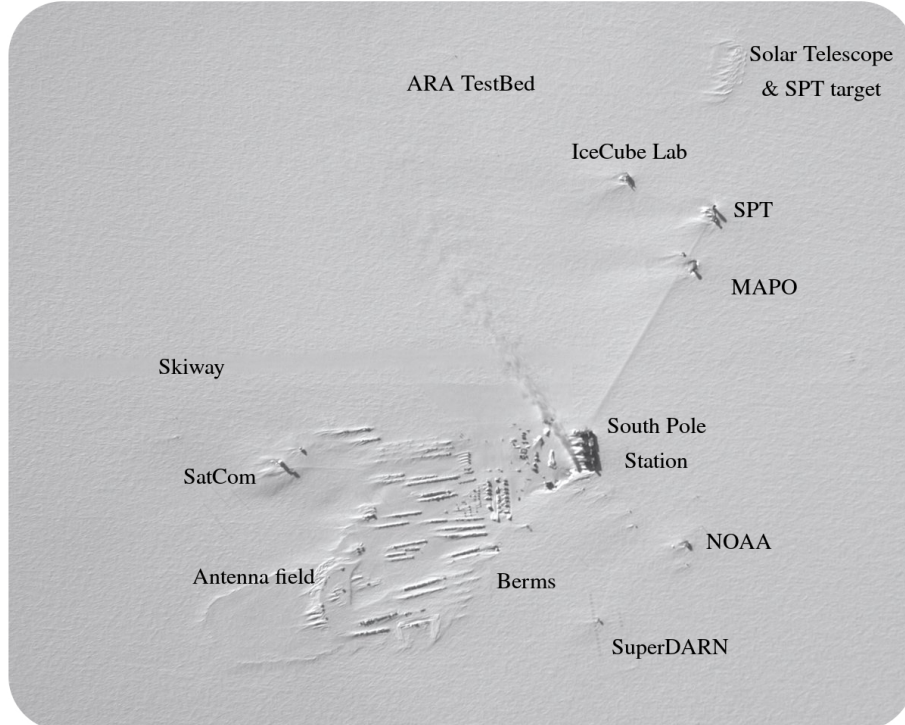


Figure 5.2: Aerial view of the South Pole. The main buildings and experimental setups are indicated in the figure. The exhaust of the South Pole Station is also visible.

In its core, a denser subdetector named *DeepCore* significantly enhances the capabilities for low-energy events of the observatory in a limited volume. The center of the DeepCore array consists of 480 sensors. On the surface of the ice, water tanks with optical modules inside are spread out over an area of approximately 1 km^2 and make up the *IceTop detector*. This surface array was built as a cosmic ray detector and veto for the in-ice array. The three components combined make the facility a multipurpose physics detector. Figure 5.1 shows the layout of the detector.

5.1.1 In-ice array

The in-ice array consists of 4680 digital optical modules (DOMs) that are able to register light that is scattered and propagated through the ice (more info about these modules can be found in Section 5.2.1). The DOMs are attached to cables and are frozen in the ice. In total, 78 of these “strings” were frozen into boreholes and spread out over a cubic kilometer in a hexagonal shape. Because only the deep ice is transparent, the DOMs are attached to the strings starting from a depth of 1450 meters to 2450 meters. The strings, as viewed from above, are spaced about 125 meters apart and along each string, 60 DOMs are attached with a vertical separation of 17 meters. This design was chosen in order to meet the primary science requirement of detecting astrophysical neutrinos in the energy range of $\mathcal{O}(\text{TeV}) - \mathcal{O}(\text{PeV})$.

5.1.2 DeepCore

A subset of in-ice DOMs is deployed along eight extra strings in the central region of the in-ice array. The optical modules are deployed deeper than 1750 meter with a denser instrumented volume. Seven additional strings, belonging to the standard in-ice strings, are also combined with the DeepCore strings to optimize the instrumented volume for this detector. The inter-string spacing on the eight specialized DeepCore strings varies from 41 meters to 105 meters. The DOM-to-DOM spacing is 7 meters for the bottom 50 optical modules (which are deployed at depths of 2100 to 2450 meters). The remaining 10 DOMs on each string are located at depths above 2000 meters deep with a spacing of 10 meters. This extra “layer” serves as a veto for downgoing atmospheric muons. Each string is instrumented with 60 DOMs, resulting in a total of 480 DOMs. Instrumentation in the ice between 2000 to 2100 meters proved to be less useful due to the *dust layer* (see Section 5.6) and was therefore left out. Six out of the eight specialized strings are also instrumented with DOMs using PMTs of higher quantum efficiency. The two remaining strings are instrumented with both regular and higher quantum efficiency DOMs. A layout of the in-ice array is given in Figure 5.3.

The DeepCore design allows us to detect neutrinos of much lower energies in the range of $\mathcal{O}(10 \text{ GeV}) - \mathcal{O}(100 \text{ GeV})$. Experiments for neutrino oscillation experiments, WIMP dark matter annihilation, galactic supernova neutrinos and point sources are made possible, or more feasible, with this dense subarray [153].

5.1.3 IceTop

IceTop is a cosmic ray air shower array, located on the surface of the ice and 2835 meters above sea level. As discussed in Chapter 3, air showers die out when they are propagating to Earth’s surface but as a consequence of the high altitude of IceTop, showers are observed near maximum*, resulting in a good energy resolution for the detector. This is important if one wants to measure changes in composition as a function of energy. In total, 162 ice-filled tanks are distributed in 81 stations (two tanks per station) in a grid similar to the in-ice array. Like the denser DeepCore infill, there are eight stations in the center of IceTop placed more closely together.

The two tanks per station are separated 10 meters apart from each other and each tank contains two IceCube DOMs. One is operated at a “low-gain” and one at “high-gain”, making them more suitable for air shower detection. The tanks measure the Cherenkov light that is produced in the ice of a tank due to the particles in a shower (electrons, positrons, muons, gamma

*The height of the shower where the maximum number of particles are produced in an air shower is often referred to as the “shower maximum”.

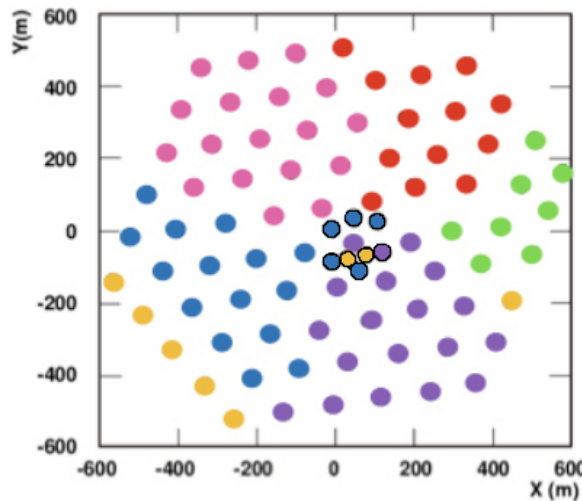


Figure 5.3: Layout of the IceCube (regular) and DeepCore strings (black edge). The string color scheme represents different deployment seasons (04-05: orange, 05-06: green, 06-07: red, 07-08: pink, 08-09: purple, 09-10: blue, 10-11: yellow). Figure from Ref. [154], with minor corrections.

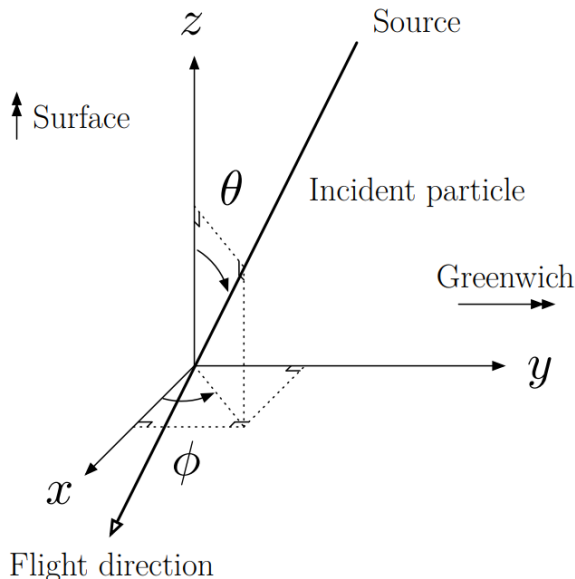


Figure 5.4: The IceCube coordinate system.

rays and hadrons). The IceTop design allows to fully cover the knee of the energy spectrum and is primarily sensitive from PeV to EeV energies. The denser infill allows the threshold to be lowered to 100 TeV. The detector is used in studies of the composition, high- p_T muons, etc.

5.1.4 IceCube coordinate system

When referring to positions and directions, one has to define a coordinate system that is able to uniquely define these variables. The system used in the IceCube collaboration is shown in Figure 5.4.

The center of the coordinate system is set close to the geometric center of the detector, at about 2000 m below the surface of the ice. The y-axis of the coordinate system is aligned with the Prime Meridian pointing toward Greenwich (United Kingdom). The x-axis is set perpendicular to the y-axis pointing in a, 90° clockwise direction. The z-axis is set perpendicular to the xy-plane, pointing upwards, normal to the Earth's surface.

A particle's direction is defined with zenith and azimuth angles, θ and ϕ respectively. The

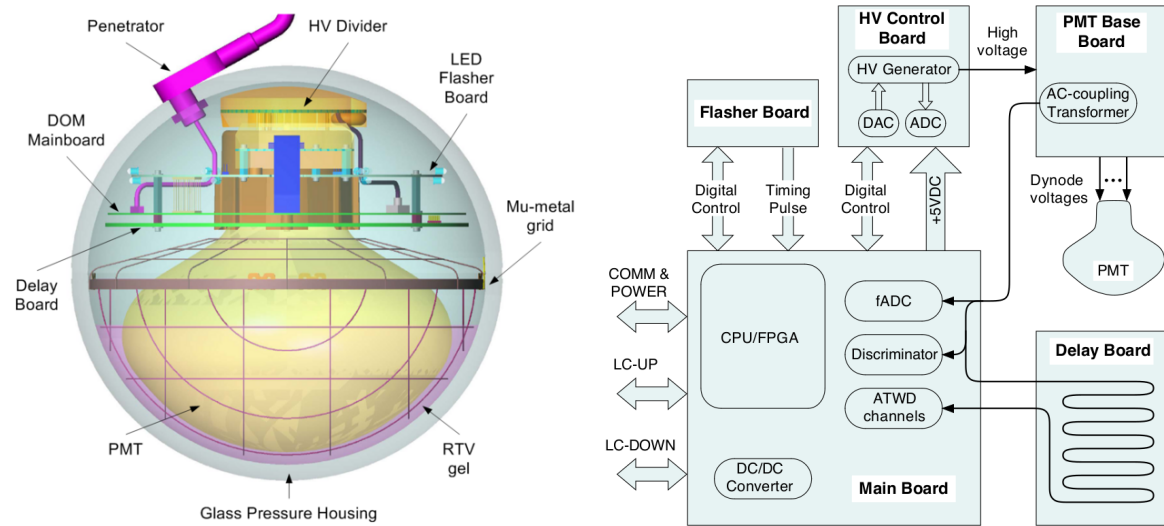


Figure 5.5: *Left:* illustration of the mechanical DOM components. *Right:* Scheme of the functional connections.

zenith angle is measured relative to the positive z-axis and the azimuth angle is measured counterclockwise from the positive xy-plane.

5.2 Hardware components

5.2.1 Digital optical modules

The Digital Optical Modules, or DOMs, convert light into electrical signals and have the necessary hardware installed to perform some basic processing of the electrical pulses. A downward facing 10"-diameter photomultiplier tube (PMT) is set with a high voltage of 2 kV, resulting in a gain of 10^7 [155]. The amplitude of the resulting waveforms ranges from 1 mV up to and beyond the linearity limit of the PMT (~ 2 V) with the width ranging from 12 ns to 1500 ns. This wide dynamic range of the waveform is processed by onboard electronics: the main board and delay board. The main board controls all the devices in the DOM (high voltage power supply for the PMT, the flasher board and pressure, temperature, and power supply voltage monitor sensors), digitizes the PMT waveforms, communicates with the data acquisition (DAQ) on the surface, houses an internal clock that is regularly calibrated with the DAQ on the surface and exchanges pulses with the adjacent DOMs. An illustration of the mechanical components of the optical module and a schematic view of the data flow starting from the PMT is shown in Figure 5.5. The optical module is housed in a 13"-glass sphere of 0.5" thick made from borosilicate. It is separated into two halves and held together with an aluminium waistband. The sphere was tested up to 690 bar hydrostatic pressure and is able to withstand the enormous pressure that the DOM is exposed to deep within the ice and during freezing (see Section 5.3). A penetrator inside the glass sphere brings out three wire pairs housed in a cable. One wire pair is connected to the string and ultimately to the IceCube Laboratory (see Section 5.2.4). The other two wires are connected to the neighboring DOMs directly above and below for local coincidence pulses (see Section 5.2.3). A detailed description is given in the detector paper [155].

5.2.1.1 PMTs

The 10" (or 25 cm) diameter PMT comes in two types: Hamamatsu R7081-02 for standard IceCube DOMs and a high-quantum-efficiency (HQE) version, Hamamatsu R7081-02MOD for the specialized DeepCore strings [156]. The peak quantum efficiency is around 25% (34% for HQE) at a wavelength of approximately 390 nm. However, the total acceptance of the optical module is the convolution of the quantum efficiency with the glass transmission (93% at 400 nm, decreasing to 50% at 340 nm and 10% at 315 nm at a normal incidence). The resulting acceptance is illustrated in Figure 5.6. The PMTs face downwards and are housed in a mu-metal

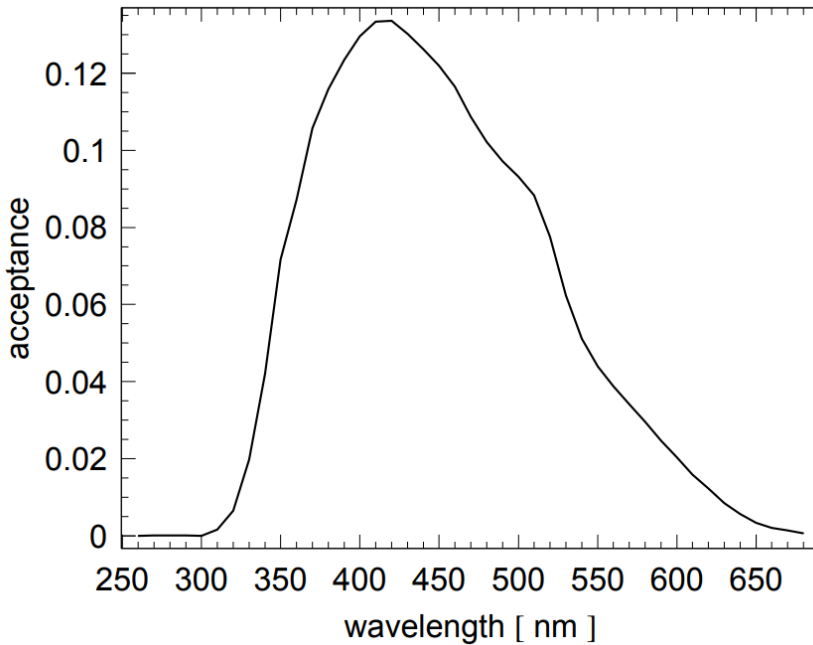


Figure 5.6: Fraction of photons arriving from a direction parallel to the PMT axis and are recorded in function of the photon wavelength. Glass and gel transmission, PMT quantum and collection efficiencies are all included. Figure from Ref. [157].

grid to shield them from the Earth magnetic field and a silicone gel necessary for optical coupling and mechanical support.

5.2.1.2 Main board and delay board

The PMT signals are sent to two ATWDs (Analog Transient Waveform Digitizer) and one fast ADC (fADC) with a delay of about 75 ns. This delay is necessary because signals are only processed if the signal exceeds a voltage that corresponds to 0.25 PE (one PE is the voltage that typically corresponds to the voltage produced by a single photoelectron). The delay board consists of a 10 m-long copper trace that delays the signal for 75 ns, necessary to be able to record the full waveform before the discriminator threshold of 0.25 PE is exceeded.

Once this threshold is crossed, the signal is compressed and included in a “DOMlaunch” or “hit”. Signals that pass the local coincidence requirement (see Section 5.2.3) have their full waveforms compressed, whereas for isolated events only a time stamp and brief charge summary is sent. For each hit, an FPGA (Field Programmable Gate Array) opens up one of the two ATWD chips. Each of the two chips is provided with three amplifier gains with nominal values of 16, 2 and 0.25. Most pulses use the highest-gain channel while the other lower-gain recordings are used as needed when pulses reach 75% of the range of a higher-gain channel. The ATWD recording duration is 427 ns, which should include light that is produced within tens of meters of a DOM. The slower fADC is used when light reaches the DOM after the ATWD time window and samples continuously. The FPGA is programmed to save an interval of 6.4 μ s after the launch. ATWD chips sample the input voltage at 300 Msps, followed by a 10-bit digitization. The fADC captures the information with a 10-bit 40 Msps.

The two sets of ATWD chips are operated alternately in order to reduce deadtime. After 50 ns, the second chip is available to be launched during the digitization step of the first. The digitization procedure is terminated for isolated hits and the ATWD is reset, reducing the DOM dead time.

5.2.1.3 Flasher board

To be able to characterize the ice and simulate light propagation, each DOM was instrumented with 12 LEDs that are aimed in six different azimuth angles (with 60° spacing) and along two

different zenith angles. The LEDs were chosen to have a wavelength spectrum centered at around 400 nm to approximate the typical wavelength of detected Cherenkov photons. Flasher data is used for:

- verifying the timing response of the DOMs throughout the analysis software chain;
- measuring the position of the deployed DOMs in ice;
- measuring the optical properties of the ice (see Section 5.6);
- verifying the performance of shower reconstruction algorithms in measuring position, direction and energy.

5.2.2 Calibration

Regular calibration of the components is necessary to be able to convert the DOM waveforms to reliable and comparable physical units. Optical efficiencies of the optical modules were determined in the lab before deployment and are also measured *in situ* with calibration procedures.

Some of these procedures do not allow for simultaneous data-taking and are performed as little as possible, without losing significant confidence in the calibration of the devices. For example, in-ice DOMs are calibrated yearly with the DOMCal procedure, whereas global time calibration can be done in parallel with data-taking and is provided by the RAPCal procedure.

As they result in the vast majority of the background hits, *dark noise* needs to be properly understood for low-energy neutrino analyses, supernova searches, and detector simulations. The total rate of dark noise averages at around 560 Hz for in-ice DOMs and 780 Hz for HQE DOMs. The origins of the noise are non-trivial and include electronic noise, thermionic emission, Cherenkov light from radioactive decays, field emission within the PMT, and scintillation/luminescence in the glass of the PMT and pressure sphere. They are simulated with a combination of uncorrelated (Poissonian) noise and a correlated component. The temperature dependence of the noise rate was determined by combining a measured temperature profile of the South Pole ice cap with a fit of the Poissonian expectation of the total dark noise rate to every individual DOM, and was verified in lab measurements. The seasonal variations of the dark noise rates are below 1%, but are tracked over time and updated yearly in a database.

More information about these and other calibration procedures can be found in Ref. [155].

5.2.3 Cable systems

The DOMs are the eyes of the detector, but the cable system connects all the modules together and links them to the readout hardware at the surface. The in-ice cables, 2505 m long, are each connected to 60 DOMs and terminate at a Surface Junction Box (SJB) between IceTop tanks. IceTop tanks also connect to the SJB. A surface cable was trenched 1 m deep at the time of deployment and runs to the IceCube Laboratory. One cable consists of 20 “quads”, a construction of four twisted wires. Four quads provide special instrumentation and local coincidence between connections and one is a spare. The remaining 15 quads are each connected to four DOMs with two wire pairs. A wire pair connects two adjacent DOMs and is attached to connectors at 30 breakouts spaced 34 m apart as can be seen in Figure 5.7. Each DOM is connected to three wire pairs. One wire pair is used for bi-directional communication to the surface and power. The two remaining wires are dedicated to determine *Local Coincidence (LC)*. Each DOM is connected to its nearest neighbor above and below. If nearest or next-to-nearest neighbors are hit within a time window of $\pm 1 \mu\text{s}$, the hits are said to be in Hard Local Coincidence (HLC). Isolated hits are referred to as Soft Local Coincidence (SLC). Most DOM hits originate from dark noise (see Section 5.2.2) and are not in HLC. Light originating from particles traveling through matter is more likely to trigger DOMs in close proximity. Therefore, LC requirements are able to drastically reduce the noise rate.

5.2.4 IceCube laboratory

The central building to which the modules of all the detectors are connected is the IceCube Laboratory (ICL). Cables/strings from the arrays run up two cable towers on either sides of the

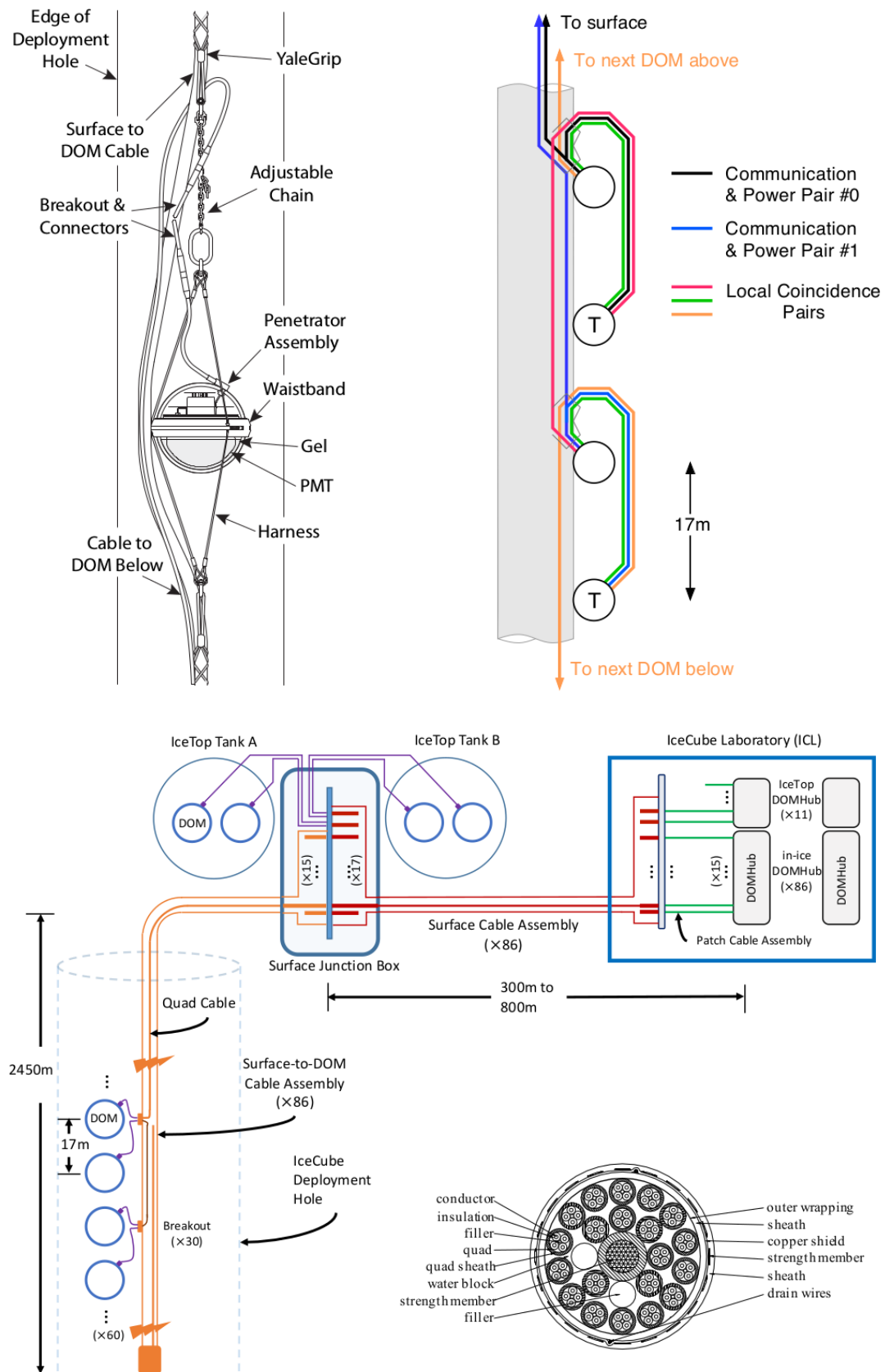


Figure 5.7: *Top:* Sketch of DOM cabling and schematic overview. The modules are connected to their nearest neighbors and the string. *Bottom:* General schematic overview of the IceCube cabling system and the connection between all components together with an in-ice cable cross section. Illustrations from Ref. [155].

structure. A picture of the ICL is shown as the header image of this chapter (pg. 67); one of the towers is visible. Inside the main part of the building is a server room to which the cables in the towers are connected. All data acquisition and online filtering computers are housed inside the server room together with the main IceCube computing system called the “South Pole System” (more information on this in Section 5.4).

5.3 Deployment

In total, 86 holes had to be drilled for all IceCube and DeepCore strings. The surface consists of a 50 m snow and firn region with a gradual transition to ice. The ice was melted with a 5 MW Enhanced Hot Water Drill (EHWD) capable of drilling about 1 hole per 48 hours. The holes were 60 cm in diameter, providing enough clearance for the optical modules that were 35 cm in diameter, and with contingency time for delays that meant holes could shrink due to refreezing. Because melting snow and firn with hot water is not practical, a specialized drill with copper tubing through which hot water flows was used to melt the firn by contact.

The IceCube drilling was completed in seven field seasons during Antarctic summers (early November to mid-January). The first season started in 2004-2005 and construction ended in 2010-2011.

After drilling one hole, all 60 DOMs were lowered one by one and connected to each other with the penetrator assembly as shown in Figure 5.7. After deployment of all DOMs, the remaining 1.5 km of in-ice cable was lowered into the hole (known as the “drop phase”). The top of the cable was then secured by an anchor trenched in the snow and connected to the Surface Junction Box.

In total, 5484 (5160 IC + 324 IT) optical modules were deployed and as of 2018, there are 5396 still in data-taking mode (98.4%). There were 55 DOMs that failed almost immediately during freeze-in, while 34 DOM failures occurred after deployment. This number includes modules on a wire pair that are taken out when the partner DOM on the same pair failed. The mean failure rate is estimated to be around $(4.1 \pm 1.2) \text{ yr}^{-1}$, which results in a survival fraction of $(97.4 \pm 0.3)\%$ in 2030.

5.4 Data taking

First processing of the photon detection is done inside the DOM as mentioned in Section 5.2.1.2. After digitization, the waveforms are sent along the cable/string to which all DOMs are attached and that runs to the ICL. Each one of the strings is connected to one of the DOMHubs, which together with servers that run various online systems, comprise the South Pole System (SPS). An overview is given in Figure 5.8.

The data acquisition (DAQ) system is run on the DOMHubs and recognizes patterns in hits that are most likely caused by particle interactions with the use of the implemented triggers and filters (see below). This combination of hits is called an “event”. Most of the DAQ data rate originates from atmospheric muons with an event rate averaging 2.7 kHz. The total bandwidth saved to tape/disk (see Section 5.4.3) is approximately 1 TB/day.

To implement possible changes in the detector settings, triggers, or filters, a full physics run spans over one year, starting in May and ending in May the following year. Data is recorded in smaller 8 hour runs, where each run has a unique run number. Over the years, with the use of both online and on-site automatic alerts, the total uptime of the detector has a steady increase of clean uptime (usable data) from 89.75% in 2011 to 98.89% in 2018.

5.4.1 Triggers

Aside from the discriminator thresholds in the module (see Section 5.2.1.2), a system of triggers is set up to further reduce the noise rate and refine searches for physics events. Below, a short description of the triggers is given. An overview of the trigger settings is given in Table 5.1.

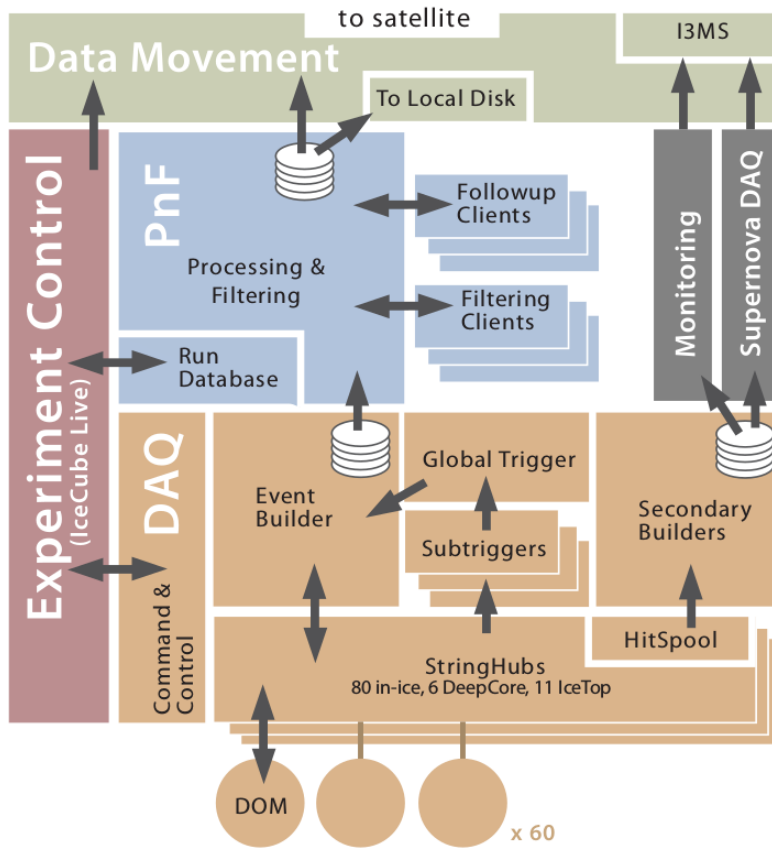


Figure 5.8: Schematic overview of the data flow in the primary IceCube online systems.

- The most important trigger is the Simple Multiplicity Trigger (SMT) used for the IceCube, DeepCore and IceTop arrays. The trigger setting requires a certain number of HLC hits within a time window of the order of a couple of μs without any locality requirements.
- The Volume Trigger requires less HLC hits, but they have to be clustered in a certain cylindrical volume.
- Locality conditions are powerful for low-energy events that do not reach far in the detector but are more prone to produce hits in a small volume and time window. Therefore, a dedicated String Trigger was designed for low-energetic upgoing events passing along a single string.
- IceCube is also sensitive to hypothetical massive particles moving at subrelativistic speeds: magnetic monopoles (see Section 5.8.3). Therefore, a dedicated Slow Particle (SLOP) trigger has been developed. It searches for triplets of HLC pairs within a window, T_{\max} , and removes HLC pairs within a time window, T_{prox} , to remove hits originating from particles traveling at the speed of light. Other velocity and geometric requirements are set with the inner angle between triplets, α_{\min} and the “velocity” along the sides of the triangle.
- A Fixed Rate Trigger (FRT) reads out hit data from the full detector at fixed intervals, useful for DOM noise studies.

If a trigger condition is fulfilled, the start of the trigger window is determined as the first HLC hit of the active volume of the trigger. The minimum length of the triggered window slides along with the hits until there is no more HLC after the last hit within the set minimum time window. The length of a triggered set of hits can therefore be longer than the minimum trigger window. As one event is able to fulfill multiple trigger requirements, the (sub)triggers are merged into one Global Trigger while keeping the information on the individual triggers. This data is subsequently sent to the Event Builder that writes DAQ events (also called *Q frames*) to a temporary file that is saved when it reaches a certain size. These events are eventually re-split into physics events (*P*

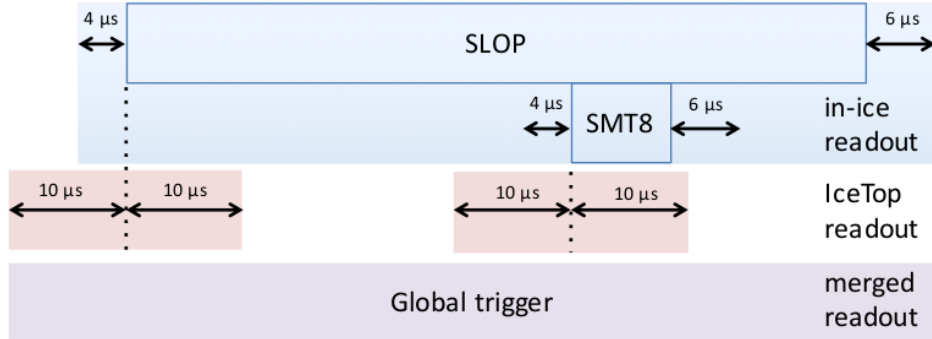


Figure 5.9: Example of a global trigger construction. Multiple triggers are combined due to their overlap with the long SLOP trigger.

Table 5.1: Parameter settings of triggers (as of May 2016) and typical trigger rates.

Trigger	DOM set	$N_{\text{HLC hits}}$	Trigger Window (μs)	Readout Window IC	Window (μs) IT	Topology	Rate (Hz)
SMT	in-ice	8	5	-4, +6	± 10	-	2100
SMT	DeepCore	3	2.5	-4, +6	± 10	-	250
SMT	IceTop	6	5	± 10	± 10	-	25
Volume	in-ice	4	1	-4, +6	± 10	cylinder ($r = 175 \text{ m}$, $h = 75 \text{ m}$)	3700
Volume	IceTop	4	0.2	± 10	± 10	cylinder ($r = 60 \text{ m}$, $h = 10 \text{ m}$)	4
String	in-ice	5	1.5	-4, +6	± 10	7 adjacent vertical DOMs	2200
SLOP	in-ice	N_{triplet}	$T_{\text{prox}} = 2.5$	$-4, +6$	± 10	$\alpha_{\min} = 140^\circ$, $v_{\text{rel}}^{\max} = 0.5$	12
			$T_{\min} = 0$				
			$T_{\max} = 500$				
FRT	all	-	-	Combined: 10000	-	-	0.003

frames) corresponding to a certain subtrigger before reconstruction and analysis. An example of a Global Trigger, here mostly determined by the very long SLOP trigger, is shown in Figure 5.9.

All triggers read out all SLC/HLC hits of all DOMs, even the ones not directly involved in the trigger construction. For this, they use the StringHub software component located on every DOMHub that is able of caching SLC and HLC hits in memory. Hits before and after the trigger window are also saved to the event to add information of early and late pulses. This is typically 4 μs before and 6 μs after the trigger window for in-ice triggers.

5.4.2 Filters

Events are sent through the online Processing and Filtering (PnF) system for additional processing. First, the triggered events have their waveforms further compressed using the Super Data Storage and Transfer format (SuperDST), which uses only 9% of the storage size of the full waveform information. Very fast, basic reconstructions are run on the SuperDST waveforms to compute the vertex position, energy, direction and goodness-of-fit that are necessary for the filter selections of possible interesting events.

Around 25 filters search for a wide range of different types of particle interactions, ranging from low-energy neutrinos for oscillation measurements to the highest-energy neutrino interactions illuminating large parts of the detector. Some filters are designed to look for neutrino events of wide astrophysical interest to the scientific community and trigger alerts that are distributed to followup observatories worldwide. One example is the “EHE alert” that searches for Extremely High Energy neutrinos that are most likely of astrophysical origin [158]. Another example is the Gamma Follow Up alert that notifies the MAGIC and VERITAS collaborations when significant bursts of neutrinos from known high-energy gamma-ray sources over periods up to three weeks occur [159]. Other filters look for events that could be caused by muons, WIMPs, monopoles, etc. The filters that were used in this analysis will be given in Section 8.1.

As a bonus, filtering reduces the data volume to a level of around 90 Gb/day, which is small enough to transfer to the North via satellite.

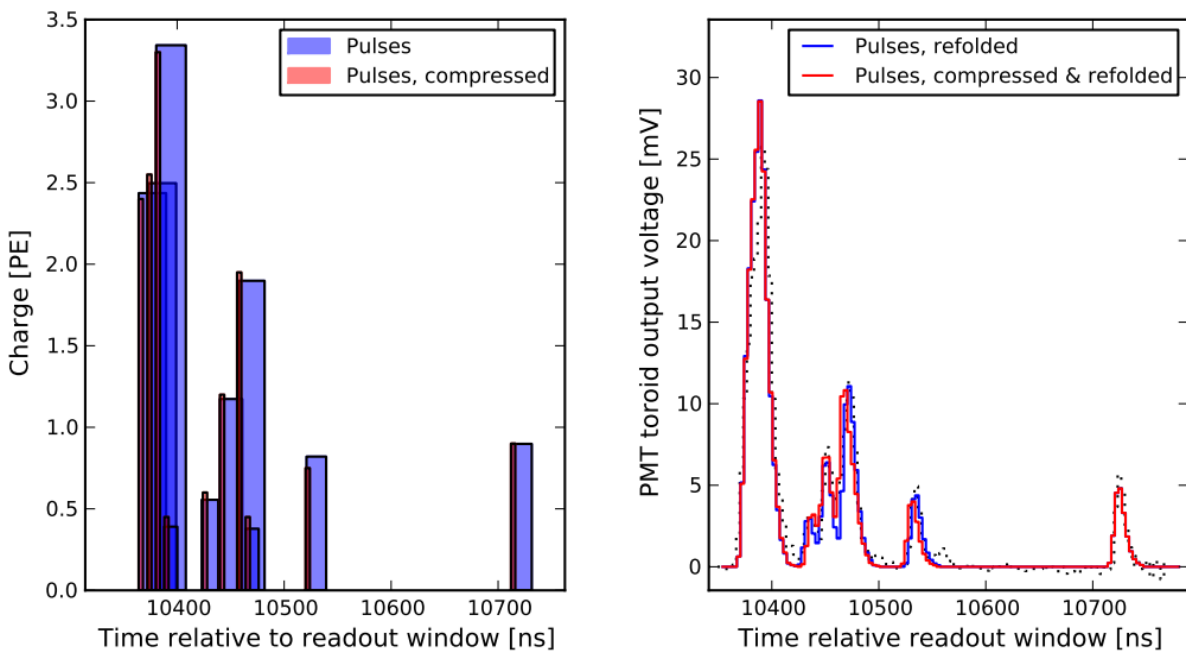


Figure 5.10: *Left:* pulse information illustrated with blue bars; the leading-edges time, width, and charge of the pulse are given by the left edge, width, and height of the bar, respectively. The red bars show the same after SuperDST compression. *Right:* Reconstructed pulses using the full pulse profiles in blue are compared to an approximation of the original waveform that is obtained by convolving the pulse times and charges with an average single-photoelectron pulse shape. Figures from Ref. [161].

5.4.3 Data handling

Most of the data is processed with the PnF system. The geometry, calibration, and detector status (GCD) information from each 8 hour run is sent via the same satellite transfer that is used for the continuously running PnF system. All the raw waveforms were written to tape before that system was retired in 2015. Since then, disks have been used to store the remaining archival data. This raw data is shipped to the North every year and is used if reprocessing of data is necessary. An example is the SPE correction for all runs starting from 2010 to 2016 referred to as *pass2 data* [160].

Events are stored in IceCube specific files and are called *i3files*.

5.5 IceCube event topology

The compressed waveforms are refolded to approximations of the original waveforms using average single-photoelectron pulse shapes as can be seen in Figure 5.10. The timing, shape and amplitude of the reconstructed waveforms in all the DOMs in an event are used to characterize the event topologies in the detector. Different interactions give rise to several possible signatures in the detector. Energetic muons propagate several hundreds of meters in the ice and give rise to tracks, whereas electrons and hadrons are stopped almost immediately, giving rise to cascades (see Section 4.3).

The track-like events, originating from charged-current muon neutrino interactions, provide an angular resolution at a typical angle of 1° for well-contained and reconstructed tracks at 1 TeV and improves to $\sim 0.3^\circ$ for neutrinos with an energy of 1 PeV [162]. Cascades, originating from electromagnetic or hadronic cascades, result in a more spherical light generation in the detector. Well-contained shower events have an average deposited energy resolution of around 15%. These event types are shown in more detail in Figure 5.11.

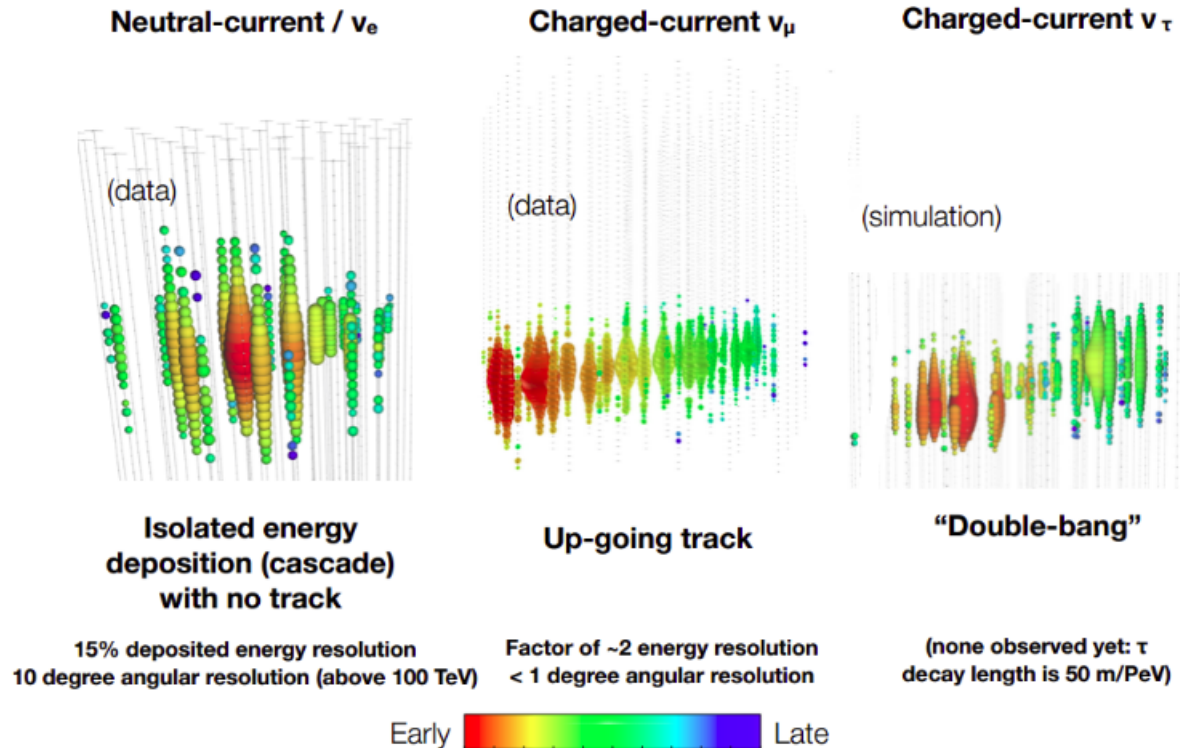


Figure 5.11: Neutrino interactions in the IceCube detector have two distinct types of interactions: cascades and tracks. Energetic taus are theorized to have double-bang signatures but have not undeniably been seen. Colors determine the timing of hits in the optical modules in the ice. Illustrations from the IceCube collaboration [163].

5.6 Antarctic ice

The ice, in which the optical modules are frozen, acts as the propagation medium for the light that is produced by relativistic particles. Therefore, the parameterization of the ice is of great importance for good reconstructions and reliable simulations. The relativistic particles that travel through the ice produce photons in a Cherenkov cone with an opening angle of around 41° (see Section 4.1). How these photons further propagate from the point of emission to the receiving sensors is determined by the absorption and scattering within the ice. The most important parameters necessary to describe the photon propagation in ice are:

- the average distance to absorption,
- the average distance between successive scatters of photons, and
- the angular distribution of the new direction of a photon at each given scattering point.

There has been a large effort into measuring and modeling the Antarctic ice that is still ongoing. A good summary (although is a bit outdated as it does not include ice anisotropy effects, cable shadowing and DOM tilts) can be found in Ref. [157].

5.6.1 Ice simulation

The ice is modeled by the six-parameter ice model introduced in Ref. [164]. Flasher data from LEDs is used to fit the model to data (see Section 5.2.1.3). In this model, the ice is described by a table of depth-dependent parameters $b_e(400)$ and $a_{dust}(400)$ related to scattering and absorption at a wavelength of 400 nm. These two parameters depend on the relative temperature $\delta\tau$, which changes in function of depth, and six global parameters. The effective scattering coefficient is equal to $b_e = b \cdot (1 - \langle \cos \theta \rangle)$, where b is the geometrical scattering coefficient that determines the average distance between successive scatters and θ is the deflection angle at each scatter. The absorption coefficient a determines the average distance traveled by a photon before it is absorbed and is the sum of two components: one due to dust and the other a temperature

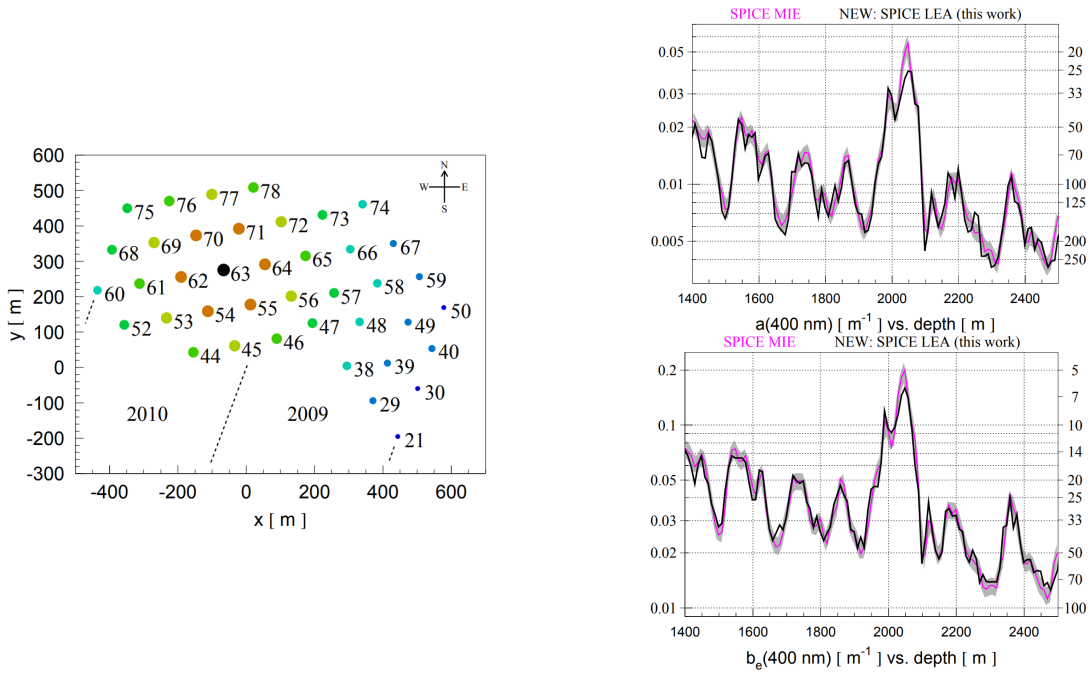


Figure 5.12: *Left:* Top view of the 2008 detector configuration when DOMs on string 63 were used to flash LEDs in a flasher run. Same colors are used for strings located at a similar distance to the central string. *Right:* values of $b_e(400)$ and $a(400)$ vs. depth for two different ice models. The scale and numbers to the right of each plot indicate the corresponding effective absorption $1/a$ and scattering $1/b_e$ lengths in [m]. Both illustrations from Ref. [165].

dependent component for pure ice.

$$b_e(\lambda) = b_e(400) \cdot \left(\frac{\lambda}{400} \right)^{-\alpha}, \quad (5.1)$$

$$a(\lambda) = a_{dust}(\lambda) + A e^{-B/\lambda} \cdot (1 + 0.01 \cdot \delta\tau), \quad (5.2)$$

with $a_{dust}(\lambda) = a_{dust}(400) \cdot \left(\frac{\lambda}{400} \right)^{-\kappa}.$

α, κ, A and B are determined in Ref. [164]*, $\delta\tau$ is equal to

$$\delta\tau(d) = T(d) - T(1730\text{m}), \quad (5.3)$$

with $T(d) = 221.5 - 0.00045319 \cdot d + 5.822 \cdot 10^{-6} \cdot d^2,$

where d is the relative depth compared to the center of AMANDA (1730 m depth). Using flasher data with 400 nm wavelengths, it is possible to measure the values of $b_e(400)$ and $a_{dust}(400)$ at certain depths and use the six-parameter ice model to extrapolate scattering and absorption for other wavelengths.

In 2008, a flasher run was launched where each DOM on string 63 was producing flashes. The layout of the detector at the time of the flasher run and results of fits to $b_e(400)$ and $a(400)$ vs. depth can be found in Figure 5.12. At a depth between 2000 meters and 2100 meters, a large increase in scattering and absorption is clearly visible. A *dust layer*, presumably originating from volcanic ash, is characterized by an increase of dust in the ice, responsible for the higher scattering and absorption factors.

*The remaining two parameters D and E were not used here.

Over the years, multiple different ice models have been constructed. For this analysis the SPICELea* model has been set as nominal. This is the most recent model that has significant Monte Carlo background simulations available. It also includes an angular sensitivity estimation due to the *hole ice*, a column of ice approximately 30 cm in radius immediately surrounding the strings with an increased amount of scattering. More information about this model can be found in Ref. [165].

5.6.2 Systematic uncertainties

The characteristics of the ice are complex. Dust particles, the tilt in the ice sheets, etc. result into non-negligible uncertainties in the ice model. Data from the flasher runs are compared to simulation and this verification was used to quantify the uncertainty on the measured values of $b_e(400)$ and $a(400)$. From this, it was determined that $(+10\%, 0)$, $(0, +10\%)$ and $(-7.1\%, -7.1\%)$ uncertainties on the scattering and absorption coefficients, respectively, was a conservative estimation.

5.7 Future upgrades

The last couple of years there has been a large focus on improving the physics work that can be done in the IceCube experiment. Several projects are in the pipeline, are under R&D, and/or have been funded to improve the full analysis case of the detector(s).

Lower-energy neutrinos can be detected with a denser infill with other optical modules (the Upgrade, see Section 5.7.1), cosmic ray measurements can be improved with a complementary scintillator array to the IceTop tanks [166] and small air Cherenkov telescopes [167]. Also, the detection of ultra-high-energy neutrinos could be made possible with a larger infill of the current IceCube in-ice array (Gen2) or radio antennas. Below a brief summary of projects that could be of potential importance to this analysis is given.

5.7.1 IceCube Upgrade

In 2018, a funding proposal for a dense 7-string infill of DeepCore was accepted by the NSF and was effective from the beginning of October later that year. This infill would have DOMs separated 2.4 m apart and start from a depth of 2140 m, reaching to 2440 m deep in the ice along seven new strings (see Figure 5.14). This very dense array would allow low-energy and oscillation experiments to reach much better sensitivities. Also, very dim tracks such as the ones from particles with an anomalous charge lower than e , might be easier to distinguish from low-energy muons that produce more Cherenkov light.

Because this project involves a restart of the drill, it also serves as a testbed for new optical modules. The Upgrade is the first step towards the much bigger Gen2 project. New types of optical modules would be used with higher angular acceptances than the currently used DOMs that have one large downward facing PMT. Examples are D-Eggs, which have two PMTs at each end of an ellipsoid glass [168], and mDOMs, where multiple smaller PMTs are positioned in a ball-shaped optical module [169].

A camera system could also be included in the new optical module designs and should help to improve the properties of the ice after refreezing [170]. Another camera system, the Precision Optical Calibration Module (POCAM) should further improve our understanding of the ice characteristics and accurately determine the efficiency and angular acceptance of the IceCube DOMs [171].

Deployment is currently planned for the 2022/2023 season.

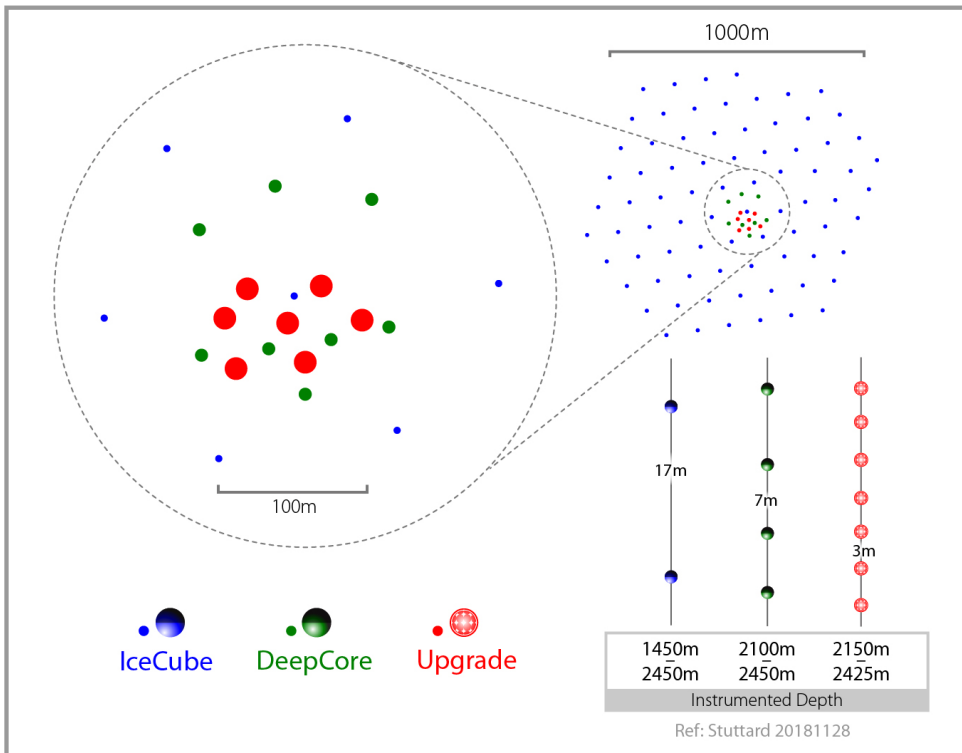


Figure 5.14: Top view of the Upgrade infill (red circles) within the DeepCore array (green) and the whole IceCube detector (blue). The area of the circles is representative of the instrumented photocathode density on a given string. Illustration from the IceCube collaboration.

5.7.2 IceCube Gen2

Although the IceCube in-ice array has successfully been able to determine the flux of astrophysical neutrinos and show the detection of a coincident neutrino with a blazar (see Section 3.1.3.2) in an active state, a next generation larger detector would greatly improve the detection possibilities of astrophysical neutrinos [172]. A 10 km^3 volume of clear glacial ice would allow for a much higher detector acceptance of high-energy neutrino interactions, helping in searches for point sources, better characterizing the spectral and flavor properties, and search for cosmogenic neutrinos among others. Point sources and cosmogenic neutrinos have, for now, not been observed even though the detector has been running stable for a couple of years. There is also only a small set of unambiguous astrophysical neutrinos. It would take extremely long running operations from the current detector (without hardware failures that are prone to happen more and more) to gather enough events for meaningful statistics. A much larger instrumented volume, such as the one proposed, is predicted to have an increase in sensitivity to transient source densities and rates by about two orders of magnitude [173]. Also, a large extension of the active volume could help to look for long tracks originating from SMPs.

Although much is undecided, the plans are to have an extra surface array for cosmic ray detection and a radio array for the highest energy neutrinos along the in-ice array.

5.7.2.1 In-ice infill

The current design for the Gen2 string configuration would be ~ 120 cables with an inter-string spacing around 250 m to 300 m. This much coarser spread of strings will result in a loss of sensitivity for neutrino events of the order of a couple of TeV but would not affect the measurements of the very energetic astrophysical neutrinos. Measurements of the absorption lengths in function of the depth in the ice indicate that the instrumentation of the strings could

*SPICE stands for South Pole Ice. Lea is an addition to distinguish the different model types, but has (as far as the author knows) no special meaning.

The IceCube Gen2 Facility

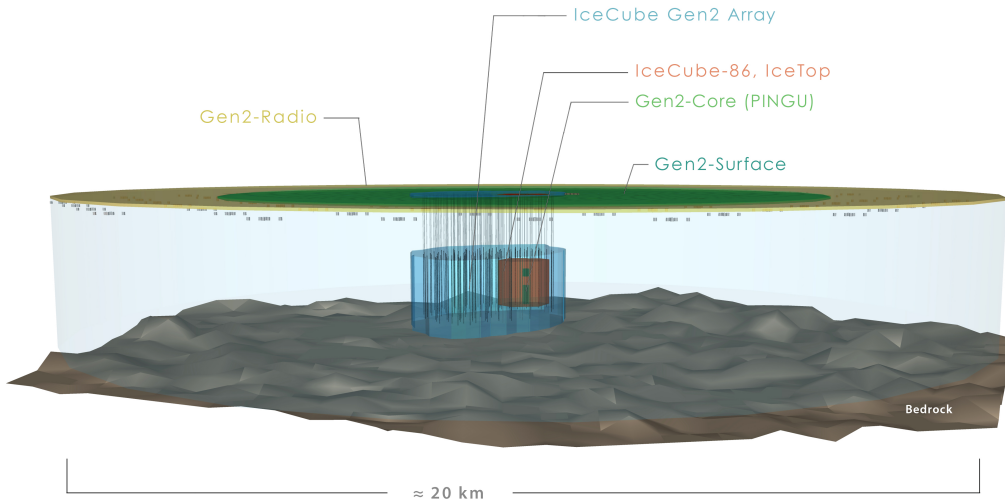


Figure 5.15: Impression of the possible Gen2 layout. The current IceCube in-ice and IceTop arrays are shown in red/brown. The 10x larger Gen2 in-ice array is given in blue. Possible layouts for the radio array (yellow) and surface array (green) are also listed. From the IceCube collaboration.

be extended with an additional 250 m in total. This total depth is comparable to the current depth of the IceCube detector, meaning the surface area should reach to an exposed area of $\sim 10 \text{ km}^2$. This would result in a drastic sensitivity improvement of (near-)horizontal muons traversing the ice that are too energetic to be contained in the current detector.

5.7.2.2 Surface array

The size of the IceTop array is too limited to be used as a veto for most analyses. Therefore, the prospects of a surface array for the Gen2 extension would have much larger designs [174]. The geometry and optimal type of detector that should be used for this configuration is still under design.

5.7.2.3 Radio array

At the critical energy of around 100 PeV, the origins of cosmic rays transitions from the highest-energy galactic sources to the even more energetic extragalactic cosmic rays. The radio wave detection technique has an energy threshold of about 100 PeV, making it a good candidate for high-energy cosmic ray detectors. A good review of radio emission from cosmic rays is given in Ref. [175].

As the technique can also be used to measure particle cascades in dense media, radio arrays can also be used in neutrino astronomy. To achieve an improved sensitivity to neutrinos in the $10^{16} - 10^{20}$ eV energy range, including GZK neutrinos, an additional radio-pulse neutrino detector could be constructed. There are ongoing experiments that act as a proof-of-principle for the radio technique in the ice: ARA (Askaryan Radio Array) [176], close to the IceCube detector at South Pole (see Figure 5.2) and ARIANNA (Antarctic Ross Ice Shelf Antenna Neutrino Array) [177] on the Ross Ice Shelf at the antarctic coast.

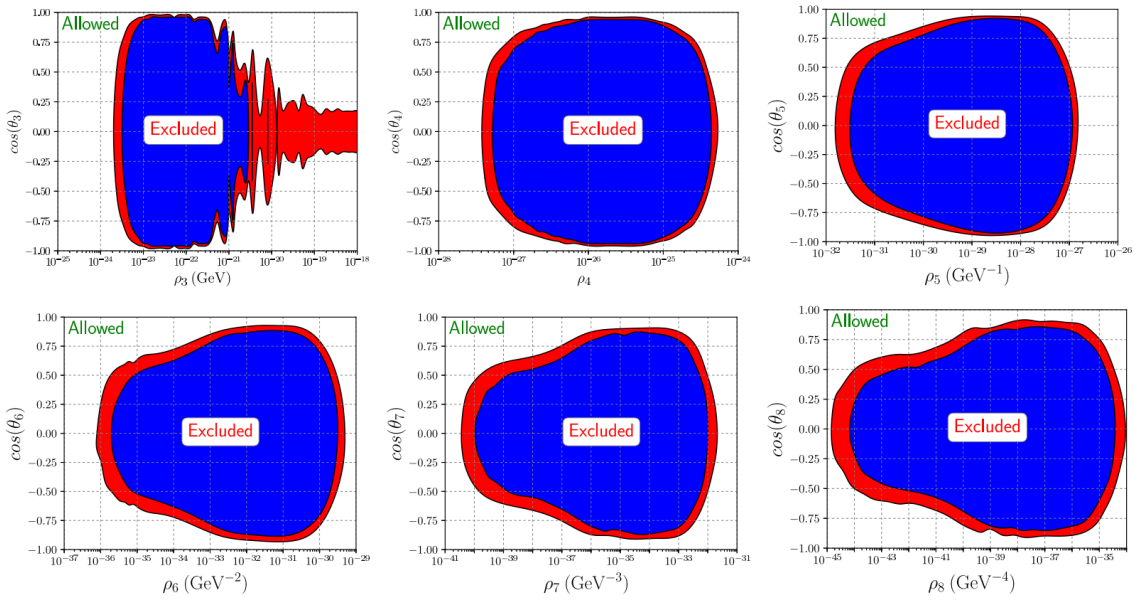


Figure 5.16: Regions excluded at 90% (99%) C.L. in the LIV parameter space in red (blue). ρ is related to the strength of the LIV and $\cos(\theta_d)$ is a combination of coefficients defining LIV in the effective Hamiltonian of Standard Model Extension [178]. The subscript d refers to the power of the corresponding operator in the Hamiltonian. More information in Ref. [179].

5.8 Beyond the Standard Model searches

The IceCube experiment consists of about 300 people from 50 institutions spread over 12 countries. A wide variety of senior scientists, graduate students, technicians, software specialists and engineers works on the continuous running operations to keep the detector running in both hardware and software. Most other people focus on physics analyses that range from low-energy oscillation physics to the rare highest-energy neutrino interactions in the ice. Below I give a general and very brief overview of some IceCube analyses that search for beyond-the-Standard-Model physics.

5.8.1 Lorentz invariance violation

is dit nu goed uitgelegd of niet?

Lorentz symmetry is one of the foundations of the SM: fundamental laws in nature are thought to be independent of the observer's inertial frame. Some SM extensions allow for spontaneous breaking of Lorentz symmetry and can lead to Lorentz-invariance violating (LIV) effects. Examples are string theory or quantum gravity. Some effects that would follow from these extensions are incorporated in the Standard Model Extension (SME) [178]. Although the size of LIV effects should be suppressed by the Planck scale ($\approx 10^{19}$ GeV), they could manifest themselves in, e.g., oscillations of atmospheric neutrinos that would modify the observed energy and zenith angle distributions of atmospheric muon neutrinos observed by the IceCube experiment. The LIV effects are often parameterized by two parameters: ρ_d and $\cos(\theta_d)$ (which are explained in the capture of Figure 5.16), where d refers to the power of the operator in the Hamiltonian. The energy reach of the IceCube detector makes it possible to go to dimensions up to 8 whereas most other experiments are sensitive up to dimension $d = 3$ or $d = 4$. This analysis was done first in the 40-string configuration [180] and later redone with the full detector configuration [179]. Results for $3 \leq d \leq 8$ are shown in Figure 5.16.

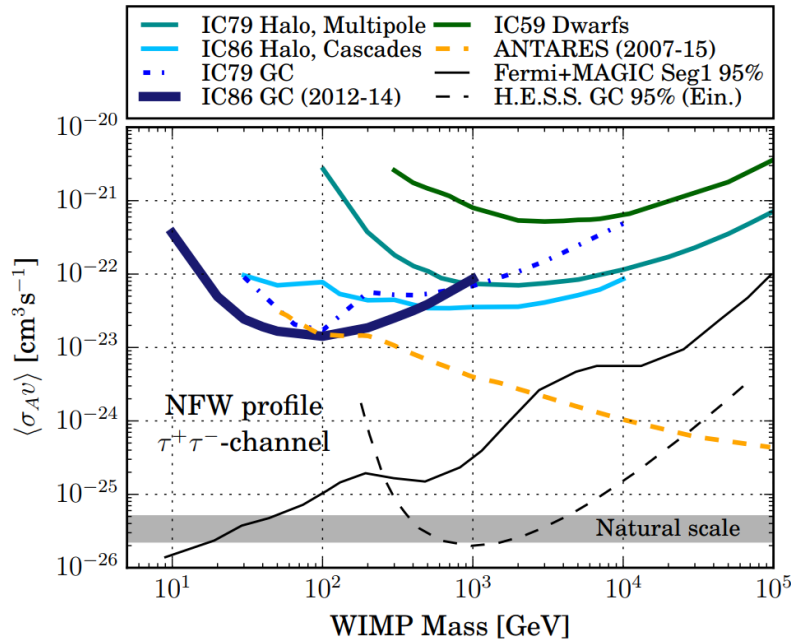


Figure 5.17: Upper limits of $\langle\sigma_A v\rangle$ in function of the WIMP mass from different experiments.

5.8.2 Dark matter

The large amount of evidence to support the existence of dark matter (DM) was given in Section 1.5. Many ongoing experimental efforts try to search for these elusive particles*. Collider experiments try to produce these particles by SM interactions (*production searches*), other experiments try to measure their interaction with SM particles through nuclear recoil (*direct detection*). It should also be possible to search for the SM products that are produced when annihilation of DM occurs and the corresponding daughter particles find their way to Earth (*indirect detection*). Most searches focus on specific regions in the sky that are more prone to produce a measurable signal. As one characteristic of DM is its non-zero mass, they are expected to be gravitationally trapped in the halo of galaxies or to accumulate in heavy celestial objects nearby such as the Sun or the Earth itself. Since most SM particles never reach us, neutrinos are probably the only possible messengers. Figure 5.17 shows a comparison of upper limits on $\langle\sigma_A v\rangle$ versus WIMP mass[†], for the annihilation channel $\chi\chi \rightarrow \tau^+\tau^-$ producing tau neutrinos. $\langle\sigma_A v\rangle$ is the WIMP-WIMP annihilation cross section and determines the strength of the expected neutrino flux. The analysis mentioned in the figure searched for signals from the center of the Milky Way [181]. Other IceCube analyses have searched for dark matter in the Sun [182, 183] and in the Earth [184].

5.8.3 Magnetic monopoles

The quantum theory of magnetic charge started with a paper by P. Dirac [185] in which he theorized the existence of magnetic monopoles in a similar fashion as he did to successfully predict the positron. If q_m is the magnetic charge and q_e the electric charge, Dirac found that the following condition should hold

$$q_m q_e = 2\pi n \quad (n \in \mathbb{Z}), \quad (5.4)$$

and could therefore explain why the electric charge is always quantized, i.e. in integer multiples of an elementary charge. The smallest possible magnetic charge would be[‡]

* Assuming that they are in fact particles.

[†]WIMP stands for Weakly Interacting Massive Particle and is one possible candidate for dark matter.

[‡]At the time of writing his paper, Dirac believed the smallest electric charge was from the electron. Since now we know the down quark holds an electric charge equal to $1/3e$, the minimal magnetic charge would be equal to $3g_D$.

$$g_D = 2\pi/e = e/2\alpha \approx 68.5e, \quad (5.5)$$

with $\alpha = e^2/\pi$ in natural units. Magnetic monopoles appear automatically in certain Grand Unified Theories that would give rise to these particles after spontaneous symmetry breaking of the GUT group, similar to the Higgs mechanism [186, 187]. Masses are typically of the order of 10^{16-17} GeV. They are searched for in IceCube analyses in multiple velocity ranges. Monopoles with velocities close to the speed of light in vacuum produce extremely bright tracks due to their high Dirac charge as shown in Eq. 5.5. At lower velocities ($\approx 0.5c$ to $0.76c$) secondary knock-off δ -electrons could have velocities above the Cherenkov threshold and produce light. Luminescence light from excitation of the ice dominates at low relativistic velocities ($\approx 0.1c$ to $0.5c$). For each of these speed ranges, searches for magnetic monopoles at the IceCube experiment are either in progress (luminescence) or have already set the world's best upper limits on the flux of magnetic monopoles over a wide range of velocities [188].

Simulation, Processing and Analysis

6	Simulation: Event Generation and Propagation	89
6.1	The software framework	
6.2	Generation	
6.3	Propagation	
6.4	Detector simulation	
6.5	Processing	
6.6	Simulation validation: burn sample	
6.7	Event viewer	
7	Reconstruction, Cleaning and Analysis Techniques	101
7.1	Reconstruction	
7.2	Pulse cleaning	
7.3	IceHive	
7.4	CoincSuite	
7.5	Event cleaning and reconstructions: summary	
7.6	Minimal-Redundancy-Maximum-Relevance	
7.7	Boosted Decision Tree classifiers	
8	The SPACE Analysis	119
8.1	Filter selection	
8.2	Level 3	
8.3	Level 4	
8.4	Level 5	
8.5	Results	
9	Summary and Conclusion	157

6. Simulation: Event Generation and Propagation

Soon there will be virtual reality, and augmented reality. If you assume any rate of improvement at all, then games will become indistinguishable from reality . . . , it would seem to follow that the odds we are in base reality are one in billions. ~ Elon Musk

To be able to search for new physics, one needs a good handle on the detector response to known physics processes. Depending on the analysis, some processes are more interesting than others. In general, the particle interactions of interest are referred to as *signal events*. Other interactions, which mimic or obscure the signal events, are typically called *background events*. These events are simulated using Monte Carlo* (MC) simulations, where one makes use of a model that describes the interactions and their probability to occur. A typical MC simulation consists of hundreds to millions of events that are constructed using these models with the use of random number generators. To determine the detector response to a particle interaction, one first has to start with the particle generation, which sets the conditions of the initial interaction. Afterwards, the propagation of the particle in the detector (medium) is simulated as best as possible. Below, an overview of the important background and signal simulations that are used in this analysis is given. A flowchart of the simulations steps is shown in Figure 6.1.

6.1 The software framework

IceTray is a modular framework written and used by the IceCube collaboration and mostly written in C++ for fast computation. A Python interface for most modules is provided for fast and easy implementation of the code. The framework is used in both online and offline processing and is stream-based with modules that act on events in the stream and essentially follows a flowchart of modules that is provided by the user.

To process the large amount of simulation that is required for the collaboration, a data processing and management framework called *IceProd* was developed. The setup is very light-weight, running as a Python application. It uses (complex) workflow DAGs (see below) across distributed

*While recovering from an illness in 1946, Stanislaw Ulam figured that the actual counting of successful attempts in playing a card game would yield him a much faster answer to the probability of success rather than doing the actual calculus. His work, shared with John von Neumann, needed to remain secret and adopted the code word “Monte Carlo”, referring to the gambling games in the Monte Carlo Casino in Monaco.

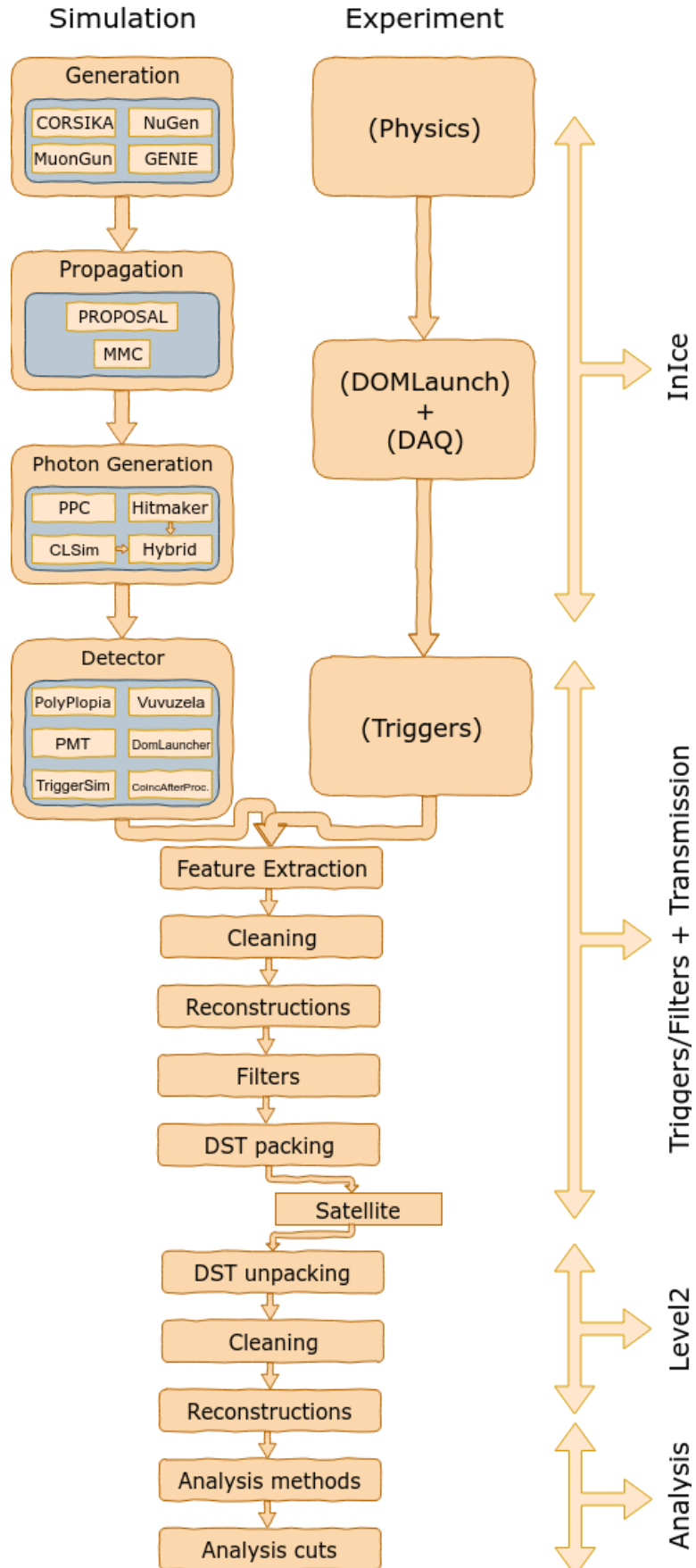


Figure 6.1: Flowchart of the simulation layout. On the left is shown how particles are injected and their interactions are simulated down to digitized waveforms. The right part shows real data processing. After triggering, both data and simulation go through the same processing chain to prepare for analysis.

computing grids in order to optimize usage of resources. A *dataset* is set up by running hundreds to thousands of jobs in parallel over multiple computing resources all over the world. Each data set has specific input parameters that are fixed and every set is given a unique number. Distributions in physical parameters such as the direction, energy, position, etc. of the particle(s) are provided by random number generators [189].

HTCondor is an open source computing software that provides a job queuing mechanism, scheduling policy, priority scheme, resource monitoring, and resource management. Users submit their serial or parallel jobs to HTCondor which places them into a queue. It chooses when and where to run the jobs based upon a policy, carefully monitors their progress, and ultimately informs the user upon completion.

DAGMans (Directed Acyclic Graph Managers) are meta-schedulers for the execution of computations. A Directed Acyclic Graph (DAG) consists out of nodes in a graph. Each node represents a certain computation that needs a certain input or depends on the output or execution from another node. Once a DAG is set up, DAGMans submit the programs to HTCondor and process the results. DAGMans are often used by analyzers for bulk computations on large amounts of data.

6.2 Generation

Simulations start with setting up the starting conditions of the physical processes one wants to simulate. For example, a shower event by itself is not well-defined. The type of primary particle (H, He, Fe,...), the energy, the inclination and so on will all determine the properties of the full air shower that is produced. Or, in the case of an SMP, do we want to simulate with charge 1/3 or 2/3?

Multiple different generators used in the IceCube collaboration serve different purposes; the ones that were used in this work are explained in more detail below.

6.2.1 Background simulation

In this work, we search for signal events that are not expected from the Standard Model. However, the IceCube neutrino observatory is not designed to look for particles with an anomalous charge. Therefore, it is necessary to properly account for the other physical processes that are not sought in this analysis but can mimic the signature of the signal. SMPs with a charge lower than the electron charge will produce less light compared to muons due to the squared charge dependency from the Cherenkov effect (see Eq. 4.7). Because the optical modules are located far away from each other, most of the light that is produced in tracks is absorbed in the ice. For this reason, there is a large uncertainty on the amount of Cherenkov photons that were produced when a track is seen in an event. Muons that originate from air shower events can produce dim tracks and are simulated with CORSIKA simulation. The NuGen program was used to simulate neutrino events. Both simulation programs are explained in more detail below. The data sets used in this analysis use SpiceLea as the ice model (see Section 5.6.1). An overview of the data samples and several simulation parameters is given in Table 6.2.

6.2.1.1 CORSIKA

A free, publicly available software framework that is widely used in the astrophysics community for the simulation of cosmic ray interactions is called CORSIKA (COsmic Ray SImulations for Kascade) [190]. It was originally developed for the KASCADE experiment and is now used by most people and collaborations to simulate air shower events. IceCube analyses, such as this one, use CORSIKA simulations to simulate the muonic component that is able to reach the in-ice detector.

The code is written in FORTRAN 77, but a C++ version is currently in the making [191].

Table 6.1: Best fit for parameters in Eq. 6.1. Numbers taken from Ref. [102].

j	R_c [V]	γ					$a_{i,j}$				
		p	He	CNO	Mg-Si	Fe	p	He	CNO	Mg-Si	Fe
1	$4 \cdot 10^{15}$	1.66	1.58	1.63	1.67	1.63	7860	3550	2200	1430	2120
2	$30 \cdot 10^{15}$			1.4			20			13.4	
3	$2 \cdot 10^{18}$			1.4			1.7			1.14	

The program initially injects a particle of specific type, energy, direction and position in the top of the atmosphere. The particles are tracked through the atmosphere until they undergo reactions with the air nuclei or - in the case of unstable secondaries - decay. Multiple different hadronic interaction models exist to describe the interactions at high energies such as QGSJET [192], SIBYLL [193] and EPOS-LHC [194]. The production of new particles after decay or interaction creates showers of particles and these particles are saved and read out at a certain altitude. Because the flux of cosmic rays is exceedingly small at the highest energies, too many resources and too much time would be required to simulate an energy distribution as measured in experiments. Therefore, one often simulates a much harder spectrum and reweights the events accordingly later on (see Appendix A.4). CORSIKA data sets in IceCube are often subdivided into a low-energy and high-energy data set. In this analysis, the former ranges from primary energies between 600 GeV to 100 TeV and uses a spectral index that is close to what is measured ($\gamma = 2.6$). The lower limit of the energy range at 600 GeV is due to the limited penetration depth of muons through the ice. The spectral index of the high-energy data set is smaller, resulting in a harder spectrum ($\gamma = 2$) leading to more statistics for rare high-energy events. The primary energy ranges from 100 TeV to 100 EeV.

The spectrum used for this analysis, after reweighting, follows the following energy distribution:

$$\Phi_i(E_{\text{prim}}) = \sum_{j=1}^3 a_{i,j} E^{-\gamma_{i,j}} \cdot \exp\left[-\frac{E}{Z_i R_{c,j}}\right]. \quad (6.1)$$

where we sum over three populations: particles accelerated from supernova remnants, a higher-energy galactic component of unknown origin and particles accelerated to ultra-high-energy from extra-galactic sources (more info in Section 3.1.2.1). γ is the spectral index, Z the particle atomic number and $a_{i,j}$ are the normalization constants for primary i in population j . R is the magnetic rigidity and R_c is the characteristic rigidity or cutoff above which a particular acceleration process reaches its limit. The 5 groups that are assumed to contribute significantly to the flux are: p, He, CNO, Mg-Si and Fe. This energy distribution follows the convention that is used in Ref. [102]. Table 6.1 summarizes the typical values for these parameters and shows the best fits for the normalization constants to describe the data.

Interactions

The atmosphere composition is always set at 78.1% N₂, 21% O₂, and 0.9% Ar, which is a good description of reality. However, the density of the air above the detector changes significantly during the year because of temperature differences in the Antarctic summer and winter. Most analyses, including this one, treat the muonic component as a background. They are not interested in the details of the showers and the changes during the year and therefore use an average of the atmospheric density. The atmospheric depth and densities were set to the averages of the month November for 5 years of data [195]. These monthly averages are shown in Figure 6.2.

The shower propagation and composition depends on the models that are used to simulate the high-energy interactions. The lowest energies are simulated with FLUKA (FLUktuierende KAskade) [196]. This model covers the energy range that can be compared with accelerator experiments. The SIBYLL model was used for the high-energy interactions. However, which model is the best for the highest energies is not known at the time of writing because there

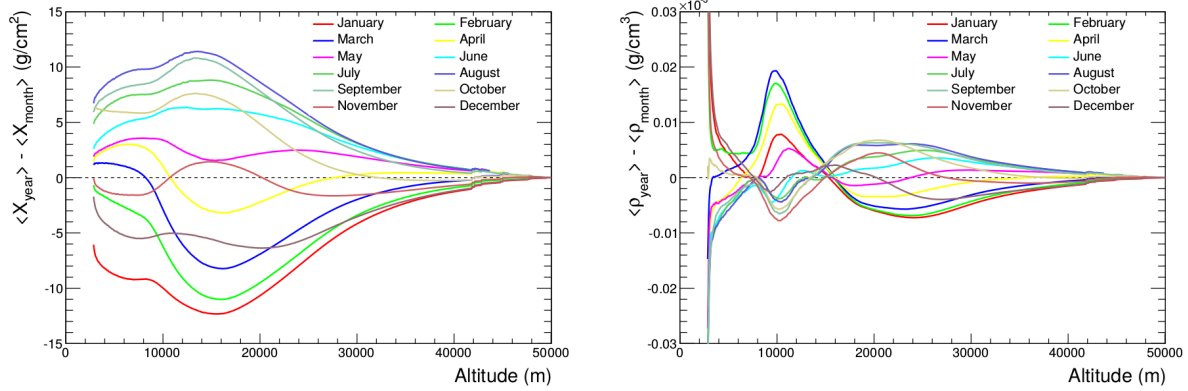


Figure 6.2: *Left:* Average atmospheric depth per month. *Right:* Average atmospheric density per month. Figures obtained with 5 years of data (2007-2011) [195].

are no controlled laboratory measurements that are capable of reaching these energies. Several studies seem to indicate that the composition changes drastically at the highest energies, i.e. IceCube [197], Pierre Auger Observatory [198], and Telescope Array [199]. However, the different experiments do not agree, presumably due to the different techniques used to determine the primary composition [195]. Recent work has shown that the most likely cause of discrepancy lies in non-perfect models [200]. Even though this discussion is far from resolved, it is fortunately of no importance for this analysis as these effects only become prominent at higher energies.

6.2.1.2 NuGen

The neutrino-generator (NuGen) is a neutrino event generator program that works with the IceTray framework. With this module, one can inject a primary neutrino on the surface of the Earth by specifying a few parameters in the steering file.

The physics implemented in this program is based on the ANIS-All Neutrino Interaction Generator [201]. However, the cross sections have been updated and the structure of the code has been changed significantly from ANIS to incorporate it in the IceTray framework.

The generator requires the first interaction to be near the detector and

- prepares a primary neutrino and injects it to the Earth,
- propagates the neutrino and works out interactions inside the Earth* (when they occur),
- makes a forced interaction inside the detection volume† (only if any neutrino reaches the detector site),
- stores injected neutrinos and all generated secondaries,
- stores interaction weight information.

The generator alternates between neutrino and antineutrino generation and assumes a neutrino-antineutrino ratio of (1:1), which is the expected ratio on Earth. The neutrino primary energy ranges from 100 GeV to 100 PeV.

The spectrum used for this analysis, after reweighting, follows the Honda2006 spectrum [135] for atmospheric neutrinos, SarcevicStd for the prompt component [138], and an astrophysical flux fit from Ref. [202] (see Section 3.3 for more information on these fluxes). The astrophysical flux measured by the IceCube collaboration follows an energy spectrum equal to

*Possible interactions are CC, NC, Glashow resonance for $\bar{\nu}_e$ and τ decay for $(\bar{\nu})_\tau$. CC interactions produce no new neutrinos and the simulation stops at the vertex point. The other interactions create new secondary neutrinos.

†In most cases, a neutrino will not interact within the medium, but for computational reasons at least one neutrino is forced to interact and the simulation is reweighted afterwards accordingly.

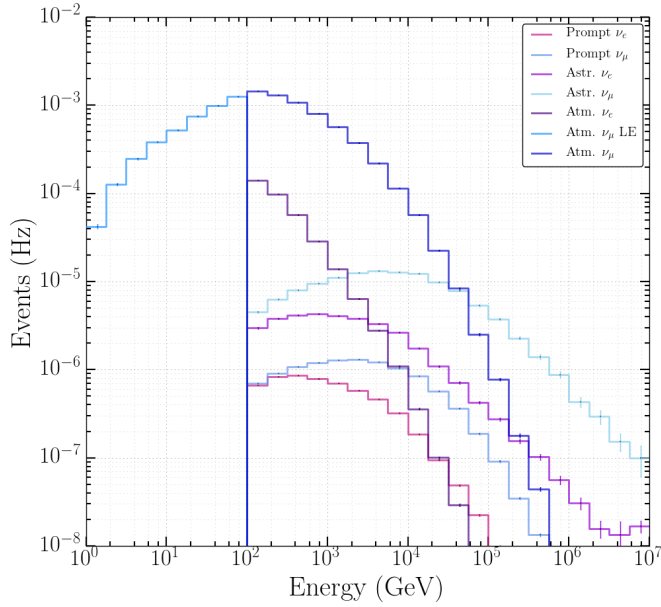


Figure 6.3: Distribution of weighted neutrino fluxes that were used for this analysis. The atmospheric ν_μ and ν_e fluxes were derived from Ref. [135], prompt from Ref. [138], and astrophysical from Ref. [202]. The energy refers to the energy of the primary neutrino.

$$E^2(\Phi) = 1.5 \cdot 10^{-8} \left(\frac{E}{100 \text{ TeV}} \right)^{-0.3} \text{ GeV cm}^{-2}\text{s}^{-1}\text{sr}^{-1}. \quad (6.2)$$

The distribution for these different components can be seen in Figure 6.3.

6.2.1.3 GENIE

To include the lowest neutrino energies, which are not included in ANIS/NuGen, the GENIE (Generates Events for Neutrino Interaction Experiments) neutrino generator was implemented in IceTray. It is a well established generator, used by collaborations worldwide and written in C++ [203, 204].

The spectrum used for this analysis, after reweighting, follows the Honda2015 spectrum [205] for low-energy atmospheric neutrinos. The primary neutrino energy ranges from 0.5 to 100 GeV.

6.2.2 Signal simulation

As mentioned in Section 2.4, the signal flux is assumed to be isotropic close to the detector. The SMP starting points are randomly placed on a disk with a direction perpendicular to it as shown in Figure 6.4. The disk has a radius of 800 m and is located at a distance of 1000 m from the detector center. The disk itself is randomly rotated around the detector center to simulate an isotropic flux. The distribution of the azimuth, ϕ , and cosine of the zenith*, $\cos(\theta)$, is shown in Figure 6.5.

Because slow moving particles would require specialized treatment[†], the minimal velocity of the particles is set as $\beta > 0.95$. The energy distribution is simulated with an E^{-1} spectrum and

*See Appendix A.3 why we show the cosine of the zenith.

[†]Cherenkov photon production in Eq. 4.7 changes for $\beta < 1$ compared to relativistic particles ($\beta \approx 1$). Similarly, ionization effects as seen in Eq. 4.17 for slow moving particles would not be comparable to relativistic particles. Also, the IceCube detector is designed to trigger on relativistic particles and most of the cleaning tools (see Section 7.2) rely on relativistic speeds. Dedicated analyses on slow moving particles like monopoles are being done but need specialized simulation and analyses. This is beyond the scope of this work.

Table 6.2: Overview of the data sets used in this analysis. GaisserH3a from Ref. [102], Honda2015 from Ref. [205], Honda2006 from Ref. [135], Sarcevic from Ref. [138], and astrophysical from Ref. [202]. The data set number is a unique number used in IceProd to distinguish data samples.

Generator	Type	Range [GeV]	Simulated γ	Weighted γ	Ice	Data set
CORS.	5-comp.	$10^5 - 10^{11}$	2	GaisserH3a	SpiceLea	11937
CORS.	5-comp.	$600 - 10^5$	2.6	GaisserH3a	SpiceLea	11499
CORS.	5-comp.	$600 - 10^5$	2.6	GaisserH3a	SpiceLea	11808
CORS.	5-comp.	$600 - 10^5$	2.6	GaisserH3a	SpiceLea	11865
CORS.	5-comp.	$600 - 10^5$	2.6	GaisserH3a	SpiceLea	11905
CORS.	5-comp.	$600 - 10^5$	2.6	GaisserH3a	SpiceLea	11926
CORS.	5-comp.	$600 - 10^5$	2.6	GaisserH3a	SpiceLea	11943
CORS.	5-comp.	$600 - 10^5$	2.6	GaisserH3a	SpiceLea	12161
CORS.	5-comp.	$600 - 10^5$	2.6	GaisserH3a	SpiceLea	12268
GENIE	ν_μ	$0.5 - 100$	1	Honda2015	SpiceMie	12475
NuGen	ν_μ	$100 - 10^8$	2	atmos.: Honda2006 prompt: Sarcevic astro.: Astro.	SpiceLea	11029
NuGen	ν_μ	$100 - 10^8$	2	atmos.: Honda2006 prompt: Sarcevic astro.: Astro.	SpiceLea	12346
NuGen	ν_μ	$100 - 10^8$	2	atmos.: Honda2006 prompt: Sarcevic astro.: Astro.	SpiceLea	11883
NuGen	ν_e	$100 - 10^8$	2	atmos.: Honda2006 prompt: Sarcevic astro.: Astro.	SpiceLea	12034
NuGen	ν_e	$100 - 10^8$	2	atmos.: Honda2006 prompt: Sarcevic astro.: Astro.	SpiceLea	12646

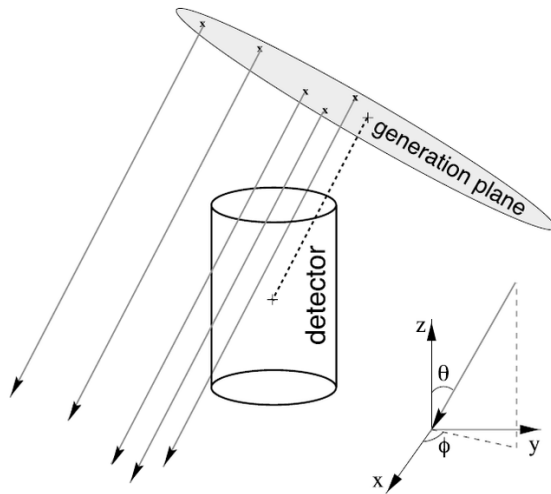


Figure 6.4: Illustration of how the particle injection works. The particle is first randomly positioned on a disk following a uniform distribution. The disk is then randomly rotated to simulate an isotropic flux.

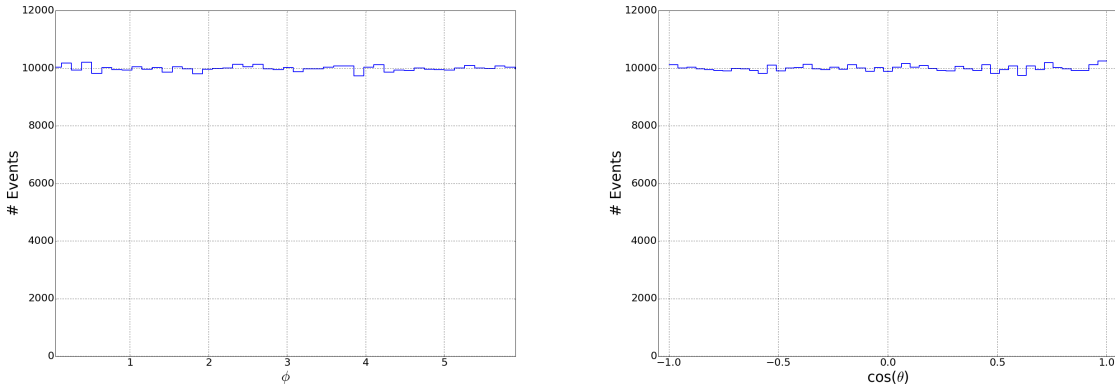


Figure 6.5: Illustration of uniform distributions of azimuth and cosine of the zenith for the particle injection in agreement with an isotropic flux (see Appendix A.1).

is later normalized to a flux of $10^{-14} \text{ cm}^{-2} \text{ s}^{-1} \text{ sr}^{-1}$ with an E^{-2} spectrum (see Appendix A.2) where the absolute flux only plays a role for illustrative purposes (as we will see in Section 8.4.3).

Similar to the background, SpiceLea was used as the nominal ice model.

6.3 Propagation

After generation, the particles need to be propagated through the ice. The particles will interact, lose energy, produce new particles, and generate light. The particle interactions and light production are done in two different modules. The former module is called PROPOSAL and runs on normal CPUs, whereas the latter is called ppc and uses GPUs to simulate enormous amounts of photons that are propagated through the ice.

6.3.1 PROPOSAL

Using the cross sections of the important interactions, together with the properties of the traversed medium and the particles (mass, charge, spin, decay time, etc.), it is possible to simulate the energy losses, secondary production and the consequent interactions of these daughter particles. This is done in the software package PROPOSAL (the Propagator with Optimal Precision and

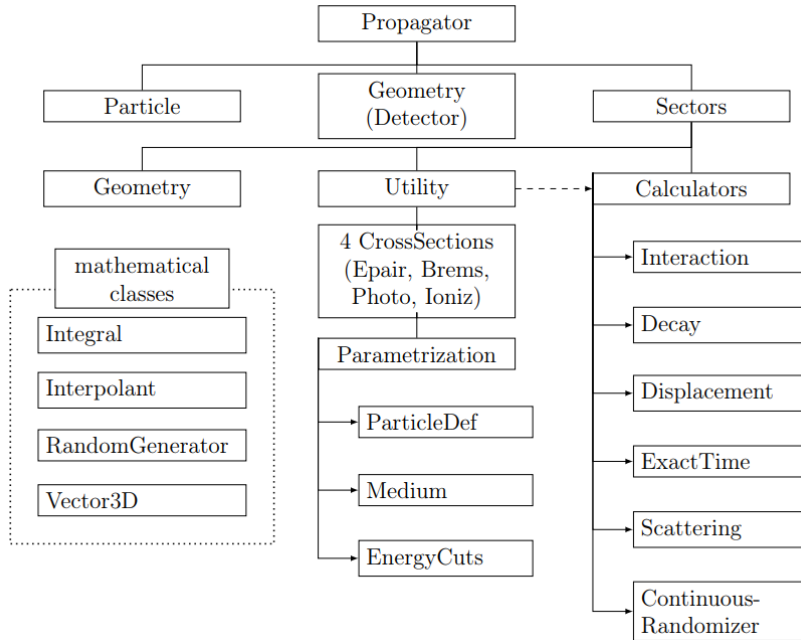


Figure 6.6: Overview of the class structure in PROPOSAL, from Ref. [206].

Optimized Speed for All Leptons), fully written in C++. It was based on its predecessor **MMC** (Muon Monte Carlo), which was written in Java. In 2018, a substantially improved version of PROPOSAL was finalized. An illustration of the workings of the code is given in Figure 6.6 and an in-depth documentation is given in Ref. [206].

PROPOSAL for SMPs

Since we assume the SMPs to behave leptonically, it was chosen to use PROPOSAL for the signal propagation as well. The mass and charge of the particle are set in the input parameters and the cross section dependence on these parameters can be seen in Section 4.4. In general, there is a small dependence on the mass, but a squared dependence on the charge, except for bremsstrahlung, which has a quartic charge dependence.

The PROPOSAL module keeps track of all the particles that are produced during propagation and the accompanying energy losses in a tree-like structure (called an *I3MCTree*). This collection of particles and their interactions are forwarded to a light-production computation module.

6.3.2 Photoelectron generators

In Section 5.6.1 we already explained how the ice is simulated in the IceCube detector. The parameters $b_e(400)$ and $a_{dust}(400)$ define the photon propagation through the ice and determine if photons are absorbed in the ice or hit a DOM. To optimize computing time, the DOMs were scaled in radius (nominally with a factor of 5) to force more photon interactions. The number of photons emitted was then appropriately scaled down with the square of this scaling factor*. With the Frank-Tamm formula (Eq. 4.7), it is possible to calculate the expected number of photons produced per unit length in the wavelength interval of interest†

$$\frac{dN}{dx} = \int_{\lambda_1}^{\lambda_2} \frac{2\pi\alpha}{\lambda^2} \sin^2(\theta_c) d\lambda = 2\pi\alpha \sin^2(\theta_c) \left(\frac{1}{\lambda_1} - \frac{1}{\lambda_2} \right). \quad (6.3)$$

From this formula, we find that the expected rate of a Cherenkov emission profile is equal to ≈ 350 photons/cm. Together with the DOM acceptance curve, as shown in Figure 5.6, which has

*The surface of a sphere scales with the square of the radius.

†From Figure 5.6 it is clear that $\lambda_1 \approx 300$ nm and $\lambda_2 \approx 650$ nm.

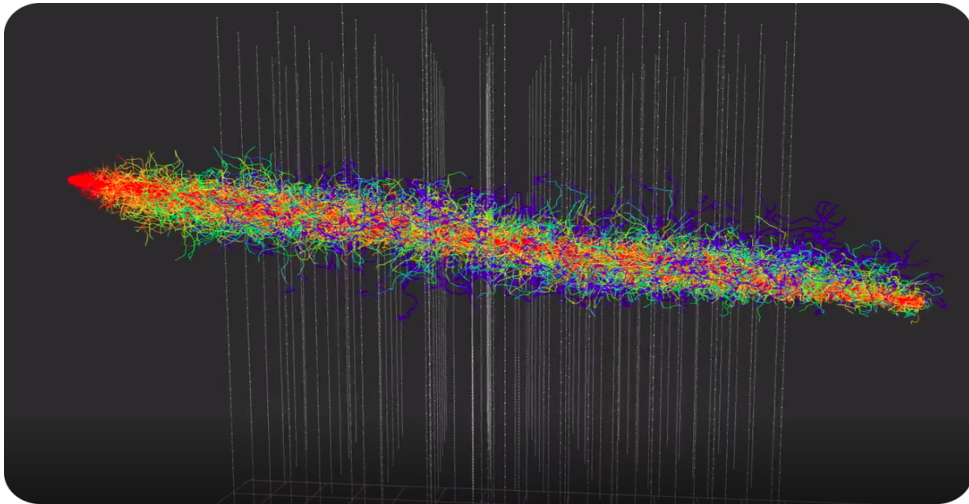


Figure 6.7: Simulation of a track event in IceCube. Each line represents a photon path and colors indicate how far they have traveled from their generation point. The color code represents a time delay with respect to a direct unscattered photon. Only 0.01% of all Cherenkov photons produced in this 100 TeV simulated muon is shown.

an overall average of around 7%, the expected *observed* number of photons is equal to 2450 m^{-1} .

PPC is a Photon Propagation Code, written in C++ that runs on graphic processing units (GPUs). This allows the code to run up to a hundred times faster than in a CPU-only environment. PPC employs both CUDA (NVIDIA GPU only) and OpenCL programming interfaces (both NVIDIA and AMD GPUs) together with multiple CPU environments. GPU environments allow the tracking of thousands of photons simultaneously, vastly improving the computational speed. For more information, see Ref. [148].

Previous photon propagation codes, such as **Photonics** [207], produced 6-dimensional photon tables (3 spatial, 2 directional and 1 temporal). This meant that at least one set of tables had to be produced per particle type and per velocity and interpolation methods had to be used, with the accompanying inaccuracies. These tables also required significant disk space and the method was therefore replaced with the GPU-codes. Direct photon simulation also allows for other non-trivial implementations such as the tilting of ice layers.

Another photon propagation code is called **CLSim**, which uses GEANT4 to propagate particles. A hybrid version called **HybridCLSim** is often used. Muons are propagated using **PROPOSAL/MMC** and their stochastic losses (which are small showers) are simulated from tables whereas the “bare muons” (with their stochastics) are simulated using direct propagation. This avoids time loss for the rare but very computationally expensive high-energy cascade events.

An illustration of photon propagation in the IceCube detector for a track simulation is shown in Figure 6.7.

6.4 Detector simulation

Further processing of the simulations involve:

- **Polyplopia**: a project dedicated to merge multiple events to account for coincident events (that are simulated independently). An estimated 15% of CORSIKA events result in coincident events and make up the bulk of bad reconstructions where downgoing muons are reconstructed as upgoing (an example will be shown in Figure 7.7);
- **Vuvuzela**: the PMT noise is simulated as having an exponential component from thermal and radioactive decays, and a log-normal contribution for scintillation;

- **PMT**: the time from the first photon entering the PMT to the readout after passing along multiple dynodes has an uncertainty, referred to as “PMT jitter”. The amplification of photoelectrons by the PMT is also not constant and is simulated in this module. Additionally, the module accounts for prepulses, late pulses, afterpulses and saturation of the PMT. More information can be found in Refs. [156, 208].
- **DOMLauncher**: the digitization of the PMT pulses and other behavior of the DOM mainboard (as explained in Section 5.2.1.2) is done in this module. The three main features of the DOM that are simulated to generate launches are the discriminator, LC, and digitization.
- **trigger-sim**: simulation of the trigger behavior as explained in Sec. 5.4.1.

6.5 Processing

After a full particle propagation and detector response simulation, the sample is sent through the same PnF procedure as is done with the data (see Section 5.4.2). The different stages of processing are referred to as “Levels”, where basic conversion from PnF formats to i3files (see Section 5.4.3) is called *Level0*. Reconstructions, calibrations and hit cleaning necessary for the filters are done at *Level1* while the filter processing is done at *Level2* (Section 5.4.2).

6.6 Simulation validation: burn sample

Getting the intricate details of physical events in non-trivial environments just right is not an easy task. In many steps of the way, simulations use fits and estimations. Some simulation data sets are reasonable to compare to the data, depending on the phase space one is looking at, while other data sets need other specifications. For example, analyses dedicated to measuring the cosmic ray interactions need much more fine-tuning in their models for the atmosphere, composition, interaction models, etc. than an analysis dedicated to search for muon tracks that first propagated through the Earth and have atmospheric muons as a background. Similarly, in this analysis the burn sample was used to compare data and MC to determine if the agreement between both made for a valid comparison. This is done throughout the analysis presented in Chapter 8.

It is for this reason that most analyses select a certain subset of the data they want to analyze to compare to the Monte Carlo simulations. For the present work, 10% of the total data, called the *burn sample*, was used to compare data to Monte Carlo. As indicated in Section 5.4.3, the data is saved in 8 hour runs and the burn sample consists of every run that ends on a ‘0’. The burn sample also allows to estimate the robustness of certain reconstructions and variables regarding differences in data and simulation.

After the discovery of an SPE offset in the DOM response in 2015, it was decided that multiple years of data were to be reprocessed in what was called *pass2 reprocessing* [160]. Aside from the SPE correction, the raw pulses were reprocessed with 2017 PnF, making the data more uniform in the course of the years for easier comparison*. This analysis makes use of data starting in the years 2011 to 2015 and are referred to as IC86-1 to IC86-5 where IC86 stands for the complete 86-string IceCube detector configuration and the last digit refers to the year of the season start. More recent years were not fully processed in time for this analysis. Only runs were considered that had

1. a positive tag from run coordinators (status == “good_i3”),
2. at least 5000 active optical modules,
3. all strings active during runtime.

The *livetime* is the total time that the detector was up and running and non-corrupted data was processed. Due to the increase in detector uptime over the years, this also means that the livetime of the different data sets has increased. The livetime for the different years is equal to

*Most filters did not undergo changes or only minor ones.

- 31.0 days of livetime for IC86-1,
- 32.2 days of livetime for IC86-2,
- 33.2 days of livetime for IC86-3,
- 36.6 days of livetime for IC86-4,
- 36.7 days of livetime for IC86-5,

resulting in a total burn sample livetime of around 170 days.

6.7 Event viewer

After a full simulation, it is possible to visualize the event in an event viewer called **Steamshovel**. Typical events in the IceCube detector are shown with this interface and are loaded from *i3files* that contain information about the detector geometry and the event (DOM positions and calibrations, detector hits, timestamps, trigger hits, etc.). Simulated events also contain the true values of the particles and can be compared with reconstructed variables. Event viewers allow for first guesses in how background events are able to be separated from signal, although both can have wide varieties in possible variables.

In such an event viewer, the number of photons seen per DOM is indicated by the size of the spheres; the larger the sphere, the more PEs were seen. The color of the spheres indicates the time of the pulse registration. The color scale can be chosen, but usually a rainbow pattern is used where red indicates the earliest pulse hits and blue the last.

An example of a track event in the event viewer is given in Figure 7.7.



7. Reconstruction, Cleaning and Analysis Techniques

Shall I refuse my dinner because I do not fully understand the process of digestion? ~ Oliver Heaviside

As explained in Chapter 5, an IceCube event consists of a series of DOM hits. One hit contains charge, timing, and positional information. This collection of multiple hits has to be translated (reconstructed) to certain properties of a particle. Some examples are the direction, position, track length, etc. Fast reconstructions of these properties, such as the ones necessary in online filtering, are usually done with simple algorithms. More sophisticated algorithms are performed offline on smaller data samples.

Because the in-ice IceCube detector is sparsely distributed, it is not straightforward to unambiguously reconstruct the particle (interactions). The scattering and absorption of photons, tilt of ice sheets, bubble columns, etc. lead to uncertainties and make reconstruction challenging. Over the years, multiple different methods have been developed in the collaboration. Several reconstruction algorithms have been used in this analysis and are explained in more detail in this chapter. We start with the algorithms that reconstruct where the particle entered and in which direction it traversed the detector and give an estimate on the direction uncertainty.

A number of hits in an event can often be attributed to DOM noise. There are several techniques possible to remove these hits, some of which are used in this analysis. They are also discussed in more detail below.

Finally, we discuss the methods that were used to discriminate signal from background events with machine learning techniques.

7.1 Reconstruction

7.1.1 Likelihood

Reconstruction algorithms usually have no unique solutions to describe the set of measured values of an event. The likelihood $\mathcal{L}(\vec{x}|\vec{a})$ describes the probability of a set of parameters \vec{a} to be expressed in a set of experimentally measured values \vec{x} . The parameters, \vec{a} , typically define the particle's characteristics (energy, direction, position, type, etc.) while the measured values \vec{x} are determined from the detector response (number of PE, timing, position of hit DOMs, etc.). This likelihood is equal to the cumulative probability

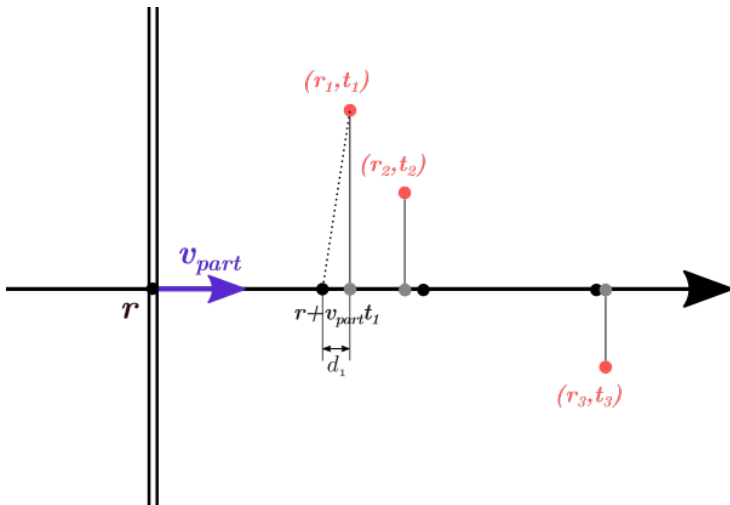


Figure 7.1: Figure illustrating how **LineFit** works. The position, \vec{r} , and velocity, \vec{v}_{part} minimizing the distance of the DOMs to the track is calculated. The dotted line is one of the distances that is minimized in Eq. 7.4.

$$\mathcal{L}(\vec{x}|\vec{a}) = \prod_i p(x_i|\vec{a}), \quad (7.1)$$

where $p(x, \vec{a})$ is the probability that we measure a certain value x from a set of independent values \vec{x} , given an initial set of parameters \vec{a} . The maximum likelihood method is used to estimate the unknown parameters \vec{a} , which is done by maximizing \mathcal{L} . The reconstruction algorithms below rely on analyzing parameters that assume a single, long track

$$\vec{a} = (\vec{r}_0, t_0, \hat{\vec{p}}, E_0), \quad (7.2)$$

where \vec{r}_0 is the position vector of the particle at a time t_0 with a direction $\hat{\vec{p}}$ and initial energy E_0 .

7.1.2 Line-Fit

One of the simplest approaches in constructing a parameter profile is by calculating the track that, overall, has the closest approach of all the hit optical modules. This is called **Line-Fit** (LF) [209]. If we assume that a particle starts at a position \vec{r} at a time $t = 0$ and travels at a velocity of \vec{v}_{part} , then its position at any given time is

$$\vec{r}' = \vec{r} + \vec{v}_{\text{part}}t. \quad (7.3)$$

We want to calculate the best possible estimate of the velocity \vec{v}_{part} and an initial position \vec{r} . Each DOM has a known location, \vec{r}_i , and measured time of a pulse, t_i . In this algorithm, one assumes that a wavefront perpendicular to the particle's direction is traveling along with the particle. If the velocity \vec{v}_{part} is fixed, then the position of the particle at later times is known (black points in Figure 7.1). However, the Cherenkov wavefront should be set at an angle and because scattering, PMT jitter, noise, etc. are not taken into account, this will not agree with the DOM position projected along the particle path (grey dots). The unknown velocity \vec{v}_{part} and position \vec{r} are the analytical solutions after minimizing the distances d_i as shown in the figure*

*Minimizing $r_i - r'$ (dotted line in Figure 7.1) is the same as minimizing d_i .

$$\begin{aligned} S(\vec{r}, \vec{v}_{\text{part}}) &\equiv \sum_{i=1}^{N_{\text{hit}}} \rho^2(\vec{r}, \vec{v}_{\text{part}}, \vec{r}_i, t_i) \\ &= \sum_{i=1}^{N_{\text{hit}}} (\vec{r}_i - \vec{r} - \vec{v}_{\text{part}} t_i)^2, \end{aligned} \quad (7.4)$$

where $\rho(\vec{r}, \vec{v}_{\text{part}}, \vec{r}_i, t_i) = |\vec{r}_i - \vec{r} - \vec{v}_{\text{part}} t_i|$ and N_{hit} is the number of pulse hits. The analytical solution by minimizing this equation is equal to

$$\vec{r} = \langle \vec{r}_i \rangle - \vec{v}_{\text{part}} \langle t_i \rangle \quad \text{and} \quad \vec{v}_{\text{part}} = \frac{\langle \vec{r}_i t_i \rangle - \langle \vec{r}_i \rangle \langle t_i \rangle}{\langle t_i^2 \rangle - \langle t_i \rangle^2}, \quad (7.5)$$

where $\langle x \rangle$ denotes the average of a parameter x over all hits i .

Because this is an analytical equation, this algorithm is very fast and is therefore often used in online processing.

7.1.2.1 Improved Line-Fit

Line-Fit is usually implemented as a seed track for other, more computationally heavy algorithms (such as SPE, see Section 7.1.3). The simplifications that are used in LF can lead to angular deviations that converge to a local minimum instead of the global. The LF algorithm assumes that all hits will be near the track and hits far away from the track enter the least squares computation quadratically. Therefore, hits from far away often dominate the reconstruction even though the simple algorithm doesn't account for

1. The Cherenkov emission profile.
2. The scattering effects of the ice medium.
3. Noise hits that occur far from the track.

To reduce the effects of outliers, it was found that a basic filter could identify these scattered hits, and improve accuracy by almost a factor of two by removing them from the dataset. More formally, for each hit h_i (that consists of a charge, position and timing), the algorithm looks at all neighboring hits within a neighborhood of radius μ , and if there exists a neighboring hit h_j with a time stamp that is t earlier than h_i , then h_i is considered a scattered hit and is not used in the basic reconstruction algorithm. Optimal values of μ and t were found to be 156 m and 778 ns by tuning them on simulated muon data [210].

This “delay cleaning” is done by computing a Huberfit on the remaining data points and minimizing

$$\sum_{i=1}^{N_{\text{hit}}} \phi(\rho(\vec{r}, \vec{v}_{\text{part}}, \vec{r}_i, t_i)), \quad (7.6)$$

where ρ is defined in Eq. 7.4 and the Huber penalty function ϕ is defined as

$$\phi(\rho) \equiv \begin{cases} \rho^2 & \text{if } \rho < \mu \\ \mu(2\rho - \mu) & \text{if } \rho \geq \mu \end{cases}. \quad (7.7)$$

An example of the Huber penalty function is given in Figure 7.2. Because of the overall performance increase of this method, all LF computations were done with the improved version (although still often referred to as “Line-Fit”).

7.1.3 SPE and MPE

A more intricate method of track reconstruction is done by taking the geometrical shape of the Cherenkov cone into account and relying on simulation fits where a seed track is implemented (usually from the fast Line-Fit algorithm) [209].

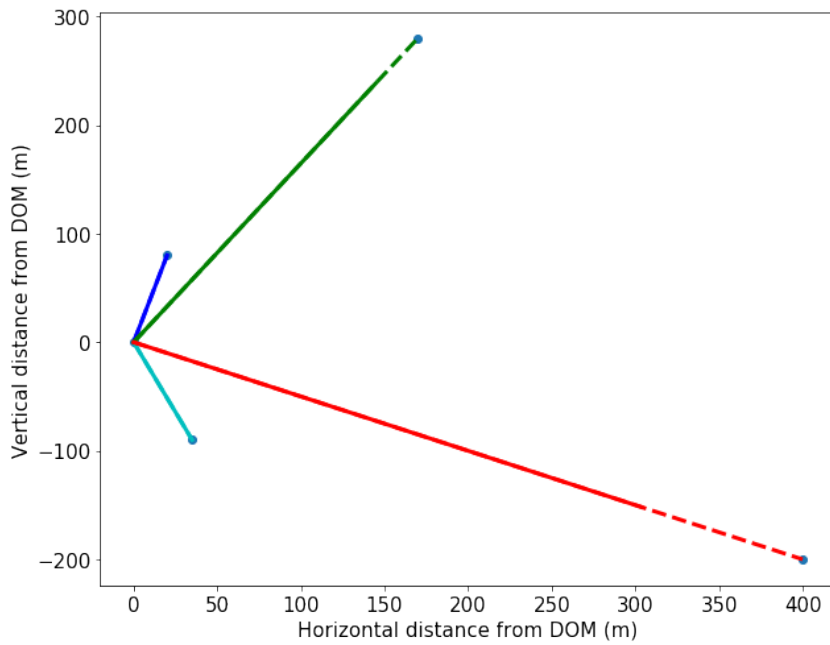


Figure 7.2: Illustration of Huber penalty for possible hit locations. The origin was set as the assumed particle position, $\vec{r} + \vec{v}_{\text{part}} t_i$. The solid line shows the result of $\phi(\rho)$ where the dotted lines show values for ρ .

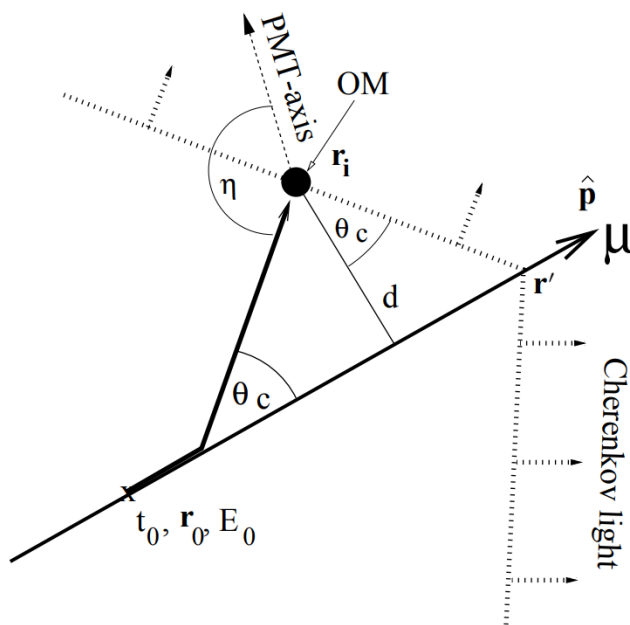


Figure 7.3: Figure illustrating a muon track passing close by an optical module and defining the parameters used in the reconstruction algorithms. Illustration from Ref. [209].

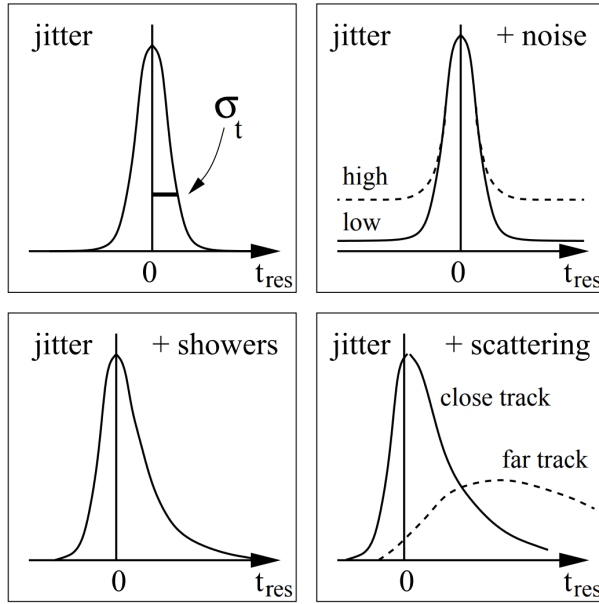


Figure 7.4: Schematic distributions of t_{res} where several effects are included. *Top left:* PMT jitter effects. *Top right:* jitter and random noise effects. *Bottom left:* adding indirect Cherenkov light from stochastic deposits along the track of a high-energy particle. *Bottom right:* adding scattering delay effects. Figure from Ref. [209].

Let us assume a particle is traveling close to a DOM with parameters as defined in Eq. 7.2 as illustrated in Figure 7.3. The minimal distance of the track to the DOM is equal to d and the PMT-axis (downwards relative to DOM) has an angle offset of η degrees of the Cherenkov wave direction. If Cherenkov photons would travel undelayed directly from the primary particle to an OM, the *time residual* (time between the observed hit time and the “expected” time) is a delta function centered around 0, where

$$t_{\text{res}} \equiv t_{\text{hit}} - t_{\text{geo}}, \quad (7.8)$$

with

$$t_{\text{geo}} = t_0 + \frac{\hat{\vec{p}} \cdot (\vec{r}_i - \vec{r}_0) + d \cdot \tan(\theta_c)}{c_{\text{vac}}}, \quad (7.9)$$

which is the time necessary for the particle to travel from the position \vec{r}_0 to \vec{r}' as illustrated in the figure. The accompanying Cherenkov wavefront that sent out photons at a time t_0 from \vec{r}_0 will cross the DOM when the particle is at a position \vec{r}' . Due to noise effects, PMT jitter, light from secondary interactions, DOM orientation, etc. the time residual is smeared and shifted as can be seen in Figure 7.4. Stochastic energy deposits along the track of a high-energy particle (as described in Section 4.3.2.1) lead to an additional shift of the time residual since these photons arrive after the Cherenkov cone.

A time likelihood function $\mathcal{L}_{\text{time}}$ can be constructed from the p.d.f. of arrival times of single photons, p_1 , at the locations of the hit DOMs. The p.d.f. of single photons was estimated with photon simulations in ice and fitted to a *Pandel function*. How this was done and for more information on this function, I refer the reader to Ref. [209].

$$\mathcal{L}_{\text{time}} = \sum_{i=1}^{N_{\text{hit}}} p_1(t_{\text{res}} | \vec{a} = d_i, \eta_i, \dots). \quad (7.10)$$

An initial particle position and direction is found by maximizing the likelihood and iterated a couple of times to find the global maximum instead of a local. This fitting is called the *Single PhotoElectron (SPE) fit*.

Unfortunately, the description of single photons arriving at the optical modules is not fully correct since electrical and optical signal channels can only resolve multiple photons separated by a few 100 ns and ≈ 10 ns, respectively. Within this time window, only the arrival time of the first pulse is recorded.

In the *Multi-PhotoElectron (MPE) fit*, one accounts for the fact that the early photons in a DOM hit scattered less in the ice. The p.d.f. for the first photon out of a total of N to arrive with a time residual of t_{res} is

$$p_N^1(t_{\text{res}}) = N \cdot p_1(t_{\text{res}}) \cdot \left(\int_{t_{\text{res}}}^{\infty} p_1(t) dt \right)^{(N-1)} = N \cdot p_1(t_{\text{res}}) \cdot (1 - P_1(t_{\text{res}}))^{(N-1)}, \quad (7.11)$$

where P_1 is the cumulative distribution of the single photon p.d.f. The MPE likelihood computation is done by replacing p_1 in Eq. 7.10 with p_N^1 .

Several variables that are obtained from these algorithms were used in this analysis. For example, the direction of the reconstructed particle was used to look for upgoing tracks, while the likelihood of the reconstruction was used to remove downgoing muon tracks that were wrongfully reconstructed as upgoing.

7.1.4 Paraboloid

In Sections 7.1.2 and 7.1.3, we discussed how a particle's direction could be estimated with likelihood estimations. The **Paraboloid** module tries to provide an estimate for the error on this direction. A highly energetic muon event with hundreds of hit DOMs will lead to a much better directional resolution than a dim track where only a handful of DOMs are hit. In general, the likelihood space around the estimated direction is scanned and compared to the likelihood of the initial track estimation. If the likelihood space around the minimum* is relatively flat, there is a larger uncertainty in the directional estimation. With this method, the module also tries to parameterize if the maximum likelihood that is found from the reconstruction algorithms is far from, or close to the global maximum likelihood. The module uses a minimizer and constructs a grid of zenith and azimuth points near the minimum of the negative likelihood. For each point on the grid, it does a three-parameter minimization for the vertex holding the zenith and azimuth constant. The likelihood values for each point on the grid are then fit to a paraboloid (2D parabola) using a χ^2 minimization since the shape of the log-likelihood space near the minimum should have a paraboloid shape. Of importance are the parameters of the corresponding error, which are assumed to correspond to an ellipse for the 1σ contours.

The module computes the lengths of the semi-major and semi-minor axes of the 1σ error ellipse σ_1 and σ_2 [†]. It was found that the quadratic mean of both uncertainties provides a good single-valued estimate for the angle uncertainty

$$\sigma_{\text{para}} = \sqrt{\frac{\sigma_1^2 + \sigma_2^2}{2}}. \quad (7.12)$$

Since σ_1 and σ_2 should follow univariate Gaussian distributions, σ_{para} will be the radius parameter in a bivariate distribution. Also, the great circle distance between the MC truth of the signal particle and the reconstruction direction, as calculated by the Vincenty formula, is a two-dimensional distribution. From the Rayleigh distribution, it follows that the mean of this distribution should be equal to $1.177\sigma_{\text{para}}$ [‡]. Therefore, if we divide the great circle distance with σ_{para} , we should obtain a variable that is distributed with a peak at 1.177 (mean). This

*Often minimizers are used in likelihood computations, which actually use $-\log \mathcal{L}$.

[†]The confidence intervals σ_θ and σ_ϕ can be found by rotating the minor and major axes σ_1 and σ_2 .

[‡]The CDF of the Rayleigh distribution $1 - e^{-x^2/2\sigma^2}$ is equal to the containment for a bivariate normal distribution. Implementing $x = 1.177\sigma$ yields a factor of 0.5.

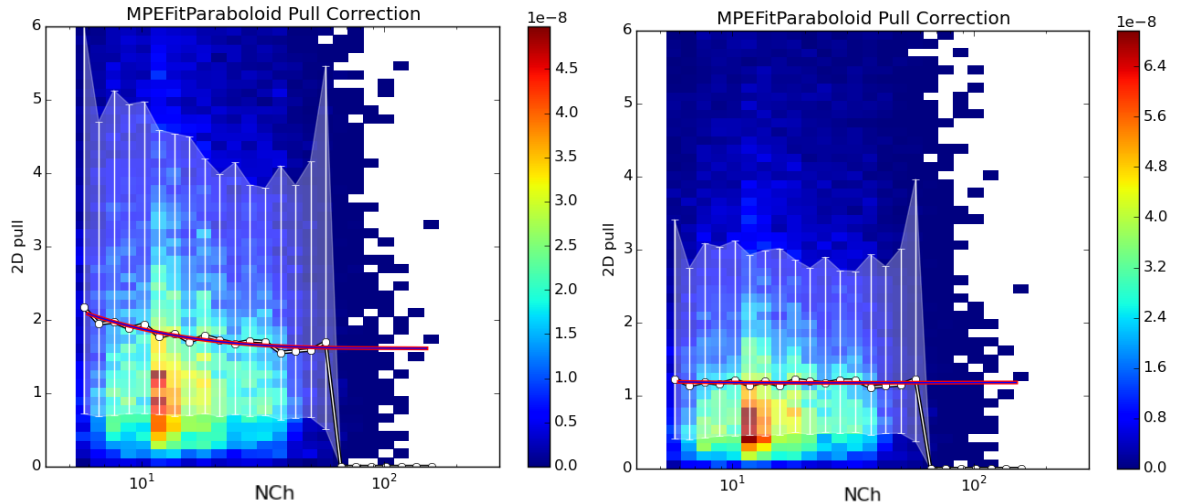


Figure 7.5: *Left:* Paraboloid pull in function of the number of hit DOMs shows that the global average (red/purple line) is not centered at 1.177. *Right:* Pull after correction.

variable is called the *paraboloid pull* and should be compared to an energy related variable (here the number of hit DOMs (NCh) is used). In Figure 7.5, it is clear that there is an offset that changes in function of the number of hit DOMs. This effect is seen in all analyses and can be explained by multiple factors in Monte Carlo simulations, but mainly stems from our incomplete knowledge and non-perfect simulations of the ice. The energy-dependent correction factor is computed from Monte Carlo events and applied to both data and MC. From the figure, it is clear that the pull is overestimated (σ_{para} is underestimated), meaning the correction will increase the directional uncertainty σ_{para} , which is by any means a conservative method. More information on this algorithm can be found in Ref. [211].

7.1.5 Millipede

To have a better handle on the particle energy and stochastic cascades along the track, the module **Millipede** was developed [212, 213]. The number of photons seen at each optical module depends on multiple factors that were mentioned throughout this text, such as the scattering and absorption in the ice, timing jitter, etc. In this module, the expected number of photons is assumed to depend on the energy that was deposited along a track and a *light yield factor*, Λ , that depends on the DOM position and the location of emission

$$\begin{aligned} N_{\text{exp},k} &= \rho_k + \sum_{i=1}^n \Lambda(\vec{r}_k, \vec{r}'_i) E_i \\ &= \rho_k + \vec{\Lambda}(\vec{r}_k, \vec{r}'_i) \cdot \vec{E}, \end{aligned} \quad (7.13)$$

where k refers to a certain DOM and i refers to a certain energy deposit such as illustrated in Figure 7.6. ρ is the average expected number of noise photons and is determined by the duration of the event. The light yield factor and energy are written as vectors to shorten the expressions.

The likelihood is assumed to follow a Poisson distribution with $N_{\text{seen},k}$ the number of hits that occurred and a mean value equal to the number of expected photons, $N_{\text{exp},k}$

$$\begin{aligned} \mathcal{L}_k &= \frac{(N_{\text{exp},k})^{N_{\text{seen},k}}}{N_{\text{seen},k}!} e^{-N_{\text{exp},k}} \\ &= \frac{(\vec{\Lambda} \cdot \vec{E} + \rho_k)^{N_{\text{seen},k}}}{N_{\text{seen},k}!} e^{-\vec{\Lambda} \cdot \vec{E} - \rho_k}. \end{aligned} \quad (7.14)$$

For easier, faster and more accurate computation, the logarithm of the likelihood is used

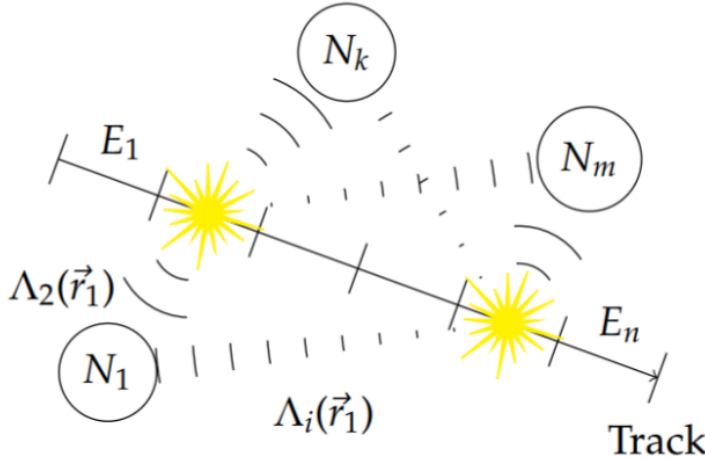


Figure 7.6: Illustration of the working principles of the `Millipede` toolkit. A track is subdivided into segments that each deposit a certain energy, E_i . Different segments can contribute to the total number photons seen per DOM, N_k .

$$\begin{aligned} \ln \mathcal{L}_k &= N_{\text{seen},k} \ln \left(\rho_k + \sum_{i=1}^n \Lambda(\vec{r}_k, \vec{r}'_i) E_i \right) - \ln (N_{\text{seen},k}!) - \sum_{i=1}^n \Lambda(\vec{r}_k, \vec{r}'_i) E_i - \rho_k \\ &= N_{\text{seen},k} \ln \left(\rho_k + \vec{\Lambda}(\vec{r}_k) \cdot \vec{E} \right) - \vec{\Lambda}(\vec{r}_k) \cdot \vec{E} - \rho_k - \ln (N_{\text{seen},k}!) \end{aligned} \quad (7.15)$$

Assuming a total of m DOMs that registered hits, we can maximize the total likelihood with respect to the energy, which gives

$$\nabla_{\vec{E}} \ln \mathcal{L} = \nabla_{\vec{E}} \sum_{k=1}^m \ln \mathcal{L}_k = \sum_{k=1}^m \left(\frac{N_{\text{seen},k} \vec{\Lambda}(\vec{r}_k)}{\vec{\Lambda}(\vec{r}_k) \cdot \vec{E} + \rho_k} - \vec{\Lambda}(\vec{r}_k) \right) = 0. \quad (7.16)$$

This equation holds if all terms in the sum vanish, i.e. if for all DOMs holds that

$$\begin{aligned} N_{\text{seen},k} &= \vec{\Lambda}(\vec{r}_k) \cdot \vec{E} + \rho_k \\ &\stackrel{\text{Eq. 7.13}}{=} N_{\text{exp},k}. \end{aligned} \quad (7.17)$$

This can be written in a set of linear equations

$$\vec{N} - \vec{\rho} = \mathbf{\Lambda} \vec{E}, \quad (7.18)$$

where

$$\mathbf{\Lambda} = \begin{pmatrix} \Lambda(\vec{r}_1, \vec{r}'_1) & \cdots & \Lambda(\vec{r}_1, \vec{r}'_n) \\ \vdots & \ddots & \cdots \\ \Lambda(\vec{r}_m, \vec{r}'_1) & \cdots & \Lambda(\vec{r}_m, \vec{r}'_n) \end{pmatrix}, \quad (7.19)$$

is the *response matrix*. This has to be inverted to find the energies in the vector \vec{E} . It describes the DOM response to light output from certain segments along a track. The entries in this matrix come from simulations that produce spline tables. Simplified sources, such as minimum ionizing muons and isotropically emitting point sources are simulated in Monte Carlo simulations at certain discrete points. Interpolation is done using spline functions. More information, such as how timing information can be implemented, can be found in Refs. [214, 215].

The `Millipede` algorithm was used to construct a handful of variables to discriminate the dim SMP tracks from muon tracks.

7.1.6 FiniteReco

Charged particles such as muons and electrons can be created from neutrino interactions. Electrons are stopped within a couple tens or hundreds of meters, but muons can travel up to kilometers and do not have a spherical light deposit. Because neutrinos do not produce Cherenkov light, this “sudden” light production from muons can look like a *starting track* in the IceCube detector. Charged particles that travel through matter also lose energy and can therefore be stopped, giving rise to *stopping tracks*. **FiniteReco** is a module that tries to reconstruct if particles are starting, stopping, contained or throughgoing. The hit DOMs around a seed track (usually the reconstructed track) are checked to have seen light and the first and last emission points along the track are used to check the possible hypotheses. Because SMPs are assumed to create long tracks, the module can be used to remove tracks that start or stop within the detector.

Because the edges of the detector are not well defined*, the likelihoods of individual DOMs to have seen a hit lead to a total likelihood that doesn’t give a conclusive answer, but the starting and stopping probabilities can be compared to a throughgoing track hypothesis.

7.2 Pulse cleaning

As explained in Section 5.2.2, each DOM in IceCube has an intrinsic noise rate. This dark noise is observed in every triggered event and seen as random hits in the detector that are added to the hit pattern of tracks and cascades. These spurious hits are a large nuisance factor in event reconstructions, leading to misidentification and errors in the result. Noise cleaning should be done in early stages of event processing and analysis to reduce a large rate of bad reconstructed events that pass cut selections. One of the most conservative ways is to only look at HLC hits (*HLC cleaning*). However, this is too demanding for most low-energetic and/or dim events that will have multiple hits from isolated DOMs.

Another method, which tries to include these isolated hits, is the **seededRT** algorithm. This method relies on the “*RT-cut*”, which was already implemented in the time of AMANDA operations. R is a designed radius and T refers to the time between multiple possible pulse times (e.g. the pulse of one DOM starts during the time window of a second DOM’s pulse, or stops during the time window). The full description can be found in Ref. [216], but can be summarized as follows: DOMs are required to be in a temporal and spacial coincidence that is physically possible (e.g. the signal between DOMs cannot exceed the speed of light in vacuum). This method is, however, computationally expensive since all DOM pairs have to be looped over[†]. The **seededRT** algorithm takes a subset of seeds that are considered to be mostly signal related hits. These seeds can be provided by, for example, using HLC information. By adding all further hits found within the seed’s *RT*-range to the list of seed hits and iterating until convergence, only those (SLC) hits are kept that cluster around the initial seed hits. Thus, the **seededRT** cleaning is applied in the opposite way as the previously used “*RT-cut*”. While the old module looks at all hits and removes the ones not fulfilling the *RT*-condition, the **seededRT** initially keeps only a subset of the launches (“seeds”) and adds those launches in the *RT*-range of the already kept ones. In this way, outlying *RT*-hit clusters from noise can be rejected and has a better noise hit rejection than the classic *RT-cut*. Therefore, the pulses used in this analysis are first cleaned using the **seededRT** algorithm.

7.3 IceHive

In Section 5.4.1, it was explained how multiple triggers were combined into one global trigger. In a first step, Q-frames (which are collections of hits in a global trigger and holds information on which triggers and filters were passed, also keeping the uncleaned pulses) are simply re-split

*Imagine a cascade 20 m below the lowest DOMs. It is still possible for light to reach the bottom modules of the detector.

[†]The number of pairs for n DOMs is equal to $\frac{1}{2}n(n - 1)$ and scales with n^2 .

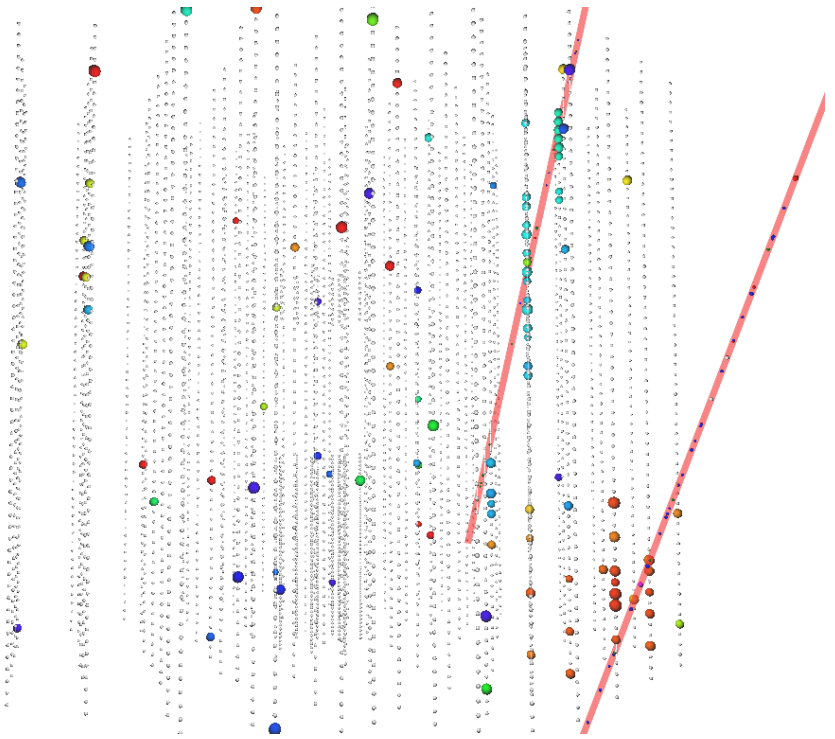


Figure 7.7: Event display of a simulated coincident event of two downgoing muons. The colors of the event range from red (early) to blue (late). The first muon hits the bottom of the detector, while the second traverses mainly the upper part. These events are reconstructed as a single upgoing event and therefore result in a large background contribution for analyses that focus on upgoing tracks such as this one. The scattered isolated hits are due to noise effects and mostly removed by pulse cleaning.

into the individual events that belong to the different subtriggers and are stored in separate P-frames (which hold all processing information and reconstructions, together with additional pulse cleaning). In about 15% of cases, the data read out in one of these P-frames contains more than one primary interaction. This pile-up effect is referred to as *coincident events*. It is a direct result of the traversal time of a couple of microseconds in the detector (the speed of light in vacuum is equal to ≈ 0.3 m/ns, meaning the particle travels around 100 m in $0.3 \mu\text{s}$, without accounting for the delayed photon propagation necessary for detection), the large flux of low-energetic events and the trigger time windows of a couple of microseconds. This can be problematic for reconstructions, as can be seen in Figure 7.7 where two downgoing muons can be reconstructed as an upgoing track. These events can be split when looking at, for example, geometric separation. How this is done is explained in more detail below.

There are two modules that try to clean events more thoroughly than pulse cleaning alone. The first is `TopologicalSplitter` (TS), which starts from the Q-frames and loops over pulses and splits the event into clusters of pulses that contain at least a number of causally* connected pulses within a certain time window. Some extra cleaning, similar to `seededRT` cleaning, is done in addition and can split coincident events that have overlapping readout windows, but are geometrically separated.

The second module, also used in this analysis, is called `IceHive`. A full description can be found in the doctoral thesis of M. Zoll [217]. The module consists of two main parts: one that splits events and handles coincident events, `HiveSplitter`, and another that has a refined pulse cleaning, `HiveCleaning`.

*The time between two DOM hits cannot be less than the time that light would have taken.

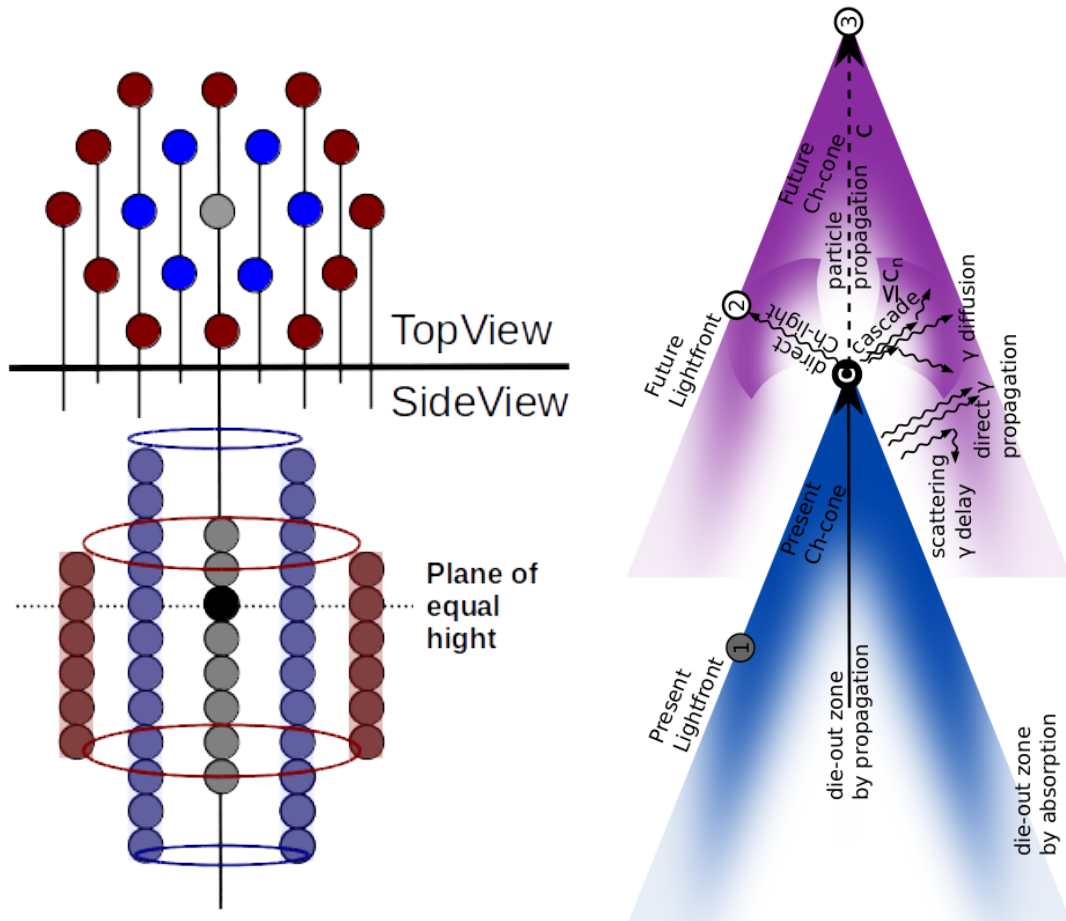


Figure 7.8: *Left:* The black circle illustrates a DOM that triggered a hit in the detector. The grey circles symbolize the DOMs along the string of the hit DOM. The number of DOMs that can be included in the active volume depends on the heights defined by the module. The blue/purple DOMs belong to the neighboring strings and the red/brown DOMs to the next-to-neighboring strings. The heights of both these sets of DOMs are also set by the module. This example shows $h_2 > h_1 > h_3$, where h_i is the height of the i -th string from the center. The heights are asymmetric in this example. *Right:* Illustration of Cherenkov emission profile of a traversing particle. Both figures from Ref. [217].

7.3.1 HiveSplitter

The module assumes that individual particles creates *clusters* of hits in the detector. A cluster can grow within a certain time window, but is separated from another cluster if it's not spatially connected. An initial cluster is formed if the multiplicity of hits exceeds a certain threshold (usually 3 or 4). The main difference in this module versus `TopologicalSplitter` is that it uses hexagons to describe the detector instead of assuming a spherical parameterization. It makes more sense to optimize the search volume, where hits are clustered together, with a shape that describes the detector well and uses a discrete spacing between larger volumes instead of a uniformly growing sphere. The hexagonal shape is set by defining three heights. The first height, h_1 , is defined along the string of the hit DOM and is equal to the vertical distance along the string. The second height, h_2 , is the vertical height along the neighboring strings. The third height, h_3 , is the vertical height along the next-to-neighboring strings. An example is shown in Figure 7.8 (*left*).

When the active region is set, there is an additional check to see if DOMs can be “connected”. `IceHive` assumes certain emission profiles (for both cascades and tracks) where light is produced. Three possible connections are assumed:

1. Hits occur at the same time, but at a spatial distance in agreement with the Cherenkov

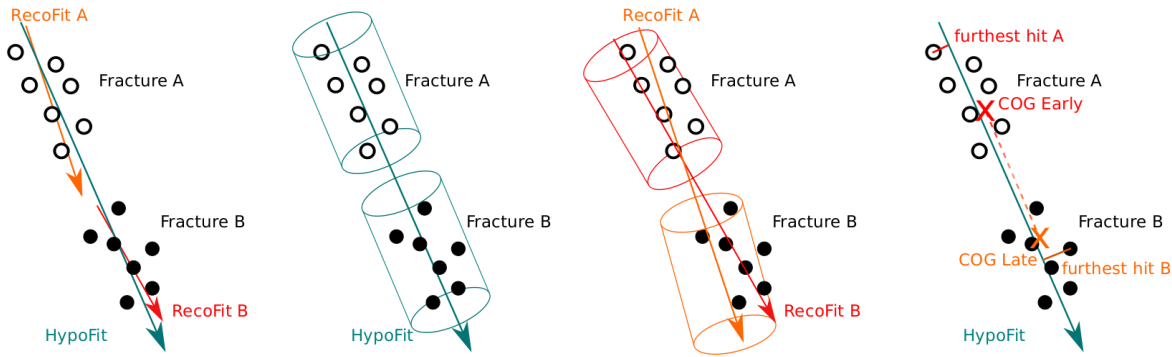


Figure 7.9: Schematic illustrations of possible recombination scenarios with the `CoincSuite` module. Two events are compared to each other or the combined event (HypoFit) in several different ways. Figure from Ref. [217].

emission profile (hits C&1 and 2&3 in Figure 7.8 (*right*)).

2. Hits occur at a different time and a different location, but in agreement with the Cherenkov emission profile (hits C&2 in Figure 7.8 (*right*)).
3. Hits on topologically identical sites of an emission pattern that has moved along with the propagation of the particle (hits C&3 and hits 1&2 on Figure 7.8 (*right*)).

These clusters are finally separated into different P-frames. Each P-frame is assumed to originate from a different primary particle.

7.3.2 HiveCleaning

Additionally, a similar cleaning as explained in Section 7.2 can be performed. Isolated hits that do not have neighboring hits occurring within a certain distance and time window, are removed. The main difference between this and `seededRT` cleaning is that the module again uses the hexagons as defined in the previous section.

7.3.3 Remark

The use of `IceHive` has a better performance in separating coincident events compared to `TopologicalSplitter` (see Ref. [217]), but often “over-performs” and splits clusters of hits that are originating from the same particle. This is predominantly the case for dim tracks that have large separations in between clusters (most of the triggered SMP events are of this type). To reduce this type of error, the module `CoincSuite` was designed, again by M. Zoll [217].

7.4 CoincSuite

Several testing algorithms allow to check if two or more split P-frames can originate from a single event. Five different scenarios were tested in this analysis, the first four are also chronologically shown in Figure 7.9:

1. Cluster alignment: the reconstructed direction of the individual clusters is compared to the direction of a reconstruction that uses the combined hits (HypoFit). The directions should be within a certain critical angle.
2. Cylinder cluster containment: the DOMs of the individual clusters should be able to be grouped together in a cylinder that has its center and direction along the HypoFit.
3. Cylinder cluster alignment: a cylinder around the reconstruction of each cluster is drawn. The cylinders should overlap within a certain fraction.
4. COG* connection: the COG of the second quarter of hits of the the first cluster and the

*Similar to COM (Center Of Mass), the COG is a weighted average position of the hit DOMs. DOMs that register more light get a higher weight.

COG of the third quarter of hits of the second cluster are computed. These COGs should lie close enough and have to be in the vicinity of the HypoFit.

5. Velocity test: tests if the velocity of the HypoFit is close to the speed of light.

The combination of `IceHive` (which does a very good job in cleaning events, but often overperforms and splits events that shouldn't be) and `CoincSuite` (which recombines events that were wrongfully split), leads to a very powerful tool to clean events.

7.5 Event cleaning and reconstructions: summary

The previous sections described how events can be cleaned and how several reconstruction algorithms work. In Chapter 5, we described how such an event is constructed. Several triggers read out series of hits in the IceCube detector within a time window to an event. A hit consists of a DOM pulse, the DOM location and a timestamp. One DOM can have multiple hits in an event.

Reconstruction algorithms try to reconstruct certain particle properties such as the direction, location and track length. Cleaning algorithms remove noise hits and split clusters of hits that originate from coincident events to separate events.

Aside from cleaning and reconstruction, which are done on single events, several analysis techniques are also used in this work. These algorithms look at large samples and try to classify events as signal- or background-like. Therefore, Monte Carlo samples of both signal and background samples are used. The first algorithm that is discussed below is “minimal-Redundancy-Maximum-Relevance”, which tries to filter out the most powerful variables from a large set of variables. Secondly, we discuss a machine learning technique called “Boosted Decision Trees”. Such an algorithm is trained with Monte Carlo samples to “learn” how to discriminate signal from background events and outputs a single-valued parameterization. This can then be applied to real data.

7.6 Minimal-Redundancy-Maximum-Relevance

Having multiple variables that are able to discriminate signal from background events is a necessary tool that ensures the ability to conclude statements on a certain theory or exotic phenomenon. Single variables can show promising results, but when multiple variables are highly correlated, much of the discriminative power diminishes. When using BDTs, analyzers often try to include variables and remove them if they show to be highly correlated in a trial-and-error fashion.

In this analysis, I made use of a technique that was originally developed for analyses in biological sciences but can be used for most analyses that involve “data mining”. Variables from a large sample set were selected with the condition of minimal-Redundancy-Maximal-Relevance (mRMR). To optimize the characterization of a certain class of events with a set of variables, these variables are selected with a *maximal relevance*. Here, “relevance” is characterized in terms of correlation of mutual information. Because combinations of individually good features do not necessarily lead to good classification performance, there is the additional requirement of *minimal redundancy*. The algorithm sorts variables according to their importance (defined as having a minimal redundancy and maximum relevance). More information about this algorithm can be found in Ref. [218].

In this analysis, mRMR was used to rank variables from a large set according to their importance and proved to lead to low correlated variables (as can be seen in the Appendix in Figure D.2).

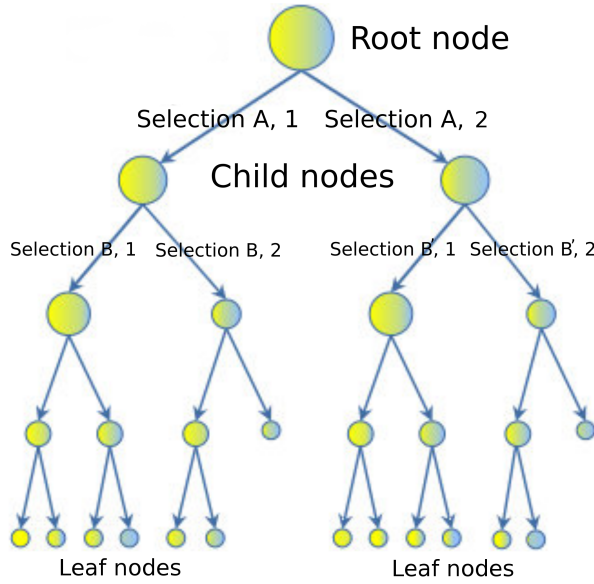


Figure 7.10: Illustration of decision tree scheme. Selection B and B' denote a selection on the same variable, but other requirement.

7.7 Boosted Decision Tree classifiers

Given a set of events that have a fixed set of variables constructed in an analysis, the question remains if the event is in fact a *signal* (dim track from an SMP) or *background* (e.g. a muon from ν_μ or air showers) event. One can rely on Monte Carlo simulations to get a handle on the variable distribution in both sets. The most general, and still widely used, method is to use a cut-and-count approach where a cut is placed on a certain variable that discards events that fail the requirement. A Boosted Decision Tree (BDT), however, inspects a set of variables by looking at large sample sets that are classified as either signal or background. The BDT is “trained” to classify an event to signal-like or background-like. This is done with a “BDT score” that ranges from -1 to 1. The higher the score, the more an event is regarded as signal-like. How this is done is given in more detail below. Boosted decision trees rely on multiple individual trees, collectively called a *forest*. Therefore, we will first explain how a single tree classification works.

7.7.1 Structure

The goal of a decision tree is to determine if an event is signal- or background-like. It uses a tree-like structure where certain selection criteria are used at different nodes as illustrated in Figure 7.10.

A decision tree is a binary tree that places an event into a certain node depending on the selection at a node. The depth of a decision tree can be arbitrarily long, but is determined by a set of criteria as defined in Section 7.7.2. An event consists of a certain set of variables $X = x_1, x_2, \dots, x_n$ that are used in the classification. Before any selection criteria, the event is said to be represented by the *root node*. A binary selection then determines to which *child node* the event should be classified, for example:

$$\begin{aligned} \text{Selection A} &= x_1 > y_1 \quad (\text{option 1}) \\ &= x_1 \leq y_1 \quad (\text{option 2}), \end{aligned} \tag{7.20}$$

where y_1 is the cut value for variable x_1 . Similarly, the other selections determine where the event is eventually placed. The last nodes are referred to as *leaf nodes* and hold the probabilities of whether an event is more signal- or background-like. These probabilities are translated into a score ranging between -1 (background) and +1 (signal).

7.7.2 Training

To construct a decision tree, one first has to “train” the algorithm on MC. Given a certain “signal set” and “background set”, all variables used in the BDT are histogrammed and at each bin for each variable the “best cut” is set at the first node selection. To determine the optimal cut, we first define the purity of a node, p , by

$$p = \frac{\sum_s w_s}{\sum_s w_s + \sum_b w_b}, \quad (7.21)$$

where w_s and w_b refer to the weights of the signal and background events*. The Gini index, g ,

$$g(p) = p(1 - p), \quad (7.22)$$

is used as a separation variable in this work[†]. Using the Gini index, the separation gain determines the effectiveness of the cut

$$\Delta S = g_p \cdot \sum w_p - \left(g_l \cdot \sum w_l + g_r \cdot \sum w_r \right), \quad (7.23)$$

where g_p and w_p denote the Gini index and weights of the parent nodes and similarly for the left and right child nodes. The cut that gives the highest separation gain is subsequently selected. The algorithm stops when one of the following criteria is met:

- a node only consists of signal or background events;
- a certain predefined maximal depth is reached;
- splitting would cause a child node to have less than a predefined minimal amount of events left;

and therefore determines the size of a tree. These selection criteria are necessary to avoid overtraining (see Section 7.7.4). An example of a very simple decision tree is given in Appendix B.

7.7.3 Boosting

As already implied in the text above, a BDT consists of a *forest* of decision trees. A user specified number of individual decision trees are trained sequentially, with a boosting process in between each training. Boosting consists of adjusting the weights of individual events according to whether the previously trained tree classifies them correctly. In this work, the AdaBoost[‡] algorithm was used for boosting in which the score of an event is a weighted average of the scores the event receives from each tree in the forest [219].

A BDT stands for “boosted decision tree”, but it must be understood that there are actually many trees (typically hundreds), and that boosting is a process that occurs between the training of consecutive trees. The approach makes use of the power of numbers: many weak single decision trees combined can be more powerful than one very good decision tree. In general, boosting follows the following steps:

1. Train a weak model on training data.
2. Compute the error of the model on each training example.
3. Give higher importance to examples on which the model made mistakes.
4. Re-train the model using “importance weighted” training examples.
5. Go back to step 2.

A simple example of a BDT is given in Appendix B.

We define a function to indicate whether an event is classified incorrectly: $I(s, y) = 0$ if $s = y$ and 1 otherwise. The error rate for a tree is then equal to

*These are the weights after scaling events to a certain spectrum.

[†]Other possible separation variables include the cross entropy $-p \cdot \ln(p) - (1-p) \cdot \ln(1-p)$ or the misclassification error $1 - \max(p, 1-p)$.

[‡]Short for Adaptive Boosting.

$$\epsilon = \frac{\sum_i w_i I(s, y)}{\sum_i w_i}. \quad (7.24)$$

The boosting factor for the tree is defined as

$$\alpha = \beta \cdot \ln \left(\frac{1 - \epsilon}{\epsilon} \right), \quad (7.25)$$

with β a user defined *boosting beta* and changes the weight of the tree to

$$\begin{aligned} w' &= w \cdot \exp(\alpha), & w' &= w \cdot \exp(-\alpha) \\ (\text{correct classification}) && (\text{incorrect classification}), \end{aligned} \quad (7.26)$$

after which the weights are renormalized so that $\sum w' = 1$. The process is repeated until the number of predefined trees is reached.

Due to its definition, the boost factor α will give good classifiers (which have low error rates) large boost values. Events that are misclassified are then given larger weights, making the algorithm more likely to classify them correctly in the subsequent tree classifier.

Once the entire BDT is trained, the events can be given a score based on the multiple tree classifiers. This is done by taking the weighted average of all the scores in the individual tree classifiers, using its boost factor α as the weight of the tree. The score of an event i is then given by

$$s_i = \frac{\sum_m \alpha_m \cdot s_{i,m}}{\sum \alpha_m}, \quad (7.27)$$

where we loop over the individual trees denoted with index m .

7.7.4 Overtraining

BDTs are very powerful tools, but if not used correctly, could lead to problems that are not easy to spot at first sight. Assume we train our BDT with a certain signal set and background set. If the BDT is trained up to the point of classifying statistical fluctuations, there is said to be *training sample overtraining*. An illustrative example is given in Figure 7.11. Another example is data/MC overtraining. The former can be dealt with with the use of *pruning*, while the latter should show clear data/MC disagreement, which is checked in the analysis.

7.7.4.1 Pruning

The problem with overtraining is essentially that there are certain splits in a classifier tree that are too specific and less important. In the method of *cost complexity pruning*, for each node the complexity is calculated as

$$\rho = \frac{\Delta S}{n_{\text{leaves}} - 1}, \quad (7.28)$$

with ΔS the separation gain as defined in Eq. 7.23 and n_{leaves} the number of leaves below the split node. The subtree of the node with the smallest value of ρ is removed and this is done repeatedly until a desired *pruning strength** is reached.

*A parameter on a scale from 0 to 100, which specifies the percentage of the pruning sequence to actually execute. 0 means no pruning is done and 100 signifies only a single root node remaining.

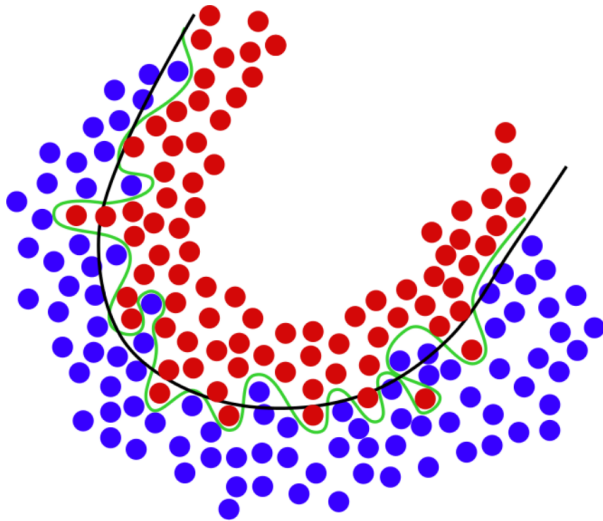


Figure 7.11: Example of overtraining. In black, the theoretical line between background (blue points) and signal (red points) is given. An overtrained BDT will have a (perfect) selection such as the green line. Illustration from [220].

7.7.4.2 Additional checks

BDTs are always trained and tested with different subsets of the same type (background or signal) of event. If the training set has significantly different scores than the testing set, the sample is most probably overtrained and one has to change the BDT input parameters. Additional to pruning, one typically uses Kolmogorov-Smirnov testing to indicate if the BDT score distributions from the training and testing sets could follow the same distribution pattern. Therefore, a p -value equal to the statistical probability that two samples are drawn from the same distribution is computed. Because training and testing samples will never be identical, there will always be some level of overtraining. As a rule of thumb, a $p_{KS} \lesssim 0.01$ indicates overtraining beyond the level of comfort. Appendix D shows the result of such checks.



8. The SPACE Analysis

A little learning is a dangerous thing; Drink deep, or taste not the Pierian Spring
~ Alexander Pope

The first chapters in this work served as an introduction to the theoretical physics models that were necessary to explain the signature of the particles under investigation and gave more details on the background contributions. Later chapters were used to explain the general workings of the detector and describe several reconstruction and analysis techniques. In this chapter, we focus on how the analysis was set up and present the results and conclusions that can be drawn. Starting from data that was processed with basic reconstructions and passed general requirements, a workflow was set up to try to discriminate events that are most likely of known physical interactions from the rare events that are sought for in this analysis: hypothetical particles with an anomalous charge (introduced in Chapter 2).

These particles are assumed to have a long lifetime and an isotropic flux close to the detector. Due to their low charge, they will produce less Cherenkov radiation compared to muons when traveling through ice, resulting in dim tracks in the IceCube detector. The most significant background contributions are from muons that originate either from air showers or ν_μ . Most of the events that pass the trigger selections in the detector originate from downgoing muons that were produced in air showers. Therefore, it was chosen to focus on upgoing tracks, which reduces the air shower background with many orders of magnitude. Even though the tracks that are reconstructed as downgoing are removed, most of the tracks that are reconstructed as upgoing still originate from mis-reconstructed downgoing muons from air shower. Only a small fraction of these muons is mis-reconstructed, but is still the largest background due to the enormous amount of air shower events. The other most prominent background consists of muons from atmospheric ν_μ that are capable of traversing Earth and produce upgoing muon tracks. Because the detector consists of sparsely distributed optical modules in the ice, these tracks can appear dim and resemble the signature of particles with a low charge. Additionally, due to the low number of DOMs that will be hit in such a dim event, noise hits have to be accounted for. Therefore, multiple variables in the analysis require a minimal amount of hits and events with a very low number of hits are removed. Also, these events often lead to data-MC disagreement due to the large noise contribution and a lack of information that is necessary in reconstruction algorithms.

The analysis consists of a number of quality cuts (where events that cannot be distinguished

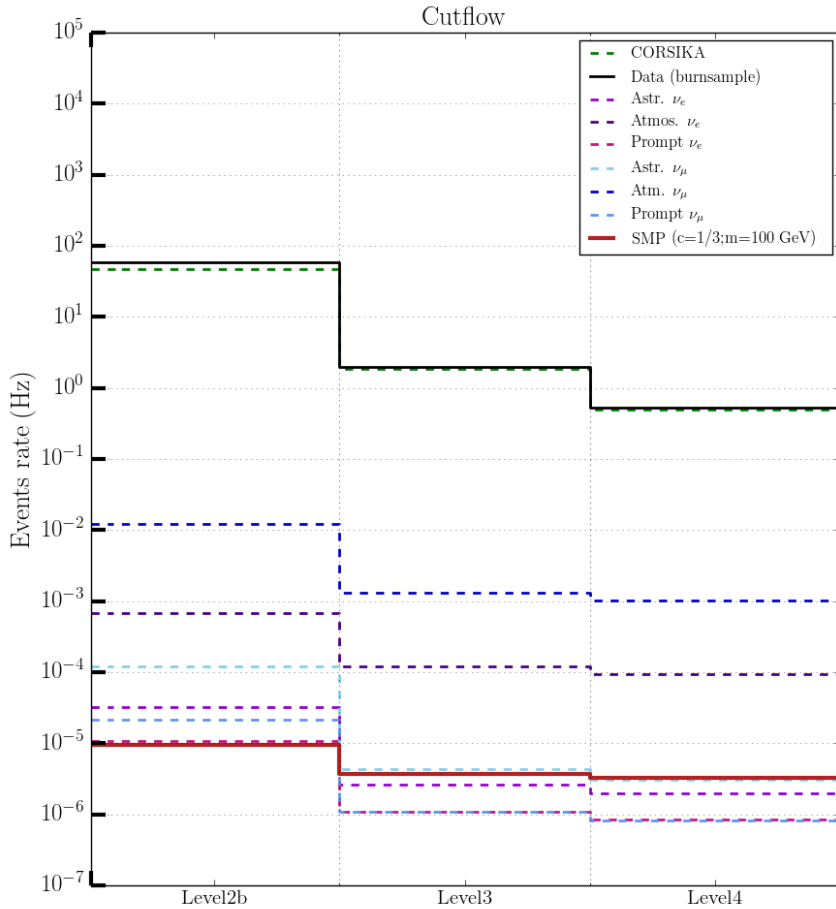


Figure 8.1: Event rate at three steps in the analysis. Data from the burn sample is shown in black, several Monte Carlo background samples are shown with dashed lines and the solid red line corresponds to one signal sample of an SMP with charge 1/3 and mass 100 GeV. “CORSIKA” corresponds to events from air shower simulations.

between signal and background are removed), variable constructions and some additional analysis techniques. The workflow of this analysis is described step-by-step in the contents of this chapter. The analysis is subdivided into several “Levels”. Figure 8.1 shows the rate of several Monte Carlo backgrounds, the burn sample, and a signal sample in function of Levels 2b, Level 3 and Level 4.

The analysis was named the “SPACE” analysis, which stands for a “Search for Particle with Anomalous ChargE”.

8.1 Filter selection

As explained in Section 5.4.2, IceCube data is processed through multiple filters. Since this analysis is the first of its kind in the collaboration, the choice was to start from scratch and not use a processed dataset from another analysis*. Therefore, a combination of filters was chosen that is able to distinguish signal events from background as best as possible at this preliminary stage. An illustration of filter combination efficiency is given in Figure 8.2. The efficiency is defined as the percentage of simulated particles that pass a certain filter. The figure shows many

*Since many searches look for similar signatures or deal with similar backgrounds, processed data sets in the collaboration are often used for multiple analyses.

possible filter combinations and are ranked in function signal efficiency. The efficiency of the filter combination should be as high as possible for the signal, and as low as possible for background events. Therefore, the combination of four filters was chosen. This filter selection will be referred to as *Level 2b* as an addition to filter processing in Level 2 (see Section 6.5). The filters that were included in this stage are the VEF, LowUp, Online Muon L2, and DeepCore filters. They are explained in more detail below.

8.1.1 VEF

The Vertical Event Filter (VEF) is originally designed for oscillation and Earth WIMP analyses and makes use of the string trigger (see Section 5.4.1). An SMP that travels in a direction following a string, or close by, can trigger optical modules even though the total light yield of an event is low (other trigger hits are unlikely in this scenario), making this filter an ideal part of the filters that are selected. The filter ignores HLC hits in the top 5 DOM layers to reduce the muonic component from air shower events and other selection cuts try to further refine the search region, in particular for WIMP events (see Section 5.8.2). For example, the LineFit zenith angle should be higher than 166.2° , focussing on upgoing tracks. More information can be found in Ref. [221].

8.1.2 LowUp

The primary motive for the LowUp filter design is again focussed on WIMP searches, but is also used in atmospheric neutrino analyses. It is set up to capture upgoing muons with an energy below 1 TeV. The majority of the events that are selected by this filter make use of the in-ice Volume Trigger, but also the in-ice SMT8, in-ice String and SMT3-DeepCore triggers are used for completeness (see Table 5.1). The selection cuts are loose selections required to look for upgoing track-like particles. For example, the zenith angle of the reconstructed particle should be 80° or higher and the difference between the maximal z -coordinate and minimal z -coordinate of hit DOMs should be less than or equal to 600 m. More information can be found in Ref. [222].

8.1.3 Online Muon L2

The Online Muon L2 filter is a subset of the Muon Filter (see Ref. [223]) and tries to select the most interesting muon-like events while reducing the rate of the filter from around 30 Hz to 5 Hz, reducing the data stream by a factor of 6. Historically, this subset of the data was processed offline from the Muon Filter, but after realizing that this could be done online and because many analyses made use of this selection, it was chosen to implement it as a separate filter. The filter tries to select both upgoing and downgoing muons, with different selection cuts depending on the zenith angle of the particle reconstruction. The four selection ranges are defined as:

- $180^\circ \geq \theta_{\text{MPE}} \geq 115^\circ$ (upgoing)
- $115^\circ > \theta_{\text{MPE}} \geq 82^\circ$ (upgoing)
- $82^\circ > \theta_{\text{MPE}} \geq 66^\circ$ (downgoing)
- $66^\circ > \theta_{\text{MPE}} \geq 0^\circ$ (downgoing)

where the particle reconstruction was done with MPE (Section 7.1.3), which was feasible if it only had to be done on the events passing the Muon Filter. The first two regions have an efficiency* higher than 99%. The downgoing region requires additional cuts to remove the less interesting muons from air showers. The main variables used are the number of hit DOMs, likelihood parameters, number of PEs, etc. More information can be found in Ref. [224].

8.1.4 DeepCore

A DeepCore specialized filter was added to account for SMP tracks that traverse the more densely instrumented DC detector. Due to the low amount of light produced by these dim tracks, adding the DeepCore filter (which is optimized for the DC instrumented volume) proved to be of significant importance.

*Here defined as having a reconstruction within 3° of the MC truth.

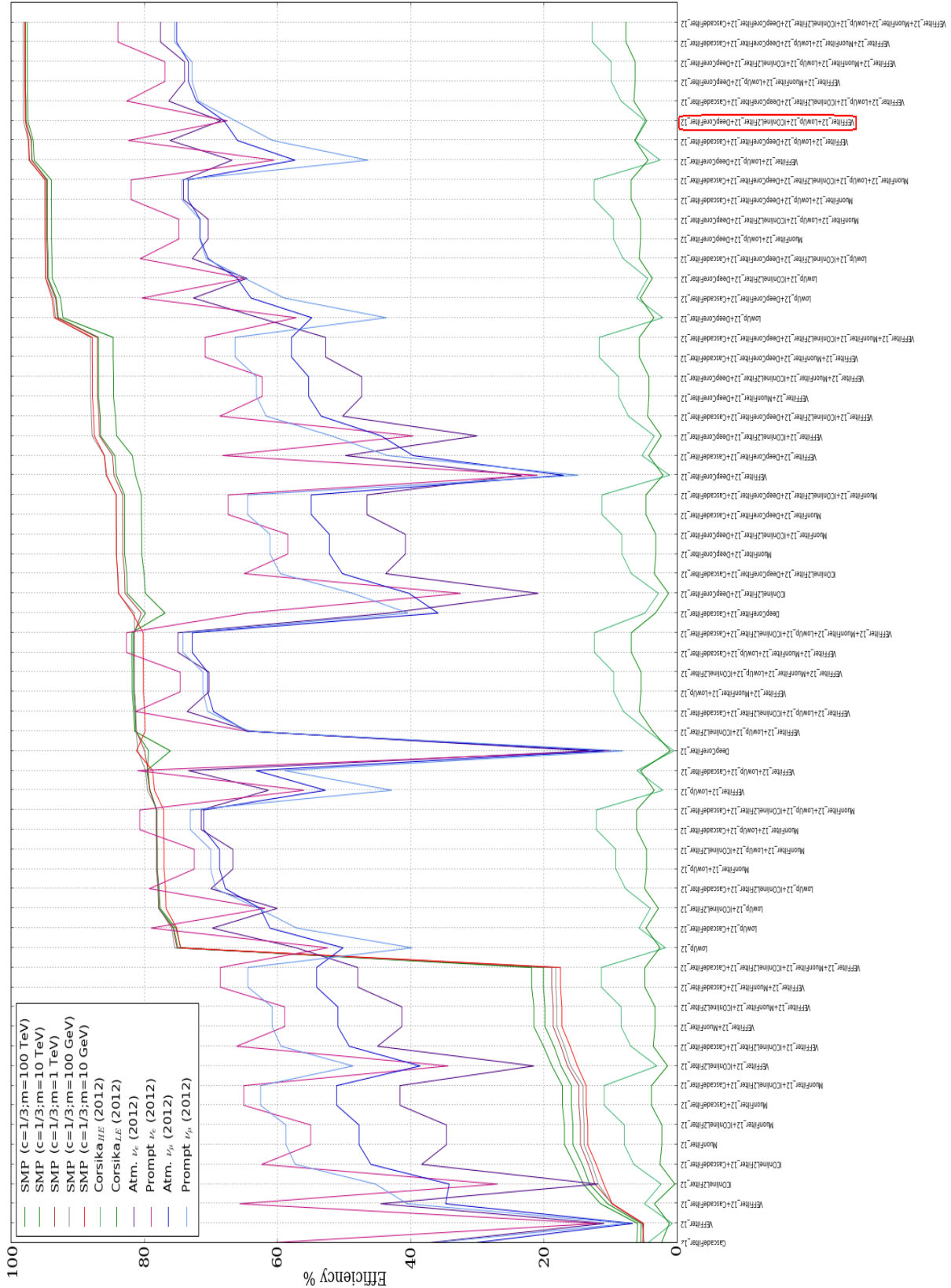


Figure 8.2: Illustration of the efficiencies of several filters and their possible combinations. The x -axis was determined by starting with filter selections that had a low efficiency in signal selection and ranges from low to high signal performance. Five signal points for a fixed charge and different mass show similar results. SMPs with charges $1/2$ and $2/3$ show similar results but are left out for a better visualization. An upgoing signal sample was used to determine the signal efficiency. The chosen filter combination is shown in red.

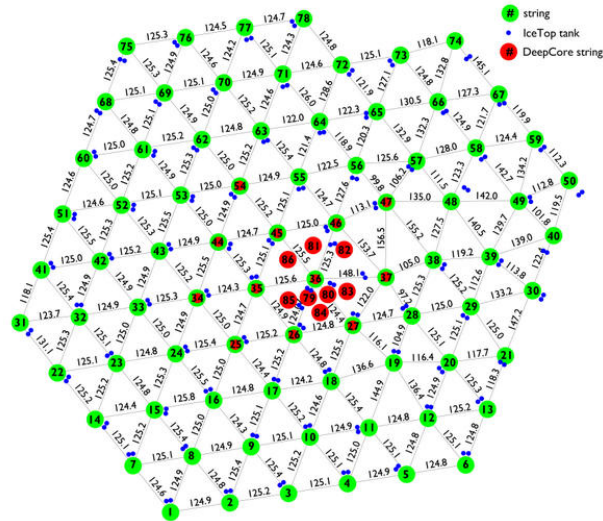


Figure 8.3: Top view of the IceCube strings (and IceTop tanks) where the DeepCore fiducial volume is defined by the DeepCore strings (red) and several surrounding in-ice IceCube strings (green and red).

The DeepCore filter was designed to look for very dim events coming from dark matter, low-energy neutrino oscillations, and for studies that are dedicated to observe atmospheric neutrinos below 100 GeV. The fiducial volume used for this filter consists of

- the bottom 22 DOMs on the IceCube strings 25, 26, 27, 34, 35, 36, 37, 44, 45, 46, 47 and 54;
 - the bottom 50 DOMs on the DeepCore strings 79-86.

These strings are indicated in Figure 8.3.

The filter uses the DeepCore SMT3 trigger and additionally, two layers are used as a veto to remove events that probably originate from atmospheric muons. This is done by comparing the position and timing of all hits to the position and timing of several COGs that are constructed from these hits (see footnote pg. 112 for the explanation of a COG). More information can be found in Ref. [225].

8.1.5 Burn sample checks

Before further processing, the burn sample (a subset of the data that is used to check if the Monte Carlo adequately describes the data) is compared over the different years that are used in the analysis. This is shown in Figure 8.4. The sine wave pattern from seasonal variations in the atmosphere (see Section 6.2.1.1) is clearly visible and consistent over the years. The x -axis is more spread out in the first years due to the larger amount of test runs. The shift in data rate in early 2011 runs is caused by a DOM software change that was introduced in the Summer of 2011 [226]. This phenomenon is well understood and since the changes are minimal, these runs are kept. More information on the burn sample can be found in Section 6.6.

8.2 Level 3

The combined filter selection leads to a total rate of \sim 60 Hz, or an expected 1.9 billion events per year of livetime. The average event size at Level 2 is around 15 kB, which would result into around 30 TB of data per year of livetime.

Therefore, five quality cuts are implemented with a goal that is threefold:

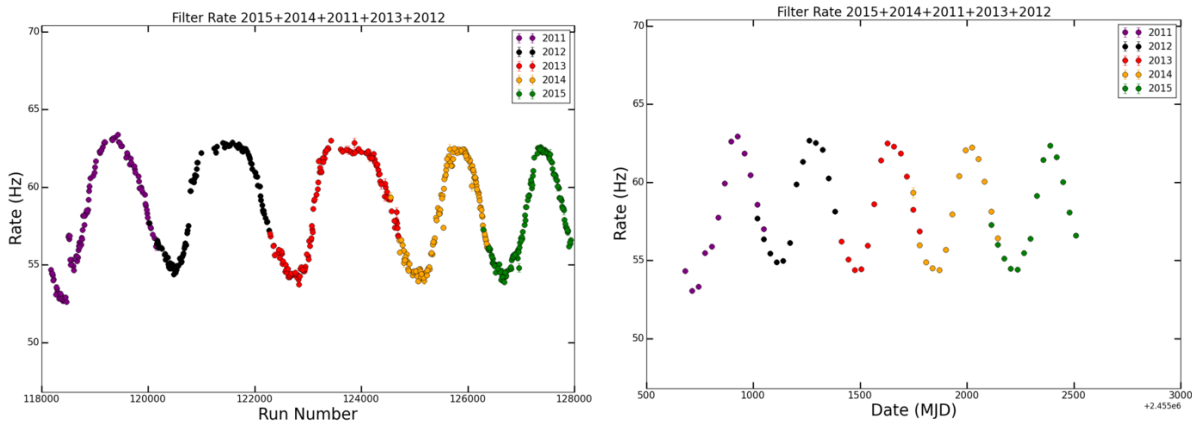


Figure 8.4: *Left:* Total rate of the combined filters as a function of the run number. *Right:* Total filter rate averaged per month. There is an overlap for each year because a new season does not necessarily start at the beginning of a month.

1. Reduce the data rate,
2. Improve the signal to background ratio, increasing the selection purity,
3. Improve the agreement between data and Monte Carlo (as can be seen in Figure 8.1).

These cuts are shown in Figures 8.5 to 8.9 and explained below.

8.2.1 The zenith angle cut

Even though there are no upgoing muons from air showers expected, the vast majority of events that pass the filter selections still originate from muons that are mis-reconstructed. Even though there is only a small chance of these events to have a reconstructed zenith angle with a large offset from the true angle, the expected flux of air showers is so much larger compared to the assumed signal flux that it still dominates by orders of magnitude. Therefore, a zenith angle cut was set at an angle of

$$\theta_{\text{zen}}(\text{MPE}) \geq 85^\circ, \quad (8.1)$$

where the cut is slightly relaxed to include events coming from the horizon. Muons passing through kilometers of air and ice have a much lower chance of reaching the detector.

The zenith angle distribution of the MPE reconstruction can be seen in Figure 8.5. Several background samples are shown in filled histograms. These samples are stacked together, where the largest samples are added last. The total rate of these Monte Carlo data samples corresponds to the top of these stacked histograms. Events from air showers are referred to as “Corsika” in the figures. The total statistical uncertainty of the background is indicated with a hatched grey color band. The burn sample is shown with black data points. The error bars correspond to the statistical uncertainty. The simulated signal samples are illustrated with a solid line.

Signal and background Monte Carlo samples are normalized to the livetime of the burn sample.

The upwards trend to higher zenith angles of several samples is due to the filter selections that depend on the angle.

8.2.2 The rlogL cut

The reduced log-likelihood, rlogL, of the track reconstruction fit is used as a goodness-of-fit variable. The term “reduced” is used because the logarithm of the likelihood is normalized by the number of degrees of freedom (NDOF) in the track fit

$$\text{rlogL} = \frac{\log \mathcal{L}}{\text{NDOF}} = \frac{\log \mathcal{L}}{\text{NCh} - \text{NPara}}, \quad (8.2)$$

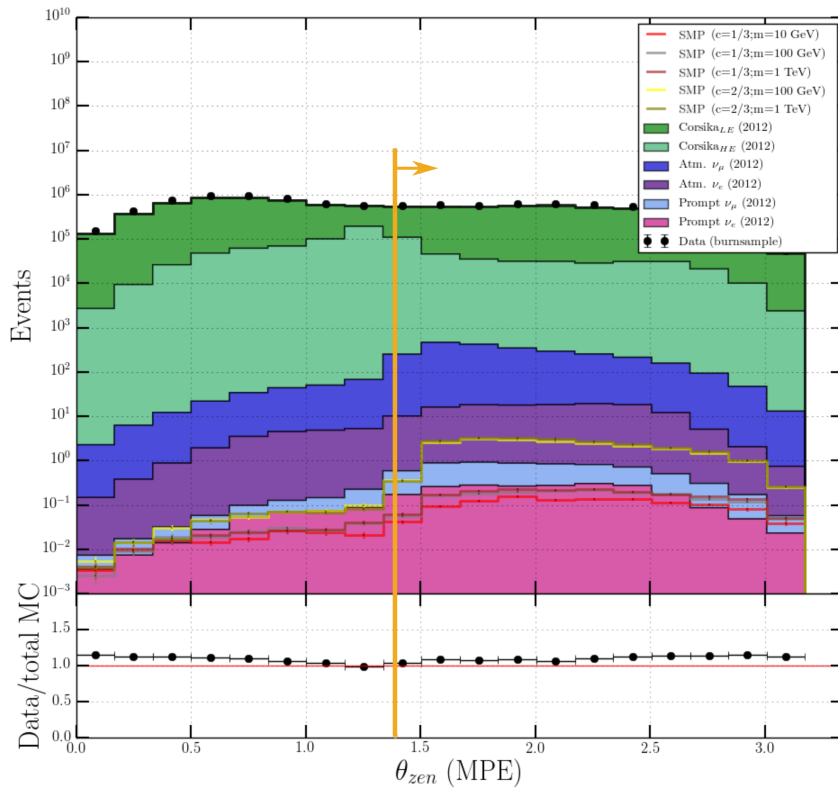


Figure 8.5: Number of events as a function of the MPE reconstructed zenith angle and normalized to the burn sample. The cut is illustrated with an orange line, the arrow points towards the events that are kept.

where NCh is the number of channels/DOMs and NPara the number of fitted parameters (3 for the position and 2 for the track direction). For Gaussian probability distributions this expression corresponds to the reduced chi-square. Lower values indicate better reconstructions*, therefore the rlogL cut was set at a value of

$$\text{rlogL} < 15. \quad (8.3)$$

The rlogL distribution can be seen in Figure 8.6. Data and Monte Carlo disagree at larger values due to non-perfect simulations. Events that lead to bad reconstructions are not, or not well, simulated and are removed with this cut.

8.2.3 The NPE cut

The total number of photoelectrons seen in the detector for an event is correlated to the number of photons that were emitted from the track. The Frank-Tamm formula in Eq. 4.7 shows that particles with a charge < 1 will produce less Cherenkov light. Therefore a cut on the total number of photoelectrons was set at a value of

$$\text{NPE} < 50. \quad (8.4)$$

The NPE distribution can be seen in Figure 8.7. Signal samples with a lower charge clearly show NPE distributions that peak at lower values, as expected.

8.2.4 The starting rlogL cut

The relative probability for tracks to be starting and/or stopping can be estimated with the `FiniteReco` module (see Section 7.1.6). Because many low-energetic muons would be starting and/or stopping in the detector, these likelihoods prove to be a powerful tool in removing these

*Here, the $-\log \mathcal{L}$ is used.

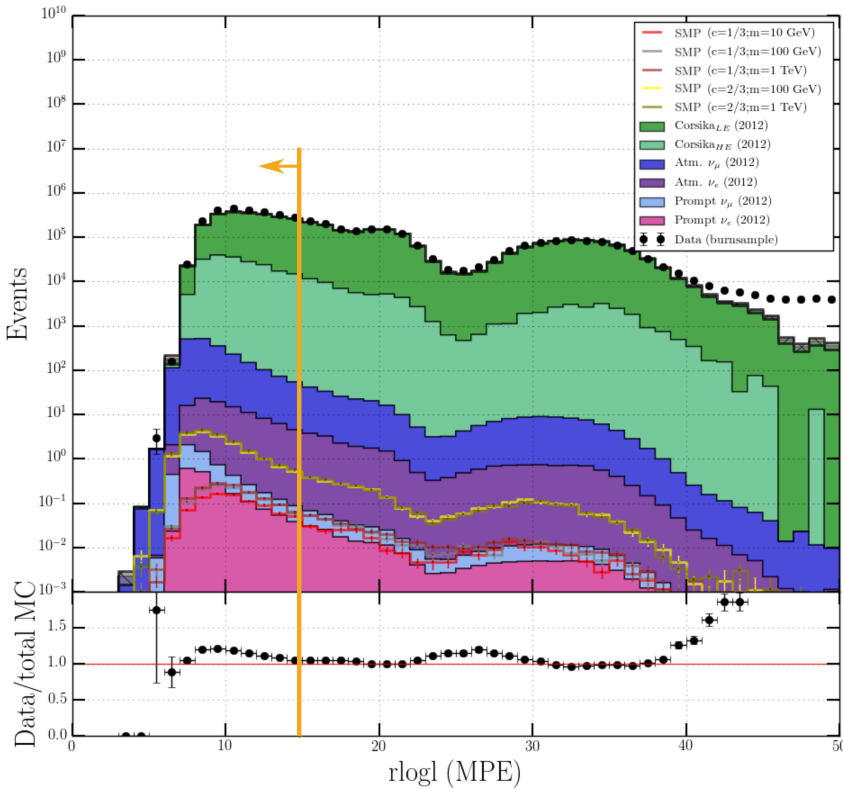


Figure 8.6: Number of events as a function of $r\log L$ normalized to the burn sample. The cut is illustrated with an orange line, the arrow points towards the events that are kept.

events. High-energetic muons will have a higher chance of being throughgoing, but would produce much more light than the dim tracks that are expected for the SMPs. These are mostly removed with the NPE cut.

The likelihood is always compared to the likelihood of throughgoing tracks, hence the “relative probability”. It was chosen to place the starting relative $\log L$ at a value of

$$\text{rel_logL(starting)} = \log L(\text{starting}) - \log L(\text{throughgoing}) > 0. \quad (8.5)$$

The starting $r\log L$ distribution can be seen in Figure 8.8. Because the log-likelihoods are negative, positive numbers indicate larger probabilities for throughgoing tracks. We can see that there is a large contribution of starting tracks in the background due to the filter requirements and previous cuts that focus on dim tracks.

8.2.5 The stopping rlogL cut

Analogous to the previous cut, it was chosen to place the stopping relative $\log L$ at a value of

$$\text{rel_logL(stopping)} = \log L(\text{stopping}) - \log L(\text{throughgoing}) > 10. \quad (8.6)$$

The stopping $r\log L$ distribution can be seen in Figure 8.9. Because the log-likelihoods are negative, positive numbers indicate larger probabilities for throughgoing tracks. We can see that there is a large contribution of stopping tracks in the background due to the filter requirements and previous cuts that focus on dim tracks.

8.3 Level 4

As can be seen in Figure 8.9, most of the background at this point in the analysis still originates from air showers. However, due to the Level 3 quality cuts, the total rate was reduced from around ~ 60 Hz to ~ 2 Hz (as can be seen in Figure 8.1), low enough for more elaborate variables to be computed and more aggressive cleaning. In Level 4, the IceHive splitting and cleaning

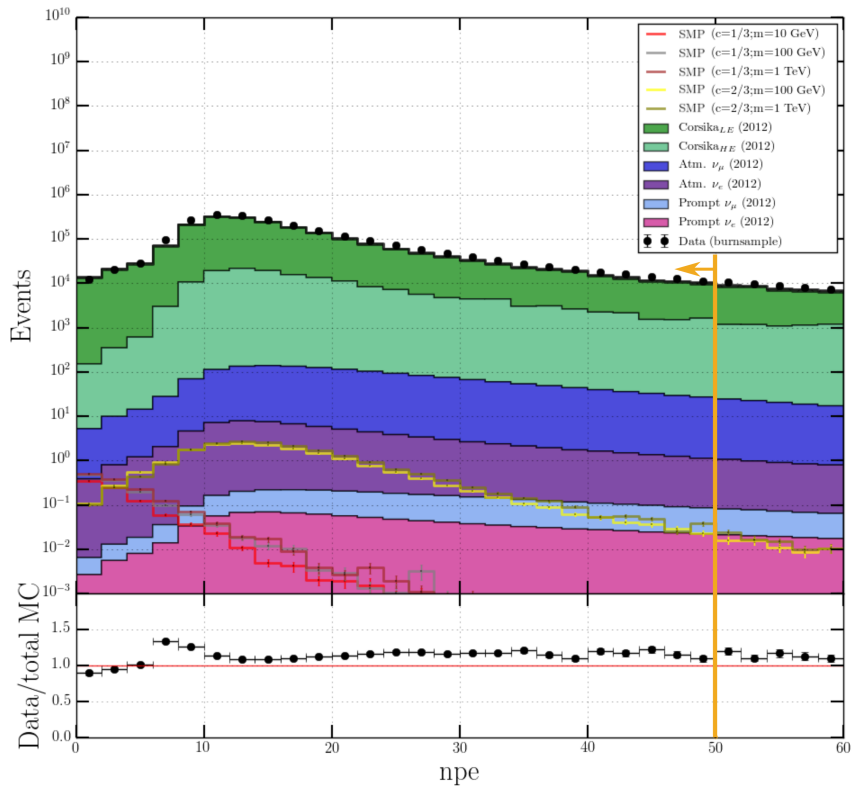


Figure 8.7: Number of events as a function of number of photoelectrons (NPE) seen in the detector. The cut is illustrated with an orange line, the arrow points towards the events that are kept.

Table 8.1: Overview of quality cuts in Level 4.

Variable	Definition	Cut	Motivation
nCh	Number of hit DOMs	≥ 5	Allows for better reconstructions
nStr	Number of hit strings	≥ 2	Allows for better reconstructions
nStr_in	The number of hit inner strings. An inner string is not located at the edge of the detector	≥ 1	Reduce leak-in events
Fitstatus MPE	Status of MPE reconstruction	Status == 'OK'	Remove bad reconstructions
θ_{HC} (MPE)	Zenith angle cut on HiveCleaned pulses	$\geq 85^\circ$	Similar to cut explained in Section 8.2.1: focus on upgoing tracks
Innerstring domination	See text inline	== True	See text inline

tools (see Section 7.3) were implemented and particle reconstructions on these “new” events were run again. Additional quality cuts were added to this level to ensure higher quality events. An overview is given in Table 8.1. Finally, new variables were constructed that will be used in Level 5.

8.3.1 Cleaning and quality cuts

IceHive provides a thorough cleaning method, sometimes resulting in events with a very low amount of hit DOMs. However, a minimal amount of hits is required to have reasonable and trustworthy particle reconstructions. Similarly, more than one string should have a hit to allow for better reconstructions due to the sparse distribution of the strings in the detector. Therefore, there are requirements on the minimum amount of DOMs and strings that should be hit as can be seen in Table 8.1. Because light is able to reach the edge of the detector even if the closest approach of very bright events is tens or hundreds of meters away, it would be near impossible to distinguish bright events far from the detector from dim tracks passing closeby. Therefore, it was required that at least one string that is not on the edge of the detector should have hit DOMs to reduce these *leak-in events*. The zenith angle cut is re-introduced on the new event that should have better reconstructions due to cleaning and finally, there is a requirement for “innerstring domination”.

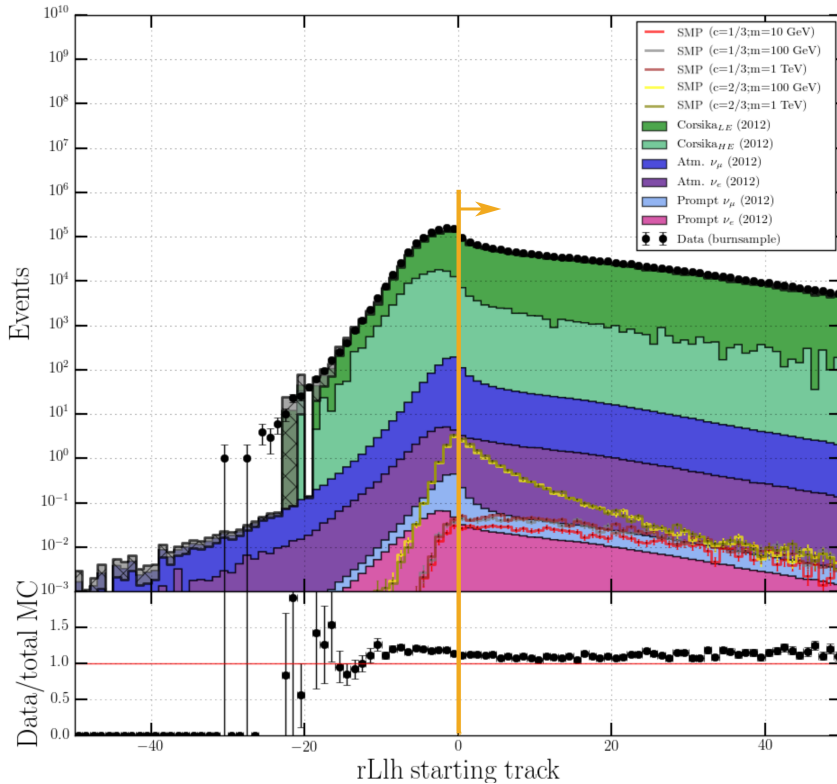


Figure 8.8: Number of events as a function of the starting likelihood. The cut is illustrated with an orange line, the arrow points towards the events that are kept.

Innerstring domination

Several types of events at the boundary of the detector can be a problem for an upgoing track analysis. This includes event classes such as:

- (Leak-in) Events from particles that are heading towards the instrumented volume, but stop right before they reach it or pass close by the detector. These “leak” light to the detector boundaries.
- (Boundary) Events from particles that partially penetrate the detector on the boundary lines and possibly have a cascade at the endpoint. These events have rather cascade-like characteristics.
- (Corner-clippers) Events from particles that are throughgoing on the corners of the detector and therefore have a COG at a corner of the detector*.
- (Leak-out) Events originating from a neutrino that passes through almost the entire length of the detector and only has an interaction vertex right before leaving the detector. Depending on position and angle, the reverse direction of reconstruction can be of similar probability and thus a nuisance.

All these event classes have a high uncertainty in the reconstruction or even fail the reconstruction completely. Most of these events are removed with the requirement of an “innerstring domination”.

DOMs are defined as outer DOMs if they are one of the following:

- part of a string on the edge of the detector,
- on the bottom of strings 1-78,
- on the top of strings 1-78.

The innerstring domination is set to `True` when

$$\frac{\#\text{outer DOMs}}{\#\text{inner DOMs}} < 0.5, \quad (8.7)$$

*Two coincident corner-clippers could be a large nuisance in this analysis.

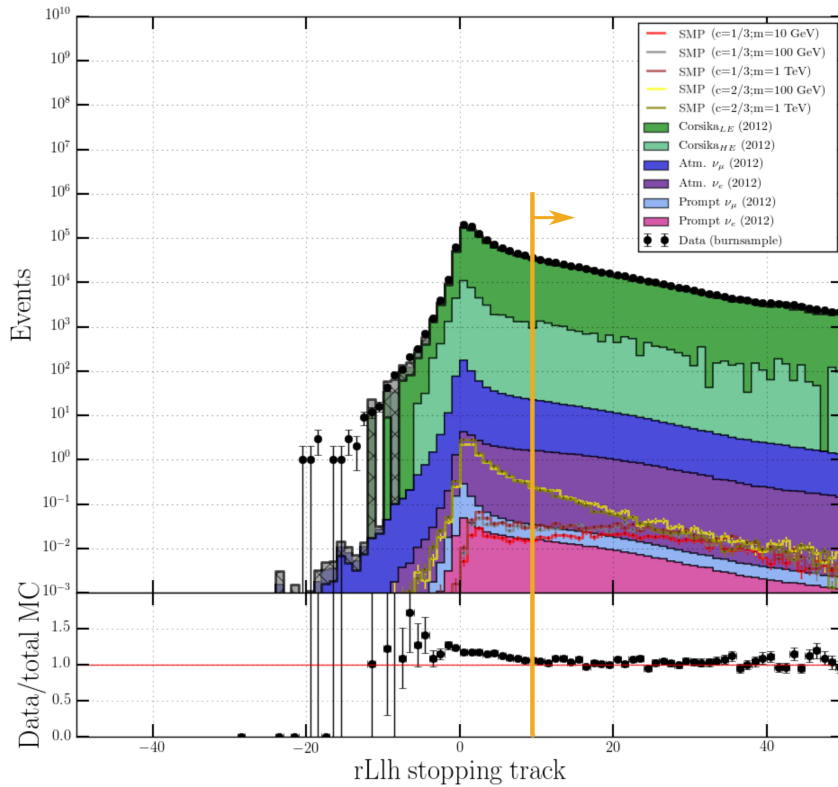


Figure 8.9: Number of events as a function of the stopping likelihood. The cut is illustrated with an orange line, the arrow points towards the events that are kept.

and set to `False` otherwise.

8.3.2 Variable construction

To distinguish signal from background events, variables that show a clear difference in their distribution have the most discriminative power. Therefore, in this part of the analysis, several new variables are introduced with this goal. Some variables used in Level 5 are already explained in Chapter 7 and are briefly mentioned in Section 8.3.2.4. A summary of all the variables that are constructed in Level 4 is given in Table 8.4.

8.3.2.1 Commonvariables

Many analyses in the collaboration characterize certain parameters of an event in a similar fashion. However, some of these parameters were constructed slightly different, making them a cause of errors*. Multiple variables were therefore combined into one project, called “Commonvariables”. The variables used here can be subdivided into three categories: track characteristics, hit statistics, and time characteristics and are summarized and explained in Table 8.2. Their distributions are shown in Figures. 8.10 to 8.17.

Because DeepCore (DC) and IceCube (IC) DOMs have different quantum efficiencies (see Section 5.1.2), the pulses from DC and IC DOMs should not be mixed for an unambiguous definition. Therefore either only DC or IC pulses are used to compute these variables depending if an event is *IC dominated* or *DC dominated*, where the former is set at $\frac{\#DOMs_{IC}}{\#DOMs_{DC}} \geq 0.5$ and the latter otherwise.

The variables used in this analysis are listed below.

*For example: how is the length of a track defined? Is it the distance between the two furthest hits? Or the length between the first and the last hit? Or is it the distance between two COGs?

Table 8.2: List of Commonvariables used in this analysis.

Category	Variable	Description
Track Characteristics [†]	AvgDistToDom	The average distance of the DOMs to the reconstructed track, weighted by the total charge of each DOM.
	EmptyHits	The maximal track length along the reconstructed track that got no hits within a cylinder around the track.
	TrackSeparation/COG Separation	Distance how far the COG positions of the first and the last quartile of the hits are separated from each other.
	TrackDistribution	The track hits distribution smoothness value [-1;1] shows how smooth the hits of the given pulse series within the specified track cylinder radius are distributed along the track.
Hit Statistics	ZTravel	ZTravel is the average difference of the z value of all hit DOMs with the first (in time) quartile z value.
	ZMax	The maximum z coordinate of all hit DOMs.
Time Characteristics	ZPattern	All first pulses per DOM are ordered in time. If a DOM position of a pulse is higher than the previous pulse's DOM position, ZPattern is increased with +1. If the DOM position is located lower in the detector, ZPattern decreases with -1. In general, this variable gives a tendency of the direction of a track.

[†] Whenever one of the track characteristics variables is shown/mentioned, the suffix (e.g. “_50”) refers to the track cylinder radius (in m) that was used around the track.

AvgDistToDom

Large values indicate bright tracks or events with many noise hits far away from the reconstructed track (seed track). Therefore, signal events peak at lower values than the backgrounds. This is shown in Figure 8.10.

EmptyHits

Large values indicate that the track is sparse, with two or more clusters of hits that are far away from each other. Background events are not expected to produce long tracks with large parts of missing hits and therefore have much larger contribution at lower values. This is shown in Figure 8.11.

COG Separation

The distance between the COG of the first and last quartile of hits is expected to be large for throughgoing tracks. Therefore, signal events should have a larger contribution at higher values. Background events are not expected to have large COG separations. This is shown in Figures 8.12 and 8.13.

TrackDistribution

The smoothness of a track is rather difficult to be parameterized. The *TrackDistribution* variable was developed and first used by P. Nießen in his PhD thesis [227]. Signal events peak more at values close to zero. This is shown in Figure 8.14.

ZTravel

The average distance between the z -position of all DOMs and the z -position of the first quartile (in time) of all DOMs should be positive for upgoing tracks. Mis-reconstruction in air shower events therefore have a much larger contribution at lower values compared to signal events. This is shown in Figure 8.15.

ZMax

Upgoing tracks should have large *ZMax* variables. Low values for signal events mostly consist of corner-clippers, corridor events, and events that did not trigger DOMs in the upper layer of the detector due to the low light yield. Muons from air shower events often stop in the top of the detector. This explains the large contribution at high values for air showers. The dip just below the origin is due to the dust layer (see Section 5.6). This is shown in Figure 8.16.

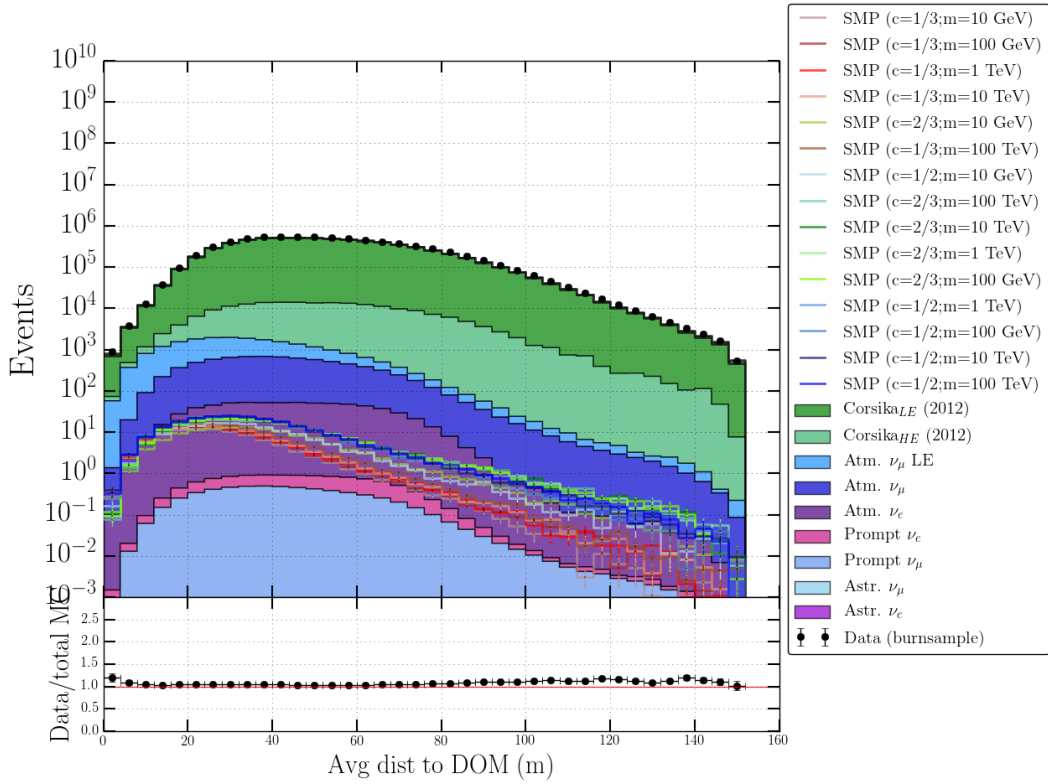


Figure 8.10: Distribution of the average distance of a hit DOM to the seed track. Signal events produce less light, making it less probable for DOMs far away from the track to record light pulses.

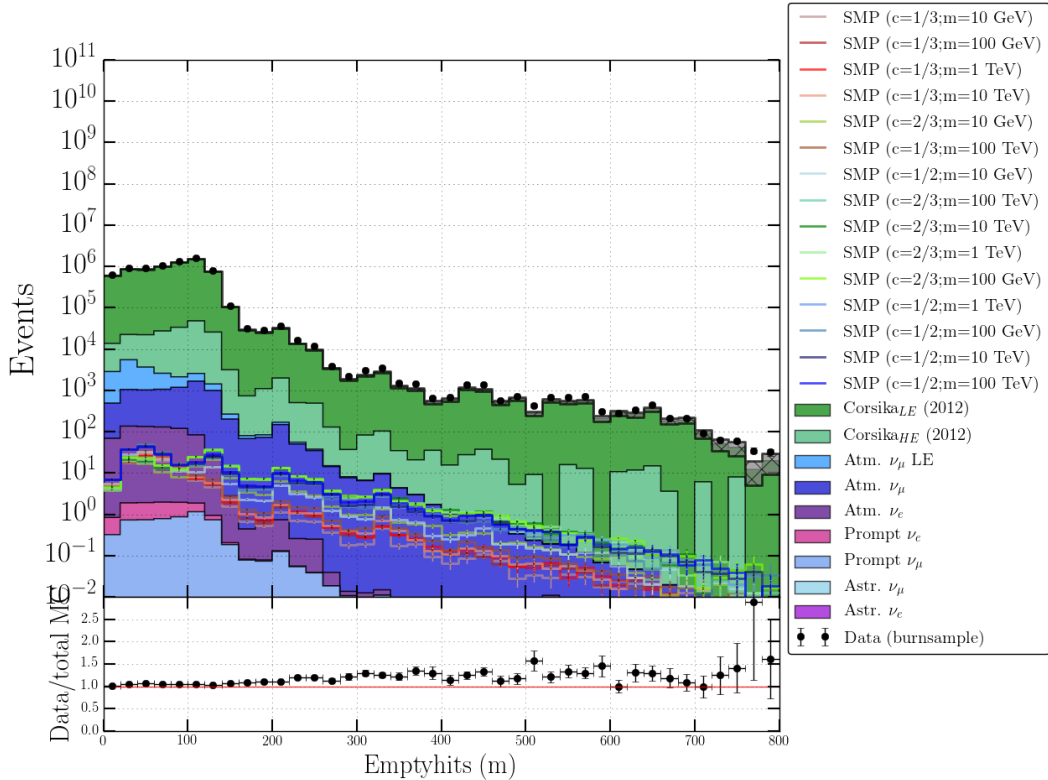


Figure 8.11: Distribution of the length of empty hits along a track. Dim signal events show longer tails in the distribution than the backgrounds.

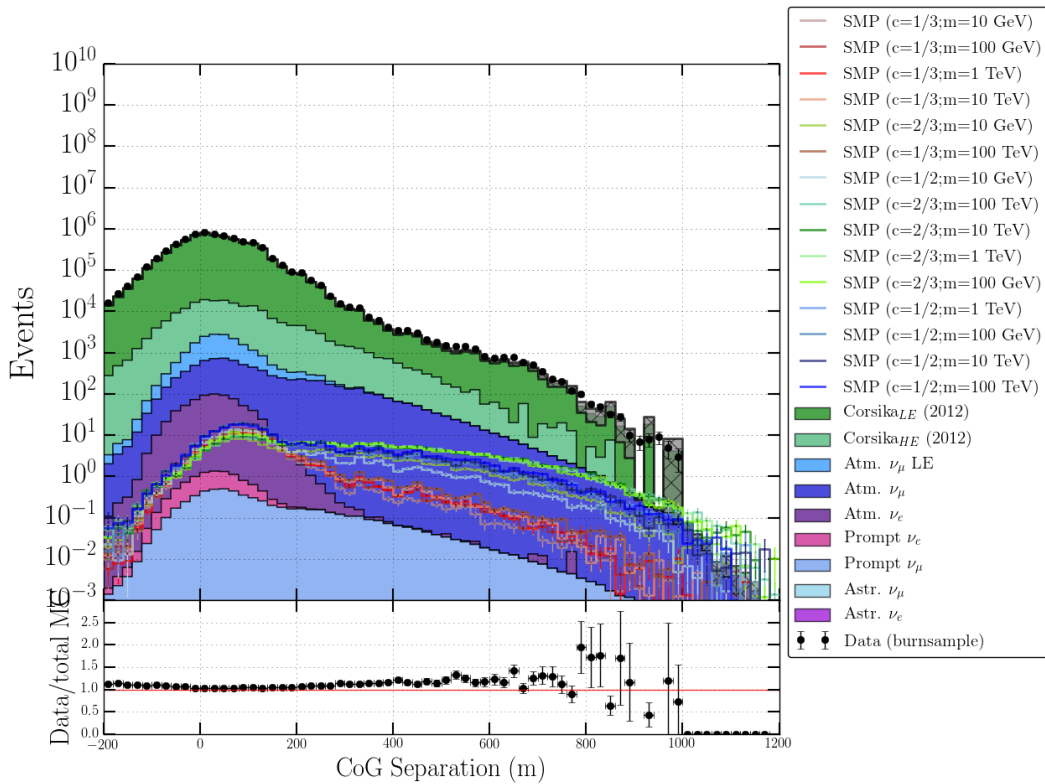


Figure 8.12: Distribution of the TrackSeparation, or COG separation, signal events show longer tails in the distribution compared to muons from air showers, as expected. A cylinder radius of 150 m was used.

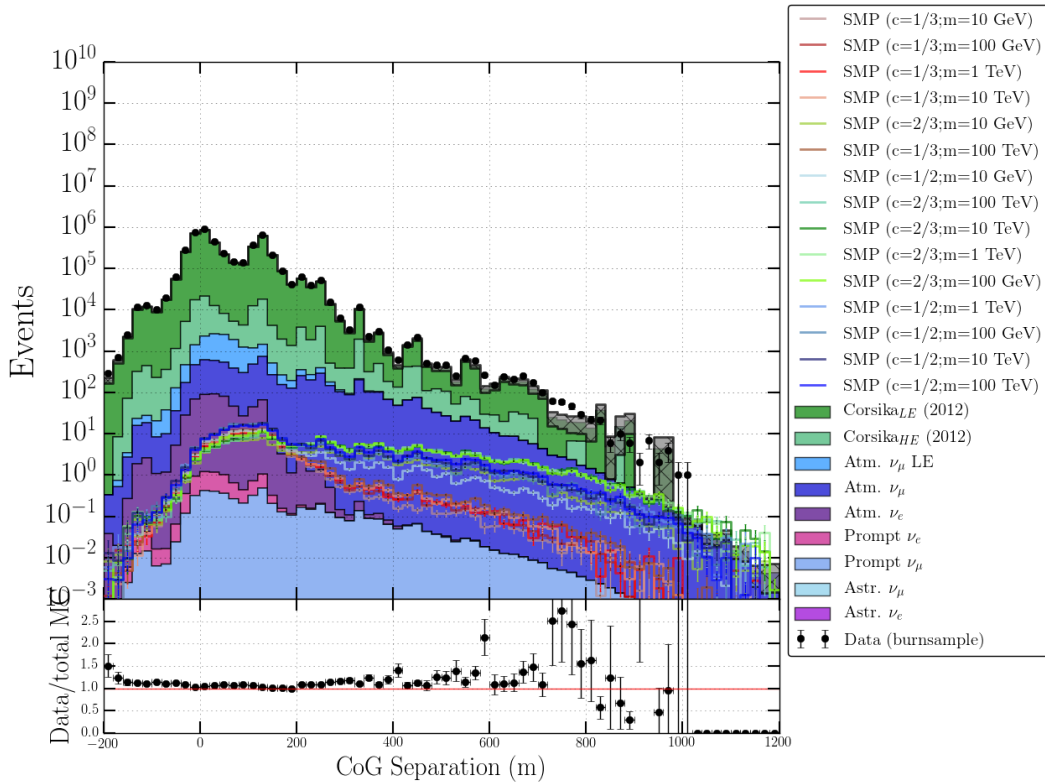


Figure 8.13: Distribution of the TrackSeparation, or COG separation, with a cylinder radius of 50 m.

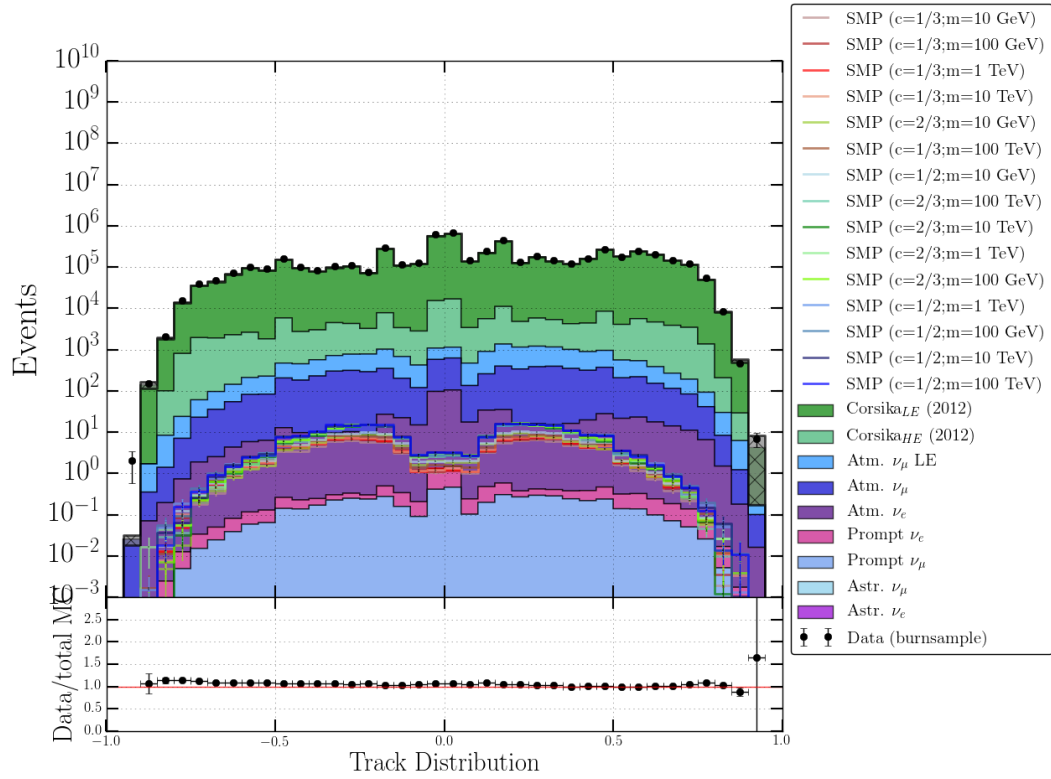


Figure 8.14: Distribution of the smoothness of the track.

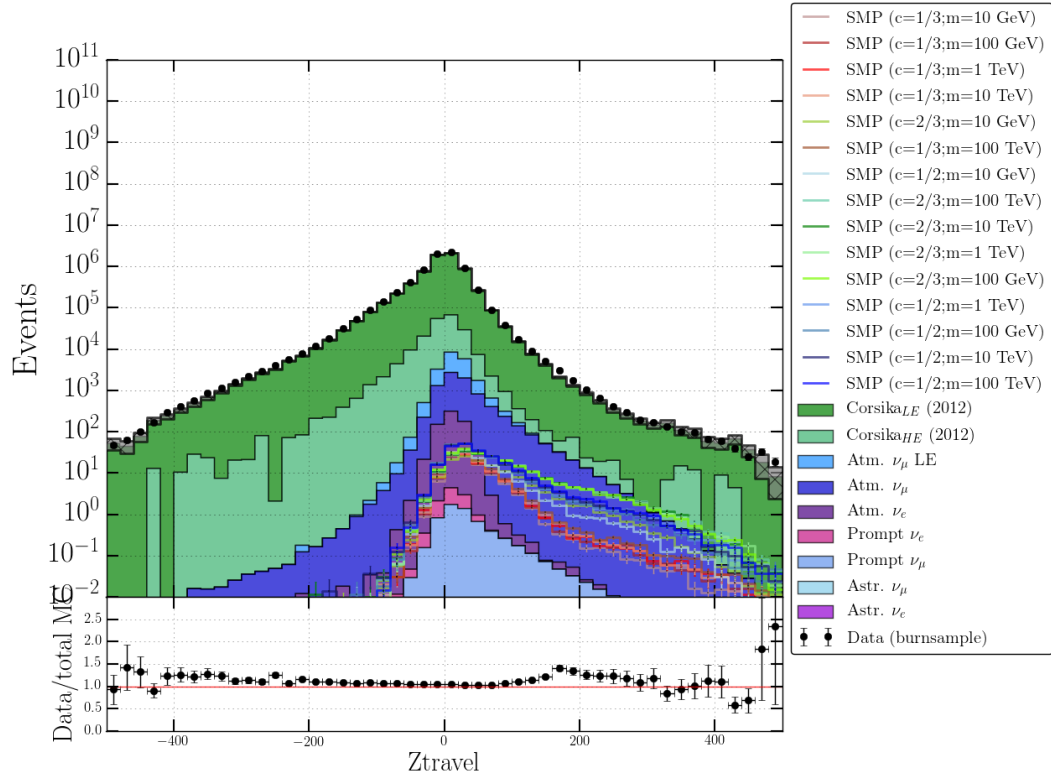


Figure 8.15: Distribution of ZTravel. Negative values indicate downgoing tracks, explaining the differences in signal and muons from air showers.

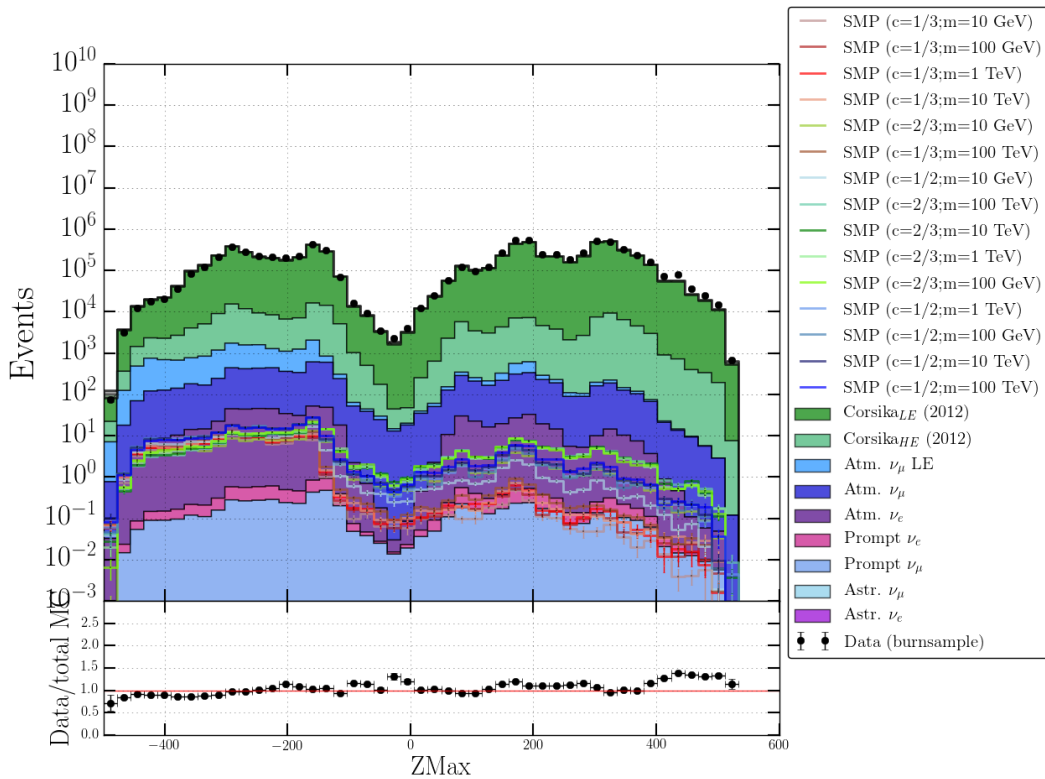


Figure 8.16: Distribution of ZMax. The dip slightly below the origin is due to the dust layer.

ZPattern

This variable is described in more detail in Table 8.2. Upgoing tracks result in positive values, making the variable a tool to discriminate from mis-reconstructed muons from air showers. This is shown in Figure 8.17.

8.3.2.2 Millipede variables

The **Millipede** toolkit was introduced in Section 7.1.5, where it was explained how energy depositions could be estimated from the light seen by the individual DOMs. Constructing multiple variables from this toolkit was the master thesis subject of Stef Verpoest. See Ref. [228] for an elaborate explanation. The variables that were used in this analysis are explained below. Figure 8.18 shows how one fit was performed and can be helpful to explain the variables. The **Millipede** algorithm tries to estimate the energy that is deposited along a track from secondary interactions. The track is subdivided in segments of 15 m long. These deposits can be very small (most of the light originates from the primary particle at low energies), but still hold some information. In the example, we see that an SMP particle had several energy deposits along the track (green lines). The algorithm estimated that more energy deposits occurred close to the true deposits (that are known from the Monte Carlo samples). From this **Millipede** fit, several variables are constructed.

Mean loss

The most straightforward use of the estimated energy loss rate is by taking the mean value and is referred to as *Mean_dEdX*. As can be seen from Figure 8.19, the distribution of SMPs peaks at lower values than known backgrounds, as expected. Energy losses that are reconstructed to come from outside the detector are removed.

Due to the squared charge dependencies, an SMP of charge 1/3 is expected to have a relative energy loss difference to muons with a factor of 9, which is the case when comparing to muons from neutrino interactions. We don't really see an exact factor of 9 difference as the algorithms still *assumes* that a muon is passing through. Nevertheless, a significant shift is visible. Atmospheric

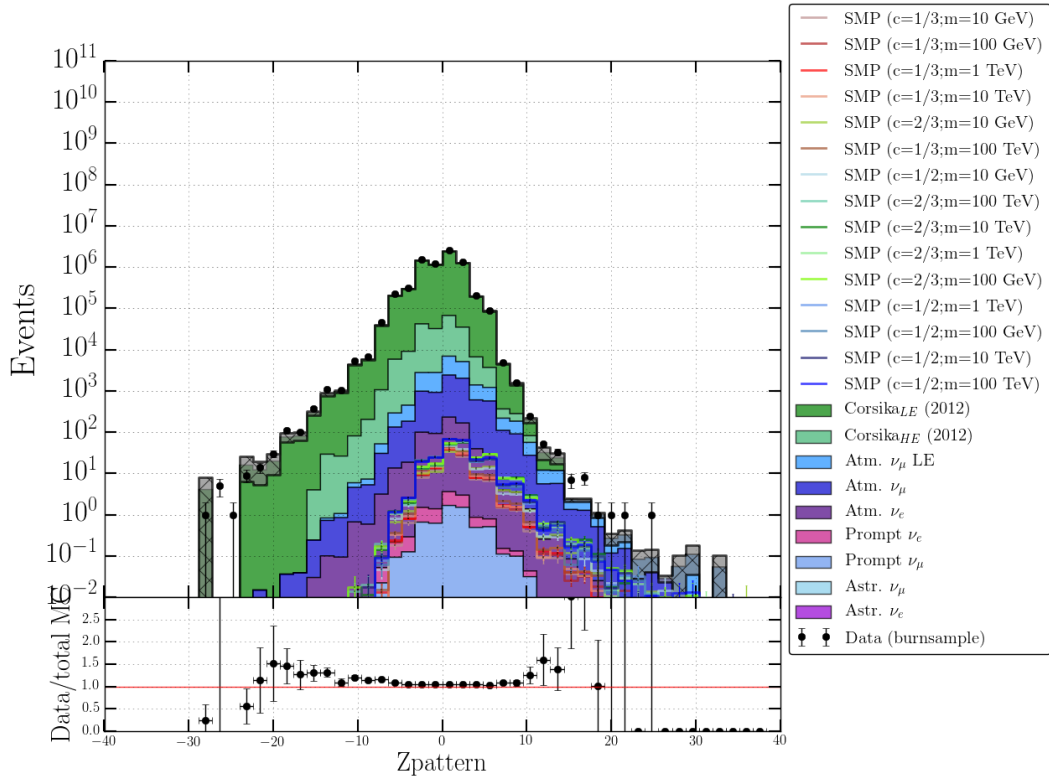


Figure 8.17: Distribution of the ZPattern of a track. Negative values indicate downgoing tracks, explaining the different behavior in signal and background.

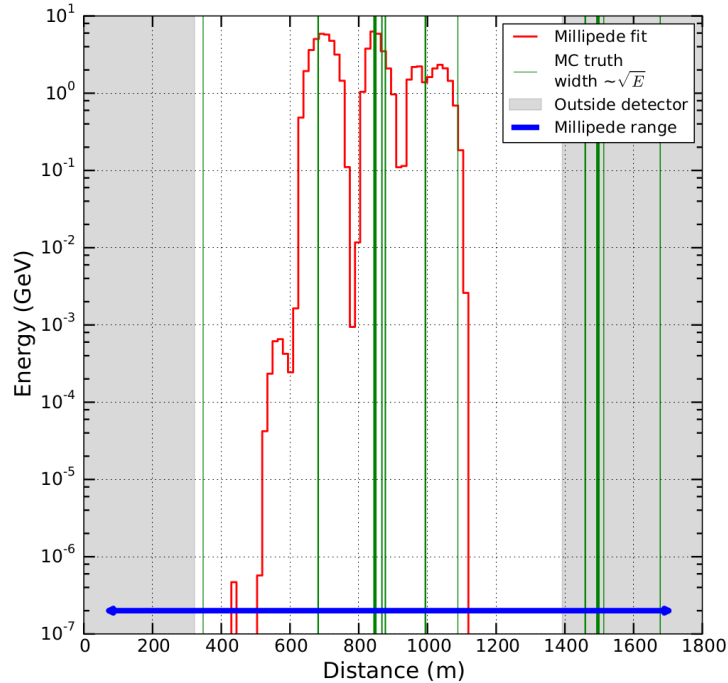


Figure 8.18: Output of a **Millipede** fit for a simulated SMP with charge $\frac{1}{3}$ and mass 10 GeV. The x -axis shows the distance the particle traveled and starts after the first energy loss event. The fit tries to estimate the energy deposited in 15 m track segments. As a comparison, the true positions of energy deposits from the MC simulation are shown in green. Locations outside the detector are shaded in grey.

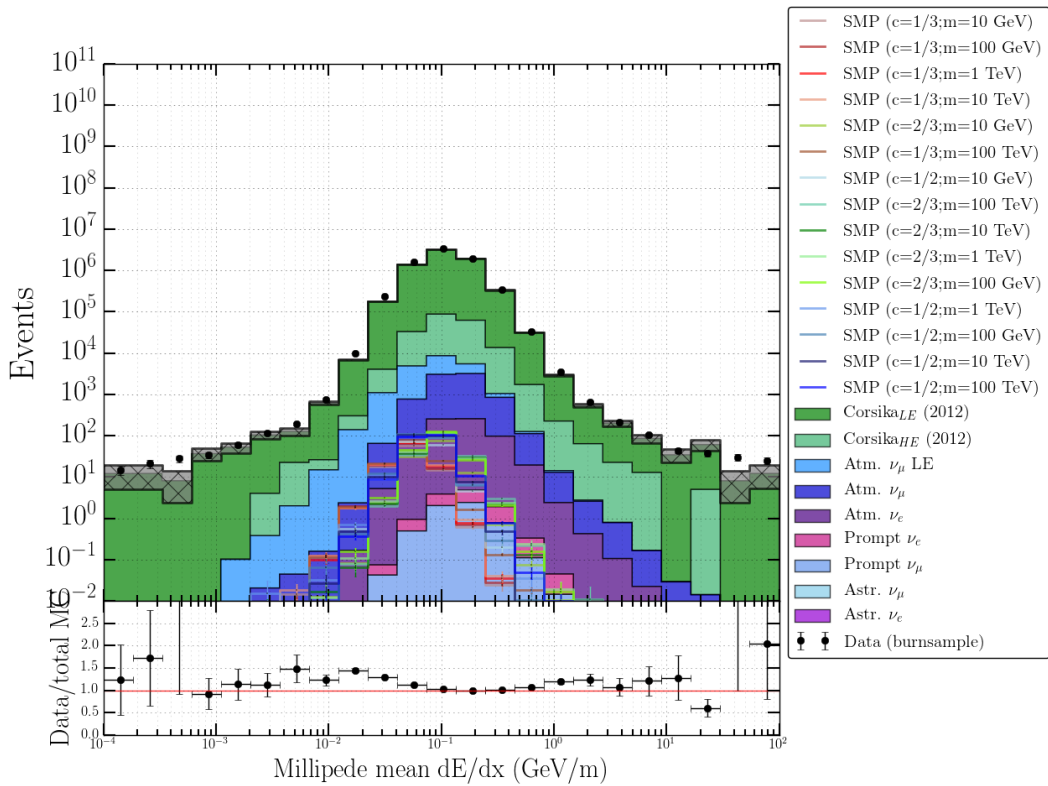


Figure 8.19: Distributions for the estimated mean energy loss from the `Millipede` toolkit.

muons in this level are almost entirely the result of mis-reconstructions, corner clippers, etc. making a comparison not valid.

Uniformity

Once the mean is computed, it is possible to count the number of times the energy distribution curve (red curve in Figure 8.18) crosses the mean value. This variable therefore parameterizes the uniformity of the track. The reasoning behind discriminating signal events from background is that most SMPs will induce triggered hits that are distributed less uniformly due to the low amount of light that is produced. Particles therefore need to travel closer to a DOM to trigger a hit. In Figure 8.20, we can see that the background distributions peak at lower values than the signal, which also has a slower dropoff.

Track length

Because of the lower energy loss, the SMP particles are also expected to travel larger distances than muons, supporting the idea to construct a variable that is sensitive to the distance traveled in the detector: a track length.

Since the tracks at this level induce very dim events, many segments from the `Millipede` output are reconstructed with zero energy. Therefore, it was chosen to use a certain part of the segments. The variable used here, `TrackLength_60`, returns the length where 60% of the energy was deposited. It is the distance between the track segments where 20% and 80% of the energy was deposited. We expected to see larger tails in the distribution of Figure 8.21 in the signal compared to the background. However, sub-optimal reconstructions result in bad millipede fits, giving a low and almost constant energy loss along the track. Additionally, coincident events that are not well separated also contribute to these events in the tail. Nonetheless, most of the background events result into low values, still making it a useful discriminative tool.

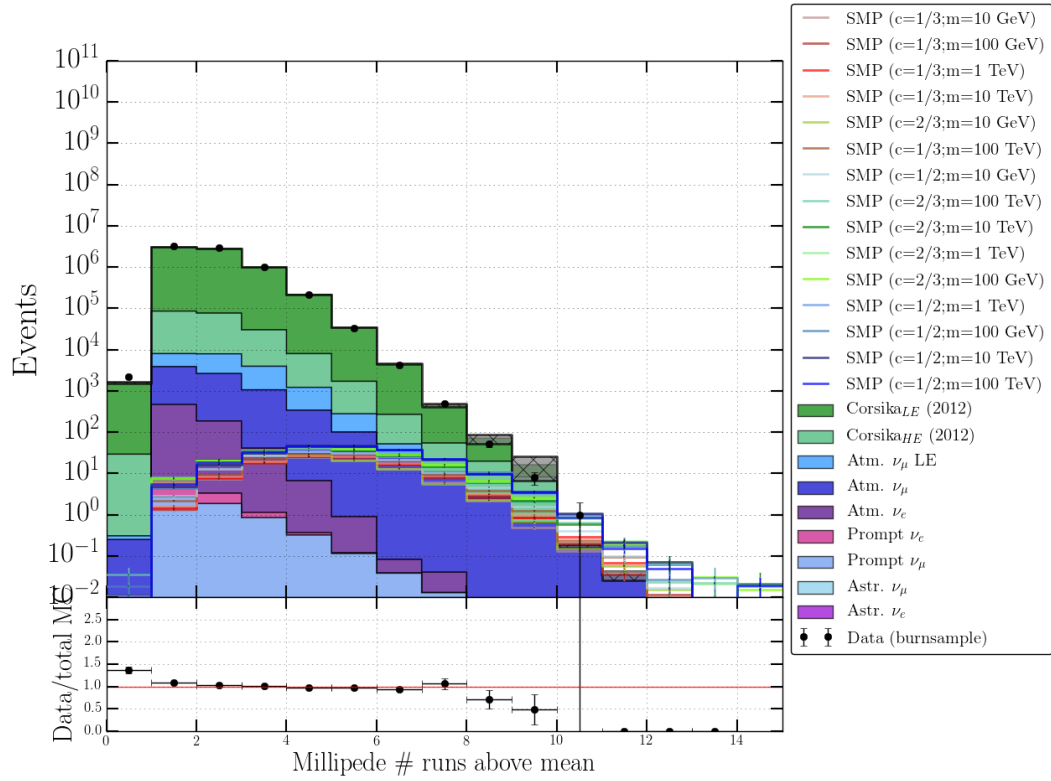


Figure 8.20: Distributions for the uniformity of the contained track.

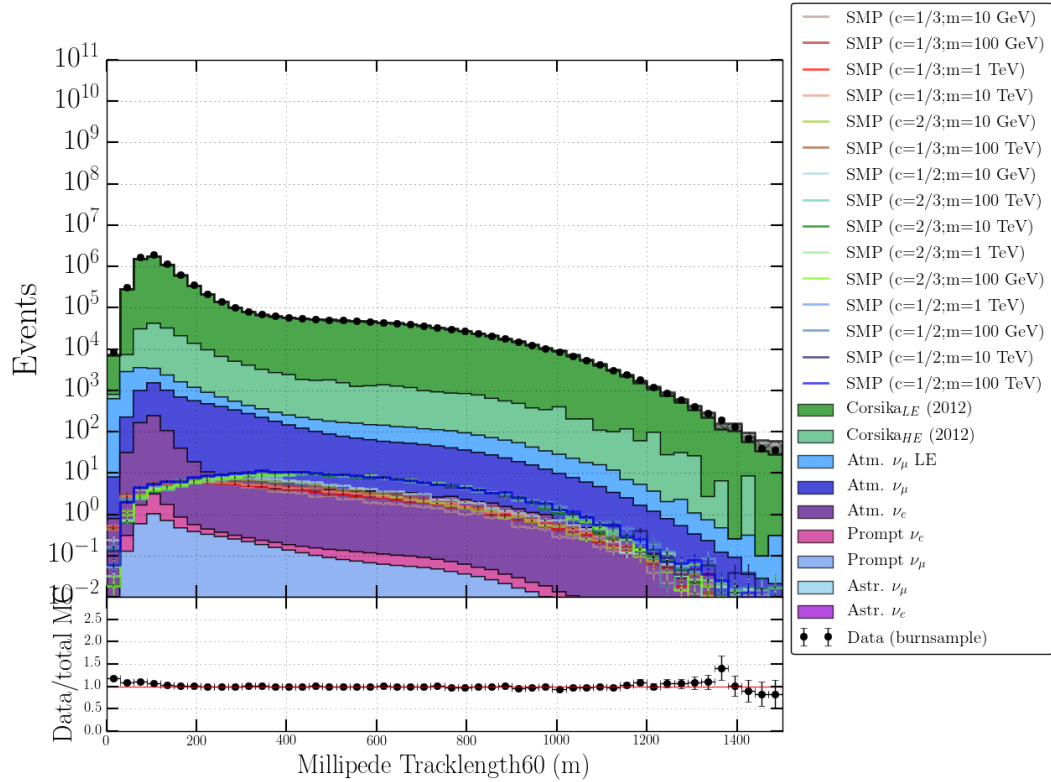


Figure 8.21: Distributions for the track length of the particle where now the **Millipede** segments are used instead of the DOM pulses.

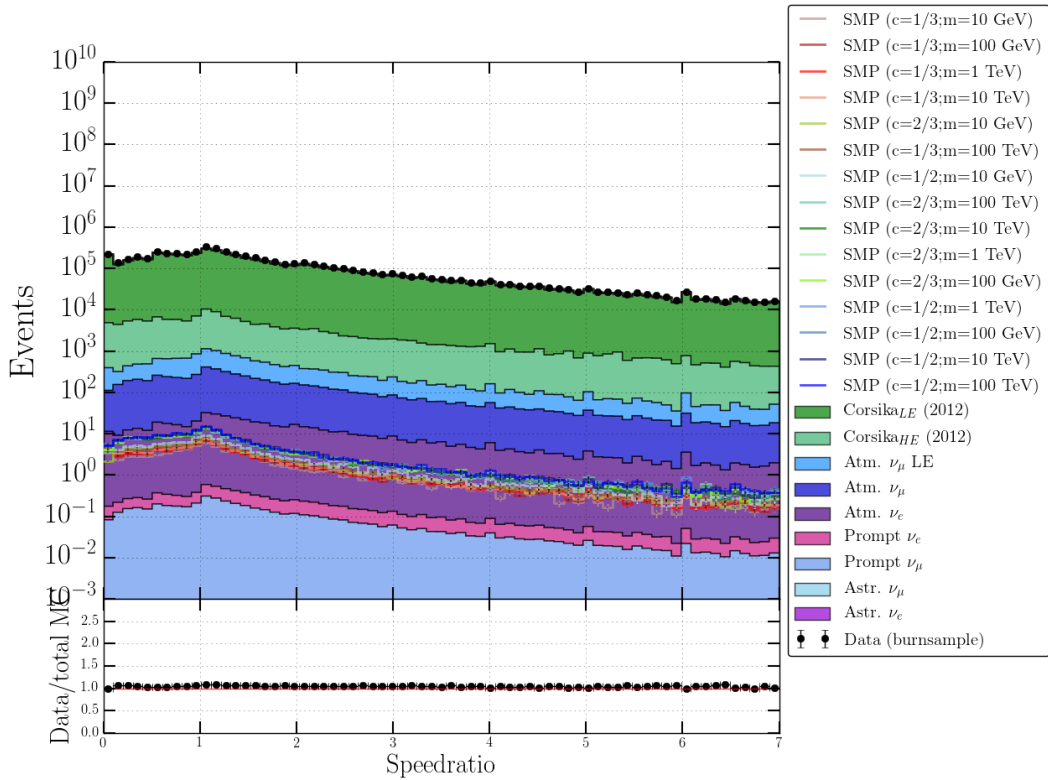


Figure 8.22: Distribution of the Speedratio variable.

8.3.2.3 New variables

Speedratio

In addition, new variables were constructed. One was adopted from Jan Künnen’s Earth WIMP analysis [229]. By looking at the “speed ratio” of the first to second and first to third HLC hits, it was possible to remove erroneous simulated detector noise, helping in data/MC agreement. In this analysis, it showed a modest addition to discriminating variables* (as can be seen in Table 8.4). The *Speedratio* is defined as

$$\frac{v_{12}}{v_{13}} = \frac{d(\text{HLC}_1, \text{HLC}_2) / \Delta t(\text{HLC}_1, \text{HLC}_2)}{d(\text{HLC}_1, \text{HLC}_3) / \Delta t(\text{HLC}_1, \text{HLC}_3)}, \quad (8.8)$$

where $d(\text{HLC}_i, \text{HLC}_j)$ is the distance between the DOMs that recorded the i th and j th HLC hits. $\Delta t(\text{HLC}_i, \text{HLC}_j)$ is the difference in time of the i th and j th HLC hits. This distribution is expected to peak at a value of 1, which is the expected result if one assumes that the photons originate from a particle traversing in a straight line passing close to the DOMs. This is illustrated in Figure 8.22.

NewLength

Because DC and IC pulses should not be mixed, essential information is lost regarding the length of a track. Many signal events are DC dominated (see Section 8.3.2.1), making those track length variables not optimal. This is especially the case for events that have both IC and DC hits and where clusters of hits are far away from each other (which is not expected from low-energetic muons). Low-energetic muons should, on average, not travel very far. High-energetic muons can have large tracks, but are almost completely removed with previous cuts that focus on dim tracks. In this analysis, new variables were constructed that use the MPE track reconstruction as a seed (*seed track*). First, the event is required to have

*In this analysis, data and MC seem to agree well, which is probably due to the newer and better simulations compared to a couple of years ago when the Earth WIMP analysis was done.

Table 8.3: Selection procedure which COGs should be used to compute a track length. f, l, h and q stand for first, last, half and quarter respectively. The left column shows possible timing conditions between IC and DC COGs. The right column indicates which COG is chosen as the first and which one as the last in the four different timing scenarios.

Timing	COG ₁
DC _{f,q} < IC _{f,h}	DC _{f,q}
DC _{f,q} ≥ IC _{f,h}	IC _{f,h}
	COG ₂
DC _{l,q} > IC _{l,h}	DC _{l,q}
DC _{l,q} ≤ IC _{l,h}	IC _{l,h}

- #DC pulses ≥ 4 ,
- #IC pulses ≥ 2 ,

since otherwise the hits would mainly consist of noise hits. Additionally, pulses that lie within a cylinder (with the seed track as the center) are selected. The radius can be chosen, but is of the order of 50-150 meters. This radius is shown with a suffix after the variable (e.g. “_100”), if the radius is infinite (all pulses are used), the suffix is “_all”.

Then the first/last quartile in DC hits and the first/last half of the IC hits are determined. For each quartile/half, one can easily calculate a COG. To determine the length of a track between four COGs, two have to be selected. The selection is based on the timing information on these COGs and given in the Table 8.3. An illustration how the NewLength variable is constructed is shown in Figure 8.23

Summarizing, the NewLength variable is another attempt in defining the length of the track in the detector. The suffix “_z” is used for the variable that only uses the z -coordinate. Negative values occur when the timing of the two selected COGs is inverted when compared to the seed track (e.g. if the seed track is downgoing but the first COG in time is located below the second) and are present when the reconstruction was not optimal.

The distributions of this variable are shown in Figures 8.24 and 8.25. Signal samples show larger contributions at higher values, showing that the variable is capable of extracting information about the length of a track for dim events. Muons from air shower events show many more low and negative values, as expected. Upgoing signal tracks can clearly be more easily distinguished from mis-reconstructed downgoing muons when only the z -coordinate is used.

8.3.2.4 Other variables

Additional to the 14 variables that were discussed in the previous sections, three extra variables were used in Level 5. These variables are constructed from the reconstruction techniques as discussed in Chapter 7. They are briefly discussed below.

LineFit velocity

The LineFit algorithm was explained in Section 7.1.2. There, we discussed how the velocity of a particle that produces a track in the detector can be estimated. The velocity for a relativistic particle is equal to ≈ 0.3 m/ns. However, because of the simplistic assumptions in the module, we expect the distribution to peak at the velocity of light in vacuum, but have a broad distribution. This can be seen in Figure 8.26. Muons from muon neutrinos and signal events indeed peak at the velocity of light in vacuum, as expected.

Paraboloid sigma

The Paraboloid module was explained in Section 7.1.4. The *Paraboloid* σ has low values for tracks that have a small uncertainty on the reconstructed direction. Longer tracks from SMPs should have lower uncertainties than the short tracks that are mostly expected from backgrounds. This can be seen in Figure 8.27.

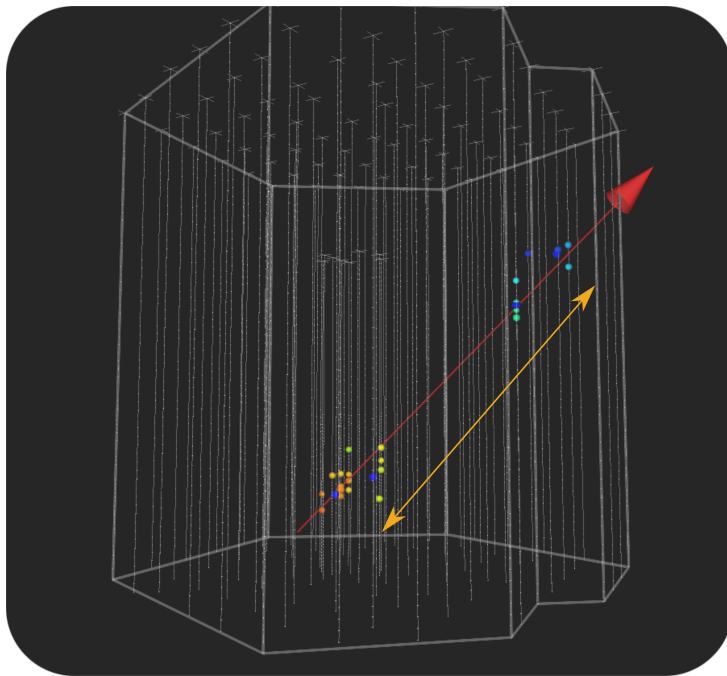


Figure 8.23: The NewLength variable is constructed by selecting the first quartile/half of the COGs of DC/IC and computing the distance from the last quartile/half of the COGs of DC/IC. Out of the four, the first and last in pulse time are chosen to compute the distance.

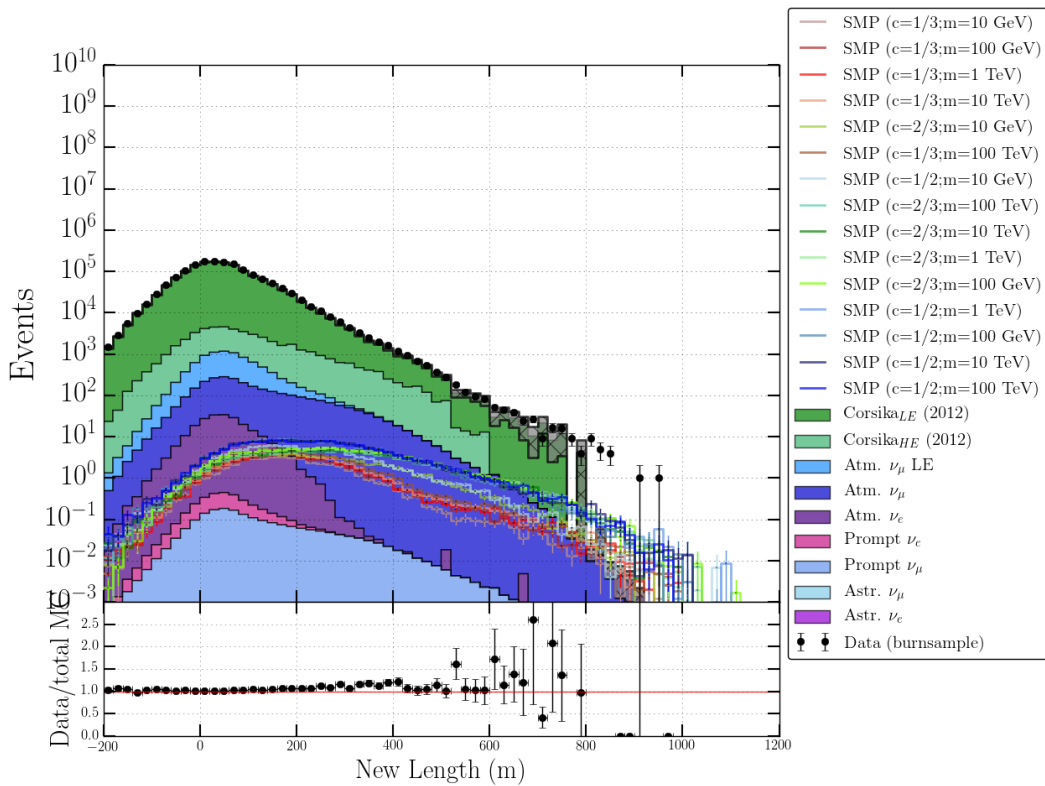


Figure 8.24: Distribution of the New Length_150 variable.

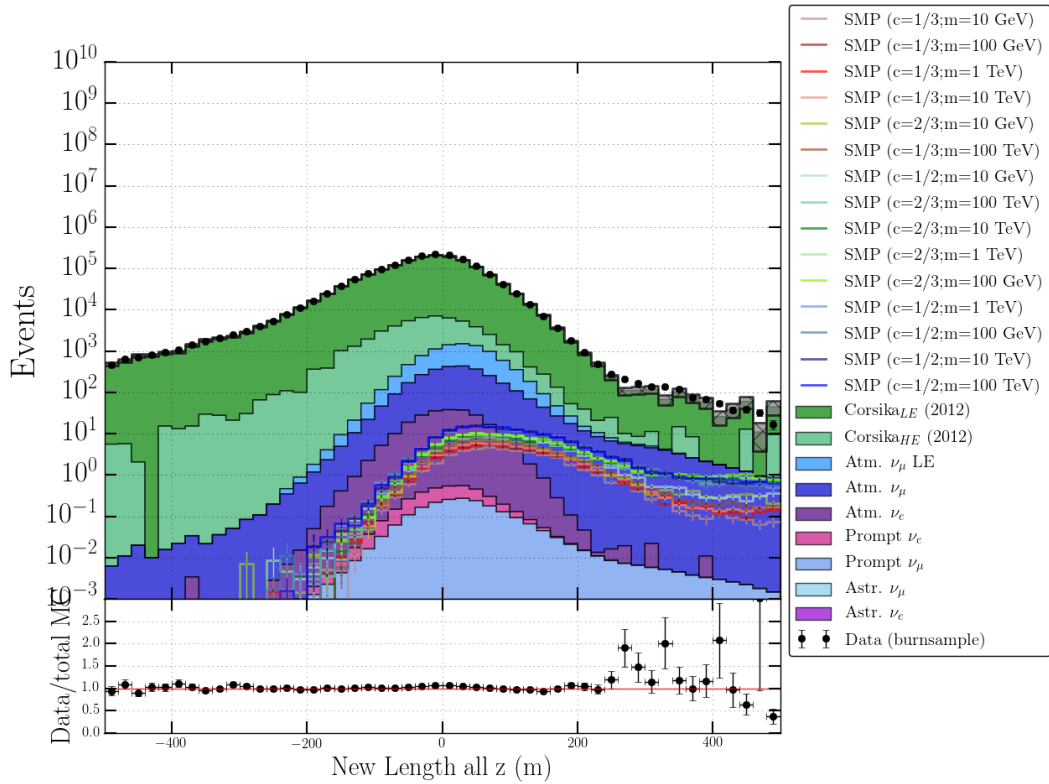


Figure 8.25: Distribution of the New Length where we only focus on the z -coordinate.

SPE zenith

After cleaning with the `IceHive` module, the SPE and MPE reconstructions were re-applied. Negative values of $\cos(\theta)$ indicate upgoing tracks. There is only a small fraction of SMP tracks that are reconstructed as downgoing after cleaning with the `IceHive` module, whereas a much larger fraction of the air shower background is now (correctly) reconstructed as downgoing. This can be seen in Figure 8.28.

8.3.3 Variable selection

The variables that are used in the BDT at Level 5 were selected by using the mRMR technique, which was explained in Section 7.6. The 17 most important variables were used in the BDT. Less variables meant a lower performance while more variables did not show to add additional power in the BDT performance and meant more computational resources were necessary. In a BDT, one variable will be more important than another since some have a much larger discrimination power than others. Therefore, an overview of all the variables used in Level 5 is shown in Table 8.4. One BDT was used to show the relative importance (number from 0 to 1) of the variables. The importance is computed by counting the amount of split nodes using each variable and weighting each count by the separation gain and by the overall weight of the tree in the forest. More information can be found in Ref. [230].

DIRK ZEGGEN

8.4 Level 5

The last part of the analysis makes use of the variables that were constructed and the 17 that were determined from the mRMR technique as the most powerful. First, the result from a single BDT is shown. Due to the lack of statistics in the final selection, the pull-validation method was used for a limit computation.

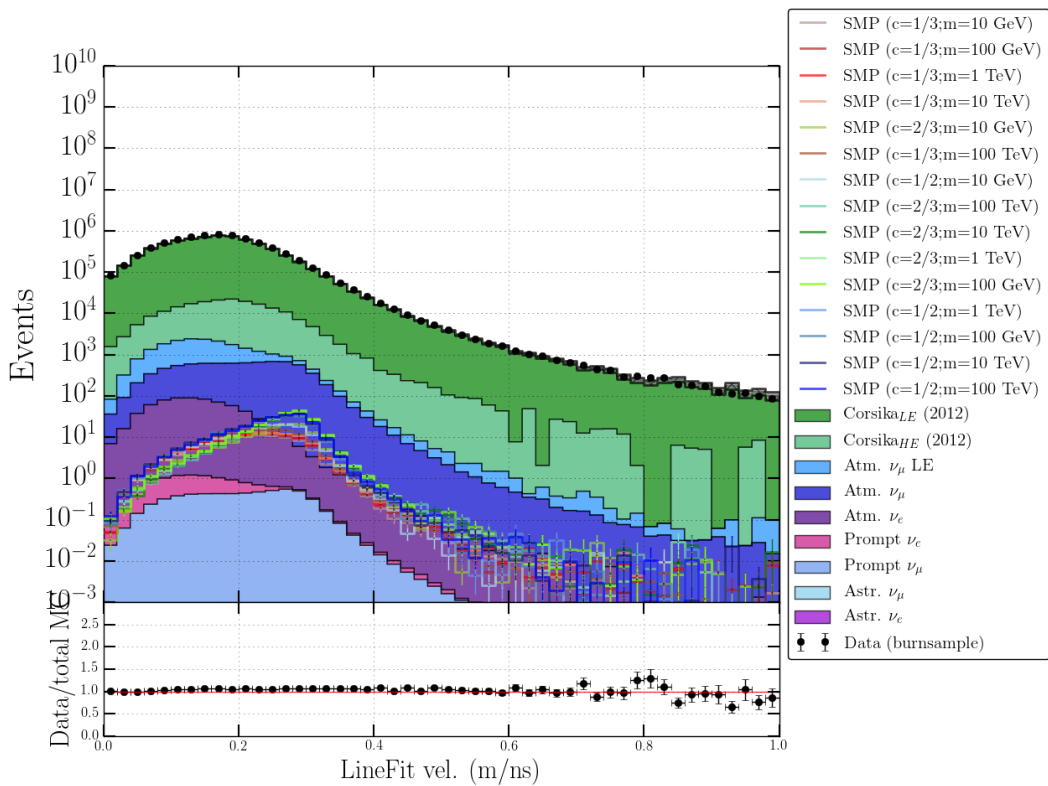


Figure 8.26: Velocity distribution of the LineFit.

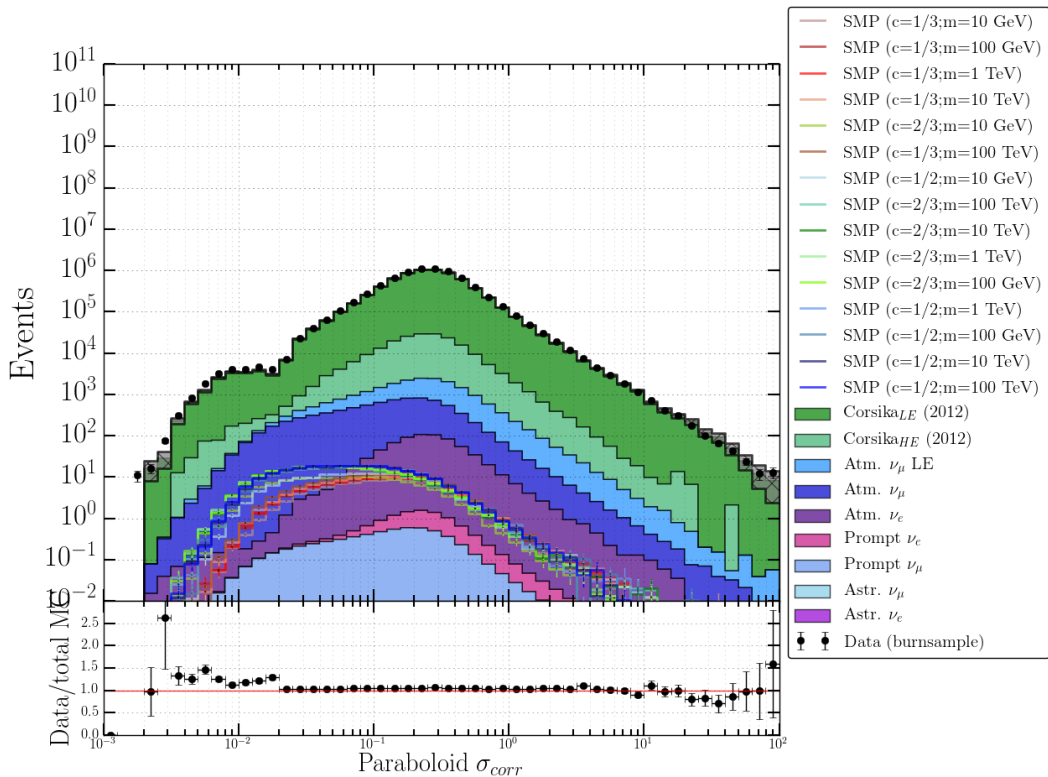


Figure 8.27: Distributions for the Paraboloid sigma.

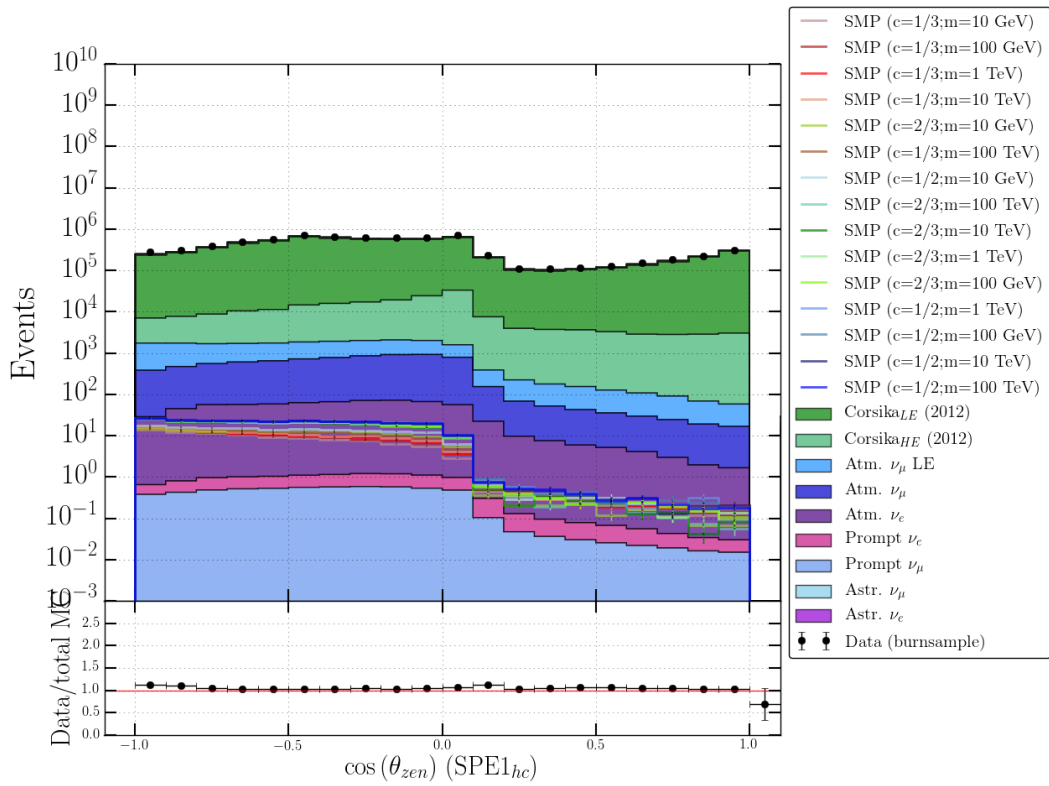


Figure 8.28: Zenith distribution of the SPE reconstruction.

Table 8.4: *Left:* The 17 variables that are used in Level 5 are grouped per class. One BDT was used to show the relative importance (number from 0 to 1) of each variable. The order indicates the rank of which variable is most useful. *Right:* The same variables shown in function of their rank.

Class	Variable	Order	Rel. importance	Order	Variable
Commonvariables	AvgDistToDom_150	9	0.048	1	NewLength_150
	EmptyHits_100	16	0.027	2	ZMax
	TrackSeparation_150	10	0.043	3	ZTravel
	TrackSeparation_50	13	0.034	4	RunsAboveMean
	TrackDistribution_50	12	0.035	5	Mean_dEdX
	ZTravel	3	0.106	6	NewLength_all_z
	ZMax	2	0.109	7	LineFit_Velocity
	ZPattern	17	0.016	8	σ_{para}
Millipede	Mean_dEdX	5	0.074	9	AvgDistToDom_150
	RunsAboveMean	4	0.105	10	TrackSeparation_150
	TrackLength_60	11	0.039	11	TrackLength_60
New variables	SpeedRatio	14	0.033	12	TrackDistribution_50
	NewLength_150	1	0.132	13	TrackSeparation_50
	NewLength_all_z	6	0.059	14	SpeedRatio
Other variables	LineFit_Velocity	7	0.055	15	$\cos(\theta)^{\text{SPE}}$
	σ_{para}	8	0.051	16	EmptyHits_100
	$\cos(\theta)^{\text{SPE}}$	15	0.033	17	ZPattern

8.4.1 BDT result

The parameters that were used for BDT training (see Section 7.7) are:

- Maximal depth: 2 (Figure 7.10)
- Boosting β : 0.8 (Eq. 7.25)
- Number of trees: 400 (Section 7.7.3)
- Pruning factor: 35 (Section 7.7.4.1)

Training is done on 10% of the available burn sample as it showed to have a better performance as opposed to training on background simulation. Training on the background samples showed a systematic disagreement between data and MC testing sets at the high BDT scores, probably due to limited statistics from the simulations at these high scores. The other 90% of the burn sample is used for testing and is shown in the following plots. Testing on the MC data sets is also shown for the sake of completeness. Contribution of possible signal events, if they exist, in the data are minimal. Together with the very good data/MC agreement that is seen in the variables used, the training on data is a valid choice.

Also, it was chosen to select a (large) subsample of the Monte Carlo signal set instead of the complete set to train the BDT to give the best possible results. Some events in the signal MC will produce corner-clippers or leak-in events, which will often be mis-reconstructed. These events should not be used to train the BDT and are therefore removed in the training set. One can see in the variable distributions of Figures 8.15 and 8.24 that there are minimal contributions of events with negative ZTravel and/or negative NewLength values. Upgoing tracks should give positive values for both and events with negative values for either variable are therefore removed from the signal sample that is used to train the BDT*.

The result of one BDT can be seen in Figure 8.29 and we can draw several conclusions:

- Data and MC show a very good agreement.
- The rate in background events is reduced by 4 to 5 orders of magnitude at a BDT score around 0.25.
- At higher BDT scores, muons from low-energetic ν_μ become a much more significant part of the total background than muons from air showers. This is mainly because the data used to train the decision tree mainly consists of atmospheric muons.
- The signal used for training is more concentrated at higher scores, as expected. The total signal sample and the subset used for training overlap at scores higher than 0.1.
- At the highest scores, where the signal dominates, it is clear that there is a lack of statistics in both CORSIKA simulations and the burn sample to draw sensible conclusions.

Additional checks can be found in Appendix D.

The limited amount of statistics in the tail of the CORSIKA data sets proves challenging. There is a need for an order of magnitude more events, which is not feasible with the available resources. Other techniques, such as defining off-source or off-time regions [231], are not available for this search as we have assumed an isotropic flux that is not time-dependent.

8.4.2 Pull-validation

Another way of dealing with limited statistics is by using re-sampling techniques. The method used here is called *Pull-Validation*[†] (PV) and was used several times before in the IceCube collaboration [184, 232, 233]. It is comparable to bootstrapping and cross-validation (see Appendix C), but uses much smaller training samples. Smaller subsamples means more can be constructed uniquely and more subsamples lead to a larger variability that can be used as an estimator for the variability of the whole sample. As opposed to most bootstrapping and cross-validation methods,

*The final signal rate is computed from the full signal sample.

[†]The term *pull* refers to the “pulling” of subsamples from a larger set, while *validation* refers to the method being used to estimate uncertainties.

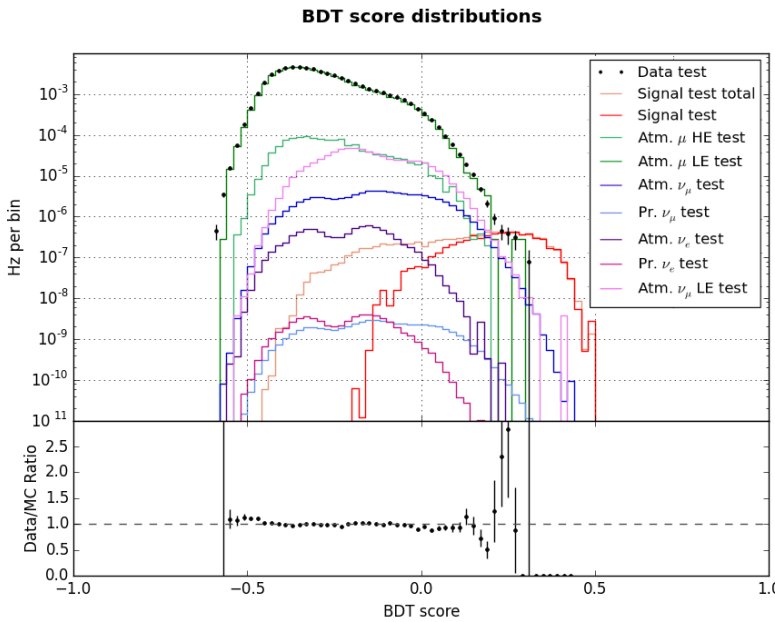


Figure 8.29: Rates of the various testing sample sets in function of the BDT score. Positive scores are more signal-like, whereas negative scores imply events that resemble the background the BDT was trained to recognize. The red curve corresponds to the subset of the signal that was used for training, while the gold curve corresponds to the total signal sample.

the resampling can be done without replacement* because the samples are much smaller.

As can be seen in Figure 8.29, there is a lack of statistics in the region of interest (at high BDT scores), mainly for the data burn sample and atmospheric muon simulations. Because we want to compute an upper limit from this distribution or set a discovery significance, a cut on the BDT score at a value that is higher than for example 0.30 does not result in a trustworthy background estimation. We cannot know from the distribution how the tail evolves into higher BDT scores. A cut on a single BDT implies a binary addition of an event to the final sensitivity: surviving the cut or not, and training the BDT on a slightly different training sample could result in a similar, but different BDT result. By using slightly different training samples, one is able to give an estimate about the tail of the background distributions in function of the BDT score.

Let us assume we have N events making up a sample S . One BDT takes a subset S_1 and uses it as a training sample and using the remaining set for testing, S_2 .

$$k \cdot |S_1| = |S_2| \text{ with } S = S_1 \cup S_2 \text{ and } S_1 \cap S_2 = \emptyset, \quad (8.9)$$

where k refers to the order of missing events that is to be compensated. This factor cannot be made too small as the variability would diminish but cannot be made too large due to the limited size of S . Therefore, k is set at 10. Because S_2 is sizeably larger, the testing sample will extend further than the training sample S_1 as can be seen in Figure D.1.

Pull-validation consists of repeating this procedure a number of times, N_p . For each iteration, the samples S_1 and S_2 are constructed from the sample S and therefore, they consist of different events at each step. By combining the N_p distributions, we can gain additional information from an event by obtaining the Probability Density Function (PDF) of an event in function of the BDT score.

A single event will have one BDT score attributed per iteration and by reprocessing this N_p times, while changing the training sample at each iteration, the variation of an event in function of the BDT score becomes visible and can be used as an estimation of the rate in the tails.

*Selecting without replacement means that when an object is selected from a set, it is removed from the set so that it cannot be chosen twice or more.

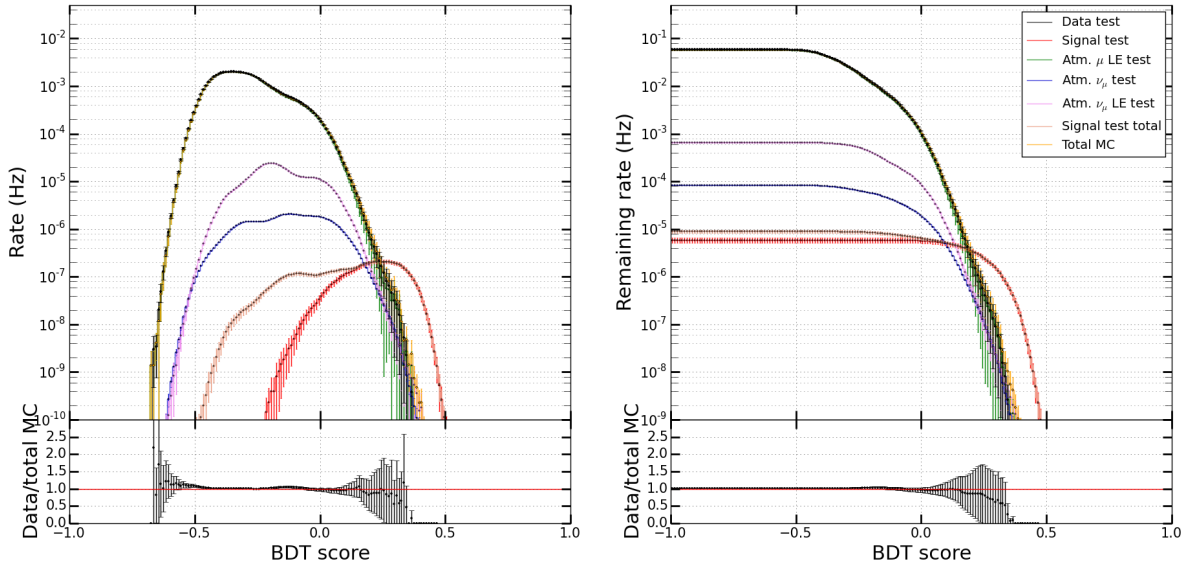


Figure 8.30: Result of the pull-validation method for an SMP with charge 1/2 and mass 100 GeV. Only the most prominent backgrounds are shown. *Left:* rate in function of the BDT score. *Right:* Cumulative rate to the right in function of the BDT score. The y-axis shows the remaining rate of a dataset when placing a cut at a certain BDT score. The weight of an event is given by Eq. 8.10.

Each event gets an appropriate weight, the *PV-weight* equal to

$$w_{PV} = \frac{\#\text{scores above cut threshold}}{N_p}. \quad (8.10)$$

The number of pull-validation iterations, N_p , should be high enough to extract as much information as possible, but low enough so that the subsamples, which are 10% of the total set chosen ad random each time, are still adding information in the variability of the BDT performance. Too many iterations would introduce correlation effects in the subsamples. Previous analyses indicated that $N_p = 200$ is good enough to fulfill these requirements [184, 232]. It is also used in this analysis. The result for an SMP with charge 1/2 and mass 100 GeV is shown in Figure 8.30 and shows the power of PV. Figure 8.31 illustrates how one bin in this histogram is constructed. For a certain BDT score range, a sample will have a rate that changes slightly when the BDT is trained with a different training sample. For example, one BDT estimates a rate of x Hz for the signal between a BDT score of 0.30 and 0.31, whereas another BDT estimates a rate of y Hz for the signal between these BDT scores. These rates, for all N_p BDTS (divided by the average rate), are shown as a histogram in the figure. We can see that lower BDT scores imply more statistics and have a Gaussian-like distribution (left plot). For higher scores, the distribution resembles that of a log-normal or Poisson (right plot). The average rate is computed and used in the pull-validation histogram.

8.4.3 Model Rejection Factor

The question remains where we should place a cut in the BDT score for a significant signal discovery potential or upper limit computation. Since we do not know beforehand if the result will be a discovery or upper limit, the Feldman and Cousins method is used [234]. In this analysis, we want to compute the 90% confidence interval $\mu_{90} = (\mu_1, \mu_2)$, which is a function of the number of observed events, n_{obs} , and of the number of expected background events, n_b

$$\mu_{90} (n_{\text{obs}}, n_b). \quad (8.11)$$

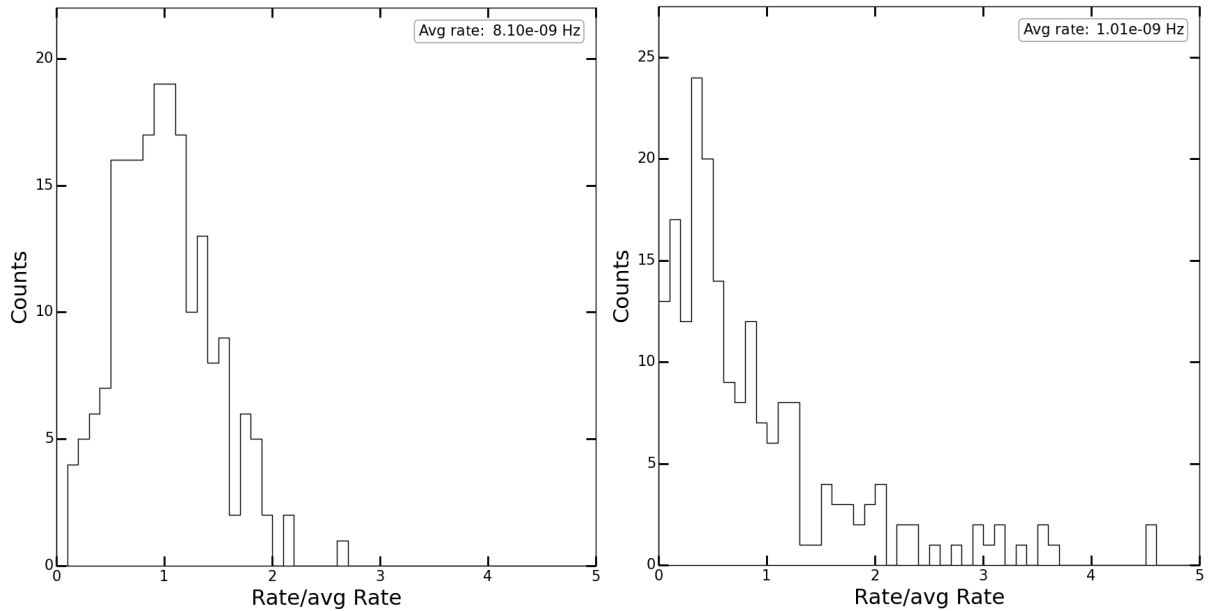


Figure 8.31: Example of an uncertainty distribution of the atmospheric ν_μ background with a BDT score between 0.29 and 0.3 (*left*) and with a BDT score between 0.34 and 0.35 (*right*).

If we assume that the expected number of signal events is n_s , then the 90% confidence upper limit on the signal flux is

$$\Phi_{90\%}(n_{\text{obs}}, n_b, n_s) = \Phi \cdot \frac{\mu_{90}(n_{\text{obs}}, n_b)}{n_s}, \quad (8.12)$$

where Φ is the assumed signal flux of $10^{-14} \text{ cm}^{-2} \text{ sr}^{-1} \text{ s}^{-1}$. It is important to mention that n_s and Φ scale linearly, making the UL *independent* of the assumed absolute flux. Unfortunately, an UL can only be computed once the number of observed events is known. The best *expected* UL could be computed by assuming that the number of observed events is equal to the expected number of events from the MC background. Setting n_{obs} equal to n_b is, however, not a good approach for analyses that have small sample sets at the final level. For example, say one expects 2.5 background events with a 1σ error of 2.1. If, after unblinding, one finds 0, 1, 2, 3, 4, or 5 events in data, this would be considered as consistent with the expected background. The 90% Feldman-Cousins UL are, however, drastically different: $\mu_{90}(0, 2.5) = 1.18$, $\mu_{90}(5, 2.5) = 7.49$. Which is more than a factor of 6 difference! Do we simply take the mean of these two numbers?

A better way is to assume that the number of observed events is the mean of a Poissonian distribution and we compute the *average upper limit* by summing over all the expected upper limits, weighted by their Poisson probability of occurring [235]

$$\begin{aligned} \bar{\mu}_{90}(n_b) &= \sum_{n_{\text{obs}}=0}^{\infty} \mu_{90}(n_{\text{obs}}, n_b) \cdot \text{Poiss}(n_{\text{obs}}, n_b) \\ &= \sum_{n_{\text{obs}}=0}^{\infty} \mu_{90}(n_{\text{obs}}, n_b) \cdot \frac{(n_b)^{n_{\text{obs}}}}{(n_{\text{obs}})!} \exp(-n_b) \end{aligned} \quad (8.13)$$

The *Model Rejection Factor* (MRF) is defined as

$$\text{MRF}(n_b, n_s) = \frac{\bar{\mu}_{90}(n_b)}{n_s}. \quad (8.14)$$

Comparing this with Eq. 8.12, we can see that minimizing this factor corresponds to the strongest possible constraint on the expected signal flux. Because in each bin in Figure 8.30 both the number of expected signal events and background events are known, the MRF can be computed in function of the BDT score. This is shown in Figure 8.32 for an SMP with charge 1/2 and

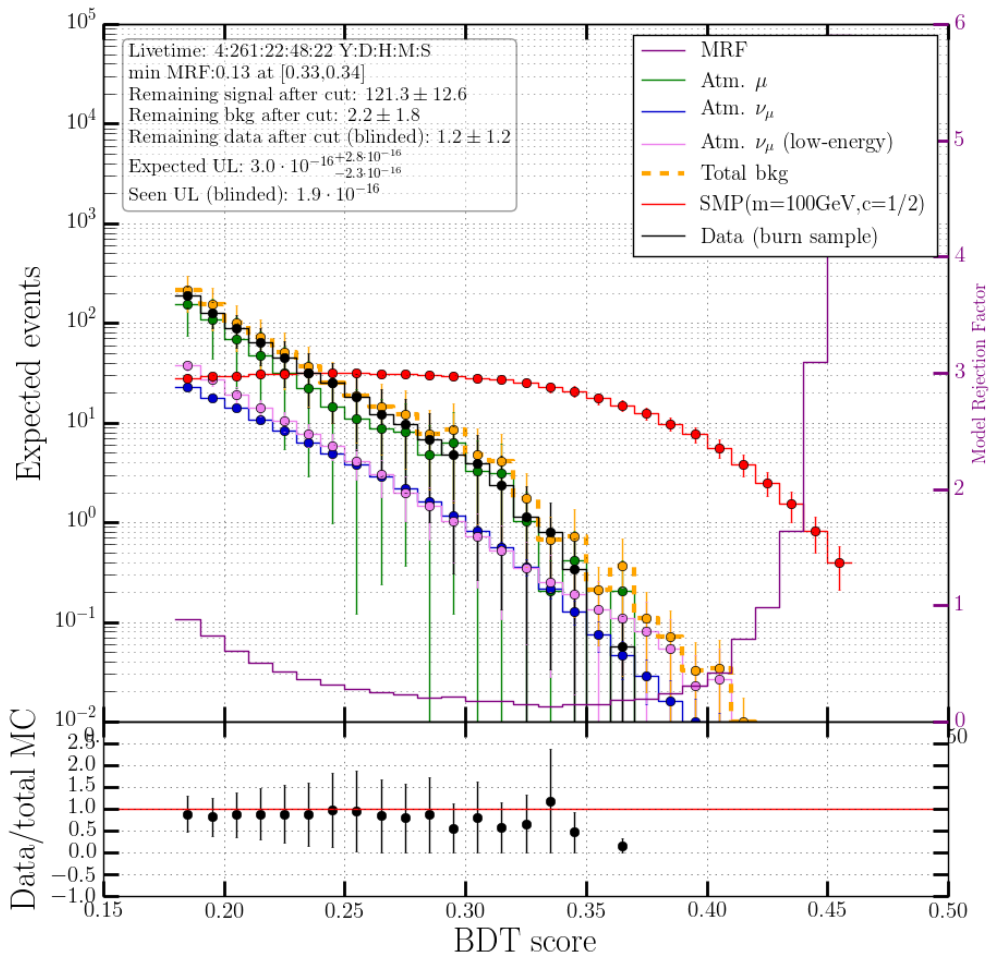


Figure 8.32: Zoomed in version of Figure 8.30, focused on higher BDT scores, again for an SMP with charge 1/2 and mass 100 GeV. Only the most prominent backgrounds are shown. The expected rate is shown on the left vertical axis, while the MRF score can be obtained from the right vertical axis. Only statistical uncertainties are shown as error bars.

mass 100 GeV. In the figure, all samples are normalized to a livetime of 1723 days (≈ 4 years and 262 days). The value of the minimal MRF is shown, together with the corresponding BDT bin. The lowest value of the bin was chosen as the BDT cut for each signal sample. Also, we present the number of expected MC signal events, MC backgrounds, and data (where the burn sample is scaled to the total live time). The uncertainties correspond to statistical uncertainties only. A fake unblinding is presented where we show the expected UL, together with the UL if we would use the burn sample that has more statistics due to the PV method.

After pull-validation, there are enough statistics for a proper MRF computation (purple). The offset of data from MC is a common feature in PV and is accounted for in the systematic uncertainties.

The MRF gives a numerical indication of where we find an optimal trade-off of expected signal and background events. At very high scores, there are less background events expected, but also less of the signal while at lower scores both have higher expectancies.

The BDT score where the MRF is minimized was chosen as the final cut; this is the cut that will probably give the most stringent upper limit or best value for an observation. It's possible that another cut yields more stringent upper limits, but this cannot be known before unblinding the

Table 8.5: Expected number of signal and background events for 5 years of data (see Section 8.5), errors are statistical only. The signal is normalized to a flux of $10^{-14} \text{ cm}^{-2}\text{s}^{-1}\text{sr}^{-1}$. The optimal BDT cut value from the MRF minimization is shown together with the expected upper limit and the statistical error.

Mass	Charge	Remaining MC signal events per 1723 days	Remaining MC background events per 1723 days	$\bar{\mu}_{90} (\text{cm}^{-2}\text{s}^{-1}\text{sr}^{-1})$ $\times 10^{-16}$	BDT cut value
10 GeV	1/2	73.2 ± 7.7	2.2 ± 1.6	$5.0^{+2.9}_{-3.8}$	0.32
100 GeV		121.3 ± 12.6	2.2 ± 1.8	$3.0^{+2.8}_{-2.3}$	0.33
1 TeV		90.7 ± 9.6	0.8 ± 0.6	$1.9^{+2.5}_{-0.18}$	0.35
10 TeV		127.8 ± 11.0	1.8 ± 1.1	$2.1^{+1.4}_{-1.2}$	0.34
100 TeV		107.7 ± 9.7	2.2 ± 1.3	$3.4^{+1.9}_{-2.6}$	0.34
10 GeV	1/3	45.3 ± 5.2	2.2 ± 1.9	$8.2^{+7.7}_{-6.2}$	0.32
100 GeV		60.5 ± 4.1	2.4 ± 1.9	$5.9^{+5.1}_{-4.5}$	0.35
1 TeV		64.0 ± 5.6	3.1 ± 2.7	$6.7^{+5.0}_{-5.4}$	0.32
10 TeV		57.6 ± 4.9	1.2 ± 1.0	$5.5^{+3.4}_{-3.1}$	0.34
100 TeV		79.7 ± 5.9	2.2 ± 1.5	$4.6^{+2.4}_{-3.5}$	0.34
10 GeV	2/3	40.4 ± 4.5	9.6 ± 3.7	$14.2^{+15.1}_{-10.4}$	0.29
100 GeV		71.5 ± 7.5	5.0 ± 1.4	$5.1^{+5.1}_{-1.5}$	0.30
1 TeV		79.3 ± 7.7	7.2 ± 2.1	$6.7^{+4.6}_{-3.1}$	0.30
10 TeV		74.4 ± 7.9	7.9 ± 2.2	$6.3^{+6.7}_{-3.1}$	0.29
100 TeV		59.0 ± 6.0	5.7 ± 1.6	$7.4^{+5.6}_{-2.7}$	0.30

total data set. This should not be done to leave the analyzer unbiased. Therefore, the MRF method uses a Poissonian weighting, which yields us the most probable stringent upper limit. The results can be found in Table 8.5.

8.4.4 Systematic uncertainties

There are four types of uncertainties that are assumed in the result of this analysis, which are listed below

1. **Statistical:** Limited statistics in the final event sample in both the expected signal and background events lead to uncertainties. We assume that the variance of this number follows a Poisson distribution where the statistical uncertainty on a rate is defined as the square root of the rate. The statistical uncertainties can be seen in Table 8.5.
2. **Detector:** Detector simulations assume certain properties of the optical modules and the ice (see Chapter 5), which can differ from true values or are oversimplistic. Therefore, the following detector uncertainties are assumed:
 - DOM efficiency +10%
 - DOM efficiency -10%
 - Ice absorption +10%
 - Ice scattering +10%
 - Ice absorption and scattering -7.1%

The DOM efficiencies originate from uncertainties in the DOM calibrations, whereas the ice absorption and scattering uncertainties are conservative estimates, determined by the collaboration. Therefore, specialized simulation data sets that include these uncertainties were developed and are shown in Table 8.6. Because of the limited statistics in the systematic background sample sets, these detector uncertainties are investigated before the BDT training at Level 4. The effects on the signal were investigated after BDT cuts of 0.30 for charge 2/3 particles and 0.32 for charge 1/3 and 1/2 particles. There were no significant differences found for different masses and these are therefore not specified. Results are

Table 8.6: Overview of the data sets used for systematic uncertainties. Polyg(onato) follows from Ref. [238], GaisserH4a from Ref. [236] and Bartol from Ref. [237].

Generator	Type	Range [GeV]	Sim. γ	Weighted γ	Ice	Dataset	Syst. Eff.
CORS.	Hoerandel	$600 - 10^5$	Polyg.	GaisserH3a	SpiceLea	11527	DOM eff. -10%
CORS.	Hoerandel	$600 - 10^{11}$	Polyg.	GaisserH3a	SpiceLea	11526	DOM eff. +10%
CORS.	5-comp.	$600 - 10^{11}$	2.6	GaisserH3a	SpiceLea	12388	Abs. +10%
							Scat. +10%
							Abs./Scat. -7.1%
CORS.	All data sets from Table 6.2			GaisserH4a (syst.)	SpiceLea	Table 6.2	GaisserH4a
NuGen	ν_μ	$100 - 10^8$	2	Bartol (syst.)	SpiceLea	11029	Bartol flux
NuGen	ν_μ	$100 - 10^7$	2	Honda2006 + Bartol (syst.)	SpiceLea	11883	DOM eff. +10%
							DOM eff. -10% Abs. +10% Scat. +10% Abs./Scat. -7.1% Bartol flux
NuGen	ν_μ	$100 - 10^8$	2	Honda2006 + Bartol (syst.)	SpiceLea	12346	DOM eff. +10% DOM eff. -10% Abs./Scat. -7.1% Bartol flux

shown in Table 8.7.

3. **Flux:** The models that were used in flux normalizations are not set in stone. Therefore, variations to the flux were assumed to determine the possible discrepancies.

- *SMP flux:* As there is no clear production model or clear possible origin of these anomalous charged particles, the signal flux is assumed to range between E^{-1} and E^{-3} .
- *Atmospheric μ flux:* We look at the difference between the GaisserH3a [102] and GaisserH4a [236] models.
- *Atmospheric ν_μ flux:* We look at the difference between the Bartol [237] and Honda2006 [135] models.

Similar to the detector uncertainties, the effects were computed at Level 4 for background data sets and at BDT cuts of 0.32, 0.32 and 0.30 for particles with charges 1/2, 1/3 and 2/3 respectively. The data sets used for detector and flux uncertainties are shown in Table 8.6. Results are shown in Table 8.7. Because these numbers were computed from relatively small sample sets*, there are uncertainties on these numbers as well. For example, the scattering +10 % uncertainties have an error of around (19.3 ± 14) %, $(3 \pm 10)\%$, and $(3.4 \pm 15)\%$.

4. **Pull-validation:** As will be explained in Section 8.5, only one BDT is used for the final event rate. Pull-validation offers us a way to get more statistics but choosing one BDT for the full data sample and comparing the data rate to the mean of a fluctuating pool of expected background events gives rise to a large uncertainty. It was found that this uncertainty is highly dominant.

For each mass point I have looked at the minimal and maximal offsets between the 200 BDT outputs. As the signal distributions again had enough statistics at higher BDT scores, cuts at values of 0.32, 0.32 and 0.30 for particles with charges 1/2, 1/3 and 2/3 were chosen respectively. Background distributions showed unrealistic large fluctuations in the tails due to very low statistics and single events with high or low weights. Therefore, the BDT cuts were lowered to 0.25 for the backgrounds. The largest discrepancy between the average and the minimum and maximum is set as the uncertainty as a conservative choice. An example is shown in Figure 8.33. The results can be found in Table 8.8.

The final systematic uncertainty is obtained by summing the individual uncertainties in quadrature.

*Data sets that were constructed for systematic uncertainty have much less statistics than the nominal ones.

Table 8.7: Results for the absolute numbers of the detector and flux uncertainties.

Effect	Atm. μ	Atm. ν_μ	SMP (charge 1/3)	SMP (charge 1/2)	SMP (charge 2/3)
DOM eff. +10%	30.9%	2.9%	7.6%	5.2%	3.6%
DOM eff. -10%	26.7%	29.4%	3.5%	16.7%	0.8%
Absorption +10%	23.9%	2.2%	22.7%	18.5%	38.3%
Scattering +10%	3.6%	2.9%	19.3%	3%	3.4%
Abs./Scat -7.1%	17.7%	5.8%	18.7%	6.4%	12.1%
Flux	0.35%	15.28%	1.7%	3%	11.8%
Total	50.7%	33.9%	36.2%	26.6%	42.5%

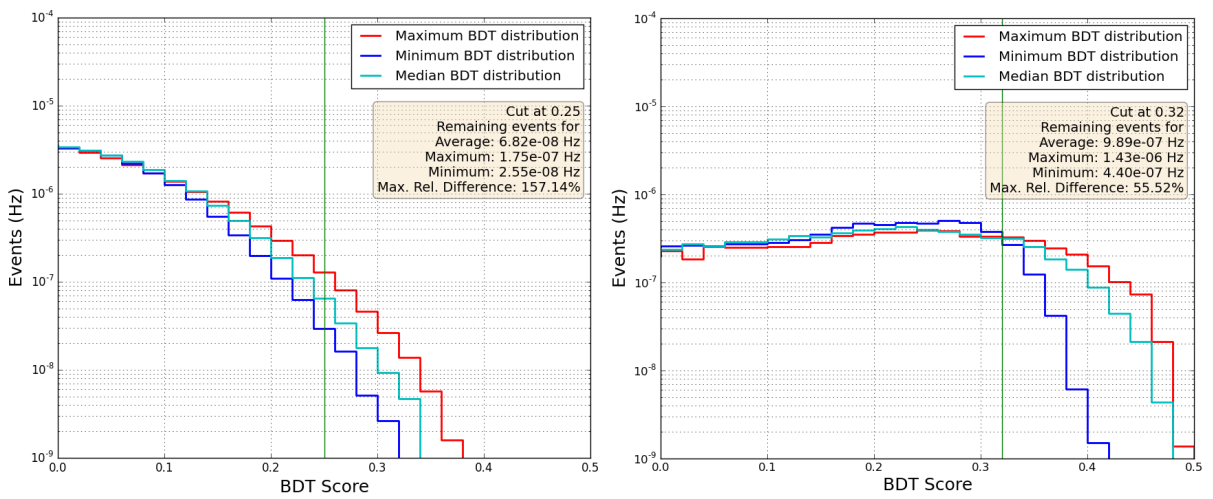
Figure 8.33: *Left:* Illustration how the pull-validation systematic error is computed. Here, the maximum rate, the median and minimum rates from 200 BDT score distributions are shown for atmospheric ν_μ events. *Right:* Similar comparison of BDT score distributions for an SMP with a charge 1/2 and mass 100 GeV.

Table 8.8: Results for the pull-validation uncertainties

Mass	Charge	Atm. μ	Atm. ν_μ	SMP
10 GeV	1/2	66.4%	216.1%	59.8%
		136.3%	157.1%	55.5%
		159.8%	136.3%	42.1%
		211.6%	73.7%	36.7%
		218.4%	135.4%	52.5%
100 GeV	1/3	142%	176.7	39.6%
		174.8%	225.6%	32.9%
		108.3%	167%	40.9%
		190.3%	150%	40.8%
		223.6%	96.8%	35.6%
1 TeV	2/3	63.8%	103.6%	54.8%
		58.7%	88.9%	52.5%
		65.4%	72.5%	61.9%
		10%	104.2%	72.1%
		51.5%	83.4%	43.6%

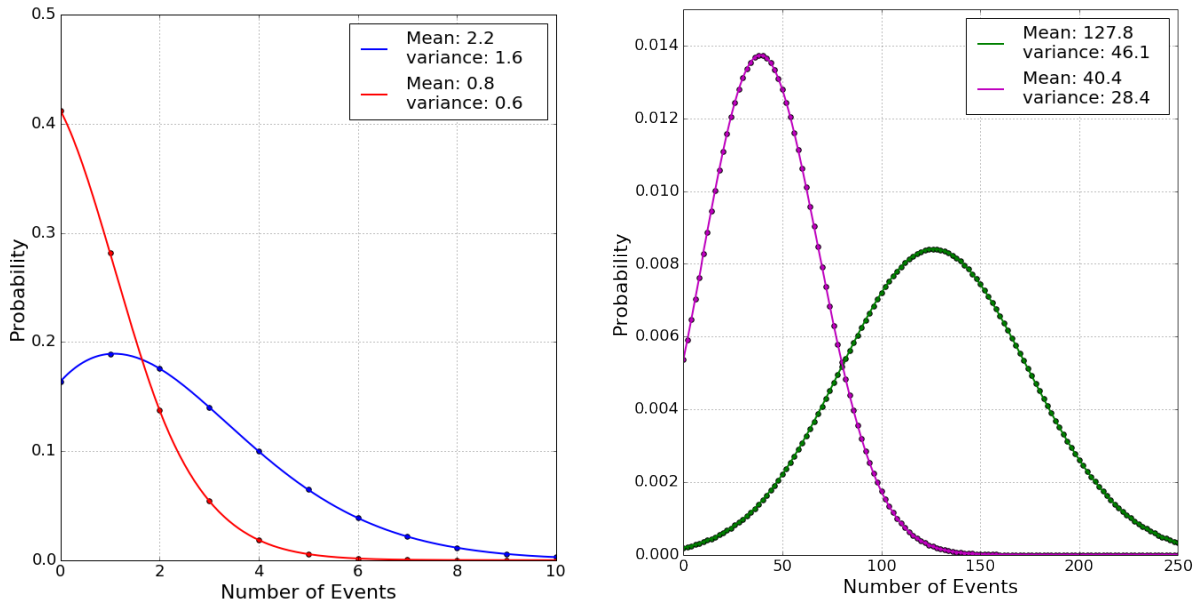


Figure 8.34: *Left:* Illustration of probability density function using Eq. 8.16 of two expected background rates with their variance. *Right:* Similar PDFs for two expected signal rates.

Implementing the uncertainties in the upper limit

Using Eq. 8.12, we are able to determine an upper limit in the scenario where we cannot claim detection. Because there are large uncertainties in both the background and signal rates, these uncertainties are included in the computation of the limit. The *observed* limit will be weighted with an uncertainty probability. Additionally, we will also show systematic uncertainty bands as can be seen in Figures 8.36 to 8.38.

Gaussian distributions with large uncertainties can overlap with negative rates, which are not physical (e.g. an expected rate of 2 events with a 150% uncertainty would yield a range of $[-1, +5]$. A rate of -1 events is unphysical.). Therefore, we assume that the uncertainties follow a truncated normal distribution

$$\Phi(n_{\text{obs}}, n_{\text{bkg}}, \sigma_{\text{bkg}}, n_s, \sigma_s)_{90\%} = \Phi \cdot \frac{\sum_{n'_b=0}^{\infty} \left[\mu_{90} \left(n_{\text{obs}}, n'_{\text{bkg}} \right) \cdot P_{\text{unc}} \left(n'_{\text{bkg}} | n_{\text{bkg}}, \sigma_{\text{bkg}} \right) \right]}{\sum_{n'_s=0}^{\infty} n'_s \cdot P_{\text{unc}} \left(n'_s | n_s, \sigma_s \right)}, \quad (8.15)$$

where

$$P_{\text{unc}}(n|\lambda, \sigma) = \int_{-\lambda}^{\infty} \frac{(\lambda + x)^n e^{-\lambda - x}}{n!} \cdot w(x, \sigma) dx, \quad (8.16)$$

with $w(x, \sigma)$ a normal distribution with mean 0 and variance σ^2 . An example of two distributions for both the signal and background are shown in Figure 8.34. We can see that large rates with large uncertainties lead to Gaussian distributions (right figure). If a part of the distribution extends to negative rates, the formula (Eq. 8.16) removes these negative rates and scales the probabilities accordingly. Therefore, the total integrated probability is always one. Very low rates with relatively large uncertainties give much larger probabilities to very low number of events (left figure). Negative numbers are again removed.

8.5 Results

8.5.1 Unblinding

This analysis was presented to the collaboration after internal review and accepted for *data unblinding**. As explained in Section 6.6, only 10% of the data was used in setting up the analysis. Expected rates, e.g. in Table 8.5, are normalized to the total livetime of the full dataset. The total livetime for the different years is equal to

- 333.1 days of livetime for IC86-1,
- 324.5 days of livetime for IC86-2,
- 345.5 days of livetime for IC86-3,
- 357.3 days of livetime for IC86-4,
- 362.6 days of livetime for IC86-5,

resulting in a total livetime of 1723 days.

The cuts in the BDT score for each signal point were fixed by computing the most stringent upper limit with the model rejection factor using pull-validation. The full dataset is run through one BDT since an average of multiple BDTs could result in a systematic offset that is non-physical and would result in data events that contribute with a factor < 1 which is prone to lead to confusion. Therefore, one BDT out of 200 was chosen ad random for each signal point.

Before unblinding, a procedure was set for the following steps depending on the outcome

- If the number of seen data events are consistent with the expected background rate, an upper limit on the SMP flux is set as described in Section 8.4.3.
- If there is a consistent overfluctuation of the data compared to the expected background, a more in-depth analysis on these events should be performed before signal discovery can be claimed.

8.5.2 Limits

After unblinding, the number of data events for all signal points were consistent with the expected background, as can be seen in Table 8.9. The upper limits were computed with Eq. 8.15.

Event displays of the types of these events can be found in Appendix E.

The resulting upper limits are shown in Figures 8.35 to 8.38 and compared to the experiments that were discussed in Chapter 2. The limits from this analysis were computed with Eq. 8.15 and are more stringent than any other experiment that was done up to now. Also shown are the upper limits for the individual charges with the large systematical error bands. Previous experiments did not present any uncertainties and could therefore not be shown in the figure.

There is an apparent optimum for discriminating SMPs from backgrounds in the IceCube experiment at a charge of 1/2. Particles with a higher charge (such as 2/3) resemble physical muons a lot more, while particles with a lower charge have a lot lower probability in producing enough light to trigger the detector.

In these figures, the obtained limits are compared to older experiments that used simplistic models for possible signatures of particles with an anomalous charge and assumed near 100% detector efficiencies. Even though the trigger and filter efficiencies (which were never optimized for these particles) are very low, the instrumented volume of the IceCube detector is orders of magnitude larger than those experiments. Therefore, it was possible to significantly improve the limits.

*By only looking at part of the data, the analyzer “blinds” himself to not (sub-)consciously tweak the analysis [239]. After approval, the analyzer can “unblind” and look at the full data, which serves as an objective way to look at the data and provides for consistency check with the expected and seen rates.

Table 8.9: Final results of the upper limit computations. For the signal, we show the expected rate from a $10^{-14} \text{ cm}^{-2} \text{s}^{-1} \text{sr}^{-1}$ flux and both background and signal are normalized to the total livetime of the full dataset.

Mass	Charge	Remaining MC signal events per 1723 days	Remaining MC background events per 1723 days	Seen events in data	$\bar{\mu}_{90} (\text{cm}^{-2} \text{s}^{-1} \text{sr}^{-1}) \times 10^{-16}$	$\mu_{90} (\text{cm}^{-2} \text{s}^{-1} \text{sr}^{-1})$
10 GeV	1/2	73.2 ± 48.5	$2.2^{+3.5}_{-2.2}$	0	$5.0^{+41.5}_{-4.4}$	$1.4 \cdot 10^{-16}$
100 GeV		121.3 ± 75.7	$2.2^{+4.4}_{-2.2}$	0	$3.0^{+24.5}_{-2.6}$	$8.1 \cdot 10^{-17}$
1 TeV		90.7 ± 46.1	$0.8^{+1.3}_{-0.8}$	0	$1.9^{+11.4}_{-1.1}$	$1.6 \cdot 10^{-16}$
10 TeV		127.8 ± 59.0	$1.8^{+3.0}_{-1.8}$	2	$2.1^{+12.4}_{-1.8}$	$2.5 \cdot 10^{-16}$
100 TeV		107.7 ± 64.2	$2.2^{+4.4}_{-2.2}$	0	$3.4^{+25.4}_{-2.96}$	$9.1 \cdot 10^{-17}$
10 GeV	1/3	45.3 ± 24.9	$2.2^{+4.6}_{-2.2}$	6	$8.2^{+53.1}_{-7.2}$	$1.5 \cdot 10^{-15}$
100 GeV		60.5 ± 29.9	$2.4^{+4.7}_{-2.4}$	5	$5.9^{+35.0}_{-5.2}$	$9.2 \cdot 10^{-16}$
1 TeV		64.0 ± 35.4	$3.1^{+6.5}_{-3.1}$	4	$6.7^{+50.7}_{-6.0}$	$5.8 \cdot 10^{-16}$
10 TeV		57.6 ± 31.8	$1.2^{+2.4}_{-1.2}$	5	$5.5^{+27.8}_{-4.8}$	$1.3 \cdot 10^{-15}$
100 TeV		79.7 ± 40.9	$2.2^{+4.3}_{-2.2}$	6	$4.6^{+27.7}_{-3.9}$	$8.9 \cdot 10^{-16}$
10 GeV	2/3	40.4 ± 28.4	$9.6^{+14.4}_{-9.6}$	9	$14.2^{+240}_{-1.3}$	$1.2 \cdot 10^{-15}$
100 GeV		71.5 ± 48.8	$5.0^{+6.4}_{-5.0}$	2	$5.1^{+71.7}_{-4.40}$	$2.7 \cdot 10^{-16}$
1 TeV		79.3 ± 60.0	$7.2^{+9.4}_{-7.2}$	9	$6.7^{+118}_{-6.1}$	$7.7 \cdot 10^{-16}$
10 TeV		74.4 ± 62.7	$7.9^{+10.3}_{-7.9}$	5	$6.3^{+210}_{-5.8}$	$3.9 \cdot 10^{-16}$
100 TeV		59.0 ± 36.4	$5.7^{+7.3}_{-5.7}$	1	$7.4^{+79.1}_{-6.7}$	$2.2 \cdot 10^{-16}$

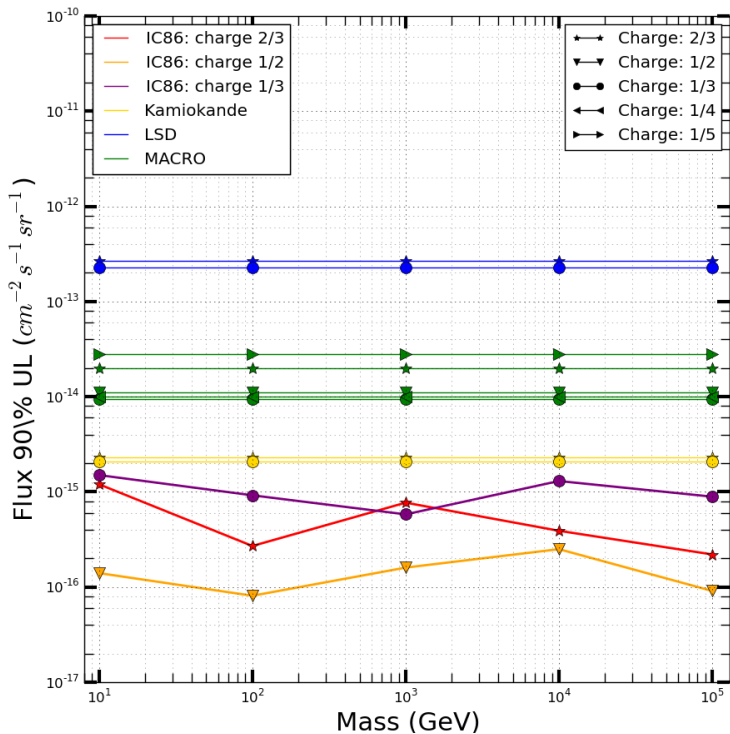


Figure 8.35: Final upper limits for SMPs with three different charges as a function of the mass. Previous experiments did not include a mass dependence and are therefore shown as straight lines.

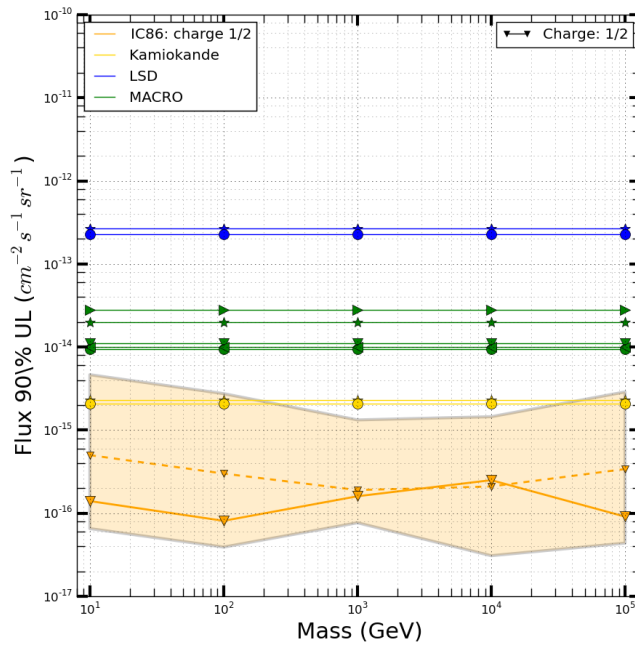


Figure 8.36: Comparison of other experiments to the upper limit obtained for SMPs with a charge 1/2 including the systematic error bands. The observed limit is shown with a solid line and the expected limit is shown with a dashed line. Other experiments did not have a mass dependence in the analysis and are therefore shown as straight lines.

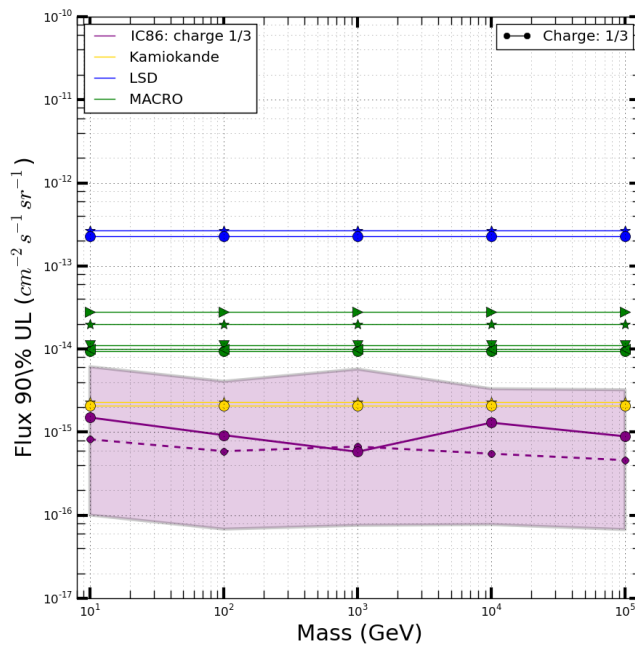


Figure 8.37: Comparison of other experiments to the upper limit obtained for SMPs with charge 1/3 including the systematic error bands. The observed limit is shown with a solid line and the expected limit is shown with a dashed line. Other experiments did not have a mass dependence in the analysis and are therefore shown as straight lines.

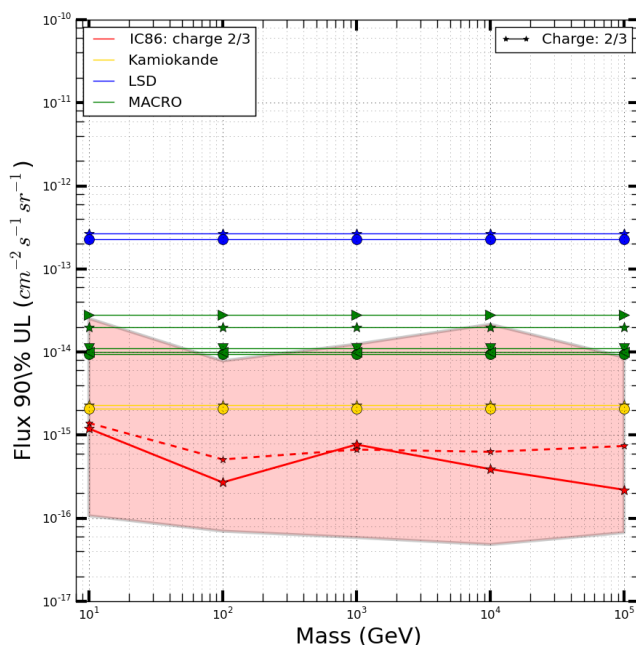


Figure 8.38: Comparison of other experiments to the upper limit obtained for SMPs with charge 2/3 including the systematic error bands. The observed limit is shown with a solid line and the expected limit is shown with a dashed line. Other experiments did not have a mass dependence in the analysis and are therefore shown as straight lines.



9. Summary and Conclusion

In this work a search for particles with an anomalous charge is obtained. These particles would have an electric charge lower than one, relative to the electron charge. The charges under investigation are $1/2$, $1/3$ and $2/3$; the masses assumed range from 10 GeV to 100 TeV, giving a total of 15 signal points. Due to the difference in charge, these particles produce less Cherenkov light as compared to muons.

Because these particles can have different signatures in the IceCube detector compared to known particles, it is possible to perform a search. Detecting these particles would provide a gateway to extensions of the Standard Model. There exists a plethora of possible models to include new physics, where the existence of particles with an anomalous charge would provide an indication of what model would be more feasible than others.

The particles were assumed to be isotropic in direction and follow an E^{-2} spectrum. The simulations were done by using the modules that are used to simulate muon interactions and changing the mass and charge in the cross-sections that are implemented in the code. Photon production, with the use of GPU intensive models, is scaled with the charge as predicted by the Frank-Tamm equation for Cherenkov photon production.

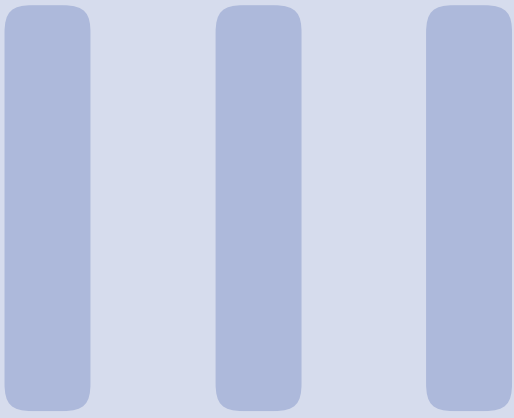
The analysis starts from data obtained from PnF from the IceCube detector that was gathered in the years 2011 to 2015 and include a total of 1723 days of livetime. The large amount of data is first sent through a series of quality cuts and cleaning algorithms. A resampling technique called pull-validation was used to handle the lack of statistics at the final level using a boosted decision tree.

We can conclude from this work that the number of data events is in agreement with the number of expected backgrounds, and therefore an upper limit on the flux of particles with an anomalous charge was determined. The observed limits are up to an order of magnitude more stringent than older experiments although a direct comparison is not well supported. All experiments set limits to a flux close to the detector, but do not include effects such as the shielding of rock or ice around the detector. Therefore, there is a need for better theoretical models that predict fluxes at the set detector locations.

Other possible improvements of the analysis should mainly focus on the triggering and filtering ef-

ficiencies of these very dim particles. Dedicated triggers and filters that do not exist for now could potentially make the limits an order of magnitude more stringent (or more), but are also expected to include more noise effects so that a proper estimate is not possible. In this analysis, boosted decision trees were used, but the last couple of years there have been many advances in other machine learning techniques, which could provide potential enhancements. Other possible improvements could come with the IceCube Upgrade and even IceCube-Gen2, but the former seems very small in instrumented volume to make use of the long tracks that are expected and the latter is even more coarsely spaced so that dim tracks will be almost indistinguishable from noise effects.

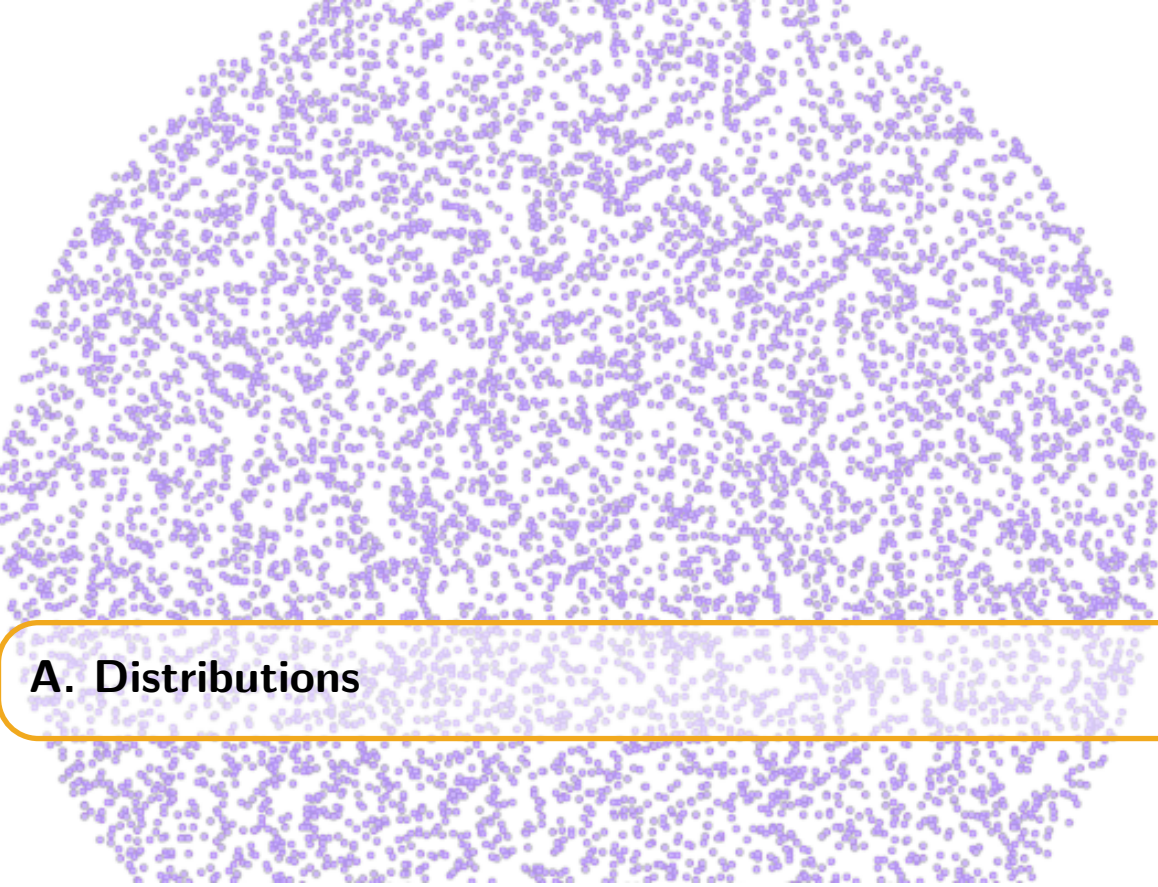
Anomalously charged particles remain undetected; the search for new physics is to be continued.



Additions

Appendices	161
A Distributions	163
A.1 Spherical random numbers	
A.2 Power law distributions	
A.3 Angular distributions	
A.4 Weighting	
B Boosted Decision Trees: examples	169
B.1 Decision Tree: simple example	
B.2 AdaBoost: simple example	
C Resampling Methods	173
C.1 Bootstrapping	
C.2 Cross-validation	
D Additional BDT Checks	175
E Data Events at Final Level	177
Bibliography	181

Appendices



A. Distributions

A.1 Spherical random numbers

Most random number generators provide uniform distributions between the range $[0, 1]$. Assume we want to make a uniform distribution along a sphere with angles ϕ and θ and radius r , in spherical coordinates. Random numbers between $[0, \pi]$, $[0, 2\pi]$ and $[0, R]$ (the ranges of the coordinates) would not give a uniform distribution as illustrated in Figure A.1 (left).

The differential surface area, dA , is equal to $dA(d\phi, d\theta) = r^2 \sin(\phi) d\phi d\theta$. If we want the distribution $f(v)$ to be constant for a uniform distribution, then $f(v) = \frac{1}{4\pi}$ since $\int \int_S f(v) dA = 1$ and $\int \int_S dA = 4\pi$. We want the distribution in function of the angles, so

$$f(v)dA = \frac{1}{4\pi}dA = f(r)f(\phi, \theta)d\phi d\theta. \quad (\text{A.1})$$

Since we know the expression for dA , we find that

$$f(\phi, \theta) = \frac{1}{4\pi} \sin(\phi), \quad (\text{A.2})$$

and separating the angles:

$$f(\theta) = \int_0^\pi f(\phi, \theta) d\phi = \frac{1}{2\pi}, \quad (\text{A.3})$$

$$f(\phi) = \int_0^{2\pi} f(\phi, \theta) d\theta = \frac{\sin(\phi)}{2}, \quad (\text{A.4})$$

where it is clear that $f(\phi)$ scales with $\sin(\phi)$; there are more points needed at the equator (this makes sense, as the surface at the equator is much larger!).

The question is now how one can get a sample to follow the distribution of $f(\phi)$. For this, we use the *inverse transform sampling* method where one makes use of the cumulative distribution function, $F(\phi)$, which increases monotonically

$$F(\phi) = \int_0^\phi f(\phi') d\phi' = \frac{1}{2} (1 - \cos(\phi)). \quad (\text{A.5})$$

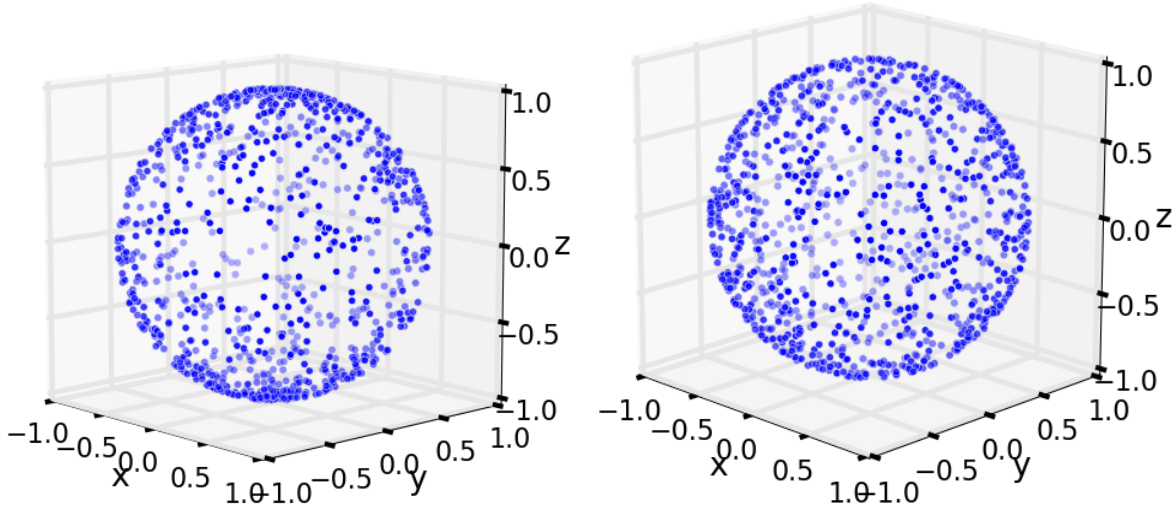


Figure A.1: *Left:* Illustration of a uniform sampling in angles ϕ and θ that doesn't give a uniform spherical distribution. *Right:* Illustration of a good spherical distribution.

The method shows that if u is a random variable drawn from a uniform distribution, we have to find the inverse function of F ,

$$F(F^{-1}(u)) = u \quad (\text{A.6})$$

$$\frac{1}{2} (1 - \cos(F^{-1}(u))) = u \quad (\text{A.7})$$

$$F^{-1}(u) = \arccos(1 - 2u). \quad (\text{A.8})$$

In other words: if u is a random variable drawn from a uniform distribution, then $\phi = \arccos(1 - 2u)$ follows a distribution necessary for a uniform spherical distribution. Similarly, $\theta = \frac{1}{2\pi}u$.

A.2 Power law distributions

Analogous to what was written in the previous section, one can produce a power law distribution from random numbers using the inverse transform sampling method:

$$\begin{aligned} f(E) &= A \cdot E^{-\gamma} \quad (\text{powerlaw}) \\ F(E) &= \int_{E_{\min}}^E A \cdot E^{-\gamma} dE = u \quad (\text{inverse sampling, } u \text{ random number } [0,1]) \\ &= A \left[\frac{E^{-\gamma+1}}{-\gamma + 1} \right]_{E_{\min}}^E \\ &= \frac{A}{-\gamma + 1} (E^{-\gamma+1} - E_{\min}^{-\gamma+1}) \end{aligned} \quad (\text{A.9})$$

Because we know that $F(F^{-1}(u)) = u$, we can find an expression for $F^{-1}(u)$:

$$\begin{aligned} u &= \frac{A}{-\gamma + 1} \left((F^{-1}(u))^{-\gamma+1} - E_{\min}^{-\gamma+1} \right) \\ &\Rightarrow \\ F^{-1}(u) &= \left(\left(\frac{-\gamma + 1}{A} \cdot u \right) + E_{\min}^{-\gamma+1} \right)^{1/(-\gamma+1)} \end{aligned} \quad (\text{A.10})$$

To find A , we use the property of a CDF:

$$F(E_{max}) = 1 \Rightarrow A = \frac{-\gamma + 1}{E_{max}^{-\gamma+1} - E_{min}^{-\gamma+1}}, \quad (\text{A.11})$$

leading to

$$F^{-1}(u) = \left((1-u) \cdot E_{min}^{-\gamma+1} + u \cdot E_{max}^{-\gamma+1} \right)^{1/(-\gamma+1)}, \quad (\text{A.12})$$

which shows how one can draw a distribution in function of E following $f(E)$ with a uniform random number u .

For $\gamma = -1$, the computations are analogous and one can see that this will produce a uniform distribution in log space. This is shown in Figure A.2.

$$\begin{aligned} E &= E_{min} \cdot 10^{u \cdot \log \frac{E_{max}}{E_{min}}} \\ &= 10^{u[\log E_{min}, \log E_{max}]} \end{aligned} \quad (\text{A.13})$$

In Figure A.3 the signal reweighting is shown.

A.3 Angular distributions

As seen in Section A.1, the differential space angle $d\Omega$ is equal to

$$d\Omega = \sin(\theta)d\theta d\phi. \quad (\text{A.14})$$

If one shows the distribution of ϕ and/or θ , then this is the same as showing partial integrations per bin. We find that

$$\Omega \propto \cos(\theta), \quad (\text{A.15})$$

or in other words: the space angle is proportional to the azimuth and the cosine of the zenith. An example is shown in Figure A.4.

A.4 Weighting

A method that is often used in simulations is *weighting*. The simulated and expected differential flux of particles is often not the same, mainly due to two reasons:

- The flux has no uniform power law behavior. As can be seen in Figure 3.2, there can be multiple “kinks” and changes in a spectrum. Instead of simulating the flux according to one model, a general uniform flux is used and later reweighted to be able to fit to other models more easily.
- A steep power law indicates very few events at the highest energy bins. This means large CPU time would be necessary to simulate these events. As an example, let us assume two different fluxes

$$f_1 = A \cdot x^{-1}, \quad (\text{A.16})$$

$$f_2 = B \cdot x^{-2}, \quad (\text{A.17})$$

where $A = 10^3$ and $B = 10^4$, so the fluxes cross at a value of $x^{-1+2} = x = \frac{10^4}{10^3} = 10$. In the interval $x \in [10^3, 10^4]$, the number of events for f_1 is equal to 10^3 , whereas for f_2 this is equal to 9.

Simulating with harder spectra* leads to more statistics in high-energy bins.

*Harder spectra equals to a lower gamma, since there will be more high-energy events.

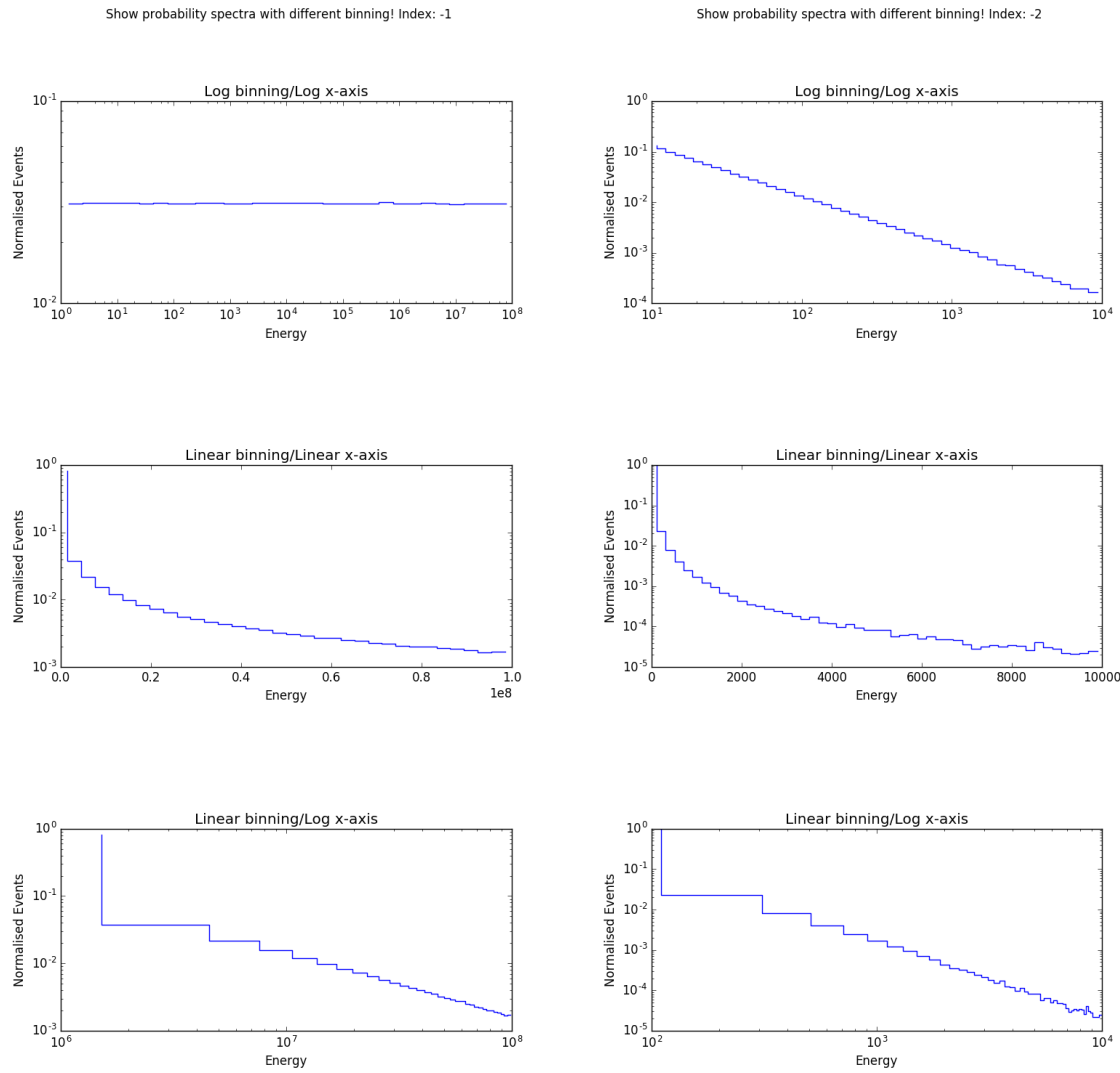


Figure A.2: *Left:* Histograms with different binnings showing the behavior of an energy spectrum with spectral index -1. *Right:* Histograms with different binnings showing the behavior of an energy spectrum with spectral index -2.

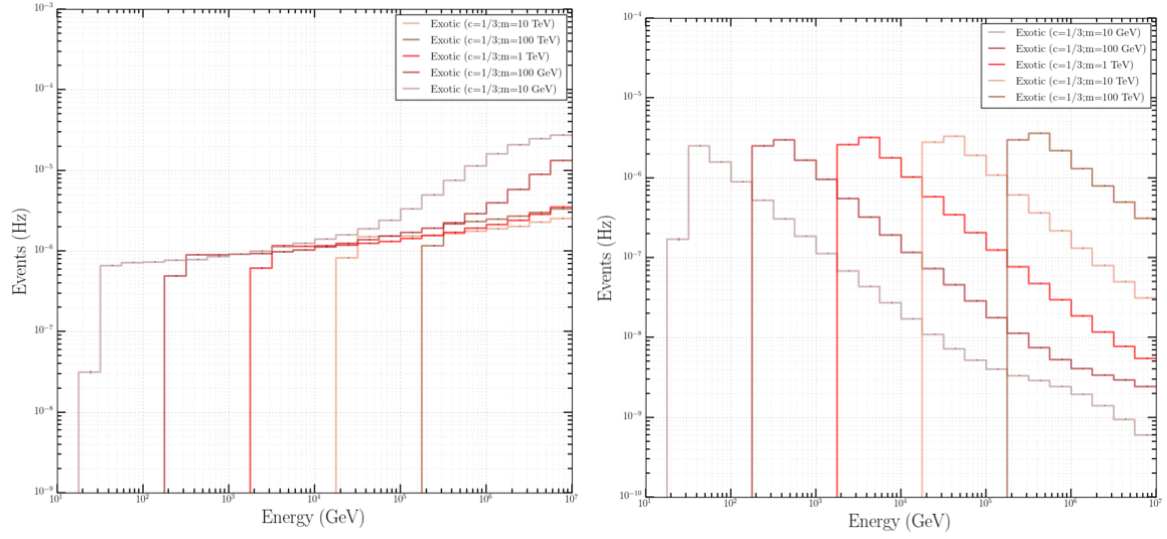


Figure A.3: *Left:* Spectrum of the signal before weighting following an E^{-1} spectrum. The rise in the rate in function of energy is due to the trigger efficiency that increases in function of energy. *Right:* Spectrum of the signal after reweighting to an energy spectrum of E^{-2} .

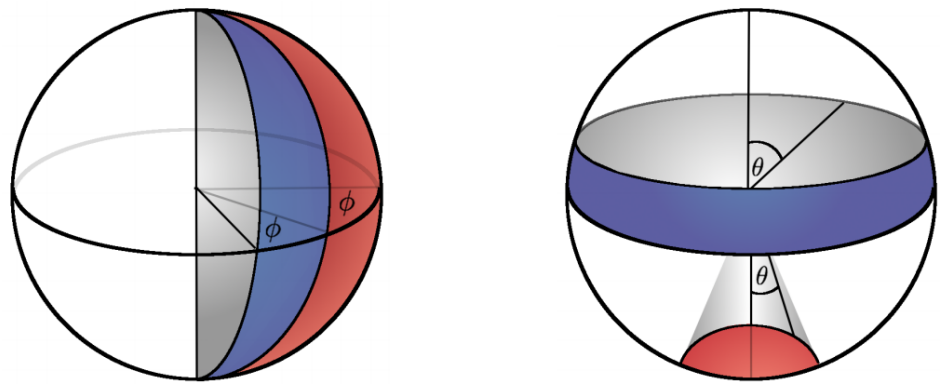


Figure A.4: Illustration of angle distributions in spherical coordinates. The blue and red surfaces are equal in size. The left figure clearly shows the surface to be proportional to the azimuth. The right figure shows how there is a non-trivial dependence on the zenith angle for equal partitions on the surface of a sphere.

The weights can be generally written down as

$$w = \frac{dN_{exp}}{dAd\Omega dEdt} \times \frac{dAd\Omega dE}{dN_{sim}}. \quad (\text{A.18})$$

A disadvantage of using weights is that certain events with a high weight are rare but can dominate or obscure the sample in the tails of certain distributions.



B. Boosted Decision Trees: examples

B.1 Decision Tree: simple example

Let us assume we want to categorize 6 people if they are *healthy* or *unhealthy*. The decision tree training can be done if we have a sample set that labels people in these two categories and some other information about these persons is known. In this example, we know if the person is older than 30, if he eats a lot of pizza and if he exercises a lot. This is summarized in Table B.1.

As an example, we can show how the first child nodes are determined. The sample set has three variables and the variable selection that allows for the largest separation (see Eq. 7.23) will be chosen. The results from ΔS for the age, pizza and exercises selections are 0, -1.7 and -2.6 respectively. Therefore, it should be clear that the age selection should be chosen first in the decision tree as it gives the largest separation for the child nodes. Deeper child nodes are selected in a similar fashion.

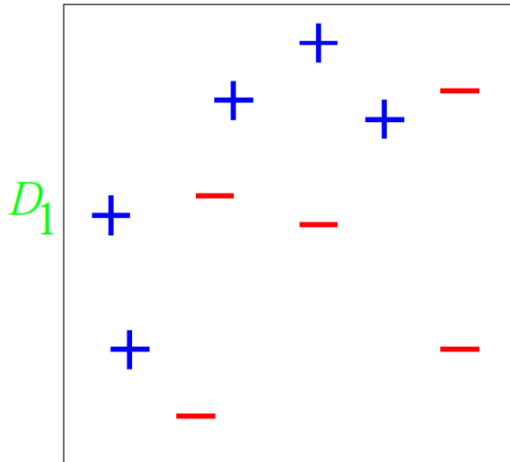
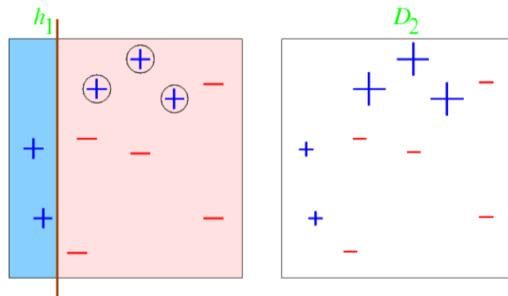
B.2 AdaBoost: simple example

Consider a binary decision tree classification with 10 training examples. The illustrations below are 2D variable distributions.

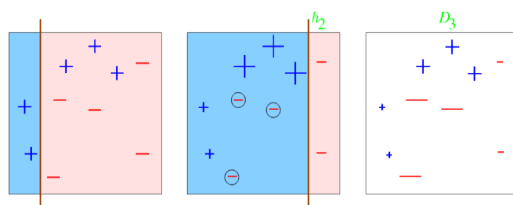
We give each event an equal weight, making the weight distribution D_1 uniform. For this simple example, each of our classifiers will be an axis-parallel linear classifier (simple cut in one of the two variables).

Table B.1: Summary of dataset used to train decision tree.

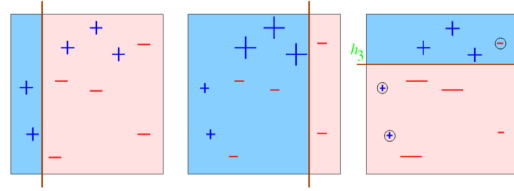
Person	Age <30	Eats lots of pizza	Exercises often	Healthy
A	1	1	1	0
B	1	0	1	1
C	1	0	0	1
D	0	0	0	0
E	0	0	1	1
F	0	0	1	1

Initial distribution**Round 1**

- Error rate of h_1 : $\epsilon_1 = 0.3$; weight of h_1 (see Eq. 7.25): $\alpha_1 = \frac{1}{2} \ln \left(\frac{1-\epsilon_1}{\epsilon_1} \right) = 0.42$
- An event that is misclassified gets a higher weight: weight multiplied with $\exp(\alpha_1)$
- An event that is correctly classified gets a lower weight: weight multiplied with $\exp(-\alpha_1)$

Round 2

- Error rate of h_1 : $\epsilon_1 = 0.21$; weight of h_2 (see Eq. 7.25): $\alpha_2 = \frac{1}{2} \ln \left(\frac{1-\epsilon_2}{\epsilon_2} \right) = 0.65$
- An event that is misclassified gets a higher weight: weight multiplied with $\exp(\alpha_2)$
- An event that is correctly classified gets a lower weight: weight multiplied with $\exp(-\alpha_2)$

Round 3

The error rate of h_1 : $\epsilon_1 = 0.21$; weight of h_2 (see Eq. 7.25): $\alpha_2 = \frac{1}{2} \ln \left(\frac{1-\epsilon_2}{\epsilon_2} \right) = 0.65$

Let us suppose to stop after this round, we now have a forest of 3 decision classifiers: h_1, h_2, h_3 .

Final step

The final classifier is a weighted linear combination of all the classifiers:

$$H_{\text{final}} = \text{sign} \left(0.42 \begin{array}{|c|} \hline \text{blue} \\ \hline \end{array} + 0.65 \begin{array}{|c|} \hline \text{blue} \\ \hline \end{array} + 0.92 \begin{array}{|c|} \hline \text{blue} \\ \hline \end{array} \right)$$

=

C. Resampling Methods

Resampling is a method used in statistical analyses and commonly refers to methods that extract information from a larger set by taking subsets and performing significance or validation tests. Two common examples are *bootstrapping* and *cross-validation* and are explained below.

C.1 Bootstrapping

The basic idea of bootstrapping is that we can draw conclusions from a certain sample in a larger, unknown, population by taking a subsample and performing inference about the sample from the subsample. The method assumes that the true probability distribution from a sample to a population can be reasonably estimated from an empirical probability distribution from a subsample to a sample.

Assume we have a total population P of size N_P and a measured sample N of size N_N , where

$$N_N < N_P \text{ and } N \subset P. \quad (\text{C.1})$$

From N , only one estimate of the mean can be computed. To get a sense of the variability one could assume a Gaussian or Poissonian probability, or what is done in this method: form a new subsample that is also of size N_N . This can only be done by *sampling with replacement* where the elements in the subsample can be repeated. If N_N is sufficiently large, this will almost certainly result in subsamples that are different from the original sample. The mean can be computed from the new subsample and this process is repeated a large number of times (typically of the order of 1,000). The distribution of the means then indicates our confidence in the sample mean where a large variability assumes large uncertainties.

C.2 Cross-validation

Another example of a resampling method is cross-validation, sometimes called *rotation estimation*, where one wants to estimate the predictive power of a model. From a sample, a subsample called the *training sample* is selected to train a model (e.g. a BDT). This model is then checked on another subsample called the *testing sample*. This allows to estimate how the model will generalize to other independent datasets. Training samples will often have a lower performance in parameter estimations from the testing sample than the training sample. In cross-validation

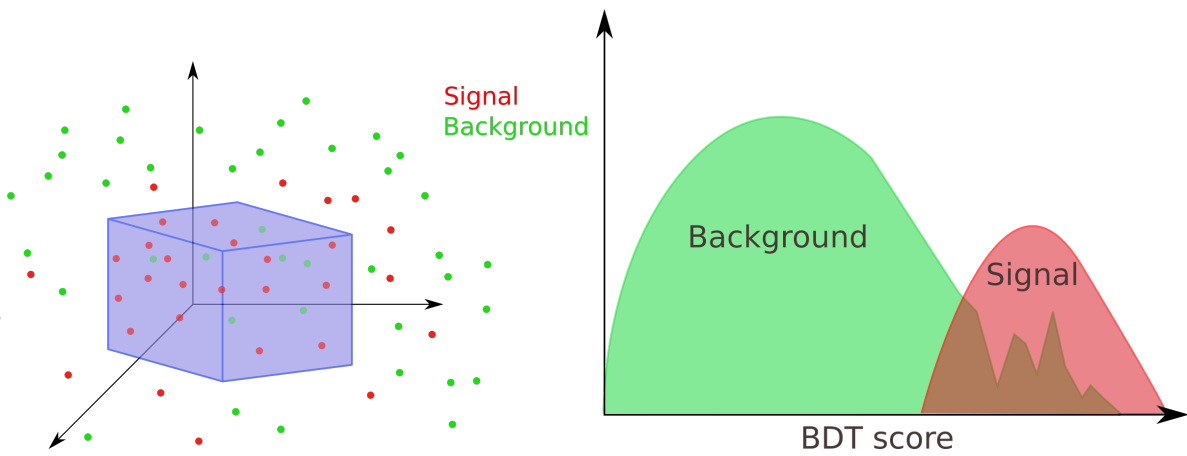


Figure C.1: Simplistic illustration of parameter space that originates from one branch in one BDT. The axes represent physical parameters that are used in the BDT. The blue box illustrates an example of cuts that are placed on the parameters. The BDT algorithm converts the survival probability of an event regarding these cuts into a score. Limited statistics for the background events are represented by a discontinuous tail.

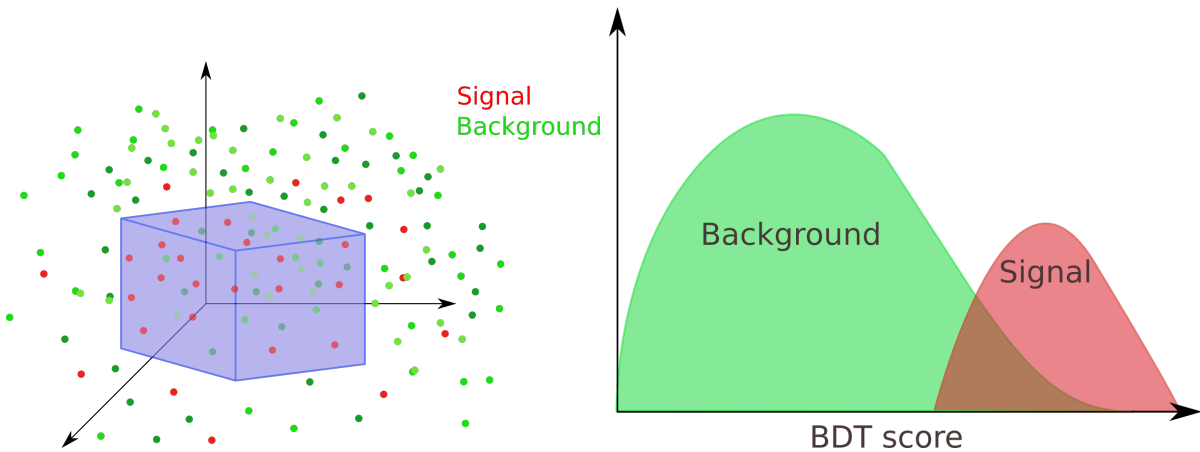


Figure C.2: Simplistic illustration of parameter space that originates from one branch in one BDT. Resampling the background (different green points) results in more statistics in the tail.

one tries to get an estimate for this effect. An often used cross-validation method is called *k-fold cross-validation*.

In this method, one iterates the procedure of selecting a training sample and a testing sample k times. If the total size of the sample set is N_N , the testing samples will have a size of N_N/k . As we have k iterations, the subsamples can be chosen without replacement and are unique each time. At each iteration, the training sample will have a size of $N_N - \frac{N_N}{k} = N_N \cdot \frac{k-1}{k}$. The k results can then be averaged to produce a single estimation.

Pull-validation is another example of a resampling method and is explained in more detail in Section 8.4.2. Illustratively, it can be visualized as in Figs. C.1 and C.2.

D. Additional BDT Checks

As explained in Section 7.7, it is important to perform some checks to see if a BDT is performing normally. A first check is done to see if the distribution of the training and testing samples show significant differences. This is shown in Figure D.1 and explained in more detail in Section 7.7.4.

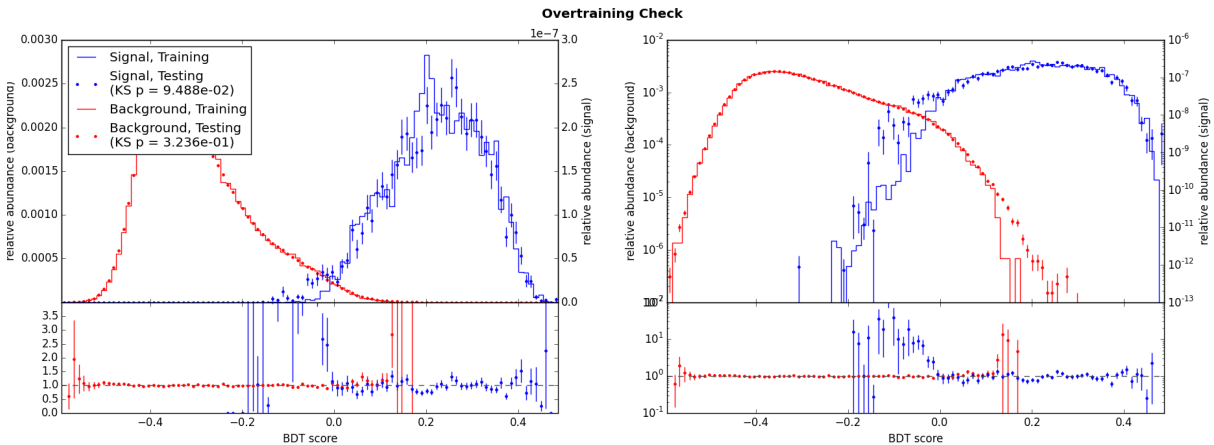


Figure D.1: No significant overtraining seems to be present in signal and background. The signal used here is an SMP of charge $\frac{1}{2}$ and mass 100 GeV.

The correlation between the 17 variables that were used in the BDT is shown in Figure D.2. These variables were selected with the mRMR feature, which shows an excellent performance since there are no significant correlations in both signal and background visible.

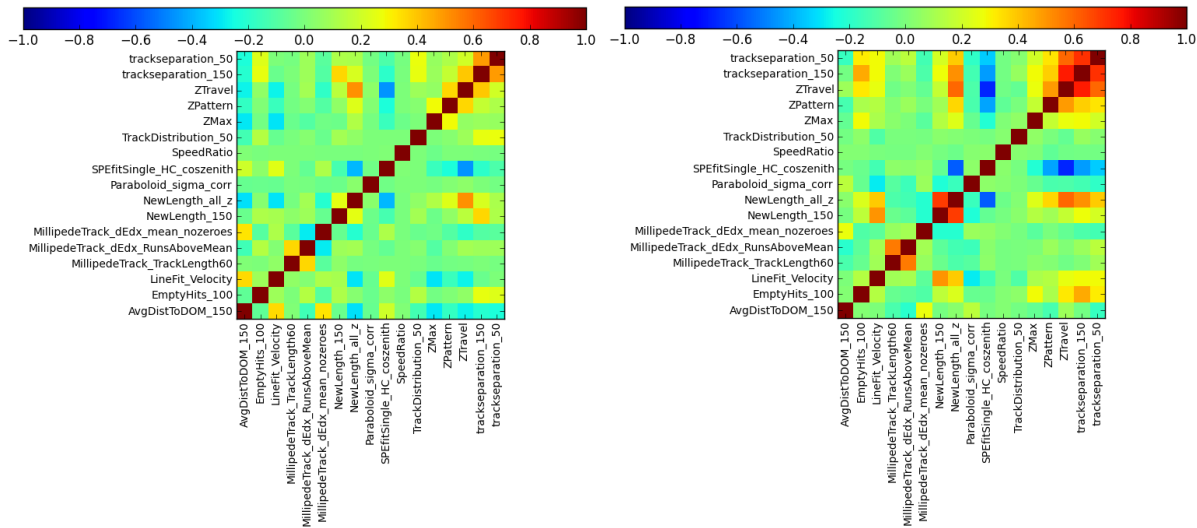


Figure D.2: Here we see the correlation between the variables that are used in the BDT. There is no significant correlation in *both* signal and background, making these variables appropriate to use.

E. Data Events at Final Level

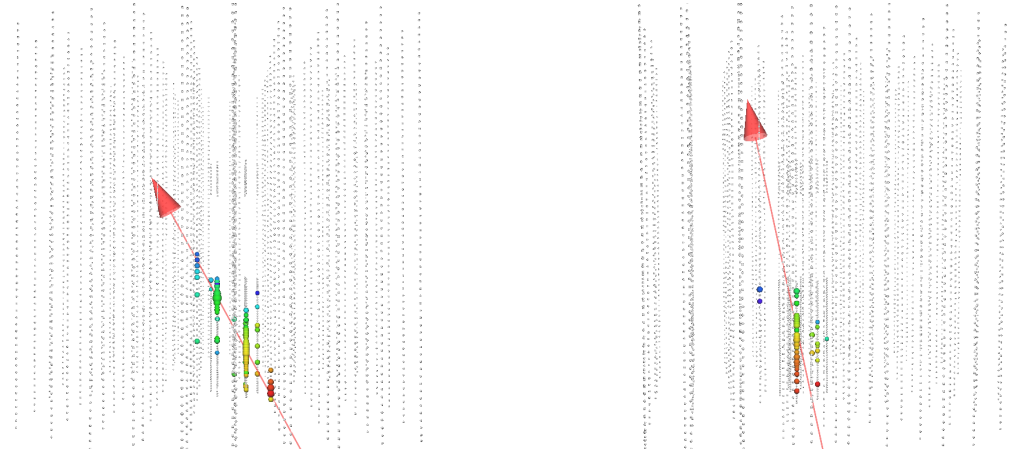


Figure E.1: Event display of events that survive the SMP with mass 10 TeV and charge 1/2 selection. *Left (real data):* A short and bright upgoing tracks corresponds to μ from an atmospheric ν_μ that stopped shortly after leaving DeepCore. *Right:* Simulated atmospheric ν_μ event that strongly resembles this data event.

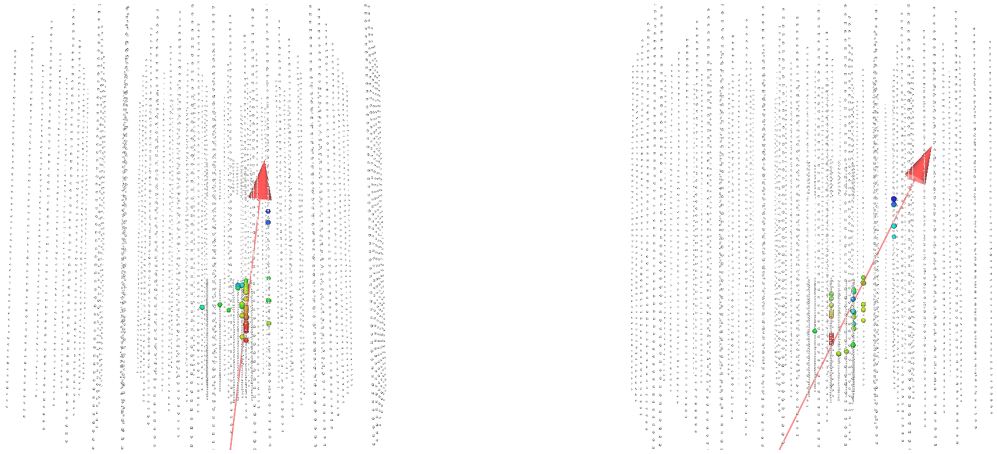


Figure E.2: Event display of events that survive the SMP with mass 10 TeV and charge 1/2 selection. *Left (real data):* Corresponds to an upgoing μ from atmospheric ν_μ that either starts or “corridors” in between strings and skims DeepCore along the side. After leaving DeepCore it only passes close to one string, giving the two hits. *Right:* Simulated atmospheric ν_μ event that strongly resembles this data event.

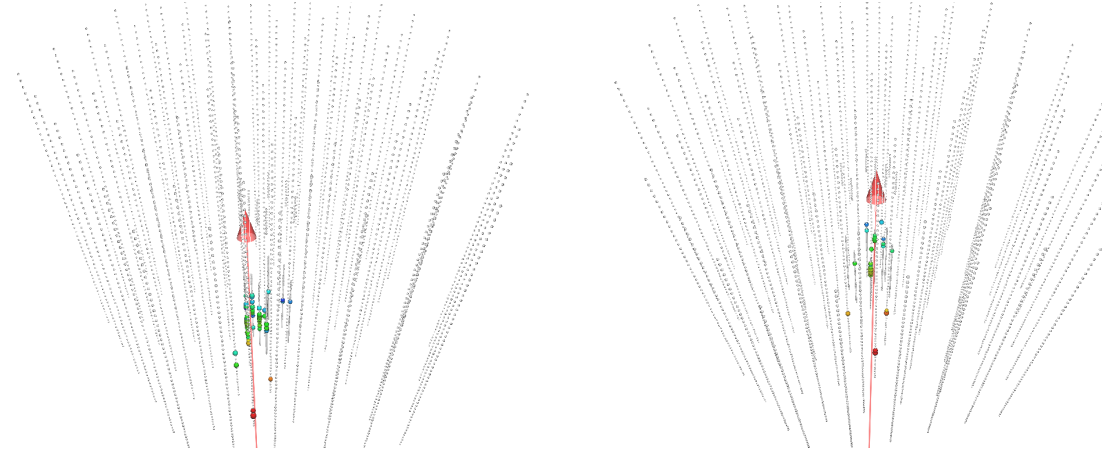


Figure E.3: Event display of events that survive the SMP with mass 10 GeV and charge 1/3 selection. *Left (real data):* Corresponds to a horizontal μ from atmospheric ν_μ that passes close to one string in IceCube and stops in DeepCore where more light is recorded. *Right:* Simulated atmospheric ν_μ event that strongly resembles this data event.

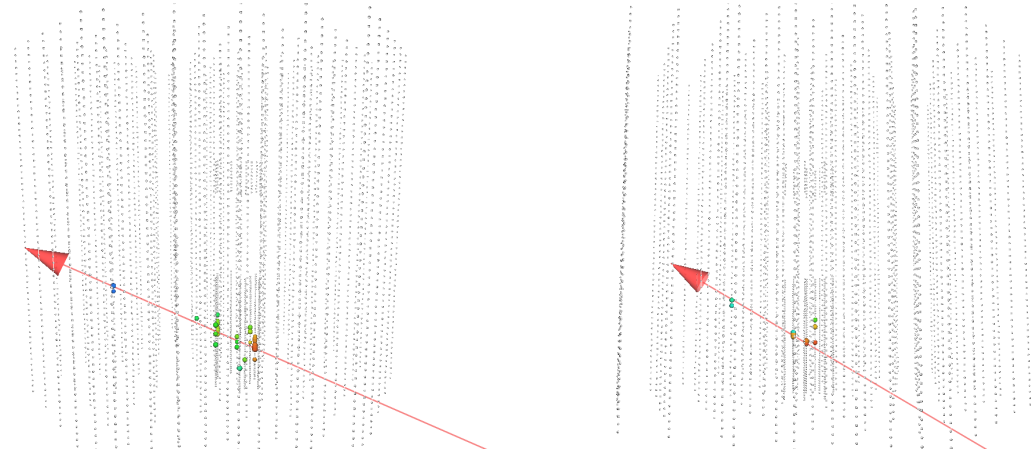


Figure E.4: *Left:* Typical simulated SMP of 100 GeV and charge 1/2 that survives the final selection. *Right:* Typical simulated SMP of 100 GeV and charge 1/3 that survives the final selection. Note that there is a lot less light produced compared to particles with higher charges.

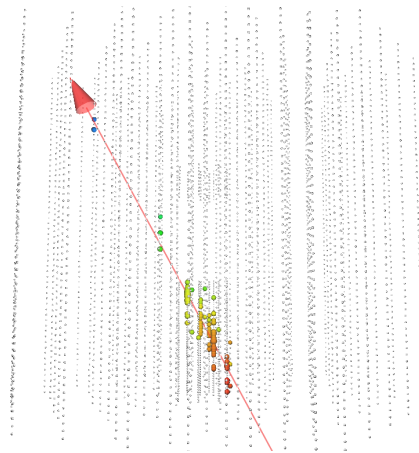
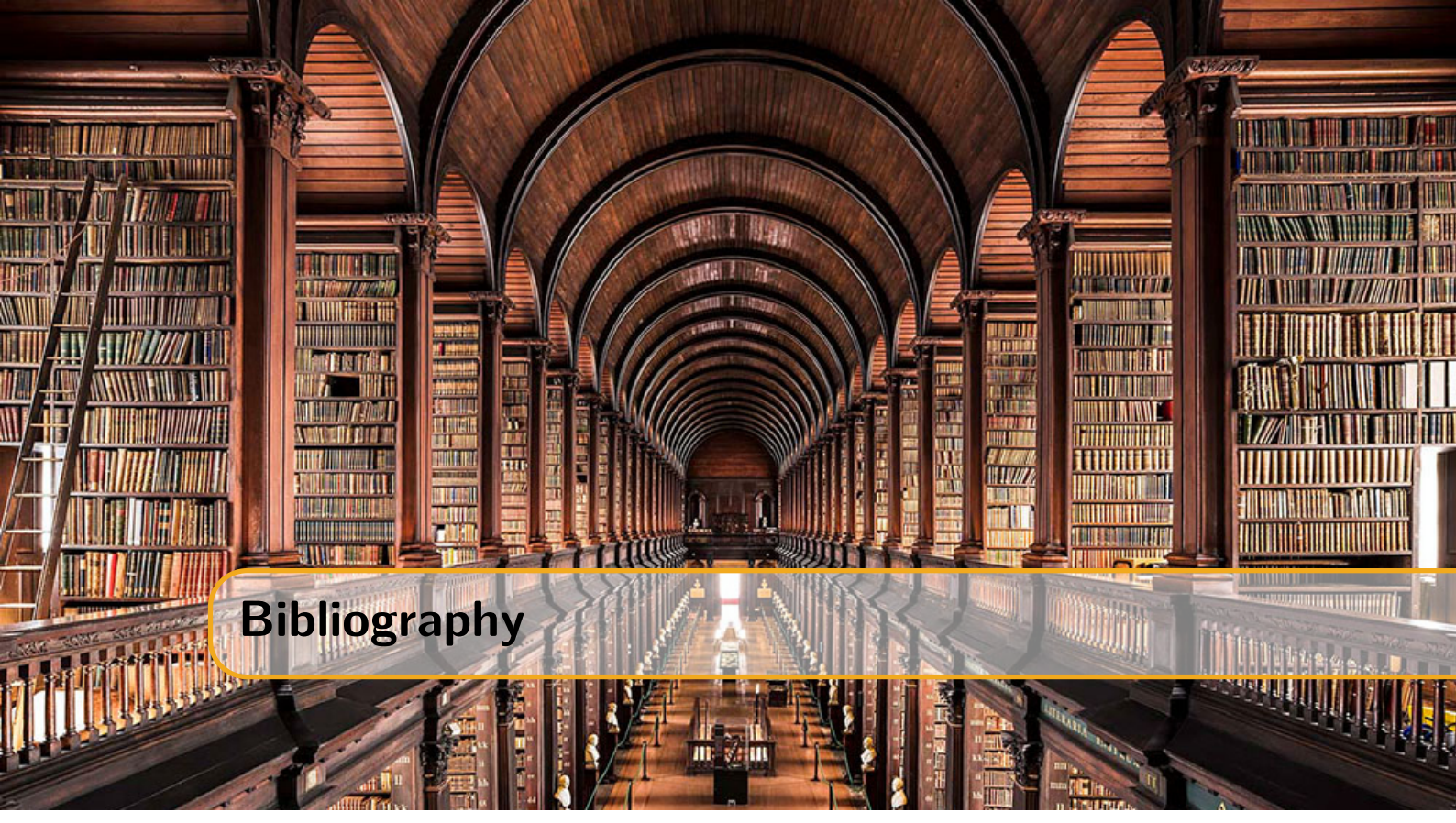


Figure E.5: Typical simulated SMP of 100 GeV and charge 1/3 that survives the final selection. Note that there is a lot more light produced compared to particles with lower charges.



Bibliography

- [1] B. Povh et al. *Particles and nuclei: An Introduction to the physical concepts*. 1995. DOI: 10.1007/3-540-36684-9 (cited on page 13).
- [2] Michael E. Peskin and Daniel V. Schroeder. *An Introduction to quantum field theory*. Reading, USA: Addison-Wesley, 1995. URL: <http://www.slac.stanford.edu/~mpeskin/QFT.html> (cited on page 13).
- [3] M. Tanabashi et al. “Review of Particle Physics”. In: *Phys. Rev. D* 98 (2018), page 030001 (cited on page 13).
- [4] Alessandro Bettini. *Introduction to elementary particle physics*. 2008. ISBN: 9780521880213. URL: <http://www.cambridge.org/catalogue/catalogue.asp?isbn=9780521880213> (cited on page 13).
- [5] CERN. URL: <https://home.cern/about/physics/standard-model> (cited on page 14).
- [6] Arthur B. McDonald. “Nobel Lecture: The Sudbury Neutrino Observatory: Observation of flavor change for solar neutrinos”. In: *Rev. Mod. Phys.* 88 (3 July 2016), page 030502. DOI: 10.1103/RevModPhys.88.030502. URL: <https://link.aps.org/doi/10.1103/RevModPhys.88.030502> (cited on page 15).
- [7] CMS. URL: <http://cms.web.cern.ch/news/jets-cms-and-determination-their-energy-scale> (cited on page 15).
- [8] URL: <http://hyperphysics.phy-astr.gsu.edu/hbase/Forces/couple.html#c1> (cited on page 16).
- [9] A. Kircher. *Athanassii Kircherii... Magnes, sive De arte magnetica opus tripartitum...* sumptibus H. Scheus, 1641. URL: <https://books.google.be/books?id=1aZ3FcTAYdUC> (cited on page 16).
- [10] G. Farmelo. *The Strangest Man: The Hidden Life of Paul Dirac, Mystic of the Atom*. Basic Books, 2009. ISBN: 9780465019922. URL: <https://books.google.be/books?id=qsodmIGDOfMC> (cited on page 17).
- [11] F. Mandl and G. Shaw. *Quantum Field Theory*. Wiley, 2013. ISBN: 9781118716656. URL: <https://books.google.be/books?id=jTBzQfctvHAC> (cited on page 18).
- [12] Flip Tanedo. URL: <https://www.quantumdiaries.org/2012/02/14/why-do-we-expect-a-higgs-boson-part-ii-unitarization-of-vector-boson-scattering/> (cited on page 21).

- [13] S. L. Glashow, J. Iliopoulos, and L. Maiani. “Weak Interactions with Lepton-Hadron Symmetry”. In: *Phys. Rev.* D2 (1970), pages 1285–1292. DOI: 10.1103/PhysRevD.2.1285 (cited on page 25).
- [14] J. H. Christenson et al. “Evidence for the 2π Decay of the K20 Meson”. In: *Physical Review Letters* 13 (July 1964), pages 138–140. DOI: 10.1103/PhysRevLett.13.138 (cited on page 25).
- [15] Ziro Maki, Masami Nakagawa, and Shoichi Sakata. “Remarks on the Unified Model of Elementary Particles”. In: *Progress of Theoretical Physics* 28.5 (1962), pages 870–880. DOI: 10.1143/PTP.28.870. eprint: /oup/backfile/content_public/journal/ptp/28/5/10.1143/ptp.28.870/2/28-5-870.pdf. URL: <http://dx.doi.org/10.1143/PTP.28.870> (cited on page 25).
- [16] Claudio Giganti, Stéphane Lavignac, and Marco Zito. “Neutrino oscillations: the rise of the PMNS paradigm”. In: *Prog. Part. Nucl. Phys.* 98 (2018), pages 1–54. DOI: 10.1016/j.ppnp.2017.10.001. arXiv: 1710.00715 [hep-ex] (cited on page 25).
- [17] C. D. Anderson. “The Positive Electron”. In: *Phys. Rev.* 43 (1933), pages 491–494. DOI: 10.1103/PhysRev.43.491 (cited on page 26).
- [18] Paul A. M. Dirac. “The quantum theory of the electron”. In: *Proc. Roy. Soc. Lond.* A117 (1928), pages 610–624. DOI: 10.1098/rspa.1928.0023 (cited on page 26).
- [19] S. H. Neddermeyer and C. D. Anderson. “Note on the Nature of Cosmic Ray Particles”. In: *Phys. Rev.* 51 (1937), pages 884–886. DOI: 10.1103/PhysRev.51.884 (cited on page 26).
- [20] C. M. G. Lattes et al. “PROCESSES INVOLVING CHARGED MESONS”. In: *Nature* 159 (1947). [,42(1947)], pages 694–697. DOI: 10.1038/159694a0 (cited on page 26).
- [21] F. J. Hasert et al. “Observation of Neutrino Like Interactions Without Muon Or Electron in the Gargamelle Neutrino Experiment”. In: *Phys. Lett.* B46 (1973). [,5.15(1973)], pages 138–140. DOI: 10.1016/0370-2693(73)90499-1 (cited on page 26).
- [22] G. Arnison et al. “Experimental Observation of Isolated Large Transverse Energy Electrons with Associated Missing Energy at $s^{**}(1/2) = 540\text{-GeV}$ ”. In: *Phys. Lett.* B122 (1983). [,611(1983)], pages 103–116. DOI: 10.1016/0370-2693(83)91177-2 (cited on page 26).
- [23] G. Arnison et al. “Experimental Observation of Lepton Pairs of Invariant Mass Around $95\text{-GeV}/c^{**2}$ at the CERN SPS Collider”. In: *Phys. Lett.* B126 (1983). [,7.55(1983)], pages 398–410. DOI: 10.1016/0370-2693(83)90188-0 (cited on page 26).
- [24] S. W. Herb et al. “Observation of a Dimuon Resonance at 9.5-GeV in 400-GeV Proton-Nucleus Collisions”. In: *Phys. Rev. Lett.* 39 (1977), pages 252–255. DOI: 10.1103/PhysRevLett.39.252 (cited on page 26).
- [25] F. Abe et al. “Observation of top quark production in $\bar{p}p$ collisions”. In: *Phys. Rev. Lett.* 74 (1995), pages 2626–2631. DOI: 10.1103/PhysRevLett.74.2626. arXiv: hep-ex/9503002 [hep-ex] (cited on page 26).
- [26] D. P. Barber et al. “Discovery of Three Jet Events and a Test of Quantum Chromodynamics at PETRA Energies”. In: *Phys. Rev. Lett.* 43 (1979), page 830. DOI: 10.1103/PhysRevLett.43.830 (cited on page 26).
- [27] S. Schael et al. “Precision electroweak measurements on the Z resonance”. In: *Phys. Rept.* 427 (2006), pages 257–454. DOI: 10.1016/j.physrep.2005.12.006. arXiv: hep-ex/0509008 [hep-ex] (cited on page 26).
- [28] Sabine Riemann. “Precision electroweak physics at high energies”. In: *Rept. Prog. Phys.* 73 (2010), page 126201. DOI: 10.1088/0034-4885/73/12/126201 (cited on page 26).
- [29] Kenji Abe et al. “A High precision measurement of the left-right Z boson cross-section asymmetry”. In: *Phys. Rev. Lett.* 84 (2000), pages 5945–5949. DOI: 10.1103/PhysRevLett.84.5945. arXiv: hep-ex/0004026 [hep-ex] (cited on page 26).

- [30] Koya Abe et al. “First direct measurement of the parity violating coupling of the Z0 to the s quark”. In: *Phys. Rev. Lett.* 85 (2000), pages 5059–5063. DOI: 10.1103/PhysRevLett.85.5059. arXiv: hep-ex/0006019 [hep-ex] (cited on page 26).
- [31] Koya Abe et al. “An Improved direct measurement of leptonic coupling asymmetries with polarized Z bosons”. In: *Phys. Rev. Lett.* 86 (2001), pages 1162–1166. DOI: 10.1103/PhysRevLett.86.1162. arXiv: hep-ex/0010015 [hep-ex] (cited on page 26).
- [32] K. Abe et al. “First measurement of the left-right charge asymmetry in hadronic Z boson decays and a new determination of $\sin^{**2} \theta(W)(\text{eff})$ ”. In: *Phys. Rev. Lett.* 78 (1997), pages 17–21. DOI: 10.1103/PhysRevLett.78.17. arXiv: hep-ex/9609019 [hep-ex] (cited on page 26).
- [33] Timo Antero Aaltonen et al. “Combination of CDF and D0 W-Boson Mass Measurements”. In: *Phys. Rev.* D88.5 (2013), page 052018. DOI: 10.1103/PhysRevD.88.052018. arXiv: 1307.7627 [hep-ex] (cited on page 26).
- [34] “Combination of CDF and D0 Results on the Width of the W boson”. In: (2010). arXiv: 1003.2826 [hep-ex] (cited on page 26).
- [35] Morad Aaboud et al. “Measurement of the W-boson mass in pp collisions at $\sqrt{s} = 7$ TeV with the ATLAS detector”. In: *Eur. Phys. J.* C78.2 (2018), page 110. DOI: 10.1140/epjc/s10052-017-5475-4. arXiv: 1701.07240 [hep-ex] (cited on page 26).
- [36] ATLAS. URL: cds.cern.ch/record/2285809/files/ATLAS-CONF-2017-071.pdf (cited on page 26).
- [37] CMS. URL: cds.cern.ch/record/2235162/files/TOP-15-012-pas.pdf (cited on page 26).
- [38] CMS. URL: cds.cern.ch/record/2284594/files/TOP-17-007-pas.pdf (cited on page 26).
- [39] NA62 collaboration. URL: <https://indico.cern.ch/event/714178/> (cited on page 26).
- [40] Cari Cesarotti et al. “Interpreting the Electron EDM Constraint”. In: (2018). arXiv: 1810.07736 [hep-ph] (cited on page 27).
- [41] M. G. Aartsen et al. “Measurement of the multi-TeV neutrino cross section with IceCube using Earth absorption”. In: *Nature* 551 (2017), pages 596–600. DOI: 10.1038/nature24459. arXiv: 1711.08119 [hep-ex] (cited on page 27).
- [42] Andrea Castro. “Recent Top Quark Mass Measurements from CMS”. In: *Proceedings, 10th International Workshop on Top Quark Physics (TOP2017): Braga, Portugal, September 17-22, 2017*. 2017. arXiv: 1712.01027 [hep-ex] (cited on page 27).
- [43] PDG. URL: <http://pdg.lbl.gov/2018/reviews/rpp2018-rev-standard-model.pdf> (cited on pages 27, 29, 44, 52, 59, 64).
- [44] P. A. R. Ade et al. “Planck 2015 results. XIII. Cosmological parameters”. In: *Astron. Astrophys.* 594 (2016), A13. DOI: 10.1051/0004-6361/201525830. arXiv: 1502.01589 [astro-ph.CO] (cited on page 28).
- [45] Evgige Corbelli and Paolo Salucci. “The Extended Rotation Curve and the Dark Matter Halo of M33”. In: *Mon. Not. Roy. Astron. Soc.* 311 (2000), pages 441–447. DOI: 10.1046/j.1365-8711.2000.03075.x. arXiv: astro-ph/9909252 [astro-ph] (cited on page 28).
- [46] S. M. Faber and R. E. Jackson. “Velocity dispersions and mass to light ratios for elliptical galaxies”. In: *Astrophys. J.* 204 (1976), page 668. DOI: 10.1086/154215 (cited on page 28).
- [47] Steven W. Allen, August E. Evrard, and Adam B. Mantz. “Cosmological Parameters from Observations of Galaxy Clusters”. In: *Ann. Rev. Astron. Astrophys.* 49 (2011), pages 409–470. DOI: 10.1146/annurev-astro-081710-102514. arXiv: 1103.4829 [astro-ph.CO] (cited on page 28).

- [48] Priyamvada Natarajan et al. “Mapping substructure in the HST Frontier Fields cluster lenses and in cosmological simulations”. In: *Mon. Not. Roy. Astron. Soc.* 468.2 (2017), pages 1962–1980. DOI: 10.1093/mnras/stw3385. arXiv: 1702.04348 [astro-ph.GA] (cited on page 28).
- [49] John F. Donoghue. “The effective field theory treatment of quantum gravity”. In: *AIP Conf. Proc.* 1483 (2012), pages 73–94. DOI: 10.1063/1.4756964. arXiv: 1209.3511 [gr-qc] (cited on page 28).
- [50] C. D. McCoy. “Does inflation solve the hot big bang model’s fine-tuning problems?” In: *Stud. Hist. Phil. Sci.* B51 (2015), pages 23–36. DOI: 10.1016/j.shpsb.2015.06.002 (cited on page 28).
- [51] R. D. Peccei. “The Strong CP problem and axions”. In: *Lect. Notes Phys.* 741 (2008). [,3(2006)], pages 3–17. DOI: 10.1007/978-3-540-73518-2_1. arXiv: hep-ph/0607268 [hep-ph] (cited on page 29).
- [52] C. Amsler et al. “Review of Particle Physics”. In: *Physics Letters B* 667.1 (2008). Review of Particle Physics, pages 1–6. ISSN: 0370-2693. DOI: <https://doi.org/10.1016/j.physletb.2008.07.018>. URL: <http://www.sciencedirect.com/science/article/pii/S0370269308008435> (cited on page 29).
- [53] Georges Aad et al. “Combined Measurement of the Higgs Boson Mass in pp Collisions at $\sqrt{s} = 7$ and 8 TeV with the ATLAS and CMS Experiments”. In: *Phys. Rev. Lett.* 114 (2015), page 191803. DOI: 10.1103/PhysRevLett.114.191803. arXiv: 1503.07589 [hep-ex] (cited on page 29).
- [54] Susanne Mertens. “Direct Neutrino Mass Experiments”. In: *J. Phys. Conf. Ser.* 718.2 (2016), page 022013. DOI: 10.1088/1742-6596/718/2/022013. arXiv: 1605.01579 [nucl-ex] (cited on page 29).
- [55] Ivan Esteban et al. “Updated fit to three neutrino mixing: exploring the accelerator-reactor complementarity”. In: *JHEP* 01 (2017), page 087. DOI: 10.1007/JHEP01(2017)087. arXiv: 1611.01514 [hep-ph] (cited on page 29).
- [56] NuFIT. URL: <http://www.nu-fit.org/?q=node/177> (cited on page 29).
- [57] nobel2004. URL: <https://www.nobelprize.org/prizes/physics/2004/popular-information/> (cited on page 30).
- [58] Xiao-Gang He, Girish C. Joshi, and B. H. McKellar. “The Quantization of the Electric Charge in Gauge Theories”. In: *Europhys. Lett.* 10 (1989), page 709. DOI: 10.1209/0295-5075/10/8/002 (cited on pages 30, 33).
- [59] Stefano Bertolini, Luca Di Luzio, and Michal Malinsky. “Intermediate mass scales in the non-supersymmetric SO(10) grand unification: A Reappraisal”. In: *Phys. Rev.* D80 (2009), page 015013. DOI: 10.1103/PhysRevD.80.015013. arXiv: 0903.4049 [hep-ph] (cited on page 30).
- [60] Hong-Wei Yu. “SU(8) GUT MODELS WITH STABLE PROTON, N ANTI-N OSCILLATIONS, FRACTIONAL CHARGES AND LOW MASS MONOPOLES”. In: *Phys. Lett.* 142B (1984), pages 42–46. DOI: 10.1016/0370-2693(84)91132-8 (cited on pages 30, 34).
- [61] Xiao-Gang Wen and Edward Witten. “Electric and Magnetic Charges in Superstring Models”. In: *Nucl. Phys.* B261 (1985), pages 651–677. DOI: 10.1016/0550-3213(85)90592-9 (cited on pages 31, 34).
- [62] Gregory G. Athanasiou et al. “Remarks on Wilson Lines, Modular Invariance and Possible String Relics in Calabi-yau Compactifications”. In: *Phys. Lett.* B214 (1988), pages 55–62. DOI: 10.1016/0370-2693(88)90451-0 (cited on pages 31, 34).
- [63] Stephen M. Barr, D. B. Reiss, and A. Zee. “Fractional Charges, Monopoles and Peculiar Photons”. In: *Phys. Rev. Lett.* 50 (1983), page 317. DOI: 10.1103/PhysRevLett.50.317 (cited on page 34).

- [64] P. H. Frampton and T. W. Kephart. “Fractionally Charged Particles as Evidence for Supersymmetry”. In: *Phys. Rev. Lett.* 49 (1982), page 1310. DOI: 10.1103/PhysRevLett.49.1310 (cited on page 34).
- [65] Katsuji Yamamoto. “Fractionally Charged Leptons in the SO(14) GUT”. In: *Phys. Lett.* 120B (1983), pages 157–160. DOI: 10.1016/0370-2693(83)90643-3 (cited on page 34).
- [66] Fang-xiao Dong et al. “Fractional Charges, Monopoles and Peculiar Photons in SO(18) GUT Models”. In: *Phys. Lett.* 129B (1983), pages 405–410. DOI: 10.1016/0370-2693(83)90129-6 (cited on page 34).
- [67] Xiang-Dong Jiang and Xian-Jian Zhou. “SO(10) X SO(8) MODEL WITH FRACTIONAL CHARGES, MONOPOLES AND PECULIAR PHOTONS. (IN CHINESE)”. In: *HEPNP* 9 (1985), pages 421–429 (cited on page 34).
- [68] K. Abe et al. “Search for proton decay via $p \rightarrow e^+ \pi^0$ and $p \rightarrow \mu^+ \pi^0$ in 0.31 megaton years exposure of the Super-Kamiokande water Cherenkov detector”. In: *Phys. Rev.* D95.1 (2017), page 012004. DOI: 10.1103/PhysRevD.95.012004. arXiv: 1610.03597 [hep-ex] (cited on page 34).
- [69] Ignatios Antoniadis and K. Benakli. “Fractionally charged particles and supersymmetry breaking in 4-D strings”. In: *Phys. Lett.* B295 (1992). [Erratum: *Phys. Lett.* B407,449(1997)], pages 219–224. DOI: 10.1016/S0370-2693(97)00755-7, 10.1016/0370-2693(92)91557-P. arXiv: hep-th/9209020 [hep-th] (cited on page 34).
- [70] Bob Holdom. “Two U(1)’s and Epsilon Charge Shifts”. In: *Phys. Lett.* 166B (1986), pages 196–198. DOI: 10.1016/0370-2693(86)91377-8 (cited on page 34).
- [71] Eder Izquierre and Itay Yavin. “New window to millicharged particles at the LHC”. In: *Phys. Rev.* D92.3 (2015), page 035014. DOI: 10.1103/PhysRevD.92.035014. arXiv: 1506.04760 [hep-ph] (cited on page 34).
- [72] David E. Brahm and Lawrence J. Hall. “U(1)-prime DARK MATTER”. In: *Phys. Rev.* D41 (1990), page 1067. DOI: 10.1103/PhysRevD.41.1067 (cited on page 34).
- [73] C. Boehm and Pierre Fayet. “Scalar dark matter candidates”. In: *Nucl. Phys.* B683 (2004), pages 219–263. DOI: 10.1016/j.nuclphysb.2004.01.015. arXiv: hep-ph/0305261 [hep-ph] (cited on page 34).
- [74] Maxim Pospelov, Adam Ritz, and Mikhail B. Voloshin. “Secluded WIMP Dark Matter”. In: *Phys. Lett.* B662 (2008), pages 53–61. DOI: 10.1016/j.physletb.2008.02.052. arXiv: 0711.4866 [hep-ph] (cited on page 34).
- [75] James D. Bjorken et al. “New Fixed-Target Experiments to Search for Dark Gauge Forces”. In: *Phys. Rev.* D80 (2009), page 075018. DOI: 10.1103/PhysRevD.80.075018. arXiv: 0906.0580 [hep-ph] (cited on page 34).
- [76] Gabriel Magill et al. “Millicharged particles in neutrino experiments”. In: (2018). arXiv: 1806.03310 [hep-ph] (cited on page 34).
- [77] R. Acciarri et al. “Long-Baseline Neutrino Facility (LBNF) and Deep Underground Neutrino Experiment (DUNE)”. In: (2015). arXiv: 1512.06148 [physics.ins-det] (cited on page 34).
- [78] M. Anelli et al. “A facility to Search for Hidden Particles (SHiP) at the CERN SPS”. In: (2015). arXiv: 1504.04956 [physics.ins-det] (cited on page 34).
- [79] Marco Battaglieri et al. “US Cosmic Visions: New Ideas in Dark Matter 2017: Community Report”. In: (2017). arXiv: 1707.04591 [hep-ph] (cited on page 34).
- [80] S. I. Alvis et al. “First Limit on the Direct Detection of Lightly Ionizing Particles for Electric Charge as Low as e/1000 with the Majorana Demonstrator”. In: *Phys. Rev. Lett.* 120.21 (2018), page 211804. DOI: 10.1103/PhysRevLett.120.211804. arXiv: 1801.10145 [hep-ex] (cited on page 34).

- [81] L. Lyons. “Quark Search Experiments at Accelerators and in Cosmic Rays”. In: *Phys. Rept.* 129 (1985), page 225. DOI: 10.1016/0370-1573(85)90011-0 (cited on page 35).
- [82] J. J. Aubert et al. “A Search for Free Quarks in Deep Inelastic Muon Scattering”. In: *Phys. Lett.* 133B (1983), page 461. DOI: 10.1016/0370-2693(83)90828-6 (cited on page 35).
- [83] A. E. Bondar et al. “SEARCH FOR LIGHT PARTICLES WITH CHARGE 2/3 IN e^+e^- ANNIHILATION”. In: *JETP Lett.* 40 (1984). [Pisma Zh. Eksp. Teor. Fiz. 40, 440 (1984)], pages 1265–1268 (cited on page 35).
- [84] H. Aihara et al. “Search for $q = 2/3e$ and $q = 1/3e$ particles produced in e^+e^- annihilations”. In: *Phys. Rev. Lett.* 52 (1984), page 2332. DOI: 10.1103/PhysRevLett.52.2332 (cited on page 35).
- [85] G. Abbiendi et al. “Search for stable and longlived massive charged particles in e^+e^- collisions at $s^{**}(1/2) = 130\text{-GeV}$ to 209-GeV ”. In: *Phys. Lett.* B572 (2003), pages 8–20. DOI: 10.1016/S0370-2693(03)00639-7. arXiv: hep-ex/0305031 [hep-ex] (cited on page 35).
- [86] P. Abreu et al. “Search for stable heavy charged particles in e^+e^- collisions at $s^{**}(1/2) = 130\text{-GeV}$ to 136-GeV , 161-GeV and 172-GeV ”. In: *Phys. Lett.* B396 (1997), pages 315–326. DOI: 10.1016/S0370-2693(97)00152-4 (cited on page 35).
- [87] R. Akers et al. “Search for heavy charged particles and for particles with anomalous charge in e^+e^- collisions at LEP”. In: *Z. Phys.* C67 (1995), pages 203–212. DOI: 10.1007/BF01571281 (cited on page 35).
- [88] D. Buskulic et al. “Search for particles with unexpected mass and charge in Z decays”. In: *Phys. Lett.* B303 (1993), pages 198–208. DOI: 10.1016/0370-2693(93)90066-Q (cited on page 35).
- [89] M. Banner et al. “A New Search for Relativistic Particles With Fractional Electric Charge at the CERN $p\bar{p}$ Collider”. In: *Phys. Lett.* 156B (1985), pages 129–133. DOI: 10.1016/0370-2693(85)91368-1 (cited on page 35).
- [90] F. Abe et al. “Limits on the production of massive stable charged particles”. In: *Phys. Rev.* D46 (1992), R1889–R1894. DOI: 10.1103/PhysRevD.46.R1889 (cited on page 35).
- [91] D. Acosta et al. “Search for long-lived charged massive particles in $\bar{p}p$ collisions at $\sqrt{s} = 1.8$ TeV”. In: *Phys. Rev. Lett.* 90 (2003), page 131801. DOI: 10.1103/PhysRevLett.90.131801. arXiv: hep-ex/0211064 [hep-ex] (cited on page 35).
- [92] Serguei Chatrchyan et al. “Search for fractionally charged particles in $p\bar{p}$ collisions at $\sqrt{s} = 7$ TeV”. In: *Phys. Rev.* D87.9 (2013), page 092008. DOI: 10.1103/PhysRevD.87.092008. arXiv: 1210.2311 [hep-ex] (cited on page 35).
- [93] M. Ambrosio et al. “Final search for lightly ionizing particles with the MACRO detector”. In: (2004). arXiv: hep-ex/0402006 [hep-ex] (cited on page 36).
- [94] M. Mori et al. “Search for fractionally charged particles in Kamiokande-II”. In: *Phys. Rev.* D43 (1991), pages 2843–2846. DOI: 10.1103/PhysRevD.43.2843 (cited on page 36).
- [95] G. Giacomelli and A. Margiotta. “The MACRO Experiment at Gran Sasso”. In: *Charles Peck Fest Pasadena, California, January 21, 2005*. 2007. arXiv: 0707.1691 [hep-ex] (cited on page 37).
- [96] Thomas K. Gaisser, Ralph Engel, and Elisa Resconi. *Cosmic Rays and Particle Physics*. Cambridge University Press, 2016. URL: <http://www.cambridge.org/de/academic/subjects/physics/cosmology-relativity-and-gravitation/cosmic-rays-and-particle-physics-2nd-edition?format=HB> (cited on pages 39, 42, 47, 50).
- [97] The Nobel Prize. URL: <https://www.nobelprize.org/prizes/physics/1936/ceremony-speech/> (cited on page 39).
- [98] J. Clay. *Penetrating radiation*. Volume 30. 1927, pages 1115–1127 (cited on page 40).

- [99] R. A. Millikan and G. H. Cameron. “The Origin of the Cosmic Rays”. In: *Phys. Rev.* 32 (4 Oct. 1928), pages 533–557. DOI: 10.1103/PhysRev.32.533. URL: <https://link.aps.org/doi/10.1103/PhysRev.32.533> (cited on page 40).
- [100] Thomas K. Gaisser and Todor Stanev. “High-energy cosmic rays”. In: *Nuclear Physics A* 777 (2006). Special Issue on Nuclear Astrophysics, pages 98–110. ISSN: 0375-9474. DOI: <https://doi.org/10.1016/j.nuclphysa.2005.01.024>. URL: <http://www.sciencedirect.com/science/article/pii/S0375947405000540> (cited on page 40).
- [101] Pasquale Blasi. “The Origin of Galactic Cosmic Rays”. In: *Astron. Astrophys. Rev.* 21 (2013), page 70. DOI: 10.1007/s00159-013-0070-7. arXiv: 1311.7346 [astro-ph.HE] (cited on page 41).
- [102] Thomas K. Gaisser, Todor Stanev, and Serap Tilav. “Cosmic Ray Energy Spectrum from Measurements of Air Showers”. In: *Front. Phys.(Beijing)* 8 (2013), pages 748–758. DOI: 10.1007/s11467-013-0319-7. arXiv: 1303.3565 [astro-ph.HE] (cited on pages 41–43, 92, 95, 150).
- [103] M A Malkov and L O’C Drury. “Nonlinear theory of diffusive acceleration of particles by shock waves”. In: *Reports on Progress in Physics* 64.4 (2001), page 429. URL: <http://stacks.iop.org/0034-4885/64/i=4/a=201> (cited on page 42).
- [104] “Detection of the Small Magellanic Cloud in gamma-rays with Fermi/LAT”. In: *Astron. Astrophys.* 523 (2010), A46. DOI: 10.1051/0004-6361/201014855. arXiv: 1008.2127 [astro-ph.HE] (cited on page 42).
- [105] M. Ackermann et al. “Detection of the Characteristic Pion-Decay Signature in Supernova Remnants”. In: *Science* 339 (2013), page 807. DOI: 10.1126/science.1231160. arXiv: 1302.3307 [astro-ph.HE] (cited on page 42).
- [106] W. D. Apel et al. “Kneelike structure in the spectrum of the heavy component of cosmic rays observed with KASCADE-Grande”. In: *Phys. Rev. Lett.* 107 (2011), page 171104. DOI: 10.1103/PhysRevLett.107.171104. arXiv: 1107.5885 [astro-ph.HE] (cited on page 43).
- [107] A. P. Garyaka et al. “All-particle primary energy spectrum in the 3-200 PeV energy range”. In: *J. Phys.* G35 (2008), page 115201. DOI: 10.1088/0954-3899/35/11/115201. arXiv: 0808.1421 [astro-ph] (cited on page 43).
- [108] Kenneth Greisen. “End to the cosmic ray spectrum?” In: *Phys. Rev. Lett.* 16 (1966), pages 748–750. DOI: 10.1103/PhysRevLett.16.748 (cited on page 43).
- [109] G. T. Zatsepin and V. A. Kuzmin. “Upper limit of the spectrum of cosmic rays”. In: *JETP Lett.* 4 (1966). [*Pisma Zh. Eksp. Teor. Fiz.* 4,114(1966)], pages 78–80 (cited on page 43).
- [110] J. Bellido et al. “Proceedings of Science”. In: *ICRC* 301 (506 2017) (cited on page 43).
- [111] D. Allard et al. “Implications of the cosmic ray spectrum for the mass composition at the highest energies”. In: *JCAP* 0810 (2008), page 033. DOI: 10.1088/1475-7516/2008/10/033. arXiv: 0805.4779 [astro-ph] (cited on page 44).
- [112] A. M. Hillas. “The Origin of Ultrahigh-Energy Cosmic Rays”. In: *Ann. Rev. Astron. Astrophys.* 22 (1984), pages 425–444. DOI: 10.1146/annurev.aa.22.090184.002233 (cited on page 44).
- [113] Pablo M. Bauleo and Julio Rodriguez Martino. “The dawn of the particle astronomy era in ultra-high-energy cosmic rays”. In: *Nature* 458N7240 (2009), pages 847–851. DOI: 10.1038/nature07948 (cited on page 45).
- [114] M. Nagano and Alan A. Watson. “Observations and implications of the ultrahigh-energy cosmic rays”. In: *Rev. Mod. Phys.* 72 (2000), pages 689–732. DOI: 10.1103/RevModPhys.72.689 (cited on page 44).

- [115] Alexander Aab et al. “Observation of a Large-scale Anisotropy in the Arrival Directions of Cosmic Rays above 8×10^{18} eV”. In: *Science* 357.6537 (2017), pages 1266–1270. DOI: 10.1126/science.aan4338. arXiv: 1709.07321 [astro-ph.HE] (cited on page 44).
- [116] E. Waxman. “IceCube’s Neutrinos: The beginning of extra-Galactic neutrino astrophysics?” In: *Proceedings, 9th Rencontres du Vietnam: Windows on the Universe: Quy Nhon, Vietnam, August 11-17, 2013.* 2013, pages 161–168. arXiv: 1312.0558 [astro-ph.HE] (cited on page 44).
- [117] P. O. Lagage and C. J. Cesarsky. “The maximum energy of cosmic rays accelerated by supernova shocks”. In: *Astron. Astrophys.* 125 (1983), pages 249–257 (cited on page 49).
- [118] T. Stanev. *High Energy Cosmic Rays*. Springer Praxis Books. Springer Berlin Heidelberg, 2010. ISBN: 9783540851486. URL: <https://books.google.be/books?id=1y9YEYHafBMC> (cited on page 49).
- [119] C. Megan Urry and Paolo Padovani. “Unified schemes for radio-loud active galactic nuclei”. In: *Publ. Astron. Soc. Pac.* 107 (1995), page 803. DOI: 10.1086/133630. arXiv: astro-ph/9506063 [astro-ph] (cited on page 49).
- [120] Robert Antonucci. “Unified models for active galactic nuclei and quasars”. In: *Ann. Rev. Astron. Astrophys.* 31 (1993), pages 473–521. DOI: 10.1146/annurev.aa.31.090193.002353 (cited on page 49).
- [121] Demosthenes Kazanas et al. “Toward a Unified AGN Structure”. In: (2012). arXiv: 1206.5022 [astro-ph.HE] (cited on page 49).
- [122] J. Abraham et al. “Correlation of the highest-energy cosmic rays with the positions of nearby active galactic nuclei”. In: *Astropart. Phys.* 29 (2008). [Erratum: *Astropart. Phys.* 30,45(2008)], pages 188–204. DOI: 10.1016/j.astropartphys.2008.06.004, 10.1016/j.astropartphys.2008.01.002. arXiv: 0712.2843 [astro-ph] (cited on page 49).
- [123] Ray W. Klebesadel, Ian B. Strong, and Roy A. Olson. “Observations of Gamma-Ray Bursts of Cosmic Origin”. In: *Astrophys. J.* 182 (1973), pages L85–L88. DOI: 10.1086/181225 (cited on page 50).
- [124] C. A. Meegan et al. “Spatial distribution of gamma-ray bursts observed by BATSE”. In: *Nature* 355 (1992), pages 143–145. DOI: 10.1038/355143a0 (cited on page 50).
- [125] B. P. Abbott et al. “GW170817: Observation of Gravitational Waves from a Binary Neutron Star Inspiral”. In: *Phys. Rev. Lett.* 119.16 (2017), page 161101. DOI: 10.1103/PhysRevLett.119.161101. arXiv: 1710.05832 [gr-qc] (cited on page 50).
- [126] B. P. Abbott et al. “GW170814: A Three-Detector Observation of Gravitational Waves from a Binary Black Hole Coalescence”. In: *Phys. Rev. Lett.* 119.14 (2017), page 141101. DOI: 10.1103/PhysRevLett.119.141101. arXiv: 1709.09660 [gr-qc] (cited on page 50).
- [127] B.. P.. Abbott et al. “GW170608: Observation of a 19-solar-mass Binary Black Hole Coalescence”. In: *Astrophys. J.* 851.2 (2017), page L35. DOI: 10.3847/2041-8213/aa9f0c. arXiv: 1711.05578 [astro-ph.HE] (cited on page 50).
- [128] Benjamin P. Abbott et al. “GW170104: Observation of a 50-Solar-Mass Binary Black Hole Coalescence at Redshift 0.2”. In: *Phys. Rev. Lett.* 118.22 (2017). [Erratum: *Phys. Rev. Lett.* 121,no.12,129901(2018)], page 221101. DOI: 10.1103/PhysRevLett.118.221101, 10.1103/PhysRevLett.121.129901. arXiv: 1706.01812 [gr-qc] (cited on page 50).
- [129] B. P. Abbott et al. “GW151226: Observation of Gravitational Waves from a 22-Solar-Mass Binary Black Hole Coalescence”. In: *Phys. Rev. Lett.* 116.24 (2016), page 241103. DOI: 10.1103/PhysRevLett.116.241103. arXiv: 1606.04855 [gr-qc] (cited on page 50).
- [130] F. Acero. “Detection of Gamma Rays From a Starburst Galaxy”. In: *Science* 326 (2009), page 1080. DOI: 10.1126/science.1178826. arXiv: 0909.4651 [astro-ph.HE] (cited on page 50).

- [131] Niklas Karlsson. “Discovery of VHE Gamma-ray Emission from the Starburst Galaxy M82”. In: (2009). arXiv: 0912.3807 [astro-ph.HE] (cited on page 50).
- [132] Kohta Murase, Susumu Inoue, and Shigehiro Nagataki. “Cosmic Rays above the Second Knee from Clusters of Galaxies and Associated High-Energy Neutrino Emission”. In: *The Astrophysical Journal Letters* 689.2 (2008), page L105. URL: <http://stacks.iop.org/1538-4357/689/i=2/a=L105> (cited on page 50).
- [133] C. Grupen. *Astroparticle physics*. 2005. ISBN: 9783540253129. URL: <http://www.springer.com/book/3-540-25312-2> (cited on pages 51, 52).
- [134] U. F. Katz and Ch. Spiering. “High-Energy Neutrino Astrophysics: Status and Perspectives”. In: *Prog. Part. Nucl. Phys.* 67 (2012), pages 651–704. DOI: 10.1016/j.ppnp.2011.12.001. arXiv: 1111.0507 [astro-ph.HE] (cited on page 53).
- [135] Morihiro Honda et al. “Calculation of atmospheric neutrino flux using the interaction model calibrated with atmospheric muon data”. In: *Phys. Rev. D* 75 (2007), page 043006. DOI: 10.1103/PhysRevD.75.043006. arXiv: astro-ph/0611418 [astro-ph] (cited on pages 54, 93–95, 150).
- [136] M. G. Aartsen et al. “The IceCube Neutrino Observatory - Contributions to ICRC 2017 Part II: Properties of the Atmospheric and Astrophysical Neutrino Flux”. In: (2017). arXiv: 1710.01191 [astro-ph.HE] (cited on page 55).
- [137] Kiyoshi Niu, Eiko Mikumo, and Yasuko Maeda. “A Possible Decay in Flight of a New Type Particle”. In: *Progress of Theoretical Physics* 46.5 (1971), pages 1644–1646. DOI: 10.1143/PTP.46.1644. eprint: /oup/backfile/content_public/journal/ptp/46/5/10.1143/ptp.46.1644/2/46-5-1644.pdf. URL: <http://dx.doi.org/10.1143/PTP.46.1644> (cited on page 54).
- [138] Rikard Enberg, Mary Hall Reno, and Ina Sarcevic. “Prompt neutrino fluxes from atmospheric charm”. In: *Phys. Rev. D* 78 (2008), page 043005. DOI: 10.1103/PhysRevD.78.043005. arXiv: 0806.0418 [hep-ph] (cited on pages 55, 93–95).
- [139] M. G. Aartsen et al. “Multimessenger observations of a flaring blazar coincident with high-energy neutrino IceCube-170922A”. In: *Science* 361.6398 (2018), eaat1378. DOI: 10.1126/science.aat1378. arXiv: 1807.08816 [astro-ph.HE] (cited on page 55).
- [140] Kate Scholberg. “Supernova Neutrino Detection”. In: *Ann. Rev. Nucl. Part. Sci.* 62 (2012), pages 81–103. DOI: 10.1146/annurev-nucl-102711-095006. arXiv: 1205.6003 [astro-ph.IM] (cited on page 55).
- [141] Lutz Kopke. “Supernova Neutrino Detection with IceCube”. In: *J. Phys. Conf. Ser.* 309 (2011), page 012029. DOI: 10.1088/1742-6596/309/1/012029. arXiv: 1106.6225 [astro-ph.HE] (cited on page 56).
- [142] Aya Ishihara. “Diffuse Neutrino Fluxes and GZK Neutrinos with IceCube”. In: *JPS Conf. Proc.* 15 (2017), page 011008. DOI: 10.7566/JPSCP.15.011008 (cited on page 56).
- [143] nobel1958. URL: <https://www.nobelprize.org/prizes/physics/1958/summary/> (cited on page 57).
- [144] M. G. Aartsen et al. “Measurements using the inelasticity distribution of multi-TeV neutrino interactions in IceCube”. In: (2018). arXiv: 1808.07629 [hep-ex] (cited on page 60).
- [145] “Design, Implementation and Test of a New Feature Extractor for the IceCube Neutrino Observatory”. In: (2010) (cited on page 60).
- [146] Paul H. Barrett et al. “Interpretation of Cosmic-Ray Measurements Far Underground”. In: *Rev. Mod. Phys.* 24.3 (1952), pages 133–178. DOI: 10.1103/RevModPhys.24.133 (cited on page 62).

- [147] Dmitry Chirkin and Wolfgang Rhode. “Muon Monte Carlo: A High-precision tool for muon propagation through matter”. In: (2004). arXiv: hep-ph/0407075 [hep-ph] (cited on pages 63–66).
- [148] Dmitry Chirkin. “Study of South Pole ice transparency with IceCube flashers”. In: *Proceedings, 32nd International Cosmic Ray Conference (ICRC 2011): Beijing, China, August 11-18, 2011*. Volume 4, page 161. DOI: 10.7529/ICRC2011/V04/0333 (cited on pages 63, 98).
- [149] S. R. Kelner, R. P. Kokoulin, and A. A. Petrukhin. “About cross-section for high-energy muon bremsstrahlung”. In: (1995) (cited on page 65).
- [150] AMANDA collaboration. URL: <http://amanda.uci.edu/> (cited on page 67).
- [151] E. Andres et al. “The AMANDA neutrino telescope: Principle of operation and first results”. In: *Astropart. Phys.* 13 (2000), pages 1–20. DOI: 10.1016/S0927-6505(99)00092-4. arXiv: astro-ph/9906203 [astro-ph] (cited on page 67).
- [152] J. Ahrens et al. “Observation of high-energy atmospheric neutrinos with the Antarctic Muon and Neutrino Detector Array”. In: *Phys. Rev.* D66 (2002), page 012005. DOI: 10.1103/PhysRevD.66.012005. arXiv: astro-ph/0205109 [astro-ph] (cited on page 67).
- [153] R. Abbasi et al. “The Design and Performance of IceCube DeepCore”. In: *Astropart. Phys.* 35 (2012), pages 615–624. DOI: 10.1016/j.astropartphys.2012.01.004. arXiv: 1109.6096 [astro-ph.IM] (cited on page 69).
- [154] Nicholas Choma et al. “Graph Neural Networks for IceCube Signal Classification”. In: (2018). arXiv: 1809.06166 [cs.LG] (cited on page 70).
- [155] M. G. Aartsen et al. “The IceCube Neutrino Observatory: Instrumentation and Online Systems”. In: *JINST* 12.03 (2017), P03012. DOI: 10.1088/1748-0221/12/03/P03012. arXiv: 1612.05093 [astro-ph.IM] (cited on pages 71, 73, 74).
- [156] R. Abbasi et al. “Calibration and Characterization of the IceCube Photomultiplier Tube”. In: *Nucl. Instrum. Meth.* A618 (2010), pages 139–152. DOI: 10.1016/j.nima.2010.03.102. arXiv: 1002.2442 [astro-ph.IM] (cited on pages 71, 99).
- [157] M. G. Aartsen et al. “Measurement of South Pole ice transparency with the IceCube LED calibration system”. In: *Nucl. Instrum. Meth.* A711 (2013), pages 73–89. DOI: 10.1016/j.nima.2013.01.054. arXiv: 1301.5361 [astro-ph.IM] (cited on pages 72, 79).
- [158] M. G. Aartsen et al. “The IceCube Realtime Alert System”. In: *Astropart. Phys.* 92 (2017), pages 30–41. DOI: 10.1016/j.astropartphys.2017.05.002. arXiv: 1612.06028 [astro-ph.HE] (cited on page 77).
- [159] Dariusz Góra. “High-Energy Gamma-Ray Follow-Up Program Using Neutrino Triggers from IceCube”. In: *Proceedings, 33rd International Cosmic Ray Conference (ICRC2013): Rio de Janeiro, Brazil, July 2-9, 2013*, page 0537. URL: <http://www.cbpf.br/%7Eicrc2013/papers/icrc2013-0537.pdf> (cited on page 77).
- [160] The IceCube Collaboration. URL: https://wiki.icecube.wisc.edu/index.php/Pass2_Re-Processing (cited on pages 78, 99).
- [161] The IceCube Collaboration. URL: https://docushare.icecube.wisc.edu/dsweb/Get/Document-56552/dst_proposal_2011.pdf (cited on page 78).
- [162] M. G. Aartsen et al. “Search for steady point-like sources in the astrophysical muon neutrino flux with 8 years of IceCube data”. In: (2018). arXiv: 1811.07979 [hep-ph] (cited on page 78).
- [163] The IceCube Collaboration. URL: https://icecube.wisc.edu/~kjero/Bootcamp/2015/Notebooks/Reconstruction_Introduction.html (cited on page 79).

- [164] M. Ackermann et al. “Optical properties of deep glacial ice at the South Pole”. In: *J. Geophys. Res. Atmos.* 111.D13 (2006), page D13203. DOI: 10.1029/2005JD006687 (cited on pages 79, 80).
- [165] Dmitry Chirkin. “Evidence of optical anisotropy of the South Pole ice”. In: *Proceedings, 33rd International Cosmic Ray Conference (ICRC2013): Rio de Janeiro, Brazil, July 2-9, 2013*, page 0580. URL: <http://www.cbpf.br/%7Eicrc2013/papers/icrc2013-0580.pdf> (cited on pages 80, 81).
- [166] Samridha Kunwar et al. “The IceTop Scintillator Upgrade”. In: *PoS ICRC2017* (2018), page 401. DOI: 10.22323/1.301.0401 (cited on page 81).
- [167] Jan Auffenberg. “IceAct: Imaging Air Cherenkov Telescopes with SiPMs at the South Pole for IceCube-Gen2”. In: *PoS ICRC2017* (2018), page 1055. DOI: 10.22323/1.301.1055 (cited on page 81).
- [168] Satoshi Shimizu et al. “Overview and performance of the D-Egg optical sensor for IceCube-Gen2”. In: *PoS ICRC2017* (2018), page 1051. DOI: 10.22323/1.301.1051 (cited on page 81).
- [169] Lew Classen et al. “The mDOM - A multi-PMT digital optical module for the IceCube-Gen2 neutrino telescope”. In: *PoS ICRC2017* (2018), page 1047. DOI: 10.22323/1.301.1047 (cited on page 81).
- [170] M. Jeong and W. Kang. “A camera system for IceCube-Gen2”. In: *PoS ICRC2017* (2018), page 1040. DOI: 10.22323/1.301.1040 (cited on page 81).
- [171] Elisa Resconi, Kai Krings, and Kai Krings Martin Rongen. “The Precision Optical CALibration Module for IceCube-Gen2: First Prototype”. In: *PoS ICRC2017* (2018), page 934. DOI: 10.22323/1.301.0934 (cited on page 81).
- [172] Erik Blaufuss, C. Kopper, and C. Haack. “The IceCube-Gen2 High Energy Array”. In: *PoS ICRC2015* (2016), page 1146. DOI: 10.22323/1.236.1146 (cited on page 82).
- [173] Markus Ahlers and Francis Halzen. “Pinpointing Extragalactic Neutrino Sources in Light of Recent IceCube Observations”. In: *Phys. Rev. D90.4* (2014), page 043005. DOI: 10.1103/PhysRevD.90.043005. arXiv: 1406.2160 [astro-ph.HE] (cited on page 82).
- [174] Sebastian Euler, Javier Gonzalez, and Ben Roberts. “Simulation Studies for a Surface Veto Array to Identify Astrophysical Neutrinos at the South Pole”. In: *PoS ICRC2015* (2016), page 1070. DOI: 10.22323/1.236.1070 (cited on page 83).
- [175] Frank G. Schröder. “Radio detection of Cosmic-Ray Air Showers and High-Energy Neutrinos”. In: *Prog. Part. Nucl. Phys.* 93 (2017), pages 1–68. DOI: 10.1016/j.ppnp.2016.12.002. arXiv: 1607.08781 [astro-ph.IM] (cited on page 83).
- [176] P. Allison et al. “Performance of two Askaryan Radio Array stations and first results in the search for ultrahigh energy neutrinos”. In: *Phys. Rev. D93.8* (2016), page 082003. DOI: 10.1103/PhysRevD.93.082003. arXiv: 1507.08991 [astro-ph.HE] (cited on page 83).
- [177] Christian Glaser. “ARIANNA: Measurement of cosmic rays with a radio neutrino detector in Antarctica”. In: *Acoustic and Radio EeV Neutrino Detection Activities (ARENA 2018) Catania, Italy, June 12-15, 2018*. 2018. arXiv: 1811.10661 [astro-ph.IM] (cited on page 83).
- [178] Don Colladay and V. Alan Kostelecky. “Lorentz violating extension of the standard model”. In: *Phys. Rev. D58* (1998), page 116002. DOI: 10.1103/PhysRevD.58.116002. arXiv: hep-ph/9809521 [hep-ph] (cited on page 84).
- [179] M. G. Aartsen et al. “Neutrino Interferometry for High-Precision Tests of Lorentz Symmetry with IceCube”. In: *Nature Phys.* 14.9 (2018), pages 961–966. DOI: 10.1038/s41567-018-0172-2. arXiv: 1709.03434 [hep-ex] (cited on page 84).

- [180] R. Abbasi et al. “Search for a Lorentz-violating sidereal signal with atmospheric neutrinos in IceCube”. In: *Phys. Rev.* D82 (2010), page 112003. DOI: 10.1103/PhysRevD.82.112003. arXiv: 1010.4096 [astro-ph.HE] (cited on page 84).
- [181] M. G. Aartsen et al. “Search for Neutrinos from Dark Matter Self-Anihilations in the center of the Milky Way with 3 years of IceCube/DeepCore”. In: *Eur. Phys. J.* C77.9 (2017), page 627. DOI: 10.1140/epjc/s10052-017-5213-y. arXiv: 1705.08103 [hep-ex] (cited on page 85).
- [182] M. G. Aartsen et al. “Search for annihilating dark matter in the Sun with 3 years of IceCube data”. In: *Eur. Phys. J.* C77.3 (2017), page 146. DOI: 10.1140/epjc/s10052-017-4689-9. arXiv: 1612.05949 [astro-ph.HE] (cited on page 85).
- [183] R. Abbasi et al. “Limits on a muon flux from Kaluza-Klein dark matter annihilations in the Sun from the IceCube 22-string detector”. In: *Phys. Rev.* D81 (2010), page 057101. DOI: 10.1103/PhysRevD.81.057101. arXiv: 0910.4480 [astro-ph.CO] (cited on page 85).
- [184] M. G. Aartsen et al. “First search for dark matter annihilations in the Earth with the IceCube Detector”. In: *Eur. Phys. J.* C77.2 (2017), page 82. DOI: 10.1140/epjc/s10052-016-4582-y. arXiv: 1609.01492 [astro-ph.HE] (cited on pages 85, 144, 146).
- [185] “Quantised singularities in the electromagnetic field,” in: *Proceedings of the Royal Society of London A: Mathematical, Physical and Engineering Sciences* 133.821 (1931), pages 60–72. ISSN: 0950-1207. DOI: 10.1098/rspa.1931.0130. eprint: <http://rspa.royalsocietypublishing.org/content/133/821/60.full.pdf>. URL: <http://rspa.royalsocietypublishing.org/content/133/821/60> (cited on page 85).
- [186] G.’t Hooft. “Magnetic monopoles in unified gauge theories”. In: *Nuclear Physics B* 79.2 (1974), pages 276–284. ISSN: 0550-3213. DOI: [https://doi.org/10.1016/0550-3213\(74\)90486-6](https://doi.org/10.1016/0550-3213(74)90486-6). URL: <http://www.sciencedirect.com/science/article/pii/0550321374904866> (cited on page 86).
- [187] Alexander M. Polyakov. “Particle Spectrum in the Quantum Field Theory”. In: *JETP Lett.* 20 (1974). [,300(1974)], pages 194–195 (cited on page 86).
- [188] M. G. Aartsen et al. “Search for non-relativistic Magnetic Monopoles with IceCube”. In: *Eur. Phys. J.* C74.7 (2014), page 2938. DOI: 10.1140/epjc/s10052-014-2938-8. arXiv: 1402.3460 [astro-ph.CO] (cited on page 86).
- [189] D Schultz. “IceProd 2: A Next Generation Data Analysis Framework for the IceCube Neutrino Observatory”. In: *Journal of Physics: Conference Series* 664.6 (2015), page 062056. URL: <http://stacks.iop.org/1742-6596/664/i=6/a=062056> (cited on page 91).
- [190] D. Heck et al. “CORSIKA: A Monte Carlo code to simulate extensive air showers”. In: (1998) (cited on page 91).
- [191] Ralph Engel et al. “Towards the next generation of CORSIKA: A framework for the simulation of particle cascades in astroparticle physics”. In: (2018). arXiv: 1808.08226 [astro-ph.IM] (cited on page 91).
- [192] Sergey Ostapchenko. “Monte Carlo treatment of hadronic interactions in enhanced Pomeron scheme: I. QGSJET-II model”. In: *Phys. Rev.* D83 (2011), page 014018. DOI: 10.1103/PhysRevD.83.014018. arXiv: 1010.1869 [hep-ph] (cited on page 92).
- [193] Felix Riehn et al. “The hadronic interaction model SIBYLL 2.3c and Feynman scaling”. In: *PoS ICRC2017* (2018). [35,301(2017)], page 301. DOI: 10.22323/1.301.0301. arXiv: 1709.07227 [hep-ph] (cited on page 92).
- [194] T. Pierog et al. “EPOS LHC: Test of collective hadronization with data measured at the CERN Large Hadron Collider”. In: *Phys. Rev.* C92.3 (2015), page 034906. DOI: 10.1103/PhysRevC.92.034906. arXiv: 1306.0121 [hep-ph] (cited on page 92).
- [195] Sam De Ridder. “Sensitivity of IceCube Cosmic Ray measurements for the hadronic interaction models”. PhD thesis. UGent, 2019 (cited on pages 92, 93).

- [196] Giuseppe Battistoni et al. “Overview of the FLUKA code”. In: *Annals Nucl. Energy* 82 (2015), pages 10–18. DOI: 10.1016/j.anucene.2014.11.007 (cited on page 92).
- [197] K. Rawlins. “Cosmic ray spectrum and composition from three years of IceTop and IceCube”. In: *J. Phys. Conf. Ser.* 718.5 (2016), page 052033. DOI: 10.1088/1742-6596/718/5/052033 (cited on page 93).
- [198] Alessio Porcelli. “Measurements of the first two moments of the depth of shower maximum over nearly three decades of energy, combining data from”. In: *PoS ICRC2015* (2016), page 420. DOI: 10.22323/1.236.0420 (cited on page 93).
- [199] John Belz. “Summary of UHECR composition measurements by the Telescope Array Experiment”. In: *PoS ICRC2015* (2016), page 351. DOI: 10.22323/1.236.0351 (cited on page 93).
- [200] H. P. Dembinski et al. “Report on Tests and Measurements of Hadronic Interaction Properties with Air Showers”. In: 2019. arXiv: 1902.08124 [astro-ph.HE] (cited on page 93).
- [201] Askhat Gazizov and Marek P. Kowalski. “ANIS: High energy neutrino generator for neutrino telescopes”. In: *Comput. Phys. Commun.* 172 (2005), pages 203–213. DOI: 10.1016/j.cpc.2005.03.113. arXiv: astro-ph/0406439 [astro-ph] (cited on page 93).
- [202] M. G. Aartsen et al. “Observation of High-Energy Astrophysical Neutrinos in Three Years of IceCube Data”. In: *Phys. Rev. Lett.* 113 (2014), page 101101. DOI: 10.1103/PhysRevLett.113.101101. arXiv: 1405.5303 [astro-ph.HE] (cited on pages 93–95).
- [203] C. Andreopoulos et al. “The GENIE Neutrino Monte Carlo Generator”. In: *Nucl. Instrum. Meth.* A614 (2010), pages 87–104. DOI: 10.1016/j.nima.2009.12.009. arXiv: 0905.2517 [hep-ph] (cited on page 94).
- [204] Costas Andreopoulos et al. “The GENIE Neutrino Monte Carlo Generator: Physics and User Manual”. In: (2015). arXiv: 1510.05494 [hep-ph] (cited on page 94).
- [205] M. Honda et al. “Atmospheric neutrino flux calculation using the NRLMSISE-00 atmospheric model”. In: *Phys. Rev.* D92.2 (2015), page 023004. DOI: 10.1103/PhysRevD.92.023004. arXiv: 1502.03916 [astro-ph.HE] (cited on pages 94, 95).
- [206] Mario Dunsch et al. “Recent Improvements for the Lepton Propagator PROPOSAL”. In: (2018). arXiv: 1809.07740 [hep-ph] (cited on page 97).
- [207] Johan Lundberg et al. “Light tracking for glaciers and oceans: Scattering and absorption in heterogeneous media with Photonics”. In: *Nucl. Instrum. Meth.* A581 (2007), pages 619–631. DOI: 10.1016/j.nima.2007.07.143. arXiv: astro-ph/0702108 [ASTRO-PH] (cited on page 98).
- [208] K. J. Ma et al. “Time and Amplitude of Afterpulse Measured with a Large Size Photomultiplier Tube”. In: *Nucl. Instrum. Meth.* A629 (2011), pages 93–100. DOI: 10.1016/j.nima.2010.11.095. arXiv: 0911.5336 [physics.ins-det] (cited on page 99).
- [209] J. Ahrens et al. “Muon track reconstruction and data selection techniques in AMANDA”. In: *Nucl. Instrum. Meth.* A524 (2004), pages 169–194. DOI: 10.1016/j.nima.2004.01.065. arXiv: astro-ph/0407044 [astro-ph] (cited on pages 102–105).
- [210] M. G. Aartsen et al. “Improvement in Fast Particle Track Reconstruction with Robust Statistics”. In: *Nucl. Instrum. Meth.* A736 (2014), pages 143–149. DOI: 10.1016/j.nima.2013.10.074. arXiv: 1308.5501 [astro-ph.IM] (cited on page 103).
- [211] Till Neunhoffer. “Estimating the angular resolution of tracks in neutrino telescopes based on a likelihood analysis”. In: *Astropart. Phys.* 25 (2006), pages 220–225. DOI: 10.1016/j.astropartphys.2006.01.002. arXiv: astro-ph/0403367 [astro-ph] (cited on page 107).
- [212] The IceCube Collaboration. URL: https://internal-apps.icecube.wisc.edu/reports/data/icecube/2014/04/001/icecube_201404001_v1.pdf (cited on page 107).

- [213] M. G. Aartsen et al. “Energy Reconstruction Methods in the IceCube Neutrino Telescope”. In: *JINST* 9 (2014), P03009. DOI: 10.1088/1748-0221/9/03/P03009. arXiv: 1311.4767 [physics.ins-det] (cited on page 107).
- [214] D. Góra et al. *Studies on millipede, IceCube Internal Report: icecube/201404001*. (Cited on page 108).
- [215] Stef Verpoest. URL: https://lib.ugent.be/fulltxt/RUG01/002/479/620/RUG01-002479620_2018_0001_AC.pdf (cited on page 108).
- [216] URL: https://wiki.icecube.wisc.edu/index.php/SLC_hit_cleaning (cited on page 109).
- [217] URL: <https://www.dissertations.se/dissertation/fef1f8e4ba/> (cited on pages 110–112).
- [218] Hanchuan Peng, Fuhui Long, and C. Ding. “Feature selection based on mutual information criteria of max-dependency, max-relevance, and min-redundancy”. In: *IEEE Transactions on Pattern Analysis and Machine Intelligence* 27.8 (Aug. 2005), pages 1226–1238. ISSN: 0162-8828. DOI: 10.1109/TPAMI.2005.159 (cited on page 113).
- [219] Yoav Freund and Robert E Schapire. “A Decision-Theoretic Generalization of On-Line Learning and an Application to Boosting”. In: *Journal of Computer and System Sciences* 51.1 (1997), pages 119–139. ISSN: 0022-0000. DOI: <https://doi.org/10.1006/jcss.1997.1504>. URL: <http://www.sciencedirect.com/science/article/pii/S002200009791504X> (cited on page 115).
- [220] S. Fink C. Böser and S. Röcker. *Introduction to boosted decision trees: A multivariate approach to clasification problems*. Presented at the KSETA Doctoral Workshop, Berlin, Germany. July 2014 (cited on page 117).
- [221] The IceCube Collaboration. URL: <https://docushare.icecube.wisc.edu/dsweb/Get/Document-56551/VEFproposal.pdf> (cited on page 121).
- [222] The IceCube Collaboration. URL: https://docushare.icecube.wisc.edu/dsweb/Get/Document-59303/lowup_2012_proposal.pdf (cited on page 121).
- [223] The IceCube Collaboration. URL: https://docushare.icecube.wisc.edu/dsweb/Get/Document-59906/MuonFilter2012_v3_with_addendum.pdf (cited on page 121).
- [224] The IceCube Collaboration. URL: <https://docushare.icecube.wisc.edu/dsweb/Get/Document-59728/onlinel2proposal2012.pdf> (cited on page 121).
- [225] The IceCube Collaboration. URL: <https://docushare.icecube.wisc.edu/dsweb/Get/Document-59397/DeepCoreFilterProposal.pdf> (cited on page 123).
- [226] The IceCube Collaboration. URL: https://wiki.icecube.wisc.edu/index.php/Effects_of_DOM_Mainboard_Release_443 (cited on page 123).
- [227] Peter Nießen. “Search for relativistic magnetic monopoles with the AMANDA detector”. PhD thesis. Humboldt-Universität zu Berlin, Mathematisch-Naturwissenschaftliche Fakultät I, 2001. DOI: <http://dx.doi.org/10.18452/14579> (cited on page 130).
- [228] S. Verpoest. “Search for particles with fractional charges in IceCube based on anomalous energy loss”. Master’s thesis. UGent, 2018 (cited on page 134).
- [229] J. Künnen. “A Search for Dark Matter in the Center of the Earth with the IceCube Neutrino Detector”. Master’s thesis. VUB, 2015 (cited on page 138).
- [230] The IceCube Collaboration. URL: <http://software.icecube.wisc.edu/documentation/projects/pybdt/> (cited on page 141).
- [231] R. J. Britto, B. S. Acharya, and G. C. Anupama. “Data analysis method for the search of point sources of gamma rays with the HAGAR telescope array”. In: *Proceedings, 32nd International Cosmic Ray Conference (ICRC 2011): Beijing, China, August 11-18, 2011*. Volume 9, page 142. DOI: 10.7529/ICRC2011/V09/0943 (cited on page 144).

-
- [232] M. G. Aartsen et al. “Searches for Relativistic Magnetic Monopoles in IceCube”. In: *Eur. Phys. J.* C76.3 (2016), page 133. DOI: 10.1140/epjc/s10052-016-3953-8. arXiv: 1511.01350 [astro-ph.HE] (cited on pages 144, 146).
 - [233] F. Scheriau. “Data-Mining in der Astroteilchenphysik”. Master’s thesis. University of Dortmund, 2014 (cited on page 144).
 - [234] Gary J. Feldman and Robert D. Cousins. “A Unified approach to the classical statistical analysis of small signals”. In: *Phys. Rev.* D57 (1998), pages 3873–3889. DOI: 10.1103/PhysRevD.57.3873. arXiv: physics/9711021 [physics.data-an] (cited on page 146).
 - [235] Gary C. Hill and Katherine Rawlins. “Unbiased cut selection for optimal upper limits in neutrino detectors: The Model rejection potential technique”. In: *Astropart. Phys.* 19 (2003), pages 393–402. DOI: 10.1016/S0927-6505(02)00240-2. arXiv: astro-ph/0209350 [astro-ph] (cited on page 147).
 - [236] Thomas K. Gaisser. “Spectrum of cosmic-ray nucleons, kaon production, and the atmospheric muon charge ratio”. In: *Astropart. Phys.* 35 (2012), pages 801–806. DOI: 10.1016/j.astropartphys.2012.02.010. arXiv: 1111.6675 [astro-ph.HE] (cited on page 150).
 - [237] G. D. Barr et al. “Three-dimensional calculation of atmospheric neutrinos”. In: *Phys. Rev. D* 70 (2 July 2004), page 023006. DOI: 10.1103/PhysRevD.70.023006. URL: <https://link.aps.org/doi/10.1103/PhysRevD.70.023006> (cited on page 150).
 - [238] Joerg R. Hoerandel. “On the knee in the energy spectrum of cosmic rays”. In: *Astropart. Phys.* 19 (2003), pages 193–220. DOI: 10.1016/S0927-6505(02)00198-6. arXiv: astro-ph/0210453 [astro-ph] (cited on page 150).
 - [239] Aaron Roodman. “Blind analysis in particle physics”. In: *eConf* C030908 (2003). [,166(2003)], TUIT001. arXiv: physics/0312102 [physics.data-an] (cited on page 153).